

Dual-Axis Tilting Quadrotor Aircraft

An investigation into the overactuatedness and control thereof



Nicholas Von Klemperer

Department of Electrical Engineering
University of Cape Town
Rondebosch, Cape Town
South Africa

October 2017

MSc thesis submitted in fulfillment of the requirements for the degree of Masters of Science in the
Department of Electrical Engineering at the University of Cape Town

Keywords: Non-linear, control, allocation, quadrotor, UAV

”We’re gonna have a superconductor turned up full blast and pointed at you for the duration of this next test. I’ll be honest, we’re throwing science at the wall here to see what sticks. No idea what it’ll do.

Probably nothing. Best-case scenario, you might get some superpowers...”

Cave Johnson -Founder & CEO of Aperture Science

Declaration

I, Nicholas Von Klemperer, hereby:

1. grant the University of Cape Town free license to reproduce the above thesis in whole or in part, for the purpose of research only;
2. declare that:
 - (a) This thesis is my own unaided work, both in concept and execution, and apart from the normal guidance from my supervisor, I have received no assistance except as stated below:
 - (b) Neither the substance nor any part of the above thesis has been submitted in the past, or is being, or is to be submitted for a degree at this University or at any other university, except as stated below.
 - (c) Unless otherwise stated or cited, any and all illustrations or diagrams demonstrated in this work are my own productions.
 - (d) All the content used to compile this report and complete the investigation revolving around the whole project is collectively hosted on the following GIT repositories:
 - LATEXreport: <https://github.com/nickvonklemp/Masters-Report>
 - STM32F303 projects: <https://github.com/nickvonklemp/Code>
 - Hardware Schematics: <https://github.com/nickvonklemp/visio> &
 - EagleCad Schematics <https://github.com/nickvonklemp/Eagle>
 - MatLab Simulink Code: <https://github.com/nickvonklemp/Simulink>
 - Results & Simulation Data: <https://github.com/nickvonklemp/results>
 - All CAD design files & assemblies: <https://grabcad.com/nick.vk-1>

Nicholas Von Klemperer
Department of Electrical Engineering
University of Cape Town
Wednesday 4th October, 2017

Abstract

Dual-Axis Tilting Quadrotor Aircraft

Nicholas Von Klemperer

Wednesday 4th October, 2017

This dissertation aims to apply non-zero attitude and position setpoint tracking to a quadrotor aircraft; achieved by solving the problem of a quadrotor's inherent under actuation. The introduction of extra actuation intends to mechanically accommodate for stable tracking of non-zero state trajectories. The requirement of the project is then to design, model, simulate and control a novel quadrotor platform which can articulate all six degrees of rotational and translational freedom (*6-DOF*) by redirecting each propeller's individual resultant thrust vector.

In light of such extended articulation the proposal is to add an additional two axes (degrees) of actuation to each propeller on a traditional quadrotor helicopter. Each lift propeller can be independently pitched and rolled relative to the body frame. Such an adaptation, to what is an otherwise well understood aircraft, produces an over-actuated control problem. Being first and foremost a control engineering project, the main focus of this work is plant model identification and control solution of the proposed aircraft design. A higher level setpoint tracking control loop designs a generalized plant input (net forces and torques) to act on the vehicle. An allocation rule then distributes that *virtual* input in solving for explicit actuator servo positions and rotational propeller speeds.

The dissertation is structured as follows; first a schedule of relevant existing works is reviewed in Chapter:1 following an introduction to the project. Thereafter the prototype's design is detailed in Chapter:2; only the final outcome of the design stage is presented. Following that, kinematics associated with generalized rigid body motion are derived in Chapter:3 and subsequently expanded to incorporate any aerodynamic and multibody non-linearities which may arise as a result of the aircraft's configuration (changes). Higher level state tracking control design is applied in Chapter:4 whilst lower level control allocation rules are then proposed in Chapter:5. Next a comprehensive simulation is constructed in Chapter:6; built upon the plant dynamics derived in order to test and compare the proposed controller techniques. Finally a conclusion on the design(s) proposed and results achieved is presented in Chapter:7...

Throughout the research, physical tests and simulations are used to corroborate proposed models or theorems. Final flight tests of the platform remain open to further investigation. The subsequent embedded systems design stemming from the proposed control plant, however, is outlined in the latter of Chapter:2, Sec:2.4. Implementations of which are not investigated here but design proposals are suggested. The primary outcome of the investigation is ascertaining the practicality and feasibility for such a design, most importantly whether the complexity of the mechanical design is an acceptable compromise for the additional degrees of control actuation introduced. Control derivations and the prototype design presented here are by no means optimal nor the most exhaustive solutions, focus is placed on the system as a whole and not just one aspect of it.

Acknowledgements

Nomenclature

In order of appearance:

DOF - Degree of Freedom(s)

μ C - micro-controller

UAV - Unmanned aerial vehicle

SISO - Single input single output, control loop

MEMS - Micro-electromechanical system

DIY - Do it yourself

VTOL - Vertical takeoff/landing

IMU - Inertial measurement unit

BLDC - Brushless direct current, motor type

KV - Kilo-volt, BLDC motor rating

μ C - Micro-controller shorthand

PWM - Pulse width modulation

CH - Channel, radio control & PWM signals typically

RC - Radio control

OAT - Opposed active tilting

dOAT - Dual axis opposed active tilting

PD - Proportional derivative, control law

PID - Proportional integral derivative, control law

IBC - Ideal backstepping control

ABC - Adaptive backstepping control

PSO - Particle swarm optimization, gradient free genetic algorithm

BEM - Blade element theory

ESC - Electronic speed controller

MPC - Model predictive control

LQR - Linear quadratic regulator

LCF - Lyupanov candidate function

ITAE - Integral time additive error

TSK - Takagi-Sugeno-kang

I/O - Input/Output

RPM - Revolution Per Minute

RPS - Revolution Per Second

W.R.T - With respect to

LCF - Lyupanov Candidate Function

iff - If and only if

P.D - Positive definite, NOT proportional derivative

S.T - such that

FTC - Fault Tolerant Control

Symbols

Propeller Rotational Speed: Ω_i [rpm] for motors: $i \in [1, 2, 3, 4]$

Rotational speeds in [RPS] are used for Blade Element Theory Calculations in Chapter:3

Net body torque: $\mu \vec{\tau} = [\tau_\phi \ \tau_\theta \ \tau_\psi]^T \in \mathcal{F}^b$

Net body thrust: $\mu \vec{T} = [T_x \ T_y \ T_z]^T \in \mathcal{F}^b$

Body Position: $\vec{E} = [x \ y \ z]^T \in \mathcal{F}^I$

Euler Angles: $\vec{\mathcal{E}} = [\phi \ \theta \ \psi]^T \in \mathcal{F}^{I,v1,b}$

Servo 1 Position: λ_i [rad]

Servo 2 Position: α_i [rad]

Motor module actuator positions: $[\Omega_i \ \lambda_i \ \alpha_i]^T \in \mathcal{F}^{M_i}$

Actuator matrix: $u = [M_1 \ \dots \ M_4]^T \in \mathbb{U}^{12}$

Motor module displacement arm: $\vec{L}_{arm} = 195.16$ [mm]

Euler Rates: $\frac{d}{dt} \vec{\eta} = \dot{\vec{\eta}} = \Phi(\eta) \dot{\omega}_b = [\dot{\phi} \ \dot{\theta} \ \dot{\psi}]^T \in \mathcal{F}^{v1,v2,I}$

Angular Velocity: $\omega = [p \ q \ r]^T \in \mathcal{F}^b$

Linear Velocity: $\nu = [u \ v \ w]^T \in \mathcal{F}^b$

Contents

Declaration	ii
Abstract	iii
Acknowledgements	iv
Nomenclature	v
Symbols	vi
1 Introduction	1
1.1 Foreword	1
1.1.1 A Brief Background to the Study	1
1.1.2 Research Questions & Hypotheses	2
1.1.3 Significance of Study	3
1.1.4 Scope and Limitations	4
1.2 Literature Review	7
1.2.1 Existing & Related Work	7
1.2.2 Notable Quadrotor Control Implementations	10
2 Prototype Design	16
2.1 Design	16
2.1.1 Actuation Functionality	17
2.2 Reference Frames Used	19
2.2.1 Reference Frames Convention	19
2.2.2 Motor Axis Layout	23
2.3 Inertial Matrices & Masses	26

2.4 Electronics	36
2.4.1 Actuator Transfer Functions	40
3 Kinematics & Dynamics	46
3.1 Rigid Body Dynamics	46
3.1.1 Lagrange Derivation	46
3.2 Aerodynamics	50
3.2.1 Propeller Torque and Thrust	50
3.2.2 Hinged Propeller Conning & Flapping	55
3.2.3 Drag	57
3.2.4 Rotation Matrix Singularity	57
3.2.5 Quaternion Dynamics	59
3.2.6 Quaternion Unwinding	60
3.3 Multibody Nonlinearities	62
3.3.1 Relative Rotational Gyroscopic & Inertial Torques	62
3.3.2 Simulation and verification of induced model	77
3.4 Consolidated Model	86
4 Controller Development	88
4.1 Control Loop	88
4.2 Control Plant Inputs	89
4.3 Stability	91
4.4 Lyapunov Stability Theorem	93
4.5 Model Dependent & Independent Controllers	94
4.6 Attitude Control	95
4.6.1 The Attitude Control Problem	95
4.6.2 Linear Controllers	95
4.6.3 Non-linear Controllers	100
4.7 Position Control	104
4.7.1 PD Controller	105
4.7.2 Adaptive Backstepping Controller	106
5 Controller Allocation	108

5.1	Allocator slack	108
5.1.1	Pseudo Inverse Allocator	111
5.1.2	Weighted Pseudo Inverse Allocator	112
5.1.3	Priority Norm Inverse Allocator	114
5.1.4	Non-linear Plant Control Allocation	115
5.1.5	Online Optimized Secondary Goal Allocator	116
6	Simulations & Results	117
6.1	Controller Tuning	118
6.1.1	Partical Swarm Based Optimization	118
6.1.2	Performance Metric	118
6.1.3	Global & Local Minima	118
6.1.4	Fmincon Differences	118
6.2	Attitude Controllers	118
6.2.1	PD	118
6.2.2	XPD	118
6.2.3	IBC	118
6.2.4	ABC	118
6.3	Position Controllers	118
6.3.1	PD	118
6.3.2	ABC	118
6.4	Allocator Optimization	118
6.5	Simulation Block	118
6.6	Optimized Controller Results	118
6.6.1	Attitude Control	118
6.6.2	Position Control	118
6.6.3	Allocator Performance	118
6.7	Stability and Disturbance Rejection	118
6.7.1	Torque Disturbance Rejection	118
6.7.2	Disturbance Force Rejection	118
6.8	State Estimation	118
6.8.1	Set-point Control Results	118

7 Conclusion	119
A Expanded Equations	120
A.1 Standard Quadrotor Dynamics	120
A.2 Blade-Element Momentum Expansion	122
A.3 Euler-Angles from Quaternions	122
B Design Bill of Materials	123
B.1 Parts List	123
B.2 F3 Deluxe Schematic Diagram	128
B.3 Strain Gauge Amplification	129
C System ID Test Data	130
C.1 Thrust and Torque Test Data	130
C.2 Cobra CM2208-200KV Thrust Data	131
C.3 Combined Simulated Torque Responses	132
C.4 Combined Torque Response Tests	133

List of Figures

1.1	Bell/Boeing V22 Osprey actuation, notations pertinent to patent [97]	2
1.2	Mechanical actuators	6
1.3	General structure for opposed tilting platform, taken from [44]	7
1.4	DJI Inspire1, the notations are with regards to the DJI patent [132]	8
1.5	Tilt-rotor mechanisms	9
1.6	Dual-axis tilt-rotor mechanism used in [38]	9
1.7	ArduCopter PI control structure for pitch angle θ ; from [76]	11
2.1	Isometric view of the prototype design	16
2.2	Tilting rotor design	17
2.3	Difference between propeller and motor planes	18
2.4	Motor module assembly	18
2.5	Digital and analogue servo timing	18
2.6	Inertial and body reference frames	19
2.7	Aligned motor frame axes	23
2.8	Intermediate motor frames	23
2.9	Body frame axes layout	24
2.10	Motor thrust force	25
2.11	Rotor assembly rotational structure	26
2.12	Inner ring rotational structure	27
2.13	Middle ring rotational structure	28
2.14	Module assembly rotational structure	29
2.15	Complete motor module attached to the body structure	29
2.16	Body structure's center of mass	30
2.17	Inertial, mass and motor modules respective centers	31

2.18 Hardware schematic diagram	36
2.19 SPRacing F3 deluxe layout	37
2.20 SBUS converter & 6CH receiver	37
2.21 S.BUS data stream	38
2.22 BLDC electronic speed controllers	39
2.23 RPM sensor calibration plots	40
2.24 Servo transfer function test rig	40
2.25 Unloaded servo transfer characteristics	41
2.26 Servo block diagram	42
2.27 Inner ring servo characteristics	42
2.28 Middle ring servo characteristics	43
2.29 BLDC rpm speed calibration and transfer function rig	44
2.30 BLDC motor characteristics	44
3.1 Generalized quadrotor net forces and torques	49
3.2 Propeller types	50
3.3 Disc Actuator Propeller Planar Flow	51
3.4 Blade element profile at radius r	52
3.5 Power & thrust coefficients	54
3.6 Propeller thrust tests	54
3.7 Static torque tests	55
3.8 Propeller blade flapping; from [55]	56
3.9 Propeller coning	56
3.10 Mechanical gimbal lock	58
3.11 Exploded inner ring inertial bodies for $\vec{\tau}_\lambda$	63
3.12 Exploded middle ring inertial bodies for $\vec{\tau}_\alpha$	66
3.13 Rotating system	69
3.14 Free-body diagram for rotational system	70
3.15 Exploded motor module inertial bodies for $\vec{\omega}_b$ response	71
3.16 Illustration of rotated center of gravity $C.M'_p$	73
3.17 Approximated and true body torque responses	76
3.18 Approximated and true body torque responses	77

3.19 Simulink Lagrangian block	79
3.20 Inner ring induced torque responses for $\Delta\lambda_i$	80
3.21 Middle ring induced torque responses for $\Delta\alpha$	81
3.22 Inner ring torque test rig	82
3.23 Inner ring response	83
3.24 Middle ring torque test rig	84
3.25	84
4.1 Generalized control loop with allocation	89
4.2 Extended control loop with over-actuation	90
4.3 Trajectory illustrations for S and US	91
4.4 Trajectory illustrations for AS and UAS	92
4.5 Exponential stability, UES	93
5.1 Weighting matrix biasing	113
5.2 Hover conditions W.R.T the inertial frame \mathcal{F}^I	114
5.3 Hover conditions W.R.T the body frame \mathcal{F}^b	115
5.4 Allocation loop iteration	116
B.1 Bearing Bracket Inner Ring Assembly	125
B.2 Servo Bracket Inner Ring Assembly	125
B.3 Servo Bracket Middle Ring Assembly	125
B.4 Bearing Holder Middle Ring Assembly	125
B.5 Servo Mount Middle Ring Assembly	125
B.6 Bearing Shaft Middle Ring Assembly	125
B.7 Bearing Holder Damping Assembly	126
B.8 Servo Mount Damping Assembly	126
B.9 Servo Mount Damping Bracket	126
B.10 Bearing Holder Damping Bracket	126
B.11 Arm Mount Damping Bracket	126
B.12 Frame Brackets	126
B.13 F3 Deluxe Flight Controller Hardware Schematic	128
B.14 Strain gauge full bridge amplifier	129

C.1	Clockwise and counterclockwise rotation tests	130
C.2	Official Test Results for Cobra Motors	131
C.3	Step changes in $\Delta\lambda_i$ with constant $\Delta\alpha_i = \pi/4$	132
C.4	Step changes in $\Delta\alpha_i$ with constant $\Delta\lambda_i = \pi/4$	132

List of Tables

1.1	A breakdown of common attitude controllers	11
B.1	Parts List	123
B.2	3D Printed Parts	124
B.3	Inner & Middle Ring Assemblies	125
B.4	Damping Assemblies	126
B.5	Laser Cut Damping Brackets	126
B.6	Laser Cut Parts	127

Chapter 1

Introduction

1.1 Foreword

1.1.1 A Brief Background to the Study

A popular topic for current control and automation research is that of quadrotor UAVs. Attitude control of a quadrotor poses a unique 6-DOF control problem, to be solved with an under-actuated 4-DOF system. As a result the pitch, ϕ , and roll, θ , plants are not directly controllable. The attitude plant is often simplified around a stable operating point. The trimmed operating region is always at the inertial frame's origin; resulting in a zero set-point tracking problem. The highly coupled non-linear dynamics of a rigid body's translational and angular motions arise from gyroscopic torques and Coriolis accelerations (Sec: 3.3.1). Such effects are mostly negligible around the origin, hence the origin trim point decouples the system's nonlinearities. The control system can therefore reduce each state variable, $\vec{x}_b = [x \ y \ z \ \phi \ \theta \ \psi]^T$, to independent single-input single-output (*SISO*) plants. Those simplifications are derived in the Appendix:A.1.

As almost every quadrotor research paper mentions, the recent interest in the platform is due to increased availability of micro-electromechanical systems (*MEMS*) and low-cost microprocessor systems. These technical advancements accomodate onboard state estimation and control algorithm processes in real time. Developmental progress in quadrotors and, to a lesser extent unmanned aerial vehicles (*UAVs*) in general, has led to rapidly growing enthusiast communities. For example; HobbyKing [54] is now a name synonymous with providing custom DIY hobbyist quadrotor assembly kits and frames, no longer retailing only prebuilt commercial products like DJI Phantom [34] or ParrotAR [1] drones.

The avenue for potential application of both fixed wing and vertical take-off and landing (*VTOL*) UAVs is expansive; supporting civil [91], agricultural [96] and security [71] industries and not just recreational hobbyists. The quadrotor design provides a mechanically simple platform on which to test advanced aerospace control algorithms. Commercial drone usage in industry is already emerging as a prolific sector; especially in Southern Africa. Subsequently, following the 8th amendment of civil aviation laws [100], commercial use of UAVs is now both legalized and regulated. Research into any non-trivial aspect of the field will therefore be extremely valuable to the field as a whole.

Large scale quadrotor, hexrotor and even octocopter UAVs are popular intermediate choices for aerial cinematography and other high payload capacity applications. The cost of a commercial drones such as the SteadiDrone Maverik [79] are significantly less than a chartered helicopter, used to achieve the same panoramic aerial scenes or on-site inspections. One foreseeable issue which may hinder commercial drone progress in the agricultural and civil sectors is the consequential inertial effects from scaling up the aerial structures. When increasing the size of any vehicle, its performance is adversely affected if actuation rates are not proportionately increased.

1.1.2 Research Questions & Hypotheses

The difficulty with quadrotor control is that fundamentally, from their uncertainty and underactuation, they are ill-posed for 6 degree of freedom (*DOF*) setpoint tracking. A quadrotor inherently has only four controllable inputs; each propeller's rotational speed, $\Omega_{1,2,3,4}$, which are then abstracted to a net virtual control input net torque, $\vec{\tau}_\mu = [\tau_\phi \tau_\theta \tau_\psi]^T$, and a perpendicular heave thrust $\vec{T}_\mu = \sum_{i=1}^4 T(\Omega_i)$ in the \hat{z}_b direction. Those four inputs are then used to effect both the translational X-Y-Z positions, $\vec{E} = [x \ y \ z]^T$, and angular pitch, roll and yaw attitude rotations, $\vec{\eta} = [\phi \ \theta \ \psi]^T$. Pitch and roll torques, τ_ϕ and τ_θ respectively, are produced from differential thrusts of each opposing propellers. Yaw torque, τ_ψ , is induced from the net aerodynamic drag about each propeller's rotational axis. Aerodynamic drag and differential thrust responses are highly non-linear (detailed later in Sec:3.2.1) and difficult to approximate as sources of control actuation. As a result the body's yaw channel control is depreciated. Stemming from the system's under-actuation. The attitude control problem is a zero setpoint problem, attempting to track attitudes is ill-posed and will only ever be locally stable (in the Layupanov sense, Sec:4.4).

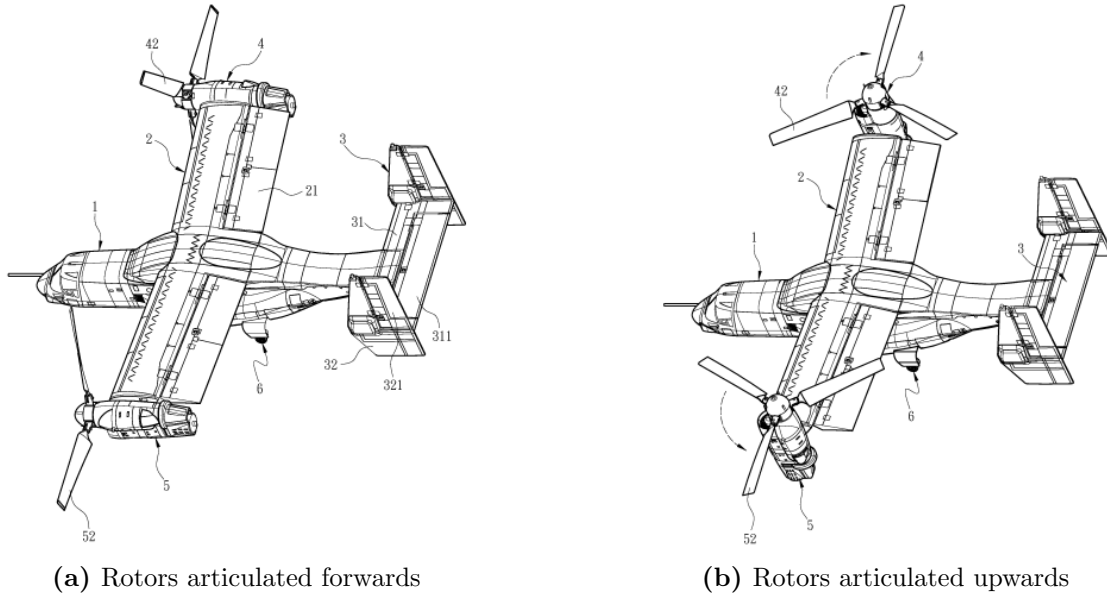


Figure 1.1: Bell/Boeing V22 Osprey actuation, notations pertinent to patent [97]

The aim of this research is to implement dynamic state set-point tracking on a quadrotor UAV by solving the problem of its inherent under-actuation. Inspired by Boeing/Bell Helicopter's V22 Osprey (Fig:1.1) and the tilting articulation of its propellers, the prototype design proposed here (described in Sec:2.1) introduces two additional actuators for each of the quadrotor's four lift propellers. Specifically, adding rotations about the \hat{X} and \hat{Y} axes for each motor/propeller pair. The result is four individually articulated 3-D thrust vectors instead of a bound perpendicular net heave force. The control problem is then posed as the design and allocation of net forces, $\vec{F}_{net} = [F_x \ F_y \ F_z]^T$, and torques, $\vec{\tau}_{net} = [\tau_\phi \ \tau_\theta \ \tau_\psi]^T$, to act on a general 6-DOF body such that for any desired trajectory, $\vec{x}_d(t) = [x \ y \ z \ \psi \ \theta \ \phi]^T$, the error state $\vec{x}_e(t) = \vec{x}_d(t) - \vec{x}_b(t)$ is asymptotically stable. Mathematically that is:

$$\lim_{t \rightarrow \infty} \vec{x}_e(t) = \vec{0} \quad \forall \vec{x} \in \mathbb{R}^n \quad (1.1)$$

Where n is number of the degrees of freedom the system has, typically a 6-DOF plant for rigid bodies. Trajectory stability is explicitly defined later in Sec:4.3 in the context of Lyapunov stability analysis (Sec:4.4). The over-actuation brings about the need for a control allocation scheme, one which distributes the 6 commanded system inputs (net torques and forces) among the actuator set (12 actuators) in order to optimize some objective function secondary to that of Eq:1.1. The potential improvement(s) for exploiting those over-actuated elements is the most novel outcome which the project could yield. Cost functions aimed at optimizing aspects unique to the aerospace body is going to be a completely unique contribution (see Ch:5).

Part of the control research question is the multivariable dynamic modeling of the system; making as few assumptions as possible to the non-linear dynamics involved in the quadrotor's motion and its operational conditions. Common linearizations often applied to the quadrotor's control plant will not hold true for more aggressive attitude maneuvers; they are dependent on small angle approximations and neglect 2nd or higher order effects. To produce a stabilizing control solution there first needs to be a plant model that incorporates both multibody and actuator dynamics, against which the controller efficacy can be tested. The final key outcomes for the project are; the prototype design, its mathematical plant model and simulation analysis, the resultant control law produced and finally conclusions drawn on all of the above.

For a rigidly connected multibody system with revolute joints between sub-bodies, the induced relative motion between those sub-bodies will produce a lot of unwanted dynamics like inertial and gyroscopic responses, amongst others... A rotating propeller will respond to pitching or rolling much like a Control Moment Gyroscope [131] or a flywheel, producing a precipitating torque cross product. A less trivial aspect which is occasionally considered are the aerodynamic effects produced from the propeller's aerofoil profile. Such induced responses manifest normal to the propeller's rotational axis. Those aspects are not typically compensated for due to a quadrotor's fundamental co-planar propeller counter-rotating pairs which mostly negate such effects. A strongly plant dependent control law is needed for dynamic compensation, reducing uncertainty associated with the subsequent stability proof.

1.1.3 Significance of Study

Owing to the huge popularity of quadrotor platforms as research tools (i.e [10,18,47], etc...), any work that builds on UAV and quadrotor fundamentals will prove to be valuable. With that being said, there is already a plethora of research on the subject of linear and non-linear control techniques for quadrotor platforms (surveyed in Table:1.1). Attitude control loops are the most common topic for research; requiring a unique under-actuated solution and mostly linearized around the origin (Appendix:A.1). Far less common is the application of optimal flight path and trajectory planning to a quadrotor's (*augmented*) autopilot system. The difficulty and ill-posed aspect of a quadrotor's attitude control does not hold true for its position plant, so standard techniques can be applied for waypoint and trajectory planning once the attitude control problem has been addressed.

The most significant aspect of this project is the attitude control, discussed later in Sec:4.6. The over-actuation of the proposed design and, more critically, the manner in which the controller's commanded (virtual) output is distributed among those control effectors would, at the time of writing, appear to be the first of its kind. Otherwise known as control allocation, the requirements of the distribution algorithm(s) are outlined in Sec:5.1. Dynamic setpoint attitude control for aerospace bodies is not a subject heavily researched outside the field of satellite attitude control. Even papers that propose similarly complicated mechanical over-actuation (expanded upon in next in the literature review, Sec:1.2) hardly broach the topic of tracking attitude set points away from the origin.

The control plant presented in this dissertation, developed in Ch:4, does indeed close both the position and attitude control loops. There is, however, no consideration of trajectory generation nor flight path planning as such topics are well discussed elsewhere. Once closed loop position and attitude control have been achieved, the control algorithms can be adjusted to incorporate higher order state derivative (acceleration, jerk and jounce) tracking needed for nodal waypoint planning. The heuristics involved with flight path planning are well documented and their application is an easily implemented task [48,80,112].

Where possible, the system identification and control (both *design* and *allocation*) for this project is as generally applicable as possible. The intention is that its pertinence falls not only within the UAV field but also to any aerospace attitude control plant, rigid or otherwise.

Ideally the investigation can be expanded upon with more focused research on one of the subsystems without compromising the stability of the remainder of the plant. Provisionally, an obvious outcome which the project could yield is improved yaw control of a quadcopter's attitude. However, if the express purpose was just to improve yaw control, it could be done with a dramatically less complicated design...

Moreover, this dissertation could provide greater insight into higher bandwidth actuation and hence faster control responses for larger aerospace bodies. Any standard quadrotor uses differential thrusts to develop a torque about its body. Such actuation suffers a second order inertial response when the propellers accelerate or decelerate; $\vec{\tau}_p = J_p \dot{\Omega}_i$ for $i \in [1 : 4]$. Prioritizing pitching the propeller's principle axis of rotation in lieu of changing the rotational speed could potentially improve the actuator plant rate response. This is entirely dependent on how the allocator block is prioritized (presented in Ch:5). The exact effects of different actuator prioritization and distribution in the context of aerospace control are, at the time of writing, unique to this research.

1.1.4 Scope and Limitations

Scope

Critical to this project is the conceptualized design, prototyping and modeling of a novel actuation suite to be used on a quadrotor platform. The control research question is to apply dynamic set-point control to the quadrotor platform. Stemming from this is an investigation into the kinematics that are potentially influenced by such a design and the structure's configuration changes. In order to apply correct control theory to achieve the state tracking on the physical prototype, plant dynamics must first be identified for the controller to be designed and optimized correctly. Aspects of the mechanical design are detailed in the next chapter; Ch:2.1. There is no scope beyond the cursory investigation for materials analysis or stress testing of the design. This dissertation's scope focuses mainly on the vehicles equations of motion and subsequent control derivation, not the structural integrity of the proposed frame given the forces it may undergo. Physical measurements are only made for critical kinematics such as inertial measurements (Sec:2.3) for the second order gyroscopic and inertial dynamic responses (Sec:3.3.2).

As mentioned in the antecedent Sec:1.1.3; trajectory and flight path planning are not ubiquitous with this dissertation. Derivations for the differential equations for a 6-DOF body's motion, throughout 3, are applicable to any aerospace body, rigid or otherwise. Some particular standards are used, like Z-Y-X Euler Aerospace rotational matrix sequences, all of which are covered in Sec:2.2. The control plant is stabilized with non-linear state-space control techniques in the time domain, aided and justified by Lyapunov stability theorem [15, 85, 105]. Alternative solutions using model predictive control (*MPC*) or quantitative feedback theory (*QFT*) could provide more refined or effective controllers, however they are not discussed here and remain open to further investigation. Quadrotor attitude control is commonly stabilized with feedback linearizations, decoupling the plant around a trim point so that SISO techniques can be applied. A derivation of such a linearization is included in App:A.1 but beyond that there are no further discussions. Any comparisons between non-zero and zero set-point attitude controller efficacy for quadrotors are difficult as the fundamental objectives are in stark contrast with one another.

Arguably the most important and potentially novel aspect of this project is the control allocation. The system has 12 plant inputs and 6 output variables to be controlled. There is then an entire set of compatible actuator solutions, $u \in \mathbb{U} \in \mathbb{R}^{12}$, which satisfy each commanded virtual input. Such a plant is classified as over-actuated. Ergo, there must be some logical process as to how those 12 inputs are combined to achieve the desired 6 control plant inputs, specifically input force \vec{F}_μ and torque $\vec{\tau}_\mu$ acting on the system.

Appropriate allocation rules are first derived in Ch:5 then simulated and compared in Ch:6 before a final solution is proposed and reviewed in Ch:7. It is not a comprehensive survey of every possible allocation or control scheme but rather an analysis of the sub-set of problems and design of what is regarded as a logical and pertinent approach. With regards to the prototype design, in Sec2.1, it is assumed that certain aspects are readily available and require no design/development. Particularly the state estimation, updated through a 4-camera positioning system fused with a 6-axis IMU through Kalman Filtering (Sec:6.8), is assumed to accurate and readily disposable at a consistent 50 Hz. Hence state estimation and its discretization effects are included in Sec:6.8 but are bereft of intricate detail, this is another topic which remains open to further investigation...

Limitations

The biggest constraint faced by the design is the net weight of the assembled frame. Lift thrusts which are required to keep an aircraft aloft and oppose the net gravitational force are obviously dependent on the body's net weight. The steady state actuator rates ought to be far less than saturation conditions to ensure sufficient actuator headroom to implement control actuations. Conversely the structure's net weight is mostly dependent on the lift motors, often being the heaviest part of the vehicle (batteries included).

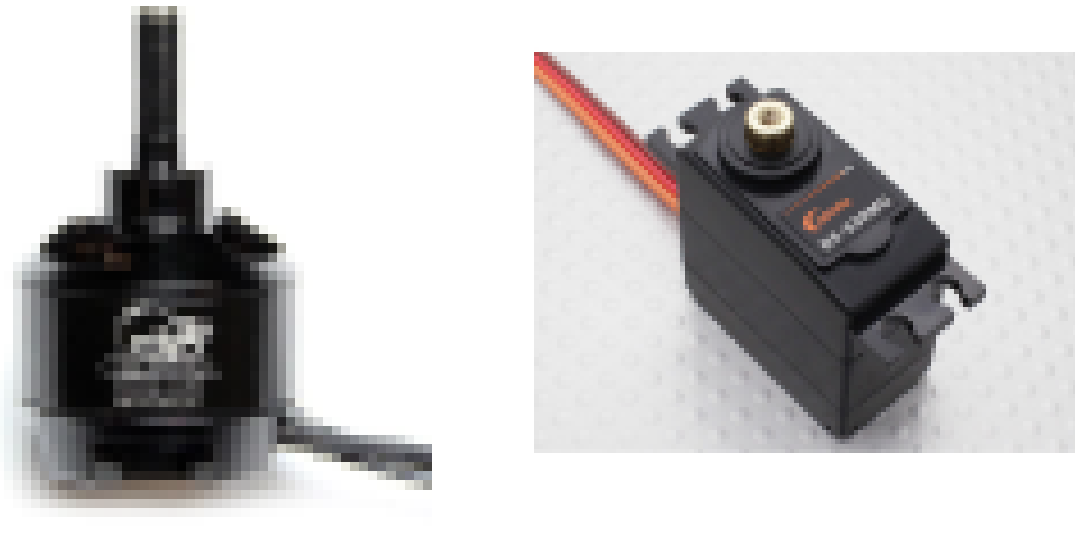
A trade-off between net weight and actuator effectiveness makes designing the prototype a balancing act of compromise; added actuation is needed to produce the desired thrust vectoring. That added actuation is going to increase the weight which then requires more thrust force to ensure the vehicle remains airborne. Larger motors then need stronger actuators to effect the relative motion and overcome the bodies inertial response. It is a compromise between the weight of the body and the strength/quality of the actuation.

To forego the deliberation detailed above, reducing the possibility of unbounded scope creep, a design limitation is self-imposed on the prototype design. Restricting the propeller diameter, and hence maximum thrust/frame size, will provide a constraint upon which all other design considerations must adhere to. Smaller propellers require far greater rotational speeds to produce similar levels of thrust than their larger diameter counterparts could provide. Electing to use 3 bladed 6×4.5 inch diameter propellers constrained the maximal overall dimensions of the prototype; but as a consequence required very high RPM motors. Specifically a set of four Cobra-2208/2000KV [30] brushless direct current (*BLDC*) motors are proposed for lift actuation (Fig:1.2a).

A direct consequence of that decision is, provisionally based on official thrust tests of the motor in App:C.2, the net thrust disposable to the control loop is limited to around $950 \text{ [g]} \approx 9.3 \text{ [N]}$, per motor at 14.1 [V] . That thrust test data is provided from the official Cobra motor's website, [30], but further verification is done through physical testing in Sec:3.2.1. The frame weight should ideally remain below 50% of the maximum available thrust; or roughly below 2 [kg] .

Another aspect of limitations produced by design decisions made, mostly to reduce the prototype's cost, is to use of 180° rotation servo motors. Here Corona DS-339MG metal gear digital servos (Fig:1.2b) were selected as they were readily available from university stores. The servos are used for each individual motor's \hat{X}_{M_i} and \hat{Y}_{M_i} axial pitch and roll actuations respectively; terms λ_i and α_i represent those respective rotations to differentiate from body pitch ϕ and roll θ .

Servos act in place of either BLDC gimbal or stepper motors with closed loop position control to articulate actuator rotations. The latter pair could both accommodate for continuous ($> 2\pi$) rotations of the actuation modules (Sec:2.1.1) but would need their own control design which includes some element of position feedback. Continuous rotation (velocity controlled) servos could otherwise be used but would similarly require rotational feedback, making the design even more complex. Any rotations beyond 2π would similarly require slip rings to transmit power throughout rotational movement to avoid mechanical interference from connection lines.



(a) Cobra CM2208/2000KV BLDC motor [40]

(b) Corona DS-339MG digital servo [54]

Figure 1.2: Mechanical actuators

Implementing such a design and maintaining an acceptable weight would prove too costly nor would it provide additional insight attained from experimental testing. The effect of servo rotational limits can be evaluated in simulation and if it proves to be significant, continuous rotation could be implemented. The initial design was constructed with flight tests in mind however subsequent dynamic and control derivations proved too time consuming; the project led to a close before final tests could be completed. Throughout the design stage in Ch:2 practical implementation was always considered. Certain elements of the whole system could potentially limit performance but were mitigated where possible. For example analogue servos have an associated 1 [ms] dead time from their 50 [Hz] refresh rate. That can be addressed by using faster, albeit more expensive, digital servos which samples at 330 [Hz].

An important element of consideration was the prototype's proposed flight controller; needing to provide a total of 12 pulse-width modulated (*PWM*) output compare channels for the 8 servos and 4 BLDC speed controllers. Moreover the system should have some form of primary state update from a ground control station and a secondary fail safe radio control receiver module, both processed by the micro-controller (μC) system. Particular attention is paid to the embedded system design and layout in Sec:2.4.

1.2 Literature Review

1.2.1 Existing & Related Work

The field of transformable aerospace frames is not new, with many commercial examples seeing successes over their operational life span. The most notable tilting-rotor vehicle is the Boeing/Bell V22 Osprey [39] aircraft. First introduced into the field in 2007, the Osprey has the ability to pitch its two lift propellers forward to aid translational flight after vertically taking off or landing. In addition to this there have been many papers published on similar tilting bi-rotor UAVs for research purposes.

Birotors

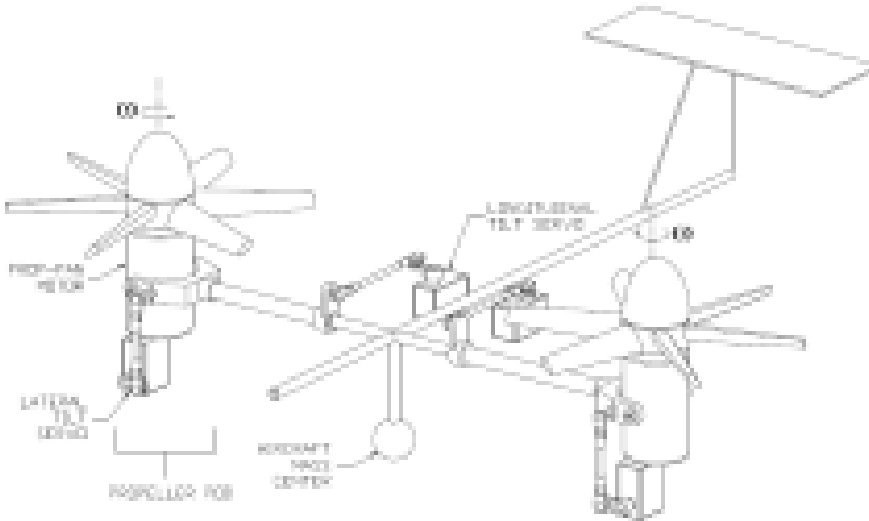


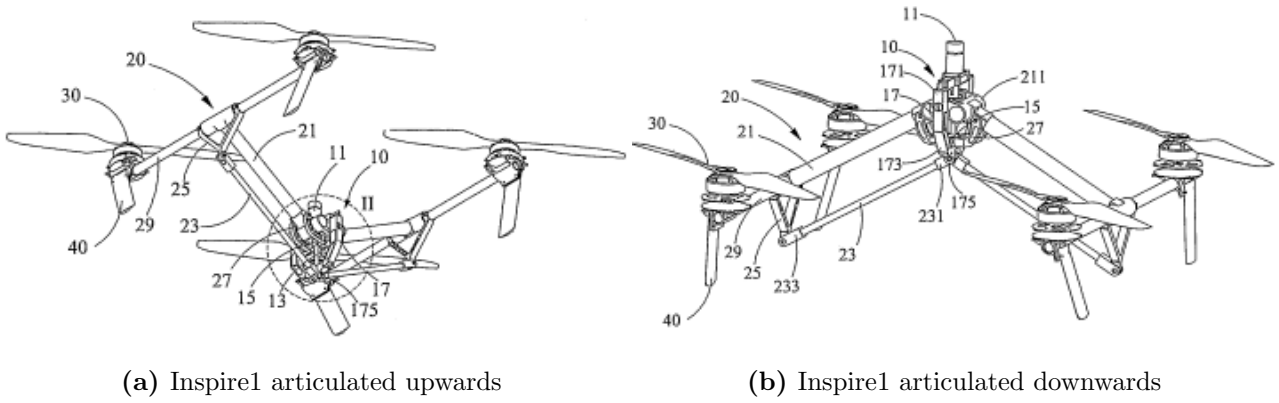
Figure 1.3: General structure for opposed tilting platform, taken from [44]

Research into birotor vehicles (Fig:1.3) with ancillary lift propeller actuation is oft termed *Opposed Active Tilting* or *OAT*. Such a rotorcraft's mechanical design applies either a single *oblique* 45° tilting axis relative to the body; [13, 45, 66], or a *lateral* tilting axis, adjacent to the body; [26, 68, 95, 114]. Leading research is currently focussed on applying doubly actuated tilting axes to birotor UAVs. *Dual axis Opposed Active Tilting* or *dOAT* introduces vectored thrust with independent propeller pitch and roll motions to further expand the actuation suite, [3, 44]. A birotor is sometimes considered preferable to higher degree of freedom multirotor platforms due to their reduced controller effort. However the controller plant derivation, typically requiring feedback linearization and virtual plant abstraction, often detracts from the quality and effectiveness of its stability solution as a result of the birotor's underactuation.

Birotor attitude control mostly introduces plant independent PD [13] and PID [95] stabilizing controller schemes. Sometimes more computationally intensive and plant dependent *ideal* or *adaptive* backstepping controllers are implemented, presented in [66, 114] and [68] respectively. The gyroscopic response of a birotor vehicle's attitude system is more pronounced than that of a quadrotor, derived in Sec:3.3, and so feedback linearisation is almost always used. In an interesting progression from the norm, [74] proposed a unique PID co-efficient selection algorithm for a bi-rotor control block. Using a particle swarm optimization (*PSO*) technique, similar to [135], the coefficients were globally optimized around a given performance metric. However their performance criterion is a standard integral time-weighted absolute error (*ITAE*) term and nothing more appropriate involving effects unique to flight systems was used. *PSO* algorithms iteratively search for a globally optimized solution and offer independent, gradient free based optimization. In subsequent chapters, controller coefficients are optimized for this project using *PSO* algorithms, shown later in Sec:6.1.

Quadruped

Expanding on bi-rotor vehicles, the quadrotor UAV is a popular and well researched multirotor platform due to its mechanical simplicity. The current popularity of quadrotors as research platforms started in 2002, with a control algorithm implemented on what is now known as the X4-Flyer quadrotor [47, 102]. Alternative iterations then followed; like the Microraptor [107] and STARMAC [55] quadcopters which have subsequently been built and tested. A multitude of literature exists around quadrotor kinematics and their control [5, 18, 29, 80, 106], however dedicated rigid body 6-DOF dynamic papers [82, 98] offer better explanations of the kinematics. Often the plant's dynamics are simplified around an origin trim point and assumed to reduce into 6 SISO plants for each degree of freedom (App:A.1). Lately research projects have begun to incorporate non-linear aerodynamic effects like drag and propeller blade-element momentum (*BEM*) theory into the plant model [22, 55, 109]. The higher fidelity models for thrust and propeller responses offer more precision by making less linearisations and assumptions; [7, 55].



(a) Inspire1 articulated upwards

(b) Inspire1 articulated downwards

Figure 1.4: DJI Inspire1, the notations are with regards to the DJI patent [132]

At the time of writing, the only commercial UAV multirotor capable of structural transformation is the DJI Inspire1 quadrotor [33], manufactured by Shenzhen DJI Technologies. DJI are better known for their hugely successful DJI Phantom commercial quadrotor [34]. The Inspire1 can articulate its supporting arms up and down as shown in Fig:1.4, the purpose of which is to both alter the center of gravity and to further expose a belly mounted camera gimbal for panoramic viewing angles. This changes the bodies inertial matrix about its center of gravity, affecting the second order inertial response opposed to changes in angular velocity; $\vec{\tau} = J\Delta\vec{\omega}_b$. That variable inertia is a detrimental consequence which makes researchers apprehensive of reconfigurable aerospace frames. The range of transformations which the Inspire1 frame can undergo is limited to just articulating its arms up and down.

In a similar fashion to the progression seen in birotor state-of-the-art, quadrotor research is engaging the topics of single and dual axis propeller tilting articulations. The extra actuation scheme(s) were first conceptualized and implemented on a prototype related to an ongoing project covered in two reports; [110, 111]. Those authors modified and tested a QuadroXL four rotor helicopter, produced by MikroKopter [41], to actuate a single axis of tilting aligned with the frame's arms (Fig:1.5a). Their proposed control solution, detailed next in Sec:1.2.2, assumes no nominal linearised conditions around hover flight, unlike a similar single axis tilting quadrotor prototype designed by Nemati in [88]. The latter is *simulated* but remains as yet untested.

One approach to improving quadrotor flight response is to alter the manner in which the thrust is mechanically actuated, potentially improving actuator bandwidth (demonstrated in [2, 38]). Drawing from helicopter design, [87] purported a novel quadrotor UAV prototype that used swashplates for varying the propeller pitch and generating torque moments. The aim was a design which was independent of propeller rotational speed power electronics (*ESCs*) for thrust force actuation.

Petrol motors were intended for use in place of BLDC motors. Furthermore, the design proposed a single axis of tilt actuation to each of the four motor modules. Whilst mechanically complex, the prototype in [87] made use of existing off-the-shelf hobbyist helicopter components to design a rotor actuation bracket (Fig:1.5b). The cyclic-pitch swashplates used could apply pitching and rolling torques [89], τ_ϕ and τ_θ , about each propeller's hub, its *principle axis of rotation*. The torques were induced by cycling the blade's angle of attack throughout the propeller's rotational cycle. The actuation rate of such a configuration is far greater than that of a differential torque produced rolling/pitching motion.

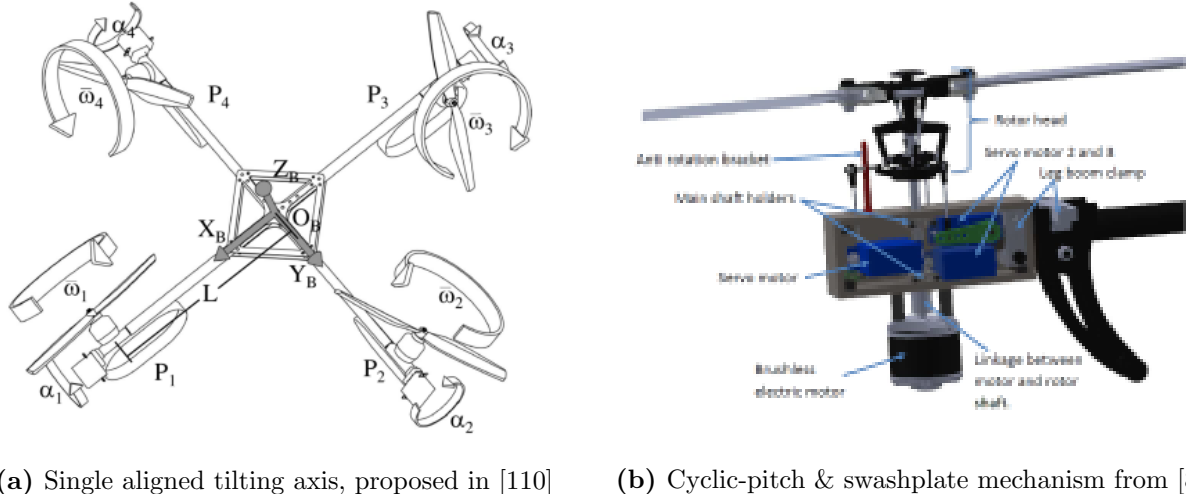


Figure 1.5: Tilt-rotor mechanisms

Irrespective of the strong initial design in the early stages of his project, it would appear that the research in [87] suffered due to time constraints. The introductory derivation on aerodynamic effects and deliberation over the design provide clear insight into the projects goals. However the control solution and system architecture, electronic and software, are severely lacking. A brief introductory proposal of an MPC attitude control system detracted from the comprehensive dynamics discussed. The project ended before testing, simulation or results could be obtained. Unfortunately, despite the novel over-actuated design, there was no discussion given on how that actuator allocation, being the most unique aspect of the project, would be achieved.



Figure 1.6: Dual-axis tilt-rotor mechanism used in [38]

Finally, the most crucial research to mention is a project completed by Pau Segui Gasco in [38], which was a dual presented MSc project with Yazan Al-Rihani whose respective research was presented in [2]. At the time of writing, this would appear to be the only project published pertaining to *over-actuation* in aerospace bodies implemented and tested on a quadrotor platform. The research was split between the two authors who completed the electronic/control design and the mechanical design for their respective MSc dissertations.

Shown in Fig:1.6, the dual-axis articulation is achieved using an RC helicopter tail bracket and servo push-rod mechanism; reducing the mass of the articulated components but limiting the range of its possible actuation. Considering the propellers as energy storing flywheels, the induced gyroscopic response was then treated as an additional controllable actuator plant. Their commanded virtual control is distributed by weighted inversion amongst the actuator set, Sec:1.2.2. The whole project justifies the extra actuation as fault tolerance redundancy (*FTC*) but does not necessarily detail how such a redundancy could be beneficial.

1.2.2 Notable Quadrotor Control Implementations

Quadcopter Attitude Control

Note that here $\vec{\eta}$ is not necessarily an Euler angle set but any attitude representative state variable.

Attitude control of a 6-DOF aerospace body, quadrotor or otherwise, is best described by [126] and referred to as *the attitude control problem*. For a rigid body that has an instantaneous (Euler) attitude state $\vec{\eta}_b$ and a desired state $\vec{\eta}_d$, the problem is to then find a stabilizing torque control $\vec{\tau}_\mu$. The control law is dependent on some feedback error state $\vec{\eta}_e$. Quaternion attitude states later replace Euler angles for attitude representation, $\vec{\eta}_b \Rightarrow Q_b$. A general torque control law is defined as:

$$\vec{\tau}_\mu = h(\vec{\eta}_d, \dot{\vec{\eta}}_d, \vec{\eta}_b, \dot{\vec{\eta}}_b, t) \in \mathcal{F}^b \quad (1.2a)$$

$$\rightarrow \vec{\tau}_\mu = h(\vec{\eta}_e, \dot{\vec{\eta}}_e, t) \text{ given some error state } \vec{\eta}_e \quad (1.2b)$$

Where the control law designs a net torque such that both the angular position and velocity rates are stabilized with the bounded limits; $\lim \vec{\eta}_b \rightarrow \vec{\eta}_d$ and $\lim \dot{\vec{\eta}}_b \rightarrow \dot{\vec{\eta}}_d$ respectively as $t \rightarrow \infty$. Stability definitions are expanded upon later in Sec:4.3. A distinction must be made between euler angular rate vector, $\dot{\vec{\eta}}_b = [\dot{\phi} \ \dot{\theta} \ \dot{\psi}]^T$ and the angular velocity vector $\vec{\omega}_b = [p \ q \ r]^T$. Depending on how the attitude is posed; with rotation matrices [70, 82, 98], quaternions [37, 43, 46, 70] or otherwise (direct cosine matrix etc ...) the error state $\vec{\eta}_e = \vec{\eta}_d - \vec{\eta}_b$ could then differ to a (Hamilton) multiplicative relationship. [126] describes these conventionally different error states.

Simulation and modelling papers often rely on Euler angle based rotation matrices for attitude representation, [16, 18, 81, 88, 108], without addressing the inherent singularity associated with such an attitude representation (known as gimbal lock, [117], Sec:3.2.4). The alternative quaternion attitude representation, first implemented in 2006 on a quadrotor UAV platform in [123], is often used in lieu of rotation matrices. Quaternions do have their own caveat of *unwinding* as a result of the dual-coverage in \mathbb{R}^3 space, discussed in [84] and derived mathematically later in Sec:3.2.6. Quaternions are $\in \mathbb{R}^4$ variables for attitude representations in \mathbb{R}^3 and so a mapping $\mathbb{R}^4 \rightarrow \mathbb{R}^3$ produces an infinite coverage set for each unique attitude state in \mathbb{R}^3 .

Quadrotor plant dynamics, as mentioned previously, are often simplified; especially when represented with a 3-variable Euler angle set, $\vec{\eta}_b = [\phi \ \theta \ \psi]^T$. The cross-coupled gyroscopic and Coriolis terms are both neglected when the angular velocity is small, $\vec{\omega}_b \approx \vec{0}$, and the inertial matrix J_b is approximately diagonal, $\text{rank}(J_b) = x$ for $x \in \mathbb{R}^x$. The consequence of such simplifications is the depreciation of both the gyroscopic torque term, $\vec{\tau}_{gyro} = -\vec{\omega}_b \times J_b \vec{\omega}_b \approx \vec{0}$ and the Coriolis force term, $\vec{F}_{cor} = -\vec{\omega}_b \times m\vec{v}_b \approx \vec{0}$ in the body's dynamics (Ch:3 for context).

Once the coupled cross-product terms are no longer of consequence, the 6-DOF state trajectory, $\vec{x}_b = [x \ y \ z \ \phi \ \theta \ \psi]^T$, can be treated as a series of independent single-input-single-output (*SISO*) plants each controlled with an appropriate technique. Quaternion represented attitude plants cannot easily be decomposed into individual SISO systems (quaternion dynamics in Sec:3.2.5). So a quaternion combined four variable attitude state-space vector is then used, $Q_b \triangleq [q_0 \ \vec{q}]^T$, for the major loop trajectory plant of $\vec{x}_b(t)$.

Opensource and hobbyist flight controller software (Arducopter [4], Openpilot [75] whose firmware stack is now maintained by LibrePilot, CleanFlight [27], BetaFlight [11], etc ...) for custom fabricated UAV platforms all apply their own flavour of structured attitude controllers and state estimation algorithms, based on onboard hardware sensor fusion. The article *Build Your Own Quadrotor* [76] summarizes the control structures implemented on a range of popular flight controllers.

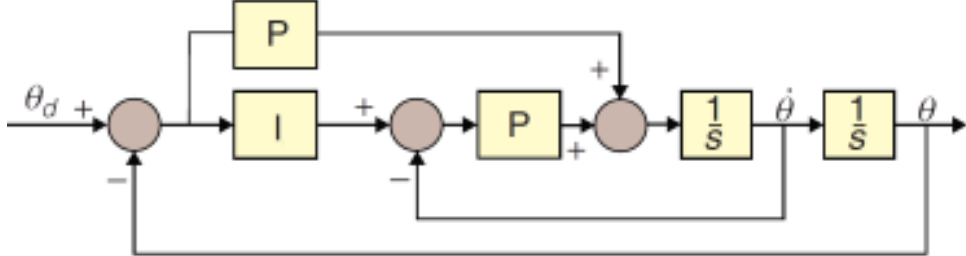


Figure 1.7: ArduCopter PI control structure for pitch angle θ ; from [76]

The most popular of which, ArduCopter, implements a feed-forward PI compensation controller, whose single channel control loop for an attitude roll channel θ is shown in Fig:1.7. PI, PD and PID controllers are all popular and effective plant independent control solutions for general attitude plants. Table:1.1 lists the common attitude control blocks (not exclusively quadrotors UAVs but MAVs too) and which projects they've been implemented in, after which a critique of the more unique adaptations is given. One ideal backstepping controller listed in Table:1.1, presented in [114], applies an algorithm derived through Hurwitz polynomials unlike the Lyapunov based backstepping control law(s) derived later in Ch:4.

Controller Type	Independent	Dependent	Total Examples
PI	[126]	[126]	2
PD	[2, 80]	[37, 88]	4
PID	[16, 19, 106, 110, 126]	[55, 108, 126]	8
Lead	[29, 102]	N/A	2
LQR	[19]	N/A	1
Backstepping controllers			
Ideal	[81, 114]	[81]	3
Adaptive	[10, 32, 68, 86]		4

Table 1.1: A breakdown of common attitude controllers

In a collection of papers, written by the most prolific early quadrotor author(s) S. Boudallah and R. Siegward [17–19]; a range of different attitude control implementations are surveyed and tested on the OS4 platform. The final paper, [18], derived and practically tested an integral backstepping attitude controller on the OS4 quadrotor platform. It builds on their research presented earlier in [19] which provides an analysis of PID vs linear quadratic regulator (*LQR*) attitude controllers, specifically in the context of underactuated quadrotor attitude control. LQR controllers aim to optimize the controller effort with actuator inputs $u \in \mathbb{U}$; controller effort is then $\|u\|_2$ or the L_2 norm (magnitude) of the plant input. Although, in theory, solving the associated Riccati cost function may produce a cost optimal, stable and efficient control law it needs exact plant matching. In reality, exact plant matching is difficult to achieve for a quadcopter or any aerospace body for that matter. The resultant controller in [19] achieved asymptotic stability but had poor steady state performance due to low accuracy of the identified actuator dynamics and poor confidence inertial measurements.

Adaptive Backstepping Control (in [130] or any other example in Table:1.1) expands on nominal ideal backstepping fundamentals by introducing disturbance and plant uncertainty terms into the Lyapunov energy function to be used for the backstepping suppression. For Lyapunov iteration the adaptive backstepping process requires a disturbance estimate derivative or *update law* which is often difficult to quantify.

Approximation of plant disturbances without *a priori* information is a complex subject. At some point in the design an approximation heuristic must be adopted and that typically involves some compromise of performance over accuracy. One example of disturbance approximation in [32] proposes using a statistical projection operator (or $\text{proj}(\cdot)$, [24]). When used in adaptive control, presented similarly in [25], the projection operator $\text{proj}(\cdot)$ ensures a derivative based estimator can be bound for adaptive regression approximation [101].

Although the control implementation is not explicitly backstepping, in [136] a sliding mode controller was used to compensate for the disturbances in an Unmanned Submersible Vehicle attitude plant. The underwater current disturbances were approximated using a fuzzy logic system, specifically a *zero-order Takagi-Sugeno-kang* fuzzy approximator. The TSK system has been shown in [83] to mimic an artificial neural network approximator; where the fuzzy TSK system is more comprehensible than the latter. Statistical analysis and investigation of approximators without *a priori* knowledge of a system are well beyond the scope of this research but are worth mentioning.

Single/Dual Axis Control & Allocation

The additional control actuation introduced with either single or dual axis articulation provides room for secondary control goals to be achieved. Of the few papers published on tilting-axis quadrotors, PD controllers (used in [88] and again in [2, 38]) and PID controllers (collectively [110, 111]) are the standard fare for attitude control blocks. For either of these systems, there needs to be an allocation rule to distribute a commanded input amongst the actuator set. In the control allocation survey [61] the author describes the control allocation problem for a dynamic plant:

$$\dot{\vec{x}} = f(\vec{x}, t) + g(\vec{x}, \vec{\nu}, t) \quad \vec{x} \in \mathbb{R}^n, \vec{\nu} \in \mathbb{R}^m \quad (1.3a)$$

$$\vec{y} = c(\vec{x}, t) \quad (1.3b)$$

State variables of [61] were changed to match this dissertation's conventions. In the state space equation Eq:1.3a, it is assumed the plant input, $\vec{\nu}$, has a linear multiplicative relationship with the input response, $g(\vec{x}, t, \vec{\nu}) \Rightarrow g(\vec{x}, t)\vec{\nu}$. That linear relationship is a prerequisite for most allocation inversion rules but is not a necessity...

In Eq:1.3a the state $\vec{x} \in \mathbb{R}^n$ has associated plant dynamics $f(\vec{x}, t)$ and a input response $g(\vec{x}, \vec{\nu}, t)$. Set-point tracking control equates the output variable with the state, in practice only state estimate (denoted by a hat accent) is available:

$$\vec{y} = c(\vec{x}, t) = h(\vec{x}) = \hat{\vec{x}} \quad (1.4)$$

Therefore the output \vec{y} has the same dimension as the state variable \vec{x} ; or rather both $\vec{x}, \vec{y} \in \mathbb{R}^n$. In an ideal, well posed system the number of actuator inputs equals the number of outputs; that being $\dim(\vec{x}) = \dim(\vec{\nu}) \in \mathbb{R}^n$.

In the case where the control input has a dimension m , for m different actuator plants $\vec{\nu} \in \mathbb{R}^m$, if $m > n$ the problem is then over-actuated and a level of abstraction is needed. The system mechanically commands a physical control input $\vec{\nu}_c$, dependent on explicit actuator positions $u \in \mathbb{U} \in \mathbb{R}^m$ as per some *effectiveness* function derived from the actuator plant's dynamics:

$$\vec{\nu}_c = B(\vec{x}, u, t) \quad \in \mathbb{R}^n \quad (1.5)$$

Assuming that some higher level control law designs well a satisfactory stabilizing virtual control input from the error state(s) $\vec{\nu}_d = h(\vec{x}_d, \dot{\vec{x}}_d, \vec{x}_b, \dot{\vec{x}}_b, t) \in \mathbb{R}^n$. The allocation rule then aims to solve for an explicit actuator position $u \in \mathbb{U} \in \mathbb{R}^m$ derived from $\vec{\nu}_d$ which actuates the physically commanded control input $\vec{\nu}_c$, minimizing the deviation or slack \vec{s} between virtual desired and physical commanded inputs $\vec{\nu}_d$ and $\vec{\nu}_c$ respectively.

Allocation is effectively a paradigm which transforms dimensions $\mathbb{R}^m \rightarrow \mathbb{R}^n$ using a commanded actuator matrix position $u \in \mathbb{R}^m$. An over-actuated plant can be summarized in non-linear state space as:

$$\dot{\vec{x}} = f(\vec{x}, t) + g(\vec{x}, \vec{\nu}_c, t) \quad \vec{x} \in \mathbb{R}^n \quad (1.6a)$$

$$\vec{\nu}_c = B(\vec{x}, u, t) \quad \vec{\nu}_c \in \mathbb{R}^n \quad (1.6b)$$

$$\text{with } u \in \mathbb{U}^m \text{ subject to some } \min(\vec{s}) \text{ such that } \vec{s} = \vec{\nu}_d - \vec{\nu}_c \quad (1.6c)$$

$$\vec{\nu}_d = h(\vec{x}_d, \dot{\vec{x}}_d, \vec{x}_b, \dot{\vec{x}}_b, t) \quad \vec{\nu}_d \in \mathbb{R}^n \quad (1.6d)$$

$$\vec{y} = c(\vec{x}, t) = \hat{\vec{x}} \quad (1.6e)$$

The effectiveness function $B(\vec{x}, u, t)$ quantifies how actuator inputs $u \in \mathbb{U}$ correlate to the physically commanded plant input $\vec{\nu}_c$. Inversion based allocation rules which solve for explicit actuator solutions (Sec:5.1.1) require that $B(\vec{x}, u, t)$ can be abstracted to a linear multiplicative relationship $B(\vec{x}, t)u$ with $B(\vec{x}, t) \in \mathbb{R}^{n \times m}$, such that a generalized inverse of $B(\vec{x}, t)$ can be found. For generic set-point tracking the control law will design a desired virtual control input $\vec{\nu}_d$, the allocation rule then has to solve u for $\vec{\nu}_c$ such that for some slack variable $s = \vec{\nu}_c - \vec{\nu}_d$ is minimized:

$$\min_{u \in \mathbb{R}^m, s \in \mathbb{R}^n} \|Q_s\| \text{ subject to } B(\vec{x}, u, t) - h(\vec{x}_e, t) = \vec{\nu}_c - \vec{\nu}_d = s \quad u \in \mathbb{U} \quad (1.7)$$

Which ensures the commanded input $\vec{\nu}_c$ tracks the desired control input $\vec{\nu}_d$; $\vec{\nu}_c \rightarrow \vec{\nu}_d$ as per some cost function of the slack variable Q_s . Mostly the L₂ norm, $Q_s = \|s\|_2$, is used. In an over-actuated system it then follows that there is a whole set of possible inputs for each commanded $\vec{\nu}_c$. A unique actuator solution (rather than a family of solutions) to Eq:1.7 needs a secondary objective function, $j(\vec{x}, u, t)$ to be solved explicitly. Eq:1.7 expands to:

$$\min_{u \in \mathbb{R}^m, s \in \mathbb{R}^n} (\|Q_s\| + j(\vec{x}, u, t)) \text{ subject to } \vec{\nu}_c - \vec{\nu}_d = s \quad u \in \mathbb{U} \quad (1.8)$$

Those same authors, Johansen and Tjønnås from [61–63], proposed multiple control allocation solutions to a variety of systems. Following [61]; in a subsequent paper [62], the authors introduced a secondary cost function, driving the solution away from the typical linear quadratic programming pseudo and weighted inversion solutions. Aiming for actuator efficiency and not just input saturation, a subsequent paper [63] proposed adaptively allocating actuator positions online. Using a Lyapunov energy equation as the online cost function, the minimization adaptive law was ensured to always settle on a feasible solution.

Over-actuation is not often applied to quadrotors and rather than providing a comprehensive literature review of associated papers here (which are all mostly theoretical derivation), the contextual application and solutions are expanded upon later in Ch:5. The only overactuated quadrotor literature which covers allocation of the extra actuators is [2, 38], where the authors apply a weighted pseudo inverse (otherwise known as the Moore-Penrose Inverse [73]) allocation rule. Birotor dual-axis tilting, detailed earlier, results in a critically actuated system and so requires no allocation. As mentioned before, a prerequisite for (*pseudo*) inversion is a multiplicative *linear* control effectiveness relationship for Eq:1.6b.

The only overactuated quadcopter paper which addressed its required control allocation was that of Gasco and Rihani in [2, 38]. Their solution applied weighted inversion, relying on some very specific assumptions to achieve that required input linearity for the system in Eq:1.6b. For the gyroscopic torque response to extra actuator η or γ pitching and rolling movement applied to a rotating propeller:

$$\tau = J\Omega\dot{\eta} \in \mathcal{F}^b \quad (1.9)$$

With Ω being that propellers rotational speed and $\dot{\eta}$ being the inducing servos rate. The authors assumed the extra actuators pitch and roll angular rates; $\dot{\eta}$ and $\dot{\gamma}$ respectively, were both proportionally related to their positions η and γ as follows:

$$\dot{\eta} \approx \frac{1}{t_{\text{settle}}} \eta \quad \text{and} \quad \dot{\gamma} \approx \frac{1}{t_{\text{settle}}} \gamma \quad (1.10)$$

Where t_{settle} is a constant derived in the actuator transfer function's settling time from a unit input step. Such an assumption holds true so long as $\Delta\eta$ or $\Delta\gamma$ is smaller than the initial step used to evaluate t_{settle} , a restrictive and unrealistic assumption but implemented nonetheless. It then follows that the gyroscopic first order torque $\tau = -\vec{\omega}_b \times J_b \vec{\omega}_b$ and second order inertial torque $\tau = J_b \vec{\omega}_b$ responses are both functions of their associated servo positions η and γ , not respective their derivatives. The extent of that consequence is contrasted with the allocation solution in proposed later in Ch:5.

Satellite Attitude Control

Unconstrained attitude set-point tracking for 6-DOF bodies, quaternion based or otherwise, is a topic well covered in the field of satellite attitude control; [60, 69, 128]. The *status quo* for recent research is on non-linear adaptive backstepping attitude control systems, wherein the adaptive update rule is the novel contribution. Plant uncertainty always adversely affects the confidence in inertial measurements critical to the attitude control of a satellite. In [60] the authors proposed applying adaptive backstepping to compensate for steady state plant uncertainty errors of the (asymmetric) inertial estimations.

Alternatively, instead of deliberating on costly non-orbital prelaunch inertial measurements, [14] suggested an algorithm for estimating the inertial matrix using controlled single axis perturbations. Such an approach does assume any initial values are sufficiently close to true body measurements such that estimates will settle and stability can be ensured, irrespective of how unacceptable the transient performance may be.

Satellite actuator suites mostly include additional redundant effectors, to ensure fault tolerance, and thus require control allocation. Often the extra allocators are control moment gyroscopic actuators (flywheels driven by DC motors) to produce rotational torques. Thrusters have a limited amount of fuel and can actuate the system only a finite number of times. The thrusters can then be scheduled with a lower priority, preferring bias of electronic CMG actuators. In [69] the authors address the over-actuation with direct pseudo inversion before applying quaternion based backstepping for attitude control. Such an inversion solves for Eq:1.8 as follows:

$$u = B^\dagger \vec{\nu}_d \quad (1.11a)$$

$$B^\dagger = B^T (BB^T)^{-1} \quad (1.11b)$$

$$u \in \mathbb{R}^m, \vec{\nu}_d \in \mathbb{R}^n, B \in \mathbb{R}^{m \times n}, B^\dagger \in \mathbb{R}^{n \times m} \quad (1.11c)$$

Where B is the effectiveness matrix which is a static effector form of the effectiveness function $B(\vec{x}, u, t)$. The generalized inverse B^\dagger is such that $BB^\dagger = \mathbb{I}_{n \times n}$. Specifically B^\dagger is the general *pseudo* inversion matrix of B (more on inversions in Ch:5). Moreover there is an assumed *affine* multiplicative relationship between the input, $u \in \mathbb{U}$, and the input effectiveness matrix from Eq:1.6b.

The higher level controller designs actuator torques, $\vec{\nu}_d$, which are then used to solve for explicit actuator positions u as per the inversion equation Eq:1.11a. Much like the over-actuation previously discussed with respect to quadcopters; the pseudo inversion method of actuator distribution applies linear quadratic programming optimization to the allocation slack cost function, Eq:1.7. The resultant quaternion attitude backstepping controller developed in [69] demonstrated global uniform asymptotic stability. The strength of that backstepping stability lies in the choice of trajectory aiming to be stabilized; $z \rightarrow \vec{0}$.

The first candidate Lyapunov trajectory was defined as:

$$z_1 = \begin{bmatrix} 1 - |q_0| \\ \vec{q}_e \end{bmatrix} \quad (1.12a)$$

Such that the Lyapunov energy function candidate is always positive definite and its derivative is positive definite descrescent. The particulars of that stability proof are omitted but it is worth detailing their chosen candidate function;

$$V_1(z) = z_1^T z_1 > 0 \quad \forall [q_0, \vec{q}_e] \quad (1.12b)$$

The absolute quaternion error scalar used in Eq:1.12a ensures a global trajectory's asymptotic stability (Sec:4.6.3), not just local stability that would otherwise be gained. The stable equilibrium points at $Q_e = [\pm 1 \ 0]^T$ apply settling of the trajectory's *error*, allowing the satellite to track its setpoint. However considering that the controller is an ideally compensating controller, the disturbance rejection and uncertainty compensation of the attitude controller could potentially disrupt that achieved stability. Something which was not discussed in the original paper...

Chapter 2

Prototype Design

2.1 Design

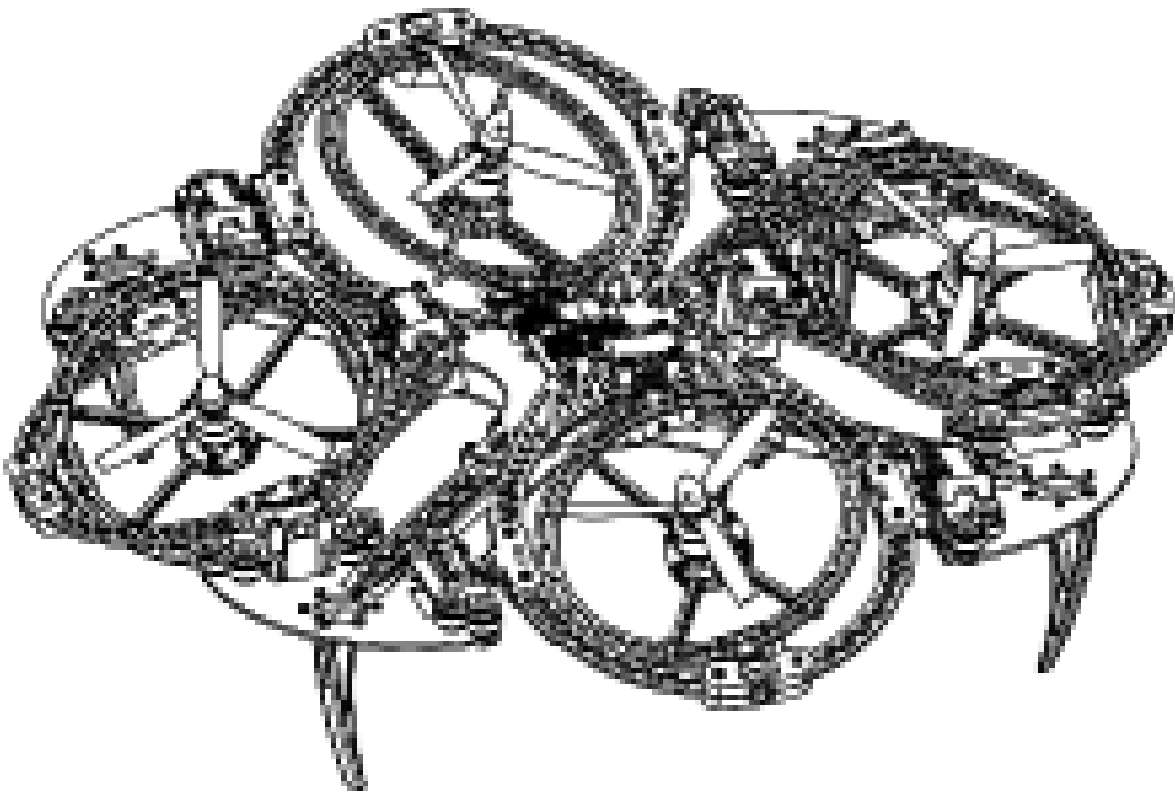


Figure 2.1: Isometric view of the prototype design

The final prototype (Fig:2.1) went through a series of different design iterations, aimed at optimizing engineering time spent on construction and reducing the associated component costs. Significant consideration for the design process was the net weight whose upper limit is inherently limited by the thrust produced from lift motors. Some of the more important design factors, like inertial matrices and associated masses (Sec:2.3), are discussed here in order to give context for the dynamics derived later in Ch:3. The reference frame orientations (which those dynamics are developed with respect to) are detailed here. A brief overview of the electrical systems layout is then given with the components associated and their electrical characteristics included. Finally the actuator suite's functionality and transfer characteristics are quantified.

2.1.1 Actuation Functionality

The most important component of the design is the articulation for each of the four vectored thrust forces. A concentric gimbal ring structure (Fig:2.2a) independently redirects each lift propeller/motor about two separate rotational axes. Within each module are servos affixed onto sequential gyroscope-like support rings to accommodate pitching and rolling of the propeller's direction. Aligned with each servo is a coaxial support bearing. The bearing and actuator servos have a mass disparity which results in an eccentric center of mass, producing a net gravitational torque arm. Unfortunately, due to weight constraints, counter balance measures cannot be introduced. Consequences from the center of mass variations must be either compensated for (*plant dependent solution*) or exploited in the dynamics (*additional non-linear actuator plants*). The precise effects are quantified numerically later in Sec:2.3.

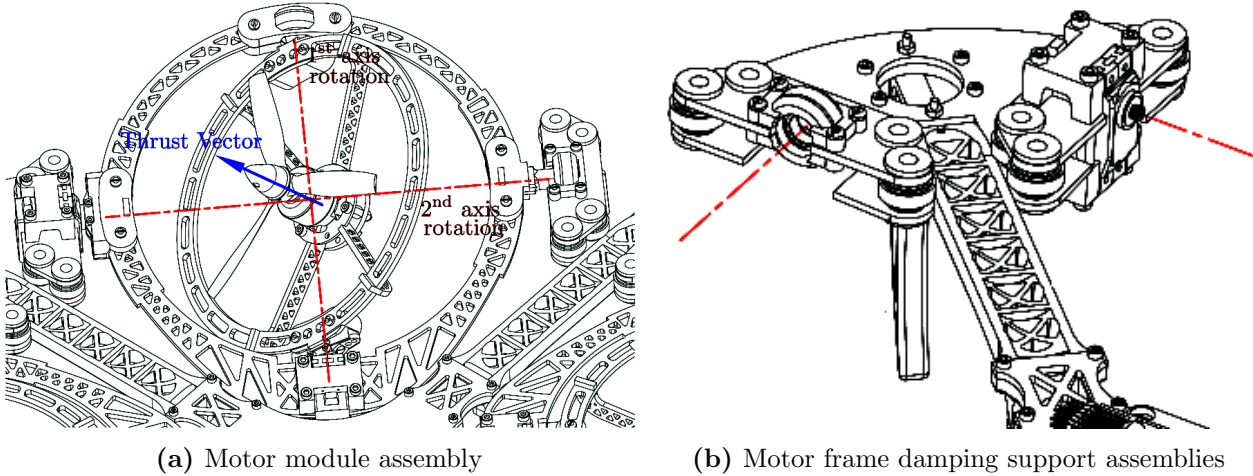


Figure 2.2: Tilting rotor design

Each motor module is positioned such that its produced thrust vector coincides with the intersection of its two rotational axes (Fig:2.2a). As a result there is only a perpendicular displacement of the thrust vector, $L_{arm} = 195.16$ mm, co-planar to the body frame's X-Y-Z origin \vec{O}_b (see subsequent Fig:2.8). That length directly affects the differential torque plant; $\vec{\tau}_{diff} = \sum \vec{L}_i \times \vec{T}_i$. An eccentric thrust vector line would make the torque arm displacement a non-orthogonal vector. The center of gravity for each module is time varying and depends on the two servo rotational positions. It is more prudent to ensure intersection of the thrust vector with the rotational center than to balance the masses undergoing rotation. A thrust varying torque is harder to approximate and hence compensate for than a gravitational torque, given the complexity of modeling a propeller's aerodynamic thrust (Sec:3.2.1).

The primary body structure is similar to a traditional quadcopter '+' configuration with adjacent propellers spinning in opposite directions. Each motor module's rotational assembly is suspended by silicone damping balls (Fig:2.2b). A smaller damping assembly in the center of the frame houses all the electronics and power distribution circuitry. All the mounting brackets affixing the motor module rings are 3D printed from CAD models using an Ultimaker V2+ [129]. A complete bill of materials for all parts used, including working drawings for each 3D printed bracket and the laser cut frame(s), is presented in Appendix:B.

The propeller's rotational plane is not aligned exactly with the plane made by the \hat{X}_{M_i} and \hat{Y}_{M_i} rotational servo axes (Fig:2.3). The offset is approximately 23.0 [mm] and must be considered when evaluating pitch/roll inertial and gyroscopic torque responses later in Sec:3.3.1. The propellers are 6 inch (6 × 4.5) 3-Blade plastic Gemfan propellers, powered by Cobra CM2208-2000KV Brushless DC motors (Fig:2.4a). The thrust produced as a function of angular velocity (in RPS) for the propellers is derived in Sec:3.2.1.



Figure 2.3: Difference between propeller and motor planes

The BLDC motors are controlled with LDPower 20A ESC modules with an in-line OrangeRx RPM Sensor. The ESCs were reflashed with BLHeli [12] firmware. The default firmware on the speed controllers had an unsatisfactory exponentially approaching (not linear) input speed curve, in contrast with the linear (unloaded) speed curve in Fig:2.23. The net transfer functions for both ESC modules and the servos are detailed later in Sec:2.4.1. Power for the quadrotor is supplied from a power tether (not from a battery bank). Tethered power will ensure consistent flight time and reduce the concern of payload restriction on the available lift actuation. Power lines to both the BLDC motors and servos are supplied through conventional wiring, however an ideal and more flexible design would see slip-rings for each module's power supply.



(a) Cobra CM2208-2000KV BLDC motor module

(b) Corona DS-339MG servo bracket

Figure 2.4: Motor module assembly

Metal gear Corona DS-339MG digital servos are used for the two axes of rotation (Fig:2.4b). Each servo has a rotational range of $\approx \pi$, positioned such that a zeroth offset aligns the motor modules, adjacent to the body frame, and has a $\pm\pi/2$ rotational range. A digital servo updates at 330 Hz, faster than a 50 Hz analogue servo equivalent (Fig:2.5). This means the otherwise 20 ms zero-order "analogue" sampling effect is a less significant 3.30 ms zero-order holding time. Both the \hat{X}_{Mi} and \hat{Y}_{Mi} axis servos will be rotating a larger inertial body, as such the open loop plant dynamics are determined empirically in Sec:2.4.1.

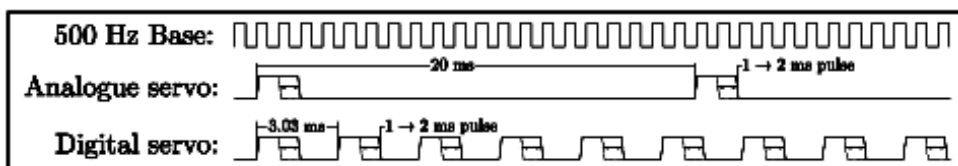


Figure 2.5: Digital and analogue servo timing

2.2 Reference Frames Used

Attitude conventions used for deriving the system's dynamics, in Ch:3, are first discussed here. Often these aspects are assumed to be obvious enough that they are omitted. It is important to clearly and unambiguously define a standard set of framing conventions to avoid uncertainty later. Rotation matrices are included but the focus is on the *contrast* between rotation and transformation operations. Both [46] and [98] provide an in-depth and thorough explanation of rotation matrices and direct cosine matrix attitude representation, if such concepts are unfamiliar to the reader. Later quaternions are introduced to replace rotation matrix notation for the dynamics in Sec:3.2.5.

2.2.1 Reference Frames Convention

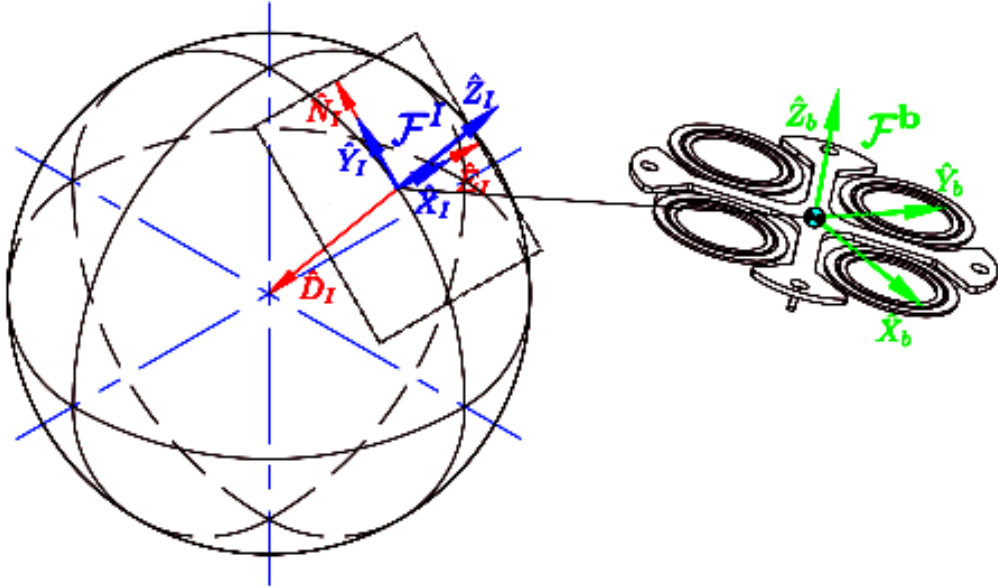


Figure 2.6: Inertial and body reference frames

NASA aerospace frames are used for principle Cartesian inertial and body coordinate representation (Fig:2.6). The inertial frame, \mathcal{F}^I , is aligned such that the \hat{Y}_I axis is in the \hat{N} orth direction, \hat{X}_I is in the \hat{E} ast direction and $-\hat{Z}_I$ is in the \hat{D} ownward direction. In Euler orbital sequences the \hat{Z} direction would be toward the Earth's center, sometimes referred to as the NED convention which differs from the NASA frames used here. The body frame, \mathcal{F}^b , then has both \hat{X}_b and \hat{Y}_b aligned obliquely between two perpendicular arms of the quadrotor's body and the \hat{Z}_b axis in the body's normal upward direction (illustrated in Fig:2.9).

The body frame's axes and center of motion relative to the prototype design's center of mass are both detailed next in Sec:2.2.2. Frame superscripts I and b represent inertial and body frames respectively whilst vector subscripts imply the reference frame in which the vector's coordinates exists or taken relative to. The function $R_I^b(\eta)$ represents a rotation operator of the Euler set $\vec{\eta}$ (expanded on in Eq:2.11) rotating from subscript frame \mathcal{F}^I to superscript frame \mathcal{F}^b .

A vector $\vec{\nu}$ has the relationship between the body and inertial frames:

$$\vec{\nu}_I = R_I^b(\eta) \vec{\nu}_b \quad \vec{\nu}_b \in \mathcal{F}^b, \vec{\nu}_I \in \mathcal{F}^I \quad (2.1)$$

Displacement between the inertial and body frames is given by $\vec{\mathcal{E}}_I$ defined in the inertial frame:

$$\vec{\mathcal{E}}_I = [x \ y \ z]^T \quad [\text{m}], \quad \in \mathcal{F}^I \quad (2.2)$$

An axial hat and upper case differentiates axis unit vectors $\hat{X}, \hat{Y}, \hat{Z}$ from inertial position quantities x, y, z in Eq:2.2. The body position's time derivative $\dot{\mathcal{E}}_I$ refers to the *inertial frame* rate:

$$\frac{d}{dt} \vec{\mathcal{E}}_I = [\dot{x} \quad \dot{y} \quad \dot{z}]^T \quad [\text{m.s}^{-1}], \quad \in \mathcal{F}^I \quad (2.3)$$

Whereas the body's *velocity* \vec{v}_b is with respect to the body frame \mathcal{F}^b . Velocity and the inertial position time derivative are related as follows:

$$\vec{v}_b = R_I^b(\eta) \dot{\vec{\mathcal{E}}}_I \quad [\text{m.s}^{-1}], \quad \in \mathcal{F}^b \quad (2.4a)$$

$$= R_I^b(\eta) [\dot{x} \quad \dot{y} \quad \dot{z}]^T \quad (2.4b)$$

Relative angular displacement between two frames is commonly measured by the three angle Euler set. The Euler angle set $\vec{\eta} = [\phi \ \theta \ \psi]^T$ represents pitch ϕ , roll θ and yaw ψ rotations about sequential \hat{X}, \hat{Y} and \hat{Z} axes respectively. Depending on how the rotation sequence is formulated, those angles can be used to construct rotation matrices which give relation to vectors or can transform coordinates.

The general rotation equation to *rotate* some vector \vec{v} about a normalized unit axis \hat{u} through a rotation angle θ [rad] is given by the formula, proven in [31]:

$$\vec{v}' = (1 - \cos(\theta))(\vec{v} \cdot \hat{u})\hat{u} + \cos(\theta)\vec{v} + \sin(\theta)(\hat{u} \times \vec{v}) \quad (2.5)$$

In Eq:2.5, when the unit vector \hat{u} is in the direction of either \hat{X} ; \hat{Y} or \hat{Z} axes the equation is simplified to produce the three fundamental rotation matrices $R_x(\phi)$; $R_y(\theta)$ and $R_z(\psi)$. That set of three principle rotation matrices about the Cartesian X-Y-Z axes are defined as:

$$R_x(\phi) = \begin{bmatrix} 1 & 0 & 0 \\ 0 & \cos(\phi) & -\sin(\phi) \\ 0 & \sin(\phi) & \cos(\phi) \end{bmatrix} \quad (2.6a)$$

$$R_y(\theta) = \begin{bmatrix} \cos(\theta) & 0 & \sin(\theta) \\ 0 & 1 & 0 \\ -\sin(\theta) & 0 & \cos(\theta) \end{bmatrix} \quad (2.6b)$$

$$R_z(\psi) = \begin{bmatrix} \cos(\psi) & -\sin(\psi) & 0 \\ \sin(\psi) & \cos(\psi) & 0 \\ 0 & 0 & 1 \end{bmatrix} \quad (2.6c)$$

The notation for a rotation matrix operation is multiplication of the matrix $R_u(\theta)$, applying a left-handed *rotation* operator about some axis \hat{u} by θ . The resultant vector of a rotation operation still exists in the same reference frame. For example an \hat{X} axis rotation by ϕ of some vector \vec{v} is given by:

$$\vec{v}' = R_x(\phi)\vec{v} \quad \vec{v}', \vec{v} \in \mathcal{F}^1 \quad (2.7a)$$

No subscripts are used in Eq:2.7 to indicate reference frame ownership because all vectors are in the same frame. The time derivative of a rotation matrix about some axis \hat{u} by a rotation θ , $\dot{R}_u(\theta)$ is shown in [106] to be:

$$\frac{d}{dt}(R_u(\theta)) = (\dot{\hat{u}} \cdot \hat{u}) \times R_u \Rightarrow [\dot{\hat{u}} \cdot \hat{u}] \times R_u \quad (2.8a)$$

Where, for some vector \vec{a} , the operator $[\vec{a}]_\times$ denotes the cross-product matrix or *skew* matrix. The symmetric skew matrix is a matrix multiplication to replace the cross-product operator, for some other vector \vec{b} ;

$$\vec{a} \times \vec{b} = [\vec{a}]_\times \vec{b} \quad (2.8b)$$

$$[\vec{a}]_\times \triangleq \begin{bmatrix} 0 & -a_3 & a_2 \\ a_3 & 0 & -a_1 \\ -a_2 & a_1 & 0 \end{bmatrix} \quad (2.8c)$$

A vector *transformation* changes the resultant vector's reference frame. The transformation is then a rotation by an angle of the *difference* (or negative angle) between the resulting and principle reference frames. A transformation from frame \mathcal{F}^1 to \mathcal{F}^2 , differing by an angle of ϕ about the \hat{X} axis is then a negative rotation operation:

$$\vec{\nu}_2 = R_x(-\phi)\vec{\nu}_1 \quad (2.9a)$$

$$\vec{\nu}_2 \in \mathcal{F}^2 \text{ and } \vec{\nu}_1 \in \mathcal{F}^1 \quad (2.9b)$$

The distinction between Eq:2.7 and Eq:2.9 is the directional sense of the angular operand ϕ , and hence the effect it has on the argument vector. The transformation or rotation of a vector from the inertial frame \mathcal{F}^I to the body frame \mathcal{F}^b is the product of three sequential operations about each principle axis. Each subsequent rotation is applied relative to a new intermediate frame; hence each Euler angle is taken relative to a specific intermediate frame and not a global one. The order of those axial rotation operations does affect the Euler set, any consequences of which are detailed in [70]. In this dissertation the Z-Y-X or yaw, pitch, roll rotation sequence is used. A rotation of the vector $\vec{\nu}$ from the inertial to the body frame, $\mathcal{F}^I \rightarrow \mathcal{F}^b$, is then applied by sequential yaw, ψ , pitch, θ , and roll ϕ operations about the \hat{Z} , \hat{Y} and \hat{X} axes respectively:

$$R_I^b(\eta) = R_I^b(\phi, \theta, \psi) \triangleq R_z(\psi)R_y(\theta)R_x(\phi) \quad (2.10a)$$

$$\vec{\nu}' = R_I^b(\phi, \theta, \psi)\vec{\nu} \quad (2.10b)$$

$$\rightarrow \vec{\nu}' = R_z(\psi)R_y(\theta)R_x(\phi)\vec{\nu} \quad (2.10c)$$

It is important to note that in Eq:2.10 both operand and output vectors are *both* in the inertial frame, namely $\vec{\nu}', \vec{\nu} \in \mathcal{F}^I$. A *transformation* of a vector from the inertial to the body frame is the negative counterpart of Eq:2.10, a distinction which is not always explicitly stated.

$$\vec{\nu}_b = R_I^b(-\eta)\vec{\nu}_I = R_I^b(-\phi, -\theta, -\psi)\vec{\nu}_I \quad (2.11a)$$

$$\text{for } \vec{\nu}_b \in \mathcal{F}^b \text{ and } \vec{\nu}_I \in \mathcal{F}^I \quad (2.11b)$$

$$\rightarrow \vec{\nu}_b = R_z(-\psi)R_y(-\theta)R_x(-\phi)\vec{\nu}_I \quad (2.11c)$$

$$= R_x(\phi)R_y(\theta)R_z(\psi)\vec{\nu}_I = R_b^I\vec{\nu}_I \quad (2.11d)$$

$$R_I^b = (R_b^I)^{-1} = (R_b^I)^T \quad (2.11e)$$

The relationship in Eq:2.11e is an inversion property (*transpose*) of the rotation matrix. A rotation matrix's inverse can be used interchangeably with its negative counterpart to maintain a positive sense of the argument angle. To ensure clarity throughout this dissertation's mathematics, a negative angular sense implies a *transformation* to a different reference frame. Where applicable, the order of rotation will indicate the sequence direction whilst the angular sign differentiates the rotation or transformation operations.

The body frame's angular velocity is taken relative to the inertial frame, represented by $\vec{\omega}_{b/I}$ mostly just simplified to $\vec{\omega}_b$ [rad.s⁻¹]. Seeing that each Euler angle is measured with respect to an intermediary frame, a distinction must then be made between $d\vec{\eta}/dt$ and $\vec{\omega}_b$. All three Euler angles need to be transformed to a common frame to define the relationship between Euler and angular rates. Exploiting vehicle frames 1 & 2, or rather \mathcal{F}^{v1} & \mathcal{F}^{v2} , as intermediary frames to describe respectively frames after $R_x(\phi)$ and $R_y(\theta)$ operations and using the rotation matrix derivative from Eq:2.8. The angular velocity $\vec{\omega}_b$ is the time derivative of Euler angles in the body frame:

$$\vec{\omega}_b = [p \quad q \quad r]^T \triangleq \frac{d}{dt}\vec{\eta} = \frac{d}{dt}\vec{\eta}_b \in \mathcal{F}^b \quad (2.12a)$$

$$\vec{\eta}_b \triangleq R_{v2}^b(\phi)\vec{\phi} + R_{v2}^b(\phi)R_{v1}^{v2}(\theta)\vec{\theta} + R_{v2}^b(\phi)R_{v1}^{v2}(\theta)R_I^{v1}(\psi)\vec{\psi} \in \mathcal{F}^b \quad (2.12b)$$

$$\therefore \vec{\omega}_b = \left[\begin{array}{c} \dot{\vec{\phi}} \\ \times \\ R_{v2}^b(\phi) + R_{v2}^b(\phi) \left[\begin{array}{c} \dot{\vec{\theta}} \\ \times \\ R_{v1}^{v2}(\theta) + R_{v2}^b(\phi)R_{v1}^{v2}(\theta) \left[\begin{array}{c} \dot{\vec{\psi}} \\ \times \\ R_I^{v1}(\psi) \end{array} \right] \end{array} \right] \end{array} \right] \in \mathcal{F}^b \quad (2.12c)$$

With Euler vectors $\vec{\phi}$, $\vec{\theta}$ and $\vec{\psi}$ being axis projections onto X-Y-Z axes respectively; $\phi \cdot \hat{i}$, $\theta \cdot \hat{j}$ and $\psi \cdot \hat{k}$. The vehicle frames used for Eq:2.12a and the subsequent rotations between each frame don't necessarily have to be in that order. The equation could change depending on what rotation sequence was used, here Z-Y-Z rotation sequences were used. The Euler rates equation then simplifies to the formal relationship between two rotating frames, with $\vec{\omega}_b = [p \ q \ r]^T$ in [rad.s⁻¹]:

$$\begin{bmatrix} p \\ q \\ r \end{bmatrix} = \begin{bmatrix} 1 & 0 & -\sin(\theta) \\ 0 & \cos(\phi) & \sin(\phi)\cos(\theta) \\ 0 & -\sin(\theta) & \cos(\phi)\sin(\theta) \end{bmatrix} \begin{bmatrix} \dot{\phi} \\ \dot{\theta} \\ \dot{\psi} \end{bmatrix} \quad (2.12d)$$

$$\Rightarrow \vec{\omega}_b = \Psi(\eta) \dot{\vec{\eta}} \in \mathcal{F}^b \quad (2.12e)$$

$$\Psi(\eta) = \begin{bmatrix} 1 & 0 & -\sin(\theta) \\ 0 & \cos(\phi) & \sin(\phi)\cos(\theta) \\ 0 & -\sin(\theta) & \cos(\phi)\sin(\theta) \end{bmatrix} \quad (2.12f)$$

$$\Rightarrow \dot{\vec{\eta}} = \Psi^{-1}(\eta) \vec{\omega}_b = \Phi(\eta) \vec{\omega}_b \in \mathcal{F}^{v1,v2,I} \quad (2.12g)$$

$$\Phi(\eta) = \begin{bmatrix} 1 & \sin(\phi)\tan(\theta) & \cos(\phi)\tan(\theta) \\ 0 & \cos(\phi) & -\sin(\phi) \\ 0 & \sin(\phi)\sec(\theta) & \cos(\phi)\sec(\theta) \end{bmatrix} \quad (2.12h)$$

The *Euler* matrix, $\Psi(\eta)$, contains a well known and problematic singularity; at $\theta = \pm\pi/2$ where the determinant of the transformation matrix is zero. The mathematical manifestation of that singularity and its physical consequences are expanded on in Sec:3.2.4. The singularity is present in the middle roll angle θ , which is a direct consequence of the chosen Z-Y-X rotation sequence adopted. Each Euler angle is potentially singular depending on the rotation order used. In later dynamics quaternions are used in lieu of Euler angles (Sec:3.2.5). Attitude in \mathbb{R}^3 , or $SO(3)$, is intuitive and well suited to the conventions defined here.

Quaternions (Sec:3.2.5), despite being in \mathbb{R}^4 , are similarly constructed in the Z-Y-X order following a three rotation sequence. Combined quaternion operations are additive but non-commutative, as such the order is important. The constructed attitude quaternion order will produce the same resultant frame orientation however the quaternion, and its rotation path, will differ. A quaternion Q_b , representing the body's attitude, and some vector $\vec{\nu}_I$ in the inertial frame is related to the body frame \mathcal{F}^b as follows:

$$\vec{\nu}_b = R_I^b(-\eta) \vec{\nu}_I \iff Q_b \otimes \begin{bmatrix} 0 & \vec{\nu}_I \end{bmatrix}^T \otimes Q_b^* \quad (2.13a)$$

$$Q_b \triangleq Q_z \otimes Q_y \otimes Q_x \text{ and it's inverse } Q_b^* \triangleq Q_x^* \otimes Q_y^* \otimes Q_z^* \quad (2.13b)$$

The symbol \otimes represents the Hamilton product, or quaternion multiplication operator. Later the Hamilton product is used again for inertial tensor transformations (Sec:2.3). Each quaternion, Q_i , is always the *unit* quaternion about the i^{th} axis. For the body quaternion, Q_b , it is the unit quaternion rotation about the body's Euler axis, [70]. A quaternion rotation operates on an argument vector with a zero quaternion scalar component. So then for some vector $\vec{\nu}$, the quaternion rotation operation in Eq:2.13a is equivalent to;

$$Q_{\vec{\nu}'} = Q \otimes (Q_{\vec{\nu}}) \otimes Q^* \quad (2.14a)$$

$$\text{Where } Q_{\vec{\nu}} = \begin{bmatrix} 0 & \vec{\nu} \end{bmatrix}^T, \quad Q_{\vec{\nu}'} = \begin{bmatrix} 0 & \vec{\nu}' \end{bmatrix} \quad (2.14b)$$

Quaternion representation in Eq:2.14b ensures that the operation is entirely in \mathbb{R}^4 space. However it is typically omitted, despite \mathbb{R}^4 being implied and as such, Eq:2.14a is then simply:

$$\vec{\nu}' = Q \otimes (\vec{\nu}) \otimes Q^* \quad (2.15)$$

Quaternion dynamics, and the quaternion operator, are later expanded upon to replace the use of Euler angles and rotation matrices as a convention for attitude representation later in Chapter:3.

2.2.2 Motor Axis Layout

The whole structure (previously in Fig:2.1) consists of multiple rigidly connected bodies with only relative rotations between each body permitted by its joints, illustrated previously in the design description in Sec:2.1. Those rigid bodies are categorized into four inter-connected motor modules, $M_{1 \rightarrow 4}$, and a single body structure, \mathbf{B} (*frame* structure, not reference frame). Each module contains two sequential gimbal rings, where each ring has one degree of relative rotation, actuated by a servo, between itself and the subsequent ring. There needs to be distinct nomenclature used for describing these motor modules such that the dynamic derivations later are clear and logical despite the complicated multibody system...

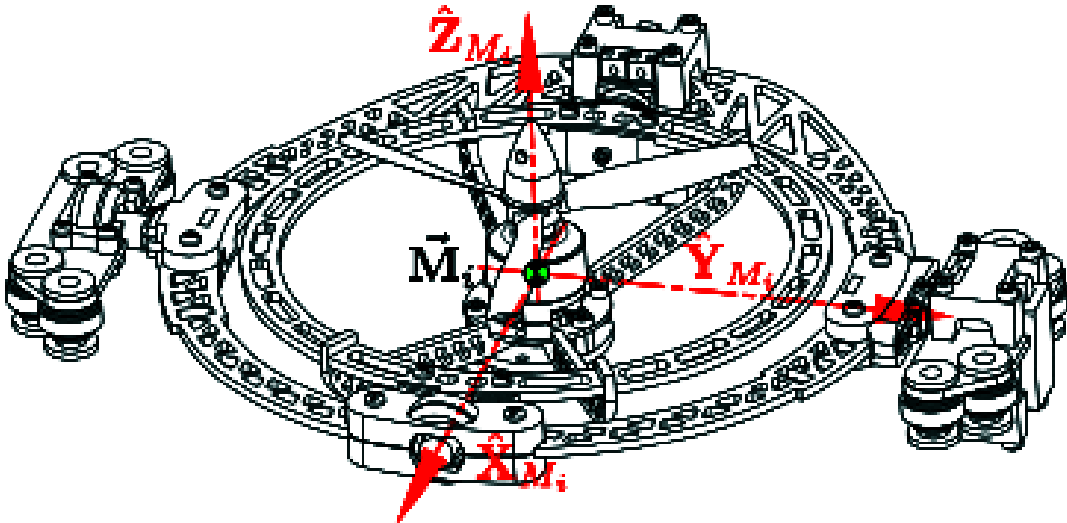


Figure 2.7: Aligned motor frame axes

Every propeller/motor is actuated by a pair of two servos about two subsequent rotational axes (Fig:2.7) in a similar fashion to an Euler rotation sequence. The i^{th} propeller, attached to the BLDC motor's rotor, rotates in frame \mathcal{F}^{M_i} with a rotational speed Ω_i in revolutions per second, or [RPS], about the \hat{Z}_{M_i} stator axis. Fig:2.8 shows the sequential relative module frames.

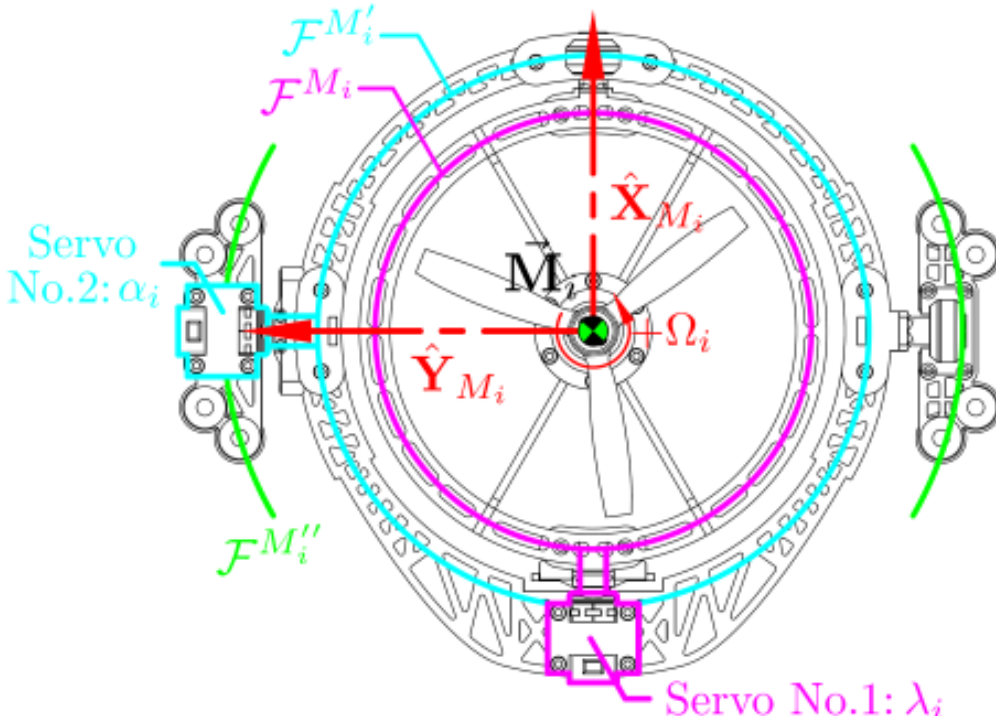


Figure 2.8: Intermediate motor frames

The motor's stator is affixed to the inner ring assembly which rotates about its \hat{X}_{M_i} axis by λ_i from the module's first servo. The first servo is attached to the middle ring assembly with the frame $\mathcal{F}^{M'_i}$. The middle ring assembly, frame $\mathcal{F}^{M'_i}$, rotates about its $\hat{Y}_{M'_i}$ axis actuated by the second α_i servo. That second servo is affixed to an intermediate $\mathcal{F}^{M''_i}$ frame, finally there's an orthogonal rotation about $\hat{Z}_{M''_i}$ between \mathcal{F}^b and $\mathcal{F}^{M''_i}$. Each module's actuation state is fully described by the rotational speed, both servo positions and all their respective rates; $[\Omega_i, \lambda_i, \alpha_i, \dot{\Omega}_i, \dot{\lambda}_i, \dot{\alpha}_i]^T$ for $i \in [1 : 4]$.

Fig:2.9 shows how the axes of each motor module aligns with the body frame's axes at rest. The body frame \mathcal{F}^b has the origin \vec{O}_b at the X-Y center of the structure, co-planar to each motor modules' center. *Neither* the body frame's origin *nor* each modules center of rotation are coincidental with body's center of mass. The exact disparity between the origin(s) of motion and the respective body's center of mass are quantified subsequently in Sec:2.3.



Figure 2.9: Body frame axes layout

The motor module pair 1 and 3 have their \hat{X} -axes in the positive and negative \hat{X}_b directions of the body frame respectively. Similarly Modules 2 and 4 have their \hat{X} -axes in the positive and negative \hat{Y}_b directions of the body frame. Motor modules 1 and 3 have clockwise rotating propellers; denoted by a positive superscript or $\Omega_{[1,3]}^+$. Conversely modules 2 and 4 have counter-clockwise rotations; denoted by a negative superscript or $\Omega_{[2,4]}^-$.

Not shown in Fig:2.9 is the relative \hat{Z}_b origin position of \vec{O}_b with respect to the entire assembly. The ΔZ height of the body's motion centroid is such that its origin is co-planar with the four motor modules rotational centers. The center of motion is not coincidental with the center of mass.

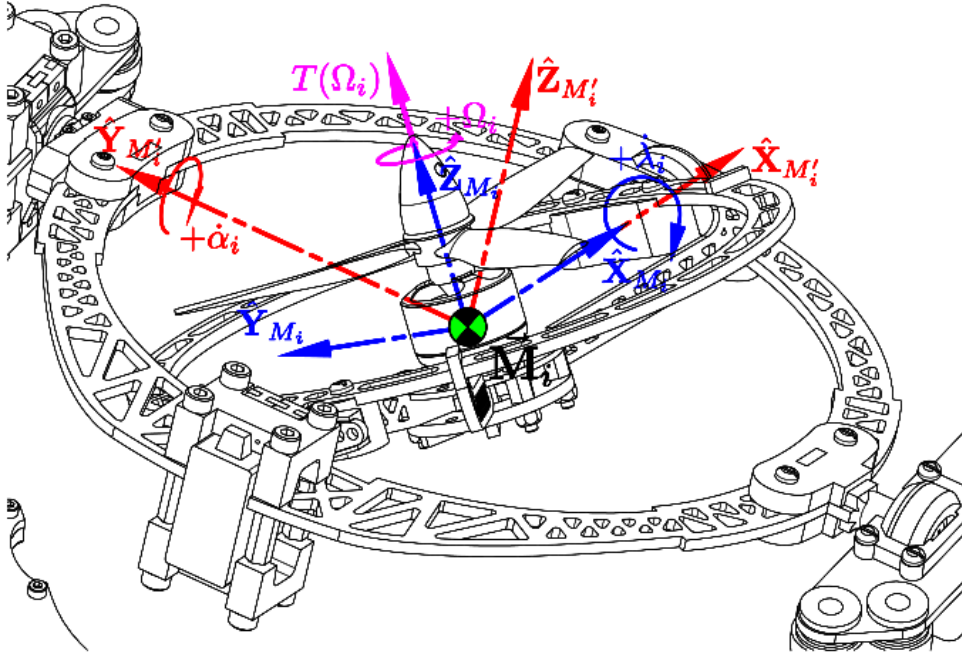


Figure 2.10: Motor thrust force

Each motor is displaced from the body frame origin by the distance $L_{arm} = 195.16$ [mm] (shown in Fig:2.9). Transformation of some vector \vec{v}_{M_i} in the motor frame \mathcal{F}^{M_i} to the body frame is given as three sequential rotation operations:

$$\vec{v}_b = R_{M_i}^b \vec{v}_{M_i} = R_z(-\sigma_i) R_y(-\alpha_i) R_x(-\lambda_i) \vec{v}_{M_i} \quad \text{for } \sigma_i \in [0 \quad \frac{\pi}{2} \quad \pi \quad \frac{2\pi}{3}] \quad (2.16a)$$

If the propeller's rotation produces some thrust force $T(\Omega_i)$ in the motor module frame (Fig:2.10) which acts through the center of rotation \vec{M}_i ; that force is similarly transformed to the body frame through Eq:2.16a. A thrust vector for $\vec{T}(\Omega_i) \in \mathcal{F}^{M_i}$ in the body frame \mathcal{F}^b is calculated:

$$\vec{T}(\Omega_i) = R_z(-\sigma_i) R_y(-\alpha_i) R_x(-\lambda_i) [0 \quad 0 \quad T(\Omega_i)]^T \quad \in \mathcal{F}^b \quad (2.16b)$$

The constant orthogonal σ_i rotations about $\hat{z}_{M''_i}$ are independent of actuator positions, σ_i is determined by the motor module's location. The rotation matrices $R_z(\sigma_i)$ for $\sigma_i = (i-1)\pi/2$ are:

$$R_z = \begin{bmatrix} 1 & 0 & 0 \\ 0 & 1 & 0 \\ 0 & 0 & 1 \end{bmatrix}, \begin{bmatrix} 0 & -1 & 0 \\ 1 & 0 & 0 \\ 0 & 0 & 1 \end{bmatrix}, \begin{bmatrix} -1 & 0 & 0 \\ 0 & -1 & 0 \\ 0 & 0 & 1 \end{bmatrix}, \begin{bmatrix} 0 & 1 & 0 \\ -1 & 0 & 0 \\ 0 & 0 & 1 \end{bmatrix} \quad \text{for } i \in [1, 2, 3, 4] \text{ respectively} \quad (2.16c)$$

The actuator space, including propeller speed Ω_i [RPS], is then $\in \mathbb{R}^{12}$, or rather $\mathbb{U} \in \mathbb{R}^{12}$, in contrast with $\mathbb{U} \in \mathbb{R}^4$ for a standard quadrotor. The actuator input set $u \in \mathbb{U}$ is then structured as:

$$u = [\Omega_1^+ \quad \lambda_1 \quad \alpha_1 \quad \dots \quad \Omega_4^- \quad \lambda_4 \quad \alpha_4]^T \quad \in \mathbb{R}^{12} \quad (2.17)$$

2.3 Inertial Matrices & Masses

When transforming inertias between reference frames it is more appropriate to use rotation matrices to apply the transformation and not quaternions. Spatial rotation of inertial matrices are ill suited to quaternion parametrization.

An undesirable consequence of relative rotations within a non-rigid body are the inertial responses associated with such movements. Given Newton's Second Law of Rotational Motion; each applied rotation is going to produce an equal but opposite reaction onto the principally inducing body. Similarly a gyroscopic cross product from rotational velocities is also present when rotating bodies that have their own relative rotation. Typically for most rigid body dynamics (Sec:3.1), such first and second order effects are negligible given that the angular rates on which they depend are small enough to approximate as zero; $\vec{\omega}_b \approx \vec{0}$. A dynamic set-point (non-zero) attitude tracking plant is, however, going to produce time varying body angular velocities and accelerations that must be accounted for.

The dynamic effects of those torque responses are derived later in Sec:3.3.1. Both inertial and gyroscopic effects are dependent on the considered body's rotational inertia about each respective axis. The magnitude of those inertias are ostensibly a by-product of the structure's design but also the vehicle's instantaneous configuration.

The following inertias presented are all calculated from a SolidWorks model with masses to match physical prototype measurements. Each rigidly connected body affected by the same angular velocity is grouped together. Every motor module then contains 3 independent inertial bodies; the propeller/rotor body, the inner ring and finally middle ring assemblies, each of which are now described in detail.



Figure 2.11: Rotor assembly rotational structure

The first rotational body to consider is that of the propeller and rotor assembly (Fig:2.11, excluding the motor's greyed out stator). The *rotor* assembly, with subscript r, has a net mass $m_r = 27$ g with a center of mass $C.M_r = [0.0 \ 0.0 \ 15.5]^T$ [mm] relative to the entire motor modules center of rotation \vec{M}_i . The propeller's rotation plane is similarly $[0.0 \ 0.0 \ 23.0]^T$ [mm] relative to \vec{M}_i (previously illustrated in Fig:2.3).

At high speeds the propeller's inertial contribution to the rotor assembly can be approximated as a solid disc. It follows that the inner ring's inertial components can then be regarded as constant with respect to Ω_i ; moreover its center of mass is independent of that propeller's rotation.

The entire rotor assembly then has a constant inertia J_r , with principle inertial axes centered and aligned as in Fig:2.11:

$$J_r = \begin{bmatrix} 105.5 & 0.0 & 0.0 \\ 0.0 & 105.5 & 0.0 \\ 0.0 & 0.0 & 41.8 \end{bmatrix} \quad [\text{g.cm}^2] \quad (2.18)$$

The net angular velocity of the rotor assembly, $\vec{\omega}_r$ [rad.s⁻¹], relative to the body frame is produced by the BLDC motor's rotational velocity Ω_i and both servo rates; $\dot{\lambda}_i$ and $\dot{\alpha}_i$. Here Ω_i and both servo rates are measured in [rad.s⁻¹], later Ω_i is needed in [rev.s⁻¹] for Blade-element momentum theory thrust calculations (Sec:3.2.1). Each servo's angular velocity is *transformed* onto the motor frame \mathcal{F}^{M_i} .

$$\vec{\omega}_r = \begin{bmatrix} 0 \\ 0 \\ \Omega_i \end{bmatrix} + \frac{d\lambda_i}{dt} R_x(-\lambda_i) \begin{bmatrix} \lambda_i \\ 0 \\ 0 \end{bmatrix} + \frac{d\alpha_i}{dt} R_y(-\alpha_i) R_x(-\lambda_i) \begin{bmatrix} 0 \\ \alpha_i \\ 0 \end{bmatrix} \in \mathcal{F}^{M_i} \quad (2.19)$$

Eq:2.19 is later replaced with a quaternion operator. That equation and the remaining angular velocity equations for each body derived here are therefore not expanded further in their current rotation matrix form(s)...



Figure 2.12: Inner ring rotational structure

The next assembly, to which the motor frame \mathcal{F}^{M_i} is attached, is the *inner ring* assembly denoted with subscript n. The inner ring structure has a mass $m_n = 92$ [g], including the rotor assembly in that calculation. The center of mass is positioned $C.M_n = [-1.44 \ 00.0 \ 5.14]^T$ [mm] relative to the module's center of rotation \vec{M}_i . The inner ring, being rotated by the λ_i servo about the \hat{X}_{M_i} axis, then has an inertial matrix which includes J_r from Eq:2.18 centered and aligned with axes as in Fig:2.12:

$$J_n = J_{M_i} = \begin{bmatrix} 520.9 & -31.7 & -0.3 \\ -31.7 & 1826.3 & 0.0 \\ -0.3 & 0.0 & 2050.8 \end{bmatrix} \quad [\text{g.cm}^2] \quad (2.20)$$

The rotational velocity of the collective inner ring assembly $\vec{\omega}_n$ in [rad.s^{-s}] (or $\vec{\omega}_{M_i}$ for the angular velocity of frame \mathcal{F}^{M_i}) is similar to that of Eq:2.19. They both occur in the same frame however the inner ring's angular velocity has no velocity contribution from Ω_i :

$$\vec{\omega}_n = \vec{\omega}_{M_i/b} = \frac{d\lambda_i}{dt} R_x(-\lambda_i) \begin{bmatrix} \lambda_i \\ 0 \\ 0 \end{bmatrix} + \frac{d\alpha_i}{dt} R_y(-\alpha_i) R_x(-\lambda_i) \begin{bmatrix} 0 \\ \alpha_i \\ 0 \end{bmatrix} \in \mathcal{F}^{M_i} \quad (2.21)$$

That first actuating servo for λ_i and its coaxial support bearing are both affixed to the intermediate *middle ring* assembly, with subscript m (middle ring only Fig:2.13). The intermediate frame $\mathcal{F}^{M'_i}$ is attached to the middle ring body with a mass $m_m = 98$ [g], excluding the inner most ring's contribution. That middle ring body alone has a center of mass $C.M_m = [-4.70 \ 0.37 \ -0.36]^T$ [cm] relative to \vec{M}_i .

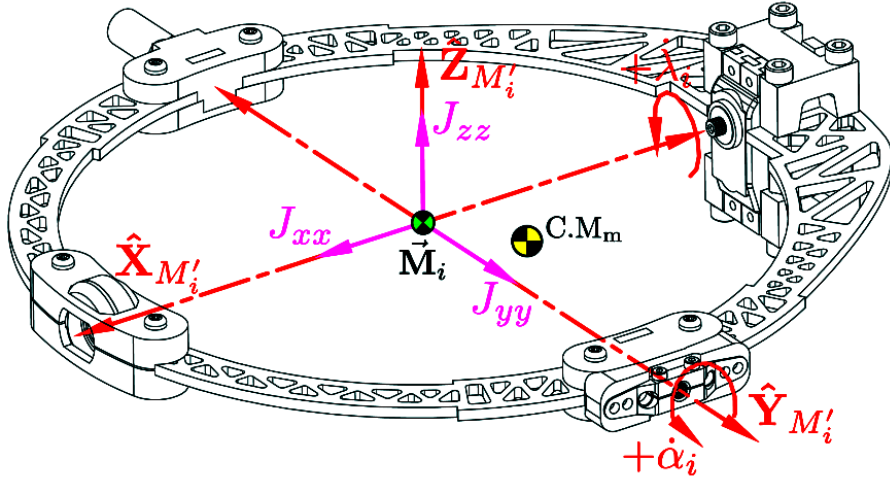


Figure 2.13: Middle ring rotational structure

Together the inner and middle rings make the whole motor module assembly (Fig:2.14), with a subscript p. The net module has a mass $m_p = 190$ [g]. The center of mass for the entire module, $C.M_p$, is a function of the inner ring's rotational position λ_i relative to the middle frame $\mathcal{F}^{M'_i}$. That module's center of mass is calculated:

$$C.M'_n = R_x(\lambda)(C.M_n) \quad (2.22a)$$

$$C.M_p = \frac{m_m(C.M_m) + m_n(C.M'_n)}{m_p} \quad (2.22b)$$

Substituting physical values into Eq:2.22b for the inner and middle rings' center of masses respectively:

$$C.M_p(\lambda) = \frac{98 [-4.70 \ 0.37 \ -0.36]^T \times 10^{-7} + 92 R_x(\lambda) [-1.44 \ 0.00 \ 3.06]^T \times 10^{-8}}{190 \times 10^{-3}} \quad (2.22c)$$

Which then has a value at rest, for reference, with the servo $\lambda_i = 0$ relative to the center of rotation \vec{M}_i :

$$C.M_p(0) = [-2.49 \ 0.19 \ 0.04]^T \Big|_{\lambda_i=0} \quad [\text{cm}] \quad (2.22d)$$

The complete motor module is rotated by the α_i servo about its $\hat{Y}_{M'_i}$ axis. The module's compound inertia J_p is a combination of the middle ring's inertia J_m and the inner ring's inertia J_n rotated by λ_i about \hat{X}_{M_i} (aligned as per Fig:2.14). The latter's contribution is dependent on the *rotation* (not transformation) angle λ_i which from the conservation of angular momentum theory, detailed in [99], produces the net inertia of that frame; $J_{M'_i}$ or J_p :

$$\text{With } J_m = \begin{bmatrix} 2905.7 & 0.0 & 390.9 \\ 0.0 & 8446.4 & 0.0 \\ 390.9 & 0.0 & 11125.7 \end{bmatrix} \quad [\text{g.cm}^2] \quad (2.23a)$$

$$J_p(\lambda_i) = J_{M'_i} = J_m + R_x(\lambda_i)(J_n)R_x^{-1}(\lambda_i) \quad (2.23b)$$

Noting that $J_{M_i} = J_n$ is the inner ring's inertia from Eq:2.20, but re-orientated through a rotation $R_x(\lambda_i)$. That inertia with $\lambda_i = 0$ and relative to the middle ring frame $\mathcal{F}^{M'_i}$ has a reference value:

$$J_p(0) = \begin{bmatrix} 3365.4 & -0.1 & 390.6 \\ -0.1 & 10210.1 & 0.0 \\ 390.6 & 0.0 & 13118.0 \end{bmatrix} \Big|_{\lambda_i=0} \quad [\text{g.cm}^2] \quad (2.23c)$$

Because R_x is a full rank square matrix its inverse R_x^{-1} , used in Eq:2.23b, always exists. The module's inertia could be further divided into constant and variable components; $J_p(\lambda_i) = J_{const} + J_{M_i}(\lambda_i)$. The variable terms can, under certain conditions, be simplified and neglected...

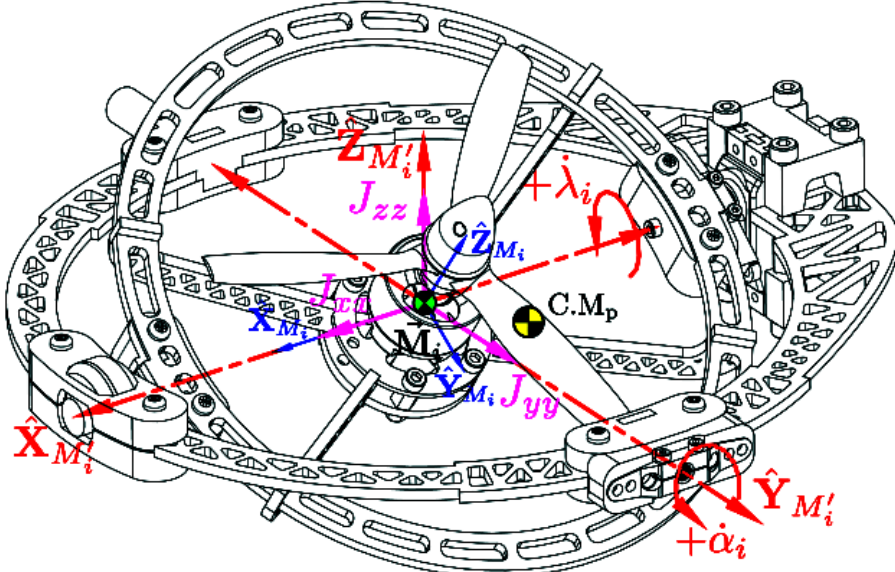


Figure 2.14: Module assembly rotational structure

Fig:2.15 shows how the complete motor module and its rotational axes (in Fig:2.14) are attached and centered relative to the body structure. The second α_i servo is affixed to the body structure and rotates the entire motor module.



Figure 2.15: Complete motor module attached to the body structure

Finally, the angular velocity experienced by the net motor assembly relative to the body frame, $\vec{\omega}_p$ in frame $\mathcal{F}^{M'_i}$, is entirely as a result of the α_i servo actuation:

$$\vec{\omega}_p = \vec{\omega}_{M'_i/b} = \frac{d\alpha_i}{dt} R_y(-\alpha_i) \begin{bmatrix} 0 \\ \alpha_i \\ 0 \end{bmatrix} \in \mathcal{F}^{M'_i} \quad (2.23d)$$

That α_i servo is affixed to the body structure and so its inertial volume and that of the outer coaxial bearing support contributes then to the body structure's inertia; whose value excludes any of the four motor modules. Attached to that servo is an intermediate frame $\mathcal{F}^{M''_i}$ (Fig:2.15) which differs from the middle ring frame by an $R_y(-\alpha_i)$ transformation and differs from the body frame F^b by an orthogonal $R_z(\sigma_i)$ rotation.

The motor modules are suspended from the body frame with a set of silicone damping balls. The *body structure* which includes those connecting masses, with a subscript y , has center of mass $C.M_y$ (without any motor modules attached, Fig:2.16). The center of mass coincides with the \hat{X}_b and \hat{Y}_b directional axes but lies $\Delta Z = -9.52$ [mm] below the body frame's origin of motion $\vec{O}_b \in \mathcal{F}^b$.

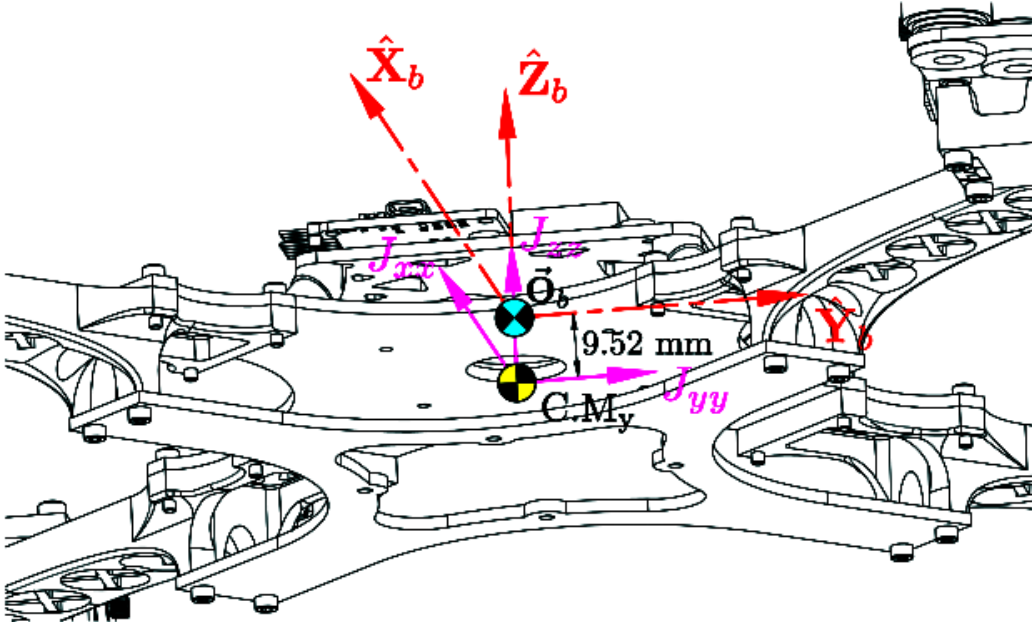


Figure 2.16: Body structure's center of mass

Note: that body frame origin \vec{O}_b which all motion is calculated with respect to is co-planar to the motor module's rotational centers, not the net center of mass.

The body structure's weight, including all four damping assemblies and electronics, totals to $m_y = 814.70$ [g]. Similarly the body structure's net inertia (*sans* motor modules) J_y , about its center of mass (Fig:2.16), is:

$$J_y = \begin{bmatrix} 181569.7 & 0.4 & -19.4 \\ 0.4 & 181692.2 & 8.9 \\ -19.4 & 8.8 & 360067.2 \end{bmatrix} \times 10^{-7} \quad [\text{kg.m}^2] \quad (2.24a)$$

Using the Parallel Axis theorem to translate that inertia to the origin of motion by $\Delta Z = +9.52$ [mm], the inertia about the origin, \vec{O}_b , is:

$$J' = J + m(\vec{d} \cdot \vec{d} - \vec{d} \otimes \vec{d}) \approx J + md^2 \quad (2.24b)$$

For the general parallel axis transformation in Eq:2.24b, \otimes represents the Hamilton product of two $[3 \times 1]$ matrices. It is used later to indicate quaternion multiplication. The vector \vec{d} is the difference between the center of mass $C.M_y$ and the body frame origin \vec{O}_b .

$$\therefore J'_y = \frac{J_y}{C.M} + m_y(\Delta \vec{Z} \cdot \Delta \vec{Z} - \Delta \vec{Z} \otimes \Delta \vec{Z}) \quad (2.24c)$$

That body's constant inertia J_y at the origin $\vec{\mathbf{O}}_b$ and aligned with the body frame \mathcal{F}^b is then:

$$\rightarrow J'_y = \begin{bmatrix} 182307.7 & 0.4 & -14.5 \\ 0.4 & 182430.1 & 6.5 \\ -14.5 & 6.5 & 360067.2 \end{bmatrix} \times 10^{-7} \text{ [kg.m}^2\text{]} \quad (2.24d)$$

Net inertia for the complete multibody vehicle, $J_b(u)$ about the origin $\vec{\mathbf{O}}_b$, is a combination of all the relative attached bodies as a function of all actuator positions $u \in \mathbb{U}$. The entire assembly's inertia $J_b(u)$ is the *net* body frame's inertia, different from J_y which is the inertia for *only* the body structure. That collective assembly being the four motor modules, each rotated first by λ_i , then α_i and finally translated to the body frame origin; and the body structure's contribution itself.

Those motor modules' inertial transformations from their respective centers of rotation, in frames \mathcal{F}^{M_i} for $i \in [1 : 4]$, to the body frame \mathcal{F}^b are analogous to that of Eq:2.16. Reiterating that $\vec{\mathbf{O}}_b$ is *co-planar* to each module's center of rotation; each motor module's inertia, $J_p(\lambda_i)$ or $J_{M'_i}$, defined in Eq:2.23b, is further rotated by α_i about the $\hat{Y}_{M'_i}$ axis and finally an orthogonal $\hat{Z}_{M''_i}$ axis rotation (aligned with \hat{Z}_b) onto \mathcal{F}^b .

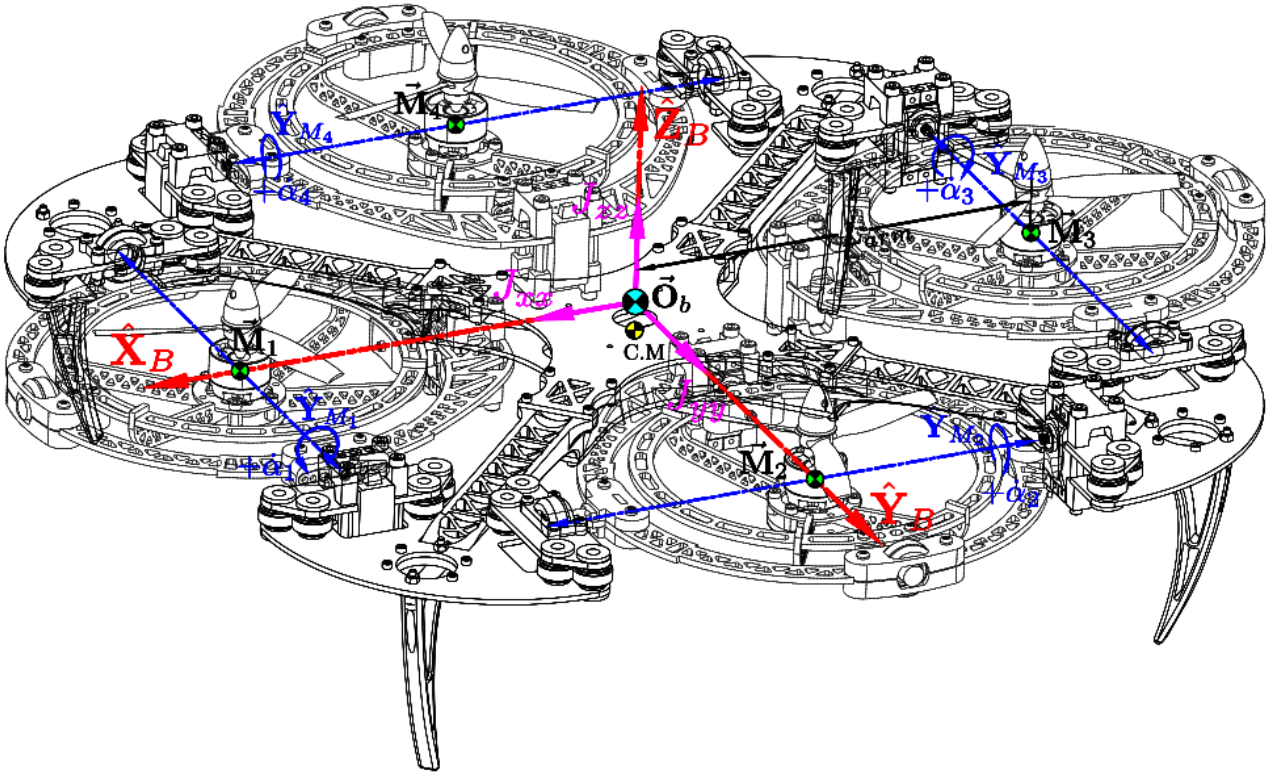


Figure 2.17: Inertial, mass and motor modules respective centers

For the entire body's net inertia each contributing assembly's inertia must be defined with respect to the body's origin; first aligned parallel to the common set of body frame axes \hat{X}_b , \hat{Y}_b and \hat{Z}_b and then translated to the origin $\vec{\mathbf{O}}_b$. Each motor module's inertia, still centered relative to each individual rotational centers $\vec{\mathbf{M}}_i$ in Fig:2.17, but re-orientated to align parallel with $\vec{\mathbf{O}}_b$ with rotations about axes $\hat{X} \in \mathcal{F}^{M_i}$, $\hat{Y} \in \mathcal{F}^{M'_i}$, $\hat{Z} \in \mathcal{F}^{M''_i}$, is calculated:

$$J_{\vec{\mathbf{M}}_i}(u \cdot i) = R_z(\sigma_i)R_y(\alpha_i)(J_p(\lambda_i))R_y^{-1}(\alpha_i)R_z^{-1}(\sigma_i) \text{ for } i \in [1 : 4] \quad (2.25a)$$

The argument $(u \cdot i)$ in Eq:2.25a is the i^{th} projection of the actuator space; that being $[\Omega_i \ \lambda_i \ \alpha_i]^T$. Furthermore the rotation $R_z(\sigma_i)$ was defined as an orthogonal \hat{Z}_b rotation previously in Eq:2.16c. Expanding each module's inertia to individual inner and middle ring inertial contributions then yields:

$$\therefore J_{\vec{\mathbf{M}}_i}(u \cdot i) = R_zR_y(\alpha_i)(J_m)R_y^{-1}(\alpha_i)R_z^{-1} + R_zR_y(\alpha_i)R_x(\lambda_i)(J_n)R_x^{-1}(\lambda_i)R_y^{-1}(\alpha_i)R_z^{-1} \quad (2.25b)$$

It's at this stage that, despite simplifications, the symbolic inertial equations all become overly cumbersome to include with numeric values... For the sake of brevity, exact calculated inertial values for the input dependent plant are omitted.

Each module's rotational center, vectors $\vec{M}_{1 \rightarrow 4}$, are all equally spaced relative to the origin of motion, \vec{O}_b , with a parallel axis arm $L_{arm} = 195.16$ [mm] (Fig:2.17). To avoid notational confusion the term $\vec{L}_i = [\pm 195.16 \ 0 \ 0]^T$ or $[0 \ \pm 195.16 \ 0]^T$ is used to represent the vector displacement between the origin \vec{O}_b and each motor modules center of rotation $\vec{M}_{1 \rightarrow 4}$. The net inertial equation $J_b(u)$, about the origin \vec{O}_b and depending on the actuator position matrix $u \in \mathbb{U}$, can be calculated as:

$$J_b(u) = J_y + \sum_{i=1}^4 J'_{\vec{M}_i}(u \cdot i) \quad [\text{kg.m}^2], \quad u \in \mathbb{U} \quad (2.26a)$$

Where $J'_{\vec{M}_i}(u \cdot i)$ is the motor module inertia from Eq:2.25 but translated to the origin \vec{O}_b using a parallel axis theorem with $m_p = 190$ [g]:

$$J'_{\vec{M}_i}(u \cdot i) = J_{\vec{M}_i}(u \cdot i) + m_p(\vec{L}_i \cdot \vec{L}_i - \vec{L}_i \otimes \vec{L}_i) \quad (2.26b)$$

Although Eq:2.26 produces the net multi-body's inertia, each equation to calculate $J'_{\vec{M}_i}$ involves cascaded transformations which may deteriorate the results certainty. Each module's inertia is first translated to their respective centers of rotation then rotated as per the two servos and then finally translated again back to the body frame's origin.

Alternatively the inertia contribution of each sub-assembly can be considered separately and translated directly to the body frame's origin from their respective mass centers. This will improve the accuracy of the produced inertial equations, each translation/rotation has with it an associated floating point concatenation. It is also perhaps more intuitive for the reader to consider each sub-body's contribution individually, despite having been derived as combined inertial bodies in the above. The vehicles net inertia can then be described as nine separate contributing bodies; four inner rings J_n , four middle rings J_m and one body structure J_y :

$$J_b(u) = J'_y + \sum_{i=1}^4 J_n(u \cdot i) + \sum_{i=1}^4 J_m(u \cdot i) \quad u \in \mathbb{U} \quad (2.27)$$

Isolating each body and considering each inertia independently; starting with the inner ring's, having an inertia J_n with respect to its *center of mass* (and not center of rotation) measured *relative* to its center of rotation. The following is then fundamentally different from the process in Eq:2.20, calculating the inner ring's inertial contribution about the origin \vec{O}_b .

For the inner ring only, with a mass m_n and center of mass $C.M_n$ relative to its center of rotation \vec{M}_i . The inner ring(s) contribution then follows:

$$m_n = 92 \quad [\text{g}] \quad (2.28a)$$

$$C.M_n = [-1.44 \ 0.0 \ 5.14]^T \quad [\text{mm}], \quad \in \mathcal{F}^{M_i} \quad (2.28b)$$

The inner ring's inertial matrix about it's center of mass (Fig:2.12) is the constant:

$$\begin{matrix} J_n \\ C.M \end{matrix} = \begin{bmatrix} 496.6 & -31.7 & 6.6 \\ -31.7 & 1800.1 & 0.0 \\ 6.6 & 0 & 2048.9 \end{bmatrix} \quad [\text{g.cm}^2] \quad (2.28c)$$

Relative to the body frame's origin \vec{O}_b the inner ring has a center of mass, rotated by λ_i and α_i servos about their respective axes with a relative orthogonal R_z rotation too, is then:

$$C.M_n''' = R_z R_y(\alpha_i) R_x(\lambda_i)(C.M_n) \quad \in \mathcal{F}^b \quad (2.28d)$$

So transforming the inertia from Eq:2.28c, still about the center of mass $C.M''_n$, but with axes aligned parallel with the body frame, or using the shorthand $\parallel \vec{\mathbf{O}}_b$. The inner ring's inertia as a function of both servo angles λ_i and α_i is:

$$\underset{\parallel \vec{\mathbf{O}}_b}{J'''}(\lambda_i, \alpha_i) = R_z R_y(\alpha_i) R_x(\lambda_i) (J_n) R_x^{-1}(\lambda_i) R_y^{-1}(\alpha_i) R_z^{-1} \quad (2.28e)$$

The vector difference between the new, rotated center of mass $C.M'''_n$ with the body origin $\vec{\mathbf{O}}_b$ is given by:

$$\Delta L = \vec{L}_i - C.M'''_n \quad (2.28f)$$

Then using the above with a parallel axis translation, adapted from Eq:2.24b, to move the rotated inertia J'''_n to the center of the body frame $\vec{\mathbf{O}}_b$:

$$\underset{\vec{\mathbf{O}}_b}{J_n} = J'''_n + m_n ((\Delta L \cdot \Delta L) \mathbb{I}_{3 \times 3} - \Delta L \otimes \Delta L) \quad (2.28g)$$

And for reference when both servos are at rest; $\lambda_i = 0$ and $\alpha_i = 0$, the inner ring's inertial contribution about the origin is explicitly:

$$\underset{\vec{\mathbf{O}}_b}{J_n} = \begin{bmatrix} 520.9 & -31.0 & 922.6 \\ -31.0 & 36348.5 & 0.0 \\ 922.6 & 0.0 & 36573.0 \end{bmatrix} \times 10^{-7} \Big|_{\lambda_i, \alpha_i=0} \quad [\text{kg.m}^2], \in \mathcal{F}^b \quad (2.28h)$$

Similarly, the same process is applied for the middle ring's rotated and translated inertia. The middle ring *only* (Fig:2.13) has a mass and center of mass relative to the module's center of rotation respectively:

$$m_m = 98 \quad [\text{g}] \quad (2.29a)$$

$$C.M_m = [-47.00 \quad 3.74 \quad -3.63]^T \quad [\text{mm}], \in \mathcal{F}^{M'_i} \quad (2.29b)$$

The inertial matrix of the middle ring body, excluding the inner ring, about its center of mass is:

$$\underset{C.M}{J_m} = \begin{bmatrix} 2879.1 & 172.3 & 223.6 \\ 172.3 & 6269.0 & 13.3 \\ 223.6 & 13.3 & 8947.5 \end{bmatrix} \quad [\text{g.cm}^2] \quad (2.29c)$$

Rotating the center of mass only by the α_i servo about the $\hat{Y}_{M'_i}$ axis yields the center of mass $C.M''_m$ relative to $\vec{\mathbf{O}}_b$:

$$C.M''_m = R_z R_y(\alpha_i) (C.M_m) \quad \in \mathcal{F}^b \quad (2.29d)$$

Then the rotated inertial matrix, aligned with axes parallel to the body frame origin $\vec{\mathbf{O}}_b$, follows:

$$\underset{\parallel \vec{\mathbf{O}}_b}{J''_m} = R_z R_y(\alpha_i) (J_m) R_y^{-1}(\alpha_i) R_z^{-1} \quad (2.29e)$$

The vector difference from the rotated center of mass to the body frame origin is calculated:

$$\Delta L = \vec{L}_i - C.M''_m \quad (2.29f)$$

Which then leads to the parallel axis translation of the middle ring's inertia to the body origin:

$$\underset{\vec{\mathbf{O}}_b}{J_m} = J''_m + m_m ((\Delta L \cdot \Delta L) \mathbb{I}_{3 \times 3} - \Delta L \otimes \Delta L) \quad (2.29g)$$

Again for reference; at rest with the middle ring servo $\alpha_i = 0$ the middle ring's inertial contribution at $\vec{\mathbf{O}}_b$ is:

$$\underset{\vec{\mathbf{O}}_b}{J_m} = \begin{bmatrix} 2905.7 & 715.4 & -303.9 \\ 715.4 & 27795.7 & 0.0 \\ -303.9 & 0.0 & 30475.0 \end{bmatrix} \times 10^{-7} \Big|_{\alpha_i=0} \quad [\text{kg.m}^2], \in \mathcal{F}^b \quad (2.29h)$$

Then, reiterating Eq:2.27, the instantaneous inertia of the entire body in motion is calculated as the contribution of the connected sub-bodies depending on the actuator matrix $u \in \mathbb{U}$.

$$J_b(u) = J'_y + \sum_{i=1}^4 J_n(u \cdot i) + \sum_{i=1}^4 J_m(u \cdot i) \quad u \in \mathbb{U} \quad (2.30a)$$

The mass for the whole vehicle is $m_b = 1574.7$ [g]. For reference and using Eq:2.30a; the inertial matrix for the assembly at the actuator rest conditions, $u = \vec{0}$, about the origin $\vec{\mathbf{O}}_b$ is:

$$J_b(\vec{0}) = \begin{bmatrix} 317448.2 & 0.4 & -14.5 \\ 0.4 & 317570.7 & 6.5 \\ -14.5 & 6.5 & 628257.5 \end{bmatrix} \times 10^{-7} \Big|_{u=\vec{0}} \quad [\text{kg.m}^2], \quad \in \mathcal{F}^b \quad (2.30b)$$

The maximal variation of the body's net inertia is determined by the maximum determinant of the inertial matrix in Eq:2.30a for some actuator state $\max(\det|J_b(u_\Lambda)|)$, $u_\Lambda \in \mathbb{U}$. A maximum $J_b(u_\Lambda)$, with a determinant $\det|J_b(u_\Lambda)| = 1017.93 \times 10^{-7}$, is:

$$J_b(u_\Lambda) = \begin{bmatrix} 384695.4 & 0.4 & -14.5 \\ 0.4 & 384717.9 & 6.5 \\ -14.5 & 6.5 & 687970.7 \end{bmatrix} \times 10^{-7} \Big|_{u_\Lambda} \quad [\text{kg.m}^2], \quad \in \mathcal{F}^b \quad (2.31a)$$

With an actuator matrix, independent of propeller speeds $\Omega_{1 \rightarrow 4}$, as follows:

$$u_\Lambda = \begin{bmatrix} \Omega_1, \lambda_1 = 178^\circ, \alpha_1 = 260^\circ \dots \\ \Omega_2, \lambda_2 = 178^\circ, \alpha_2 = 260^\circ \dots \\ \Omega_3, \lambda_3 = 178^\circ, \alpha_3 = 0^\circ \dots \\ \Omega_4, \lambda_4 = 0^\circ, \alpha_4 = 0^\circ \end{bmatrix} \quad (2.31b)$$

Conversely, the minimum net inertia for the body is determined from the smallest determinant of Eq:2.30a, for the actuator state $\min(\det|J_b(u_\Upsilon)|)$, $u_\Upsilon \in \mathbb{U}$. A minimum $J_b(u_\Upsilon)$, with a determinant $\det|J_b(u_\Upsilon)| = 633.48 \times 10^{-7}$, is:

$$J_b(u_\Upsilon) = \begin{bmatrix} 317469.0 & 0.4 & -1219.0 \\ 0.4 & 317591.5 & 1195.3 \\ -1219.0 & 1195.3 & 628298.1 \end{bmatrix} \times 10^{-7} \Big|_{u_\Upsilon} \quad [\text{kg.m}^2], \quad \in \mathcal{F}^b \quad (2.32a)$$

When an actuator matrix for that minimum inertia is:

$$u_\Upsilon = \begin{bmatrix} \Omega_1, \lambda_1 = 178^\circ, \alpha_1 = 0^\circ \dots \\ \Omega_2, \lambda_2 = 0^\circ, \alpha_2 = 260^\circ \dots \\ \Omega_3, \lambda_3 = 0^\circ, \alpha_3 = 0^\circ \dots \\ \Omega_4, \lambda_4 = 0^\circ, \alpha_4 = 0^\circ \end{bmatrix} \quad (2.32b)$$

The inclusion of Eq:2.31 and Eq:2.32 is used for maximum and minimum Eigen values of the body's inertial matrix at a later stage in the control derivation, Sec:4.6. It is interesting to note that both extremes of $J_b(u)$ are still symmetrical, and *roughly* diagonal. Actuator positions hardly affect the skew products of inertia in $J_b(u)$ but can vary the diagonal moments of inertia by almost 20% of their principle value.

Unless otherwise specified; any inertia $J_b(u)$ indicates an instantaneous calculated solution to Eq:2.30a given a particular $u(t) \in \mathbb{U}$. The purpose of the derivations for rotated centers of mass in Eq:2.28 and Eq:2.29 is twofold; highlighting both the inertial contributions *and* the variable center of masses for each sub-body. Seeing that the origin of motion $\vec{\mathbf{O}}_b$ in the body frame \mathcal{F}^b and the body's effective center of mass $C.M_b$ are not coincidental, it is important to quantify the net center of mass's variation with actuator positions $u \in \mathbb{U}$.

In the general case for a collection of n bodies, with each body's center of mass at some position \vec{X}_i and each having a mass m_i , resultant center of mass is:

$$C.M = \frac{\sum_{i=1}^n m_i \cdot \vec{X}_i}{\sum_{i=1}^n m_i} \quad (2.33a)$$

Using $C.M_n'''$ and $C.M_m''$ as rotated centers of mass defined in Eq:2.28d and Eq:2.29d respectively and $C.M_y$ for the body structure, the vehicle has a variable center of mass $C.M_b(u)$:

$$C.M_b(u) = \frac{m_y C.M_y + \sum_{i=1}^4 m_n C.M_n'''(u \cdot i) + \sum_{i=1}^4 m_m C.M_m''(u \cdot i)}{m_b} \quad (2.33b)$$

So the net center of gravity when all actuators are at their zero positions is: $C.M_b(\vec{0}) = [0 \ 0 \ -4.94]^T$ [mm]. Using a gravity force vector \vec{G}_b in the body frame as a result of gravitational acceleration $g = -9.81$ [m.s⁻²] acting on the vehicle:

$$\vec{G}_b = R_I(\vec{\eta})^b \vec{G}_I \quad [\text{N}], \in \mathcal{F}^b \quad (2.34a)$$

$$= R_I^b(\vec{\eta}) [0 \ 0 \ -9.81(m_b)]^T \quad (2.34b)$$

The resultant gravitational torque about the origin \vec{O}_b in the body frame \mathcal{F}^b from the varying eccentric center of mass for the vehicle is:

$$\Delta C.G = \vec{O}_b - C.M_b(u) \quad (2.34c)$$

$$\vec{\tau}_g = \Delta C.G \times m_b \vec{G}_b \quad [\text{N.m}], \tau_g \in \mathcal{F}^b \quad (2.34d)$$

Uncertainty with inertial measurements, proven to be destabilizing and detrimental to control efforts in [72, 133], can indeed be incorporated into state dependent plant uncertainty compensation like in [10]. Controllers with strong disturbance and uncertainty rejection, like a well designed H_∞ controller, would be ideally suited to controlling an attitude plant without having to explicitly specify all of the above inertias.

It is, however, worth the mathematical deliberation to detail each inertial equation given that Lagrange dynamics are later applied to determine the servo actuator dynamic responses (Sec:3.3). Such equations of motion will later need explicit terms defined for instantaneous transformed inertias.

2.4 Electronics



Figure 2.18: Hardware schematic diagram

An abstracted hardware diagram for the proposed (electronic) system layout is shown in Fig:2.18. It is an illustration for the connection of different electronic peripherals to aid the on-board control system. The structure of the implemented autopilot system and control loops are addressed later. This section aims to provide a brief overview of the specific modules intended for the flight controller, their purpose and a description of how they are interfaced. No control loops or code structures are discussed yet, those are detailed in Sec:4.1 and Sec:6.8.1 respectively.

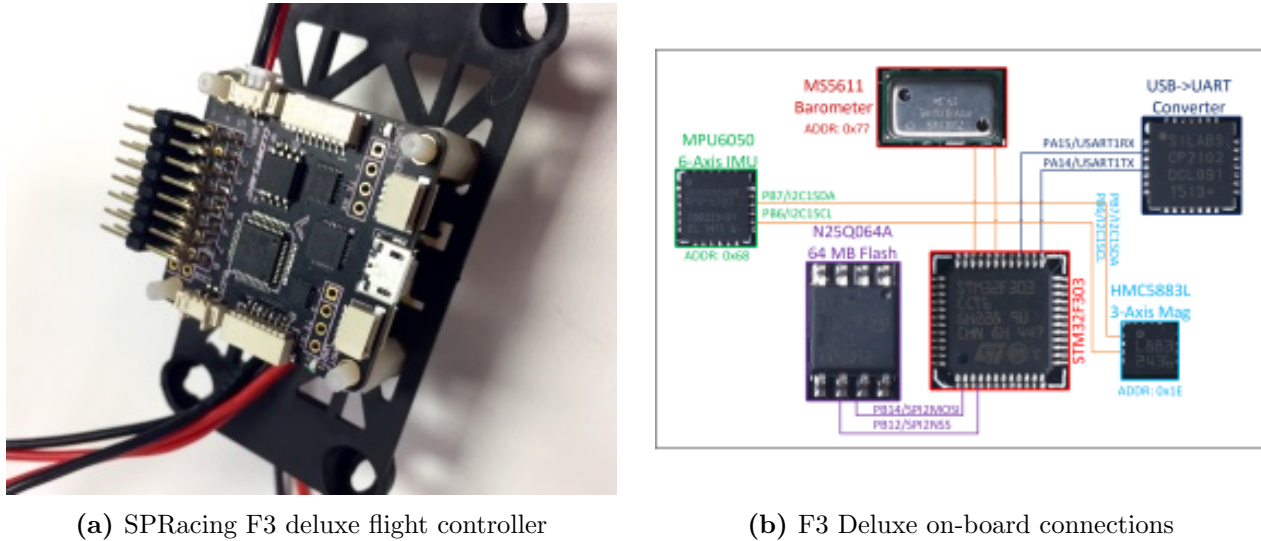


Figure 2.19: SPRacing F3 deluxe layout

The embedded system is constructed around an ARM STM32F303 [121] based microcontroller. The micro-processor board is a commercial flight control board, specifically an SPRacing F3 Deluxe [28]. CleanFlight or BetaFlight opensource software (from [27] and [11] respectively) are typically used for this SPRacing F3 board; but despite open-source software its hardware specifications are however not openly available. The reverse engineered electrical schematic for the board is included in App:B.2 but a simplified overview of its internal connections is shown in Fig:2.19b.

The flight-controller has the following onboard peripherals; an I2C MPU-6050 6-axis gyroscope and accelerometer [58] with an I2C connected HMC5883 magnetometer compass [35]; an I2C MS5611 barometer [119] and finally 64 Mb of SPI flash memory. Sensor fusion for the above state estimators is dealt with subsequently in Sec:6.8. The caveats of Kalman filtering and discretized effects on the simulation loop are similarly discussed in that particular section.

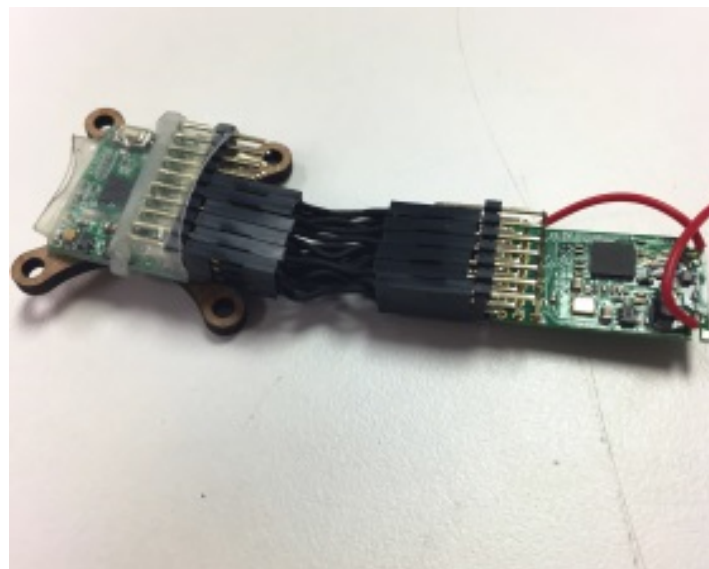


Figure 2.20: SBUS converter & 6CH receiver

Two separate wireless communication loops are to be used. First; the system relays full state information for a complete 6-DOF X-Y-Z position and $\phi - \theta - \psi$ orientation autopilot system. Sent from an independent ground control station (*GCS*) using 2.4 GHz XBEE S1 module(s) [59] which is connected to the flight controller via USART. Full state-estimation, using a multi-camera system (??), and basic trajectory generation is performed on the GCS for the vehicle to track that trajectory.

Secondly; a partial trajectory (basic orientation) augmented pilot control input system, fail safe and secondary to the autopilot loop, is transmitted through a 6 channel 2.4 GHz radio frequency module. The secondary system allows for physical control without the need of a trajectory generation loop. The 6 CH received signals, otherwise permeated as six individual 20 kHz PWM signals via an OrangeRx R615x receiver [93], are encoded into a single proprietary S.BUS data stream (Fig:2.20).

The need for a serial bus (S.BUS) encoder, specifically using [52], comes about as a consequence of the introduction of the 8 additional servos. As a result, there are no longer 6 free additional timer input/output channels which can be dedicated to input capture of those RC channels. Encoding the received data to a serial data line means the 6CH commands can be processed with a single RX channel by the microcontroller. The encoder implements a USART derivative communications standard called S.BUS. Shown in Fig:2.21 the S.BUS data, captured with a logic analyzer [113], was used to ascertain the data stream's following parameters:

- 25 Bytes per packet
- 8-Bit byte length
- 1 Start byte 0x240
- 1 Byte of state flags
- 1 Stop byte 0x0
- Bytes are:
 - MSB First
 - 1 start & 2 stop bits
 - Even parity bit
 - Inverted
 - 100000 baud ($b.s^{-1}$)
- 22 total bytes of CH data
- Each channel's data is 11 bits long
- 16CH encoded
- Channel data is little endian prioritized
- 14 ms idle time between packets
- Packets are arranged:

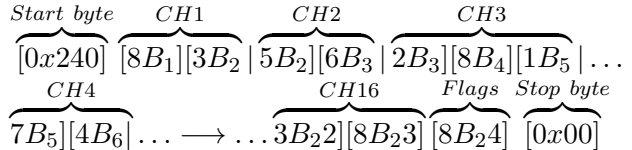


Figure 2.21: S.BUS data stream

The received information from the transmitted 6 channels is smoothed with a digital filter, using an infinite impulse response moving average filter. The filters difference equation can be as follows:

$$y_n = \left(1 - \frac{1}{N}\right)y_{n-1} + \frac{1}{N}x_n \quad (2.35)$$

Moving over an average of $N = 5$ samples which, each with a propagation delay of 14 ms due to S.BUS transmission, the filter has a 70 ms zero order holding time. The signal's sampling delays are sufficiently faster than the transfer times of the signals to not be consequence.

Similarly all the measured RPM signals measured by the OrangeRx RPM speed sensors are filtered over 5 samples as well. Any received signals referred to are all post filtration. Filtering for state estimation made without using the inertial-measurement unit (using the camera system) is to be performed separately on the Ground Control Station computer.

Each of the eight digital servo actuators are controlled individually from 330 [Hz] center aligned PWM timer output compare channels (TIM2:CH1→CH4 and TIM3:CH1→CH4). Output pulses typically range from 1 – 2 [ms] to linearly control the rotational position. The servo's exact range and transfer function(s) is empirically determined next in Sec:2.4.1. The four 20 [A] brushless DC electronic speed controllers (*ESCs*) are each driven from a 20 [Hz] PWM output (TIM4:CH1→CH4), similarly with 1 – 2 [ms] input pulse widths.

There is a total of 12 PWM output compare signals drawn from the flight controller, 8 for the servos and 4 for the *ESCs*. The servos are powered by a regulated 6 [V] DC 10 [A] power supply [51] whilst the *ESCs* switch unregulated 14.1 [V] DC supplied from an external power tether. The DC supply could be drawn from a battery bank but that would adversely affect the weight of an already heavy platform.

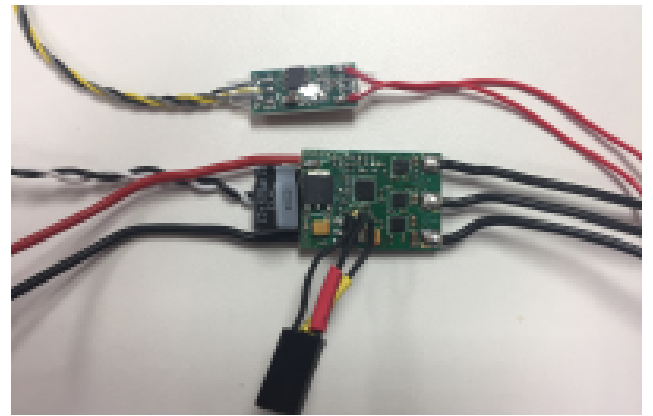
There is no integrated feedback for instantaneous RPM values available from the *ESCs*. Dedicated OrangeRX BLDC RPM sensors, [50], are used to measure each of the four motor's rotational speeds. Despite being termed *brushless DC motors*, the motors are actually 3-phase motors which, when used with an *ESC*, behave like closed loop DC motors. The RPM sensors physically measure switching phases across two of the three motor phases, following that exact RPM can be ascertained. In general, the switching signal of a 3-Phase induction motor is shown by [78] to be proportional to the rotational velocity:

$$F_{rps} = \frac{2 \times F_{poles}}{\text{No. of rotor poles}} \quad [\text{Hz}] \quad (2.36)$$

The output signal generated by the OrangeRx RPM sensors varies the period of a 50% duty cycle square wave, that wave frequency is directly proportional to the motor's pole switching frequency. The sensor output signal has a gain of 7 for the 14 pole BLDC Cobra motors. That gain is verified with the linear relationship(s) physically measured using an optical rotation sensor, plotted in Fig:2.23. Knowing exact RPM rates means the subsequent thrust and aerodynamic torques for the control plant inputs can be calculated with greater certainty.



(a) XRotor 20A ESC connection guide [49]



(b) LDPower 20A ESC with RPM sensor

Figure 2.22: BLDC electronic speed controllers

The *ESCs*, although LDPower 20A devices, are re-flashed with BLHeli firmware [12]. The LDPower *ESCs* (Fig:2.22b) match Hobbywing Xrotor 20A ones (Fig:2.22a) which both use SiLabs F396 microcontrollers; the same firmware can be flashed onto both MCUs. Custom BLHeli software provides greater refinement over configurations like the deflection range of inputs, but default values were used. The plot in Fig:2.23a shows the rotation per second, or otherwise frequency in Hz, speed curve for an unloaded motor; similarly in Fig:2.23b shows the speed curve when loaded for a 6×4.5 prop.

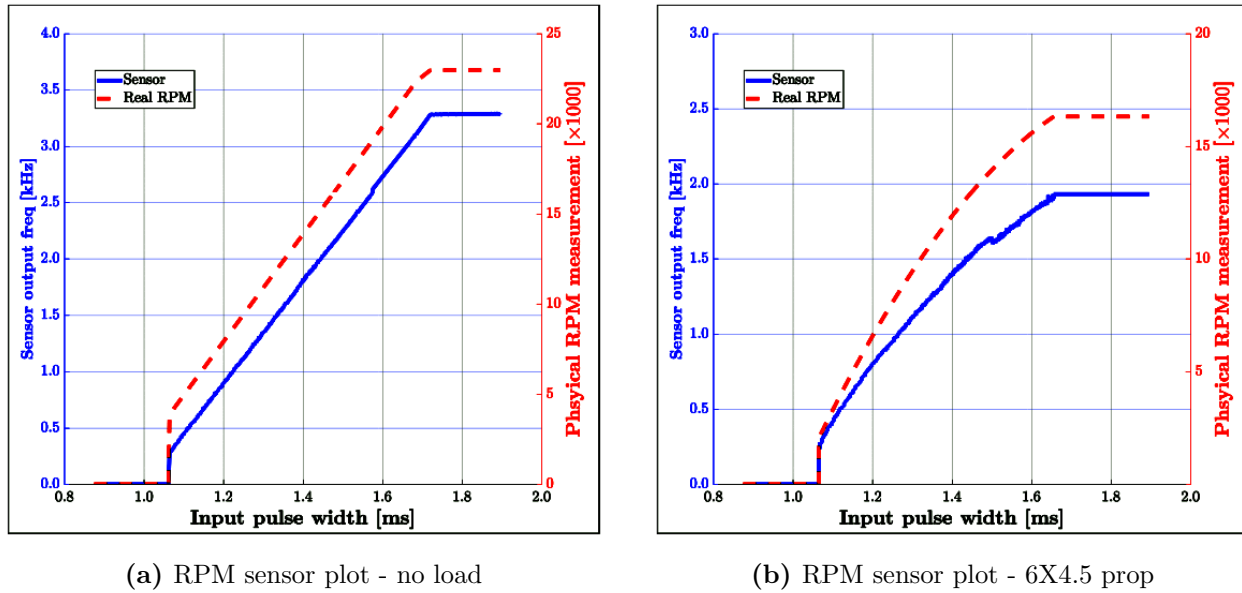


Figure 2.23: RPM sensor calibration plots

The loaded speed plot for a BLDC motor with an attached prop in Fig:2.23b is slightly quadratic; the loaded response is due to second order aerodynamic; quadratic with respect to the propeller's revolutions per second (expanded on in Sec:3.2.1). Moreover, when the motor is torque loaded by the propeller, the ESC current limits rotational speeds at just over 16×10^3 [RPM].

Timer channels are used to measure the varying frequency output from the RPM sensors. General purpose Timers 15 (TIM15:CH1→CH2), 16 (TIM16:CH1) and 17 (TIM17:CH1) are configured to capture the input PWM signal generated by the speed sensors. Included on the I2C communication line is an I2C O-LCD display for debugging and status update purposes.

Any STM32 μ controller is programmed through a dedicated debugging device. The ST-Link V2 [120] is the current proprietary device which, itself, is a specially programmed STM32F10 chip. The chip connects to the dedicated **Serial Wire Debugging** ports of the target STM (*SWD-CLK*, *SWD-IO* & *SWD-NRST*) and is interfaced via regular USB-D+ and USB-D- data lines.

2.4.1 Actuator Transfer Functions

Servo Transfer Functions

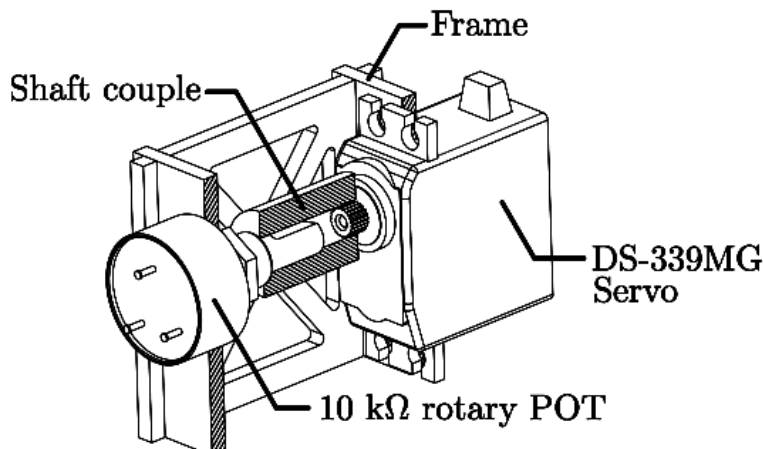


Figure 2.24: Servo transfer function test rig

The full scale deflection for digital servos are in fact greater than their quoted 180° range. Each servo has a rotational input range of around 230° (Fig:2.25a). In the prototype control loop the servos are left in open loop; the major loop controller coefficients are expected to account for minor loop actuator dynamics. With that being said, for such an expectation to be validated the simulation would need to represent the servo's response accurately.

Seeing that the 180° limitation was imposed as a design decision, one of the first points of contention is the effect such a constraint would have on the feasible operating trajectories. The control algorithms derived in Ch:4 are first tested with an ideal, continuous rotation servo actuator with similar rate limits and transfer characteristics. Following that servo saturation limitations are introduced and the constraints to feasibly achievable trajectories are investigated in Sec:6.8.1.

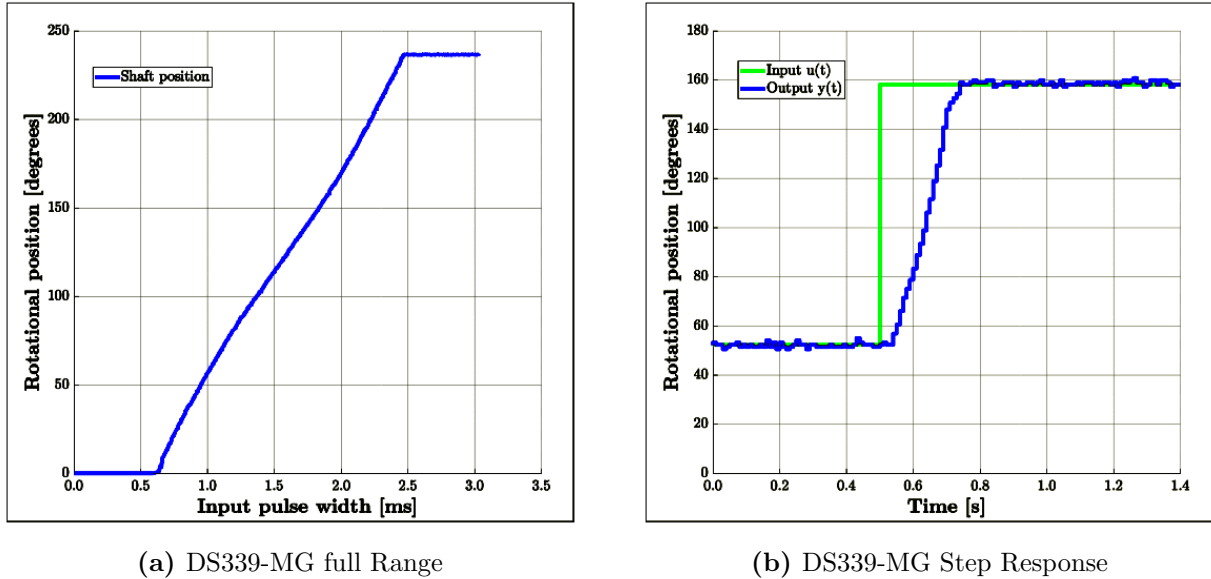


Figure 2.25: Unloaded servo transfer characteristics

For the servos whose rotational range and step response are shown in Fig:2.25, the relationship between the input pulse-width x [m.s] and the rotational output position y [°] is given by:

$$y(x) = \begin{cases} 0^\circ & x < 0.65 \text{ ms} \\ 129.12x - 82.64 & 0.64 \text{ ms} \leq x \leq 2.46 \text{ ms} \\ 230^\circ & x > 2.46 \text{ ms} \end{cases} \quad (2.37)$$

In practice the equation Eq:2.37 is changed such that 0° offset is taken at around a 50% input, making its operational range $\pm 90^\circ$. Each servo is mechanically rate limited to 60°/0.15s or 400 degrees per second with a dead time of $t_d \approx 1.2$ [ms] and a (*negligible*) mechanical deadband of 4 [μs]. Each servo has an approximate (*critically damped*) second order transfer function

$$G_{servo}(s) = e^{-t_{ds}} \frac{w_n^2}{s^2 + 2\zeta w_n s + w_n^2} \quad (2.38a)$$

$$= \frac{e^{-0.012s}(14.869)^2}{s^2 + 2(1)(14.869)s + (14.869)^2} \quad (2.38b)$$

With saturation limits from $|U(s)|$ for the PWM magnitude:

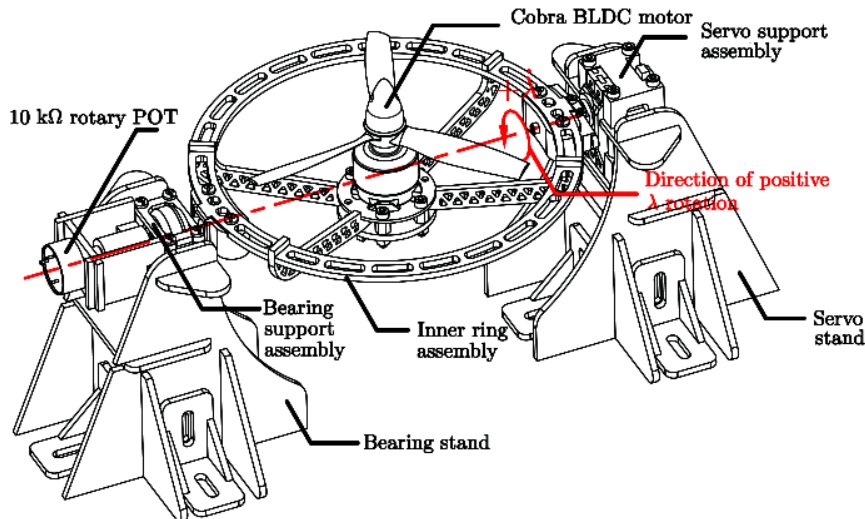
$$Y_{servo}(s) = \begin{cases} 0^\circ & |U(s)| < 0.65 \\ G(s) & 0.65 \leq |U(s)| \leq 2.46 \\ 230^\circ & |U(s)| > 2.46 \end{cases} \quad (2.38c)$$

The net transfer block for the servo is shown in Fig:2.26, including saturating non-linearities but neglecting the afore mentioned mechanical deadband...

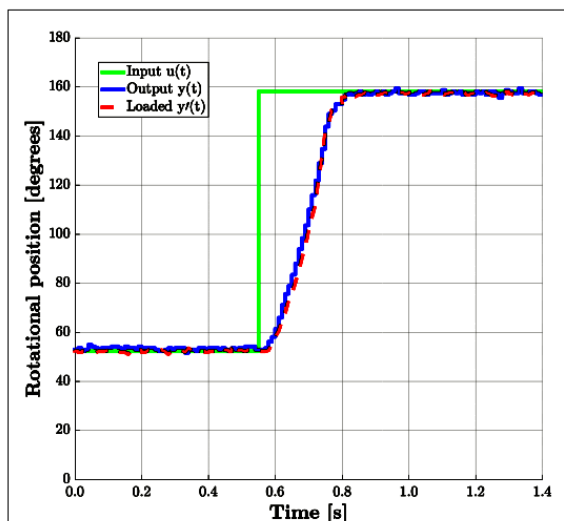


Figure 2.26: Servo block diagram

The plot in Fig:2.25b shows the transfer characteristics, at the *shaft output*, of an unloaded servo. When rotating the inertial body of the inner ring assembly, arranged as in Fig:2.27a. Plotted in Fig:2.27b is the plant response of $y(t)$ which is consistent with the transfer function in Eq:2.38, $\therefore G(s)_{inner} = G(s)_{servo}$. Despite rotating a load and hence requiring a greater torque. The servo's characteristics remains unchanged, even when the BLDC motor (with a 6×4.5 prop) with a rotational velocity of 6500 RPM is introduced, plotted $y'(t)$, further increasing the torque load of the assembly as a result of the gyroscopic response, Eq:2.18.



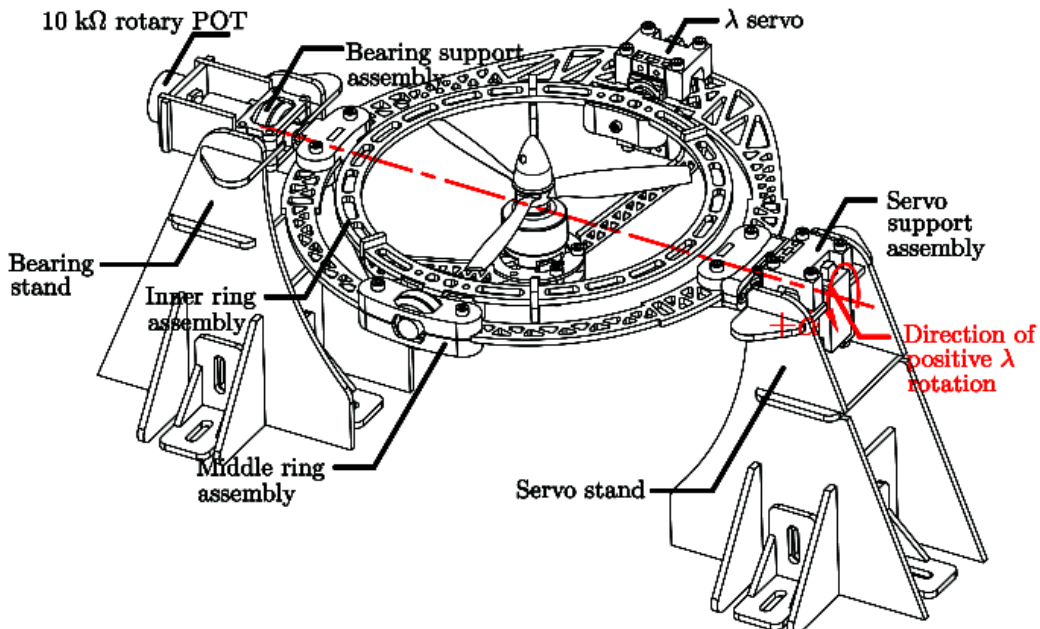
(a) Inner ring servo rig



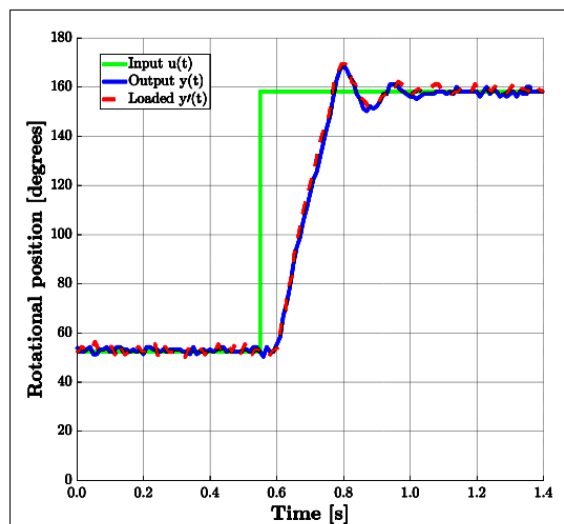
(b) Servo response plot

Figure 2.27: Inner ring servo characteristics

Fig:2.28b plots the step response for the servo driving the middle ring assembly. Whilst its transients remain the same oscillations are introduced at the settling point; demonstrating a second order under-damped plant. Those oscillations are as a result of the larger rotational inertia (Eq:2.23), introducing flexure within the frame structure. It is important to specify that the oscillations are not at the servo's output shaft; the rotational position was measured with respect to the bearing supported shaft, coaxial to the servos (Fig:2.28a). An under-damped transfer function needs to be used because the rotation position of the frame is to be used for force calculations in Eq:2.16b. Those harmonics are still present under load, plotted in $y'(t)$, despite the frame being tensioned by a thrust.



(a) Middle ring servo test rig



(b) Servo response plot

Figure 2.28: Middle ring servo characteristics

The mechanical structure could indeed be strengthened to reduce the oscillations present in Fig:2.28a. Strengthening the frame would introduce greater mass to an already constrained system. Instead the under-damped transfer function is included into the plant, that transfer function is:

$$G(s)_{middle} = \frac{e^{-0.012s}(12.591)^2}{s^2 + 2(0.454)(12.591)s + (12.591)^2} \quad (2.39)$$

BLDC Transfer Functions

Each Cobra 2208 BLDC motor, when loaded with a 6×4.5 propeller has a quadratic speed curve (plotted in Fig:2.30a). This is as a result of the propeller's opposing aerodynamic drag, *approximately* proportional to the square of the propellers angular velocity (more on propeller aerodynamics in Sec:3.2.1).

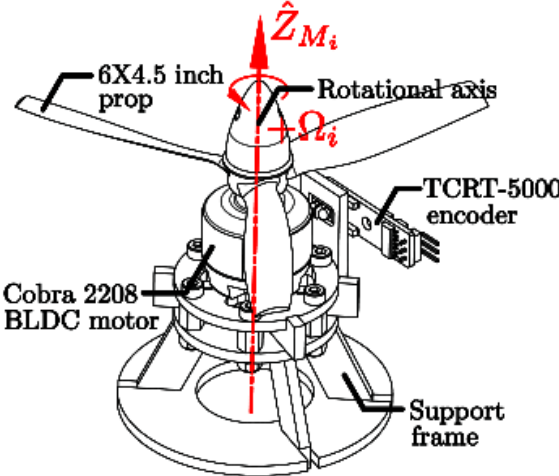
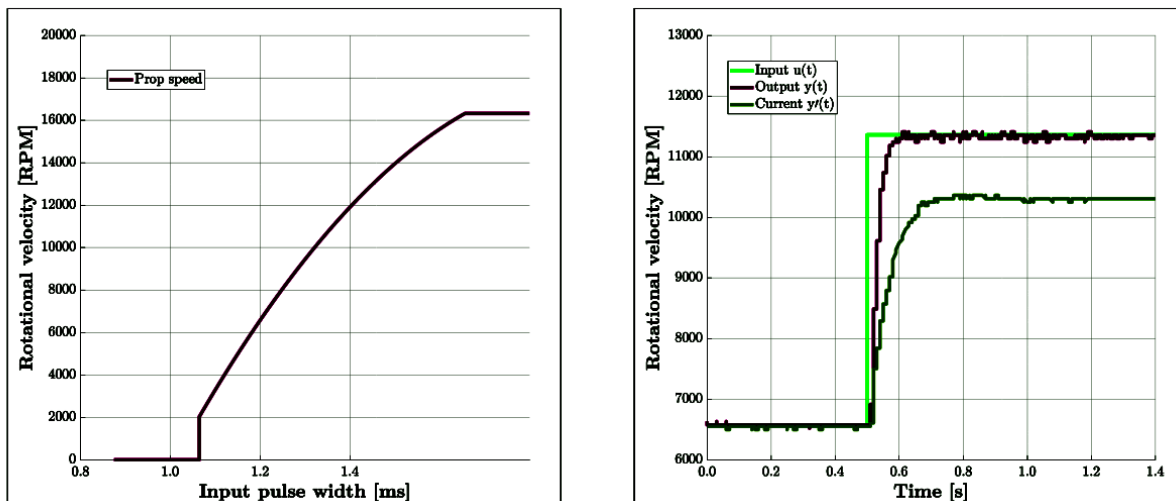


Figure 2.29: BLDC rpm speed calibration and transfer function rig

Using the BLHeli interface, the input range for the motor's speed controllers can be adjusted, but for the purposes of this project were left unchanged. That relationship between input pulse-widths to the ESC and output RPM sensor signal is given by the hybrid state equations for input range limits:

$$y(x) = \begin{cases} 0 & x < 1.065 \text{ ms} \\ -20593x^2 + 80187x - 60004 & 1.065 \text{ ms} \leq x \leq 1.655 \text{ ms} \\ 16300 & x > 1.655 \text{ ms} \end{cases} \quad [\text{RPM}] \quad (2.40)$$

The upper limit in Eq:2.40 and the motor's step response are both governed by the ESC's maximum current limit; in this case 20 [A]. Imposing 10 [A] current limiting, a consequence of using lower power ESCs is plotted $c(t)$ in Fig:2.30b, significantly restricts the motor's transient and steady-state performance.



(a) BLDC RPM range

(b) Cobra BLDC step response

Figure 2.30: BLDC motor characteristics

The motor's step response, $\mathbf{y}(\mathbf{t})$, has a negligible dead time and 2nd order dynamics, with a transient time constant far faster than the servo's plant. The motor's transfer function for speed in RPM is:

$$G_{BLDC}(s) = \frac{1}{(1 + 1.7583s \times 10^{-3})(1 + 1.7494s \times 10^{-3})} \quad [\text{RPM}] \quad (2.41\text{a})$$

And saturation limits with input $|U(s)|$ for the PWM magnitude:

$$Y_{BLDC}(s) = \begin{cases} 0 & |U(s)| < 1.065 \\ G(s) & 1.065 \leq |U(s)| \leq 1.655 \\ 16300 & |U(s)| > 1.655 \end{cases} \quad (2.41\text{b})$$

Chapter 3

Kinematics & Dynamics

The following generally applicable, rigid body dynamics are first derived with respect to net forces and torques acting on the vehicle. Following that, the dynamics are adapted to the non-linear, multibody case which incorporates constrained relative rotational motion between bodies is permitted; the same motion which the prototype can undergo. Aerodynamic effects are subsequently included in the plant's model. Finally a consolidated, quaternion based plant model is presented which is used for the later control plant development in Ch:4.

3.1 Rigid Body Dynamics

3.1.1 Lagrange Derivation

Fundamentally any body, rigid or otherwise, can undergo two kinds of motion; namely rotational and translational. Often a Lagrangian approach for combined angular and translational movements is used to derive the differential equations of motion for each degree of freedom [103, 125]. The Lagrangian principle ensures that (translational and rotational) energies are conserved throughout the system's state progression. When combined with Euler-Rotation equations, the Euler-Lagrangian formulation from [127] fully defines the aerospace 6-DOF equations.

Lagrangian formulation is regarded as especially useful in non-Cartesian (*spherical etc...*) co-ordinate frames and with multi-body systems. With that being said, Cartesian co-ordinates were already defined (in Sec:2.2.2) for the plant. Alternatively; relative co-ordinates could be used for implicit-Euler based dynamics as in [90]. Rigid body dynamics in Cartesian co-ordinates do lend themselves to Newtonian mechanics. Both Newton-Euler and Euler-Lagrange formulations result in the same differential equations of motion, but follow different derivations. The Lagrangian operator, \mathcal{L} , is a scalar term defined as the difference between kinetic and potential energies, T and U respectively. Considering some generalized path co-ordinates $\vec{r}(t)$ for a body, with both position $\vec{\xi}$ and attitude \vec{H} terms included:

$$\vec{r}(t) = \begin{bmatrix} \vec{\xi} & \vec{H} \end{bmatrix}^T \in \mathcal{F}^\Lambda \quad (3.1)$$

Note that co-ordinates in Eq:3.1 are generalized and taken with respect to some hypothetical shared frame \mathcal{F}^Λ . Those generalized co-ordinates are later refined to Cartesian body co-ordinates with respect to the inertial frame. The Lagrangian is the difference of the trajectory's kinetic and potential energies, by definition:

$$\mathcal{L}(\vec{r}, \dot{\vec{r}}, t) = T(\vec{r}, \dot{\vec{r}}) - U(\vec{r}, \dot{\vec{r}}) \quad (3.2a)$$

Where the trajectory's kinetic and potential energy function(s) are T and U respectively. Introducing a rigid body's general (translational and rotational) kinetic and potential energies, both defined with respect to that shared reference frame \mathcal{F}^Λ ...

Noting first that there is no attitude contribution for stored potential energy, so $U(\vec{r}, \dot{\vec{r}})$ consists entirely of gravitational potential energy. A gravitational acceleration vector in the inertial frame $\in \mathcal{F}^I$ is:

$$\vec{G}_I = [0 \ 0 \ -9.81]^T \quad [\text{m.s}^{-2}], \in \mathcal{F}^I \quad (3.2b)$$

Where \vec{G}_I acts in the negative \hat{Z}_I , downward, direction. Substituting translational kinetic and potential energies into the Lagrangian yields the following scalar term:

$$\mathcal{L}(\vec{r}, \dot{\vec{r}}, t) = \frac{1}{2} \dot{\xi}^T (m_b) \dot{\xi} + \frac{1}{2} \dot{H}^T (J_b) \dot{H} - m_b \vec{G}_\Lambda (h \cdot \vec{Z}_I) \quad (3.2c)$$

The body's mass is m_b and its generalized inertia matrix is similarly J_b , aligned and translated with respect to the common frame \mathcal{F}^Λ . The Euler-Lagrange formulation equates partial derivatives of the Lagrangian to any generalized forces, \vec{V} , acting on the system in frame Λ . In the rigid body motion case those *generalized* forces are net forces \vec{F}_{net} and net torques $\vec{\tau}_{net}$ in the shared frame $\in \mathcal{F}^\Lambda$.

$$\frac{d}{dt} \left(\frac{\partial \mathcal{L}}{\partial \dot{\vec{r}}} \right) - \frac{\partial \mathcal{L}}{\partial \vec{r}} = \vec{V} = \begin{bmatrix} \vec{F}_{net} \\ \vec{\tau}_{net} \end{bmatrix} \quad \in \mathcal{F}^\Lambda \quad (3.3)$$

Evaluating symbolic partial derivatives of Eq:3.2c with respect to the path co-ordinates $\vec{r}(t)$ and path rates $\dot{\vec{r}}(t)$ respectively produces the two following equations:

$$\frac{\partial \mathcal{L}}{\partial \vec{r}} = \begin{bmatrix} m_b \vec{G}_\Lambda \\ 0 \end{bmatrix} \quad \in \mathcal{F}^\Lambda \quad (3.4a)$$

$$\frac{d}{dt} \left(\frac{\partial \mathcal{L}}{\partial \dot{\vec{r}}} \right) = \left[\frac{d}{dt} m_b \dot{\xi} \quad \frac{d}{dt} J_b \dot{H} \right]^T \quad \in \mathcal{F}^\Lambda \quad (3.4b)$$

Where \vec{G}_Λ is the gravitation force transformed to the common frame \mathcal{F}^Λ which $\mathcal{L}(\vec{r}, \dot{\vec{r}})$ is defined with respect to. The body mass m_b and inertia J_b could potentially have some non-zero time derivative, but for now are treated as constant. Time varying inertias are later defined in Sec:2.3 and incorporated into the dynamics subsequently in Sec:3.3.1. Here only the general rigid body case is considered...

Any vector in some non-Newtonian rotating reference frame \mathcal{F}^a has a time derivative, relative to another frame \mathcal{F}^b with an angular velocity $\vec{\omega}_{a/b}$, as per the Reynolds Transportation Theorem [122]:

$$\frac{d \vec{f}_b}{dt_a} = \frac{d \vec{f}_b}{dt_b} + \vec{\omega}_{a/b} \times \vec{f}_b \quad (3.5)$$

Applying Eq:3.5 to those partial derivatives in Eq:3.4b and further defining the generalized co-ordinates $[\dot{\xi}, \dot{H}]^T$ as 6-DOF Cartesian body co-ordinates with respect to the inertial frame \mathcal{F}^I or the body frame \mathcal{F}^b .

Reiterating that the angular orientations $\vec{\xi}$ are with respect to a common frame \mathcal{F}^Λ , unlike Euler angles $\vec{\eta} \in \mathcal{F}^{v2,v1,I}$. Recalling the definition of attitude in a common frame $\vec{\eta}_b$ from Eq:2.12d, where $\vec{\omega}_b = \dot{\vec{\eta}}_b$ and $\vec{\eta}_b \in \mathcal{F}^b$, the trajectory's definition is refined:

$$\vec{r} = [\dot{\xi} \ \dot{H}]^T \triangleq \begin{bmatrix} \vec{\mathcal{E}} \\ \vec{\eta}_b \end{bmatrix} \quad (3.6a)$$

Which leads to the path rate definition $\dot{\vec{r}}(t)$:

$$\rightarrow \dot{\vec{r}} = [\dot{\xi} \ \dot{H}]^T \triangleq \frac{d}{dt} \begin{bmatrix} \vec{\mathcal{E}} \\ \vec{\eta}_b \end{bmatrix} = \begin{bmatrix} \vec{v} \\ \vec{\omega} \end{bmatrix} \quad \in \mathcal{F}^b \quad (3.6b)$$

Substituting the changed path co-ordinates from Eq:3.6 into the Lagrangian Eq:3.2c yields a familiar Lagrangian scalar in the body frame \mathcal{F}^b :

$$\mathcal{L} = \frac{1}{2} \vec{v}_b^T (m_b) \vec{v}_b + \frac{1}{2} \vec{\omega}_b^T (J_b) \vec{\omega}_b - m_b \vec{G}_b z_I \quad \in \mathcal{F}^b \quad (3.7)$$

With \vec{G}_b being the gravitational force vector from Eq:3.2b transformed to the body frame \mathcal{F}^b and z_I as the vertical height of the vehicle (in the inertial frame). The time derivative of the substituted path co-ordinates in the partial derivative Eq:3.4b is then:

$$\frac{d}{dt} \left(\frac{\partial \mathcal{L}}{\partial \dot{\vec{r}}} \right) = \begin{bmatrix} m_b \frac{d}{dt} \vec{v}_b & J_b \frac{d}{dt} \vec{\omega}_b \end{bmatrix}^T \quad (3.8a)$$

With respective time derivatives using the Reynolds transportation theorem:

$$\rightarrow m_b \frac{d}{dt} \vec{v}_b = m_b \dot{\vec{v}}_b + \vec{\omega}_{b/I} \times m_b \vec{v}_b \quad (3.8b)$$

$$\rightarrow J_b \frac{d}{dt} \vec{\omega}_b = J_b \dot{\vec{\omega}}_b + \vec{\omega}_{b/I} \times J_b \vec{\omega}_b \quad (3.8c)$$

Which, when substituted back into the Euler-Lagrange formulation Eq:3.3, produces the familiar Newton-Euler rigid body equations for translational and rotational motion:

$$\begin{bmatrix} m_b \dot{\vec{v}}_b + \vec{\omega}_{b/I} \times m_b \vec{v}_b \\ J_b \dot{\vec{\omega}}_b + \vec{\omega}_{b/I} \times J_b \vec{\omega}_b \end{bmatrix} - \begin{bmatrix} m_b \vec{G}_b \\ 0 \end{bmatrix} = \vec{\mathbf{V}} = \begin{bmatrix} \vec{F}_{net} \\ \vec{\tau}_{net} \end{bmatrix} \quad (3.9a)$$

$$\rightarrow \vec{F}_{net} = m_b \dot{\vec{v}}_b + \vec{\omega}_b \times m_b \vec{v}_b - m_b R_I^b(-\eta) \vec{G}_I \quad [\text{N}], \in \mathcal{F}^b \quad (3.9b)$$

$$\rightarrow \vec{\tau}_{net} = J_b \dot{\vec{\omega}}_b + \vec{\omega}_b \times J_b \vec{\omega}_b \quad [\text{N.m}], \in \mathcal{F}^b \quad (3.9c)$$

Reiterating that $\vec{\eta}_b \neq \vec{\eta}$ because each Euler Angle is defined in a sequentially rotated reference frame. Four equations are then needed to completely describe a body's position and attitude state dynamics:

$$\dot{\vec{\mathcal{E}}} = R_b^I(-\eta) \vec{v}_b \quad [\text{m.s}^{-1}], \in \mathcal{F}^I \quad (3.10a)$$

$$\vec{F}_{net} = m_b \dot{\vec{v}}_b + \vec{\omega}_b \times m_b \vec{v}_b - m_b \vec{G}_b \quad [\text{N}], \in \mathcal{F}^b \quad (3.10b)$$

$$\dot{\vec{\eta}} = \Phi(\eta) \vec{\omega}_b \quad [\text{rad.s}^{-1}], \in \mathcal{F}^{v2,v1,I} \quad (3.10c)$$

$$\vec{\tau}_{net} = J_b \dot{\vec{\omega}}_b + \vec{\omega}_b \times J_b \vec{\omega}_b \quad [\text{N.m}], \in \mathcal{F}^b \quad (3.10d)$$

Where $\Phi(\eta)$ is the Euler matrix defined previously in Eq:2.12e. State differentials from Eq:3.10 can be simplified to a set of two equations defined entirely in the reference frames of the state variables which they represent. The non-linear form of those equations substitutes $d\vec{\eta}/dt = \Phi(\eta)\vec{\omega}_b$ into the Lagrangian derivative, Eq:3.4b.

$$\frac{d}{dt} \left(\frac{\delta \mathcal{L}}{\delta \dot{\vec{r}}} \right) = \begin{bmatrix} m_b \frac{d}{dt} \vec{v}_b & J_b \frac{d}{dt} \dot{\vec{\eta}}_b \end{bmatrix}^T \Rightarrow \begin{bmatrix} m_b \frac{d}{dt} \vec{v}_b & J_b \frac{d}{dt} \Phi(\eta) \vec{\omega}_b \end{bmatrix}^T \quad (3.11)$$

Which affects only the angular component because the two kinetic energies are independent of one another. Applying the differential chain rule yields:

$$J_b \frac{d}{dt} \Phi(\eta) \vec{\omega}_b = J_b (\dot{\Phi}(\eta) \vec{\omega}_b + \Phi(\eta) \dot{\vec{\omega}}_b) \quad (3.12)$$

Drawing from [90] and recognizing that J_b must be transformed to the common intermediate Euler axes, $J \triangleq \Psi(\eta)^T J_b \Psi(\eta)$. The state differential equation for angular acceleration in Eq:3.9c, then defined in intermediate (non-inertial) Euler frames for each angle, becomes:

$$M(\eta) \ddot{\vec{\eta}} + C(\eta, \dot{\eta}) \dot{\vec{\eta}} = \Psi(\eta) \vec{\tau}_\mu \quad \in \mathcal{F}^{v2,v1,I} \quad (3.13a)$$

$$M(\eta) = \Psi(\eta)^T J_b \Psi(\eta) \quad (3.13b)$$

$$C(\eta, \dot{\eta}) = -\Psi(\eta) J_b \Psi(\dot{\eta}) + \Psi(\eta)^T [\Psi(\eta) \dot{\vec{\eta}}]_\times J_b \Psi(\eta) \quad (3.13c)$$

The relationship $\dot{\Phi} \equiv \Phi\dot{\Psi}\Phi$ was used to simplify Eq:3.13, the singularity present in Φ remains. The equation in Eq:3.13a completely describes the state derivative $\ddot{\eta}$ in its own reference frame(s), $\mathcal{F}^{v2,v1,I}$. The two differential equations which fully describe the entire body's 6-DOF motion are:

$$\vec{F}_{net} = m_b \dot{\vec{\mathcal{E}}} + R_b^I(-\eta) \vec{\omega}_b \times m_b \dot{\vec{\mathcal{E}}} - m_b \vec{G}_I \quad \in \mathcal{F}^I \quad (3.14a)$$

$$\vec{\tau}_{net} = \Psi(\eta)^{-1} M(\eta) \ddot{\vec{\eta}} + \Psi(\eta)^{-1} C(\eta, \dot{\eta}) \quad \in \mathcal{F}^{v2,v1,I} \quad (3.14b)$$

The generalized net forces and torques, \vec{F}_{net} and $\vec{\tau}_{net}$ respectively, are due to the system's controllable inputs as well as any disturbances acting on the body. The control inputs are directly affected by the vehicle's actuators. How actuator positions produce the control forces and torques depends on the actuator's associated *effectiveness* function. In the general case, which is expanded in Sec:3.2, the control inputs for a quadrotor (Fig:3.1) are as follows.

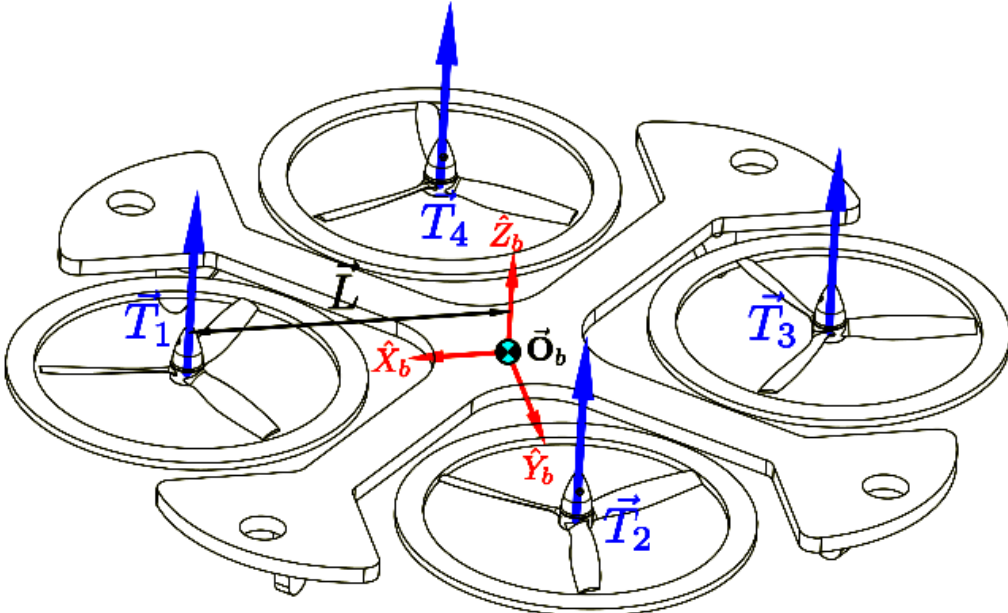


Figure 3.1: Generalized quadrotor net forces and torques

Typically \vec{F}_{net} is the net heave or sum of all thrust forces produced by rotating propellers, as some function of those rotational speeds; $\vec{T}(\Omega_i)$.

$$\vec{F}_{net} = \sum_{i=1}^4 \vec{T}(\Omega_i) \quad [\text{N}], \quad \in \mathcal{F}^b \quad (3.15a)$$

Similarly net torque $\vec{\tau}_{net}$ is the sum of all *differential* torque arms produced from opposing propeller thrust vectors. Each torque arm $\vec{l}_{1 \rightarrow 4}$ is relative to the origin of motion \vec{O}_b .

$$\vec{\tau}_{net} = \sum_{i=1}^4 \vec{l}_i \times \vec{T}(\Omega_i) \quad [\text{N.m}], \quad \in \mathcal{F}^b \quad (3.15b)$$

In Eq:3.15, the thrust vector $\vec{T}(\Omega_i)$ is a function of the i^{th} motor's rotational velocity Ω_i , fixed in the \hat{z}_b direction. Each thrust vector could potentially be $\in \mathbb{R}^3$ such as the redirected vector from Eq:2.16b. The displacement \vec{l}_i is that thrust vector's perpendicular distance from the origin \vec{O}_b . All of the above equations are still applicable to any 6 DOF body; common simplifications applied to the system(s) for quadrotor control are explored in App:A.1. Aerodynamic components pertinent for thrust and torque generation relative to Eq:3.15 are now introduced; obviously the contextual focus is on quadrotor and tilting quadrotor platforms...

3.2 Aerodynamics

Aerodynamic effects described here and subsequent non-linear responses in Sec:3.3 affect the net forces and torques acting on the body. The relationship between a propeller's rotational speed, Ω_i in [RPS], and its perpendicular thrust vector, $\vec{T}(\Omega_i)$, is more complicated than the quadratic simplification taken at static conditions which most papers assume (e.g [80, 102] etc...). Produced thrust is mostly dependent on the incident air stream flowing through the propeller's rotational plane; typically being the component of the body velocity normal to that propeller. Fluid flowing *tangentially* across the propeller's plane contributes toward in-plane aerodynamic drag (and hence torque).

The combination of aerodynamic blade-element [94, 109] and fluid-dynamics momentum (*disc actuator*) theories equate an integral term generated across the propeller's length with the produced thrust or torque. A schedule of all aerodynamic effects encountered by a quadrotor's propellers is thoroughly detailed in both [8] and [7]. The following is a review of pertinent aerodynamic theories; vortex ring state and parasitic drag effects are not included as they will be approximately negligible given the aircraft's proposed flight envelope with low translational velocities.

3.2.1 Propeller Torque and Thrust

A possible situation which the prototype could encounter is where an upstream propeller provides the incident fluid flow to another downstream propeller. Such a situation presents a complicated fluid dynamics and vortex wake effect problem. Propeller overlapping effects are discussed in [124] but remain open to further research in the context of the aircraft considered here.

To expedite the system identification process some simplifications are made on the aerodynamics to construct an approximate model; specifically using coefficients in place of complete local chord and pitch based integrals. Such an assumption holds true given that twisted, fixed pitch propellers are used (Fig:3.2a) and not variable pitch swash-plate actuated propellers (Fig:3.2b).



(a) Twisted, fixed pitch



(b) Swash-plate variable pitch; [53]

Figure 3.2: Propeller types

A propeller's profile applies a perpendicular thrust force, T , onto the fluid in which it rotates. To build the following theoretical explanation propellers are first considered in terms of momentum theory; only perpendicular fluid flow through the propeller's plane is regarded. That fluid stream (Fig:3.3) has an incident upstream velocity, v_∞ , and a resultant slip velocity, v_s , downstream relative to the rotational plane. The change of fluid flow as a result of the propeller's rotation can be given as:

$$v_s = \Delta v + v_\infty \quad (3.16)$$

Where Δv is the net change in fluid velocity caused by the propeller blade's rotating aerofoil profile. The propeller induces a velocity directly in front of its rotational plane, v_i , such that the net fluid flow into the plane is $v_b = v_i + v_\infty$. That induced inflowing fluid velocity is different to the net velocity contribution of the propeller; $v_i \neq \Delta v$.



Figure 3.3: Disc Actuator Propeller Planar Flow

It is shown in [8] that, using Bernoulli's pressure theorem, the net fluid flow through the propeller's plane is:

$$v_b = \frac{1}{2}(v_s - v_\infty) = \frac{1}{2}\Delta v = \frac{1}{2}v_s|_{v_\infty=0} \quad (3.17)$$

Stemming from classical disc actuator (fluid *momentum*) theory [104], the scalar force $T(\Omega)$ acting on the fluid is calculated as a function of mass flow rate with respect to the change in fluid velocity (or *pressure differential*):

$$T = (A_b v_b)\Delta v = \rho\pi R_b^2 v_b \Delta v = \rho\pi R_b^2 (v_i + v_\infty) \Delta v = \frac{1}{2} \rho\pi R_b^2 \Delta v^2 \quad (3.18)$$

Where R_b is the disc (propeller) radius in [m] for the fluid stream under consideration, A_b is the area of that propeller disc. The fluid density of that stream, ρ , is typically 1.225 [kg.m^{-3}] at standard temperature and pressure (*stp*). However, the desired form of thrust generated is as a function of propeller rotational velocity $T(\Omega_i)$ in [RPS] or [rad.s^{-1}], so Eq:3.18 is not satisfactory.

Eq:3.18 can be solved as a function of the aerodynamic propulsive power expended, $\Delta P = T\Delta v$. Rotational kinetic energy of a propeller and its transferred propulsive power is difficult to quantify, with compound parasitic losses deteriorating the efficiency of the propeller. Furthermore, the local fluid velocity through the propeller is not purely normal to the propeller plane but is in fact a vector.

In reality fluid flow induced by the propeller's rotation, v_i , directly in front of its plane of rotation is not purely perpendicular but has axial and tangential induced components, termed a and a' respectively. Those induced components for the fluid velocity can be abstracted to induction factors dependent on the incident fluid velocity to the propeller's plane of rotation:

$$v_i = av_\infty \text{ in the axial direction} \quad (3.19a)$$

$$v_\theta = a'\Omega_i R_b \text{ in the tangential direction} \quad (3.19b)$$

From induction factors defined Eq:3.19, the velocity components can be written as factors of upstream velocity v_∞ .

$$v_b = (1 + a)v_\infty \quad (3.20a)$$

$$v_s = (1 + 2a)v_\infty \quad (3.20b)$$

A consequence of the tangential fluid flow is that an angular momentum flow rate exists across the propeller plane. This produces a fluid-momentum torque opposing the rotational motion about the propeller's axis, analogous but perpendicular to Eq:3.18:

$$\vec{Q} = \rho\pi R_b^3(v_\theta - v_\infty)v_b \quad (3.21)$$

Together, Eq:3.18 and Eq:3.21 comprise propeller momentum theory but cannot be solved on their own. Blade-element theory analyses incremental aerofoil sections of width dr of the propeller profile (the sectional view of which is illustrated in Fig:3.4) at some radius r . Each aerofoil element has a net local fluid velocity \vec{U} across its profile, calculated as:

$$\vec{U} = \sqrt{(v_\infty + v_i)^2 + (v_\Omega + v_\theta)^2} \quad (3.22)$$

Where each profile has a chord length c and an inclination (or *pitch*) θ of the aerofoil *zero-lift line* relative to the horizontal. Local fluid velocities incident to the propeller profile (shown in Fig:3.4) make their own angle of attack ϕ such that a true effective angle of attack α_{eff} is encountered:

$$\phi = \theta - \alpha_{eff} \quad (3.23)$$

That local angle of attack varies with the incident fluid flow magnitude v_∞ and the induced axial velocity v_i . That trigonometric ratio between the two is given as:

$$\phi = \tan^{-1}\left(\frac{v_\infty + v_i}{v_\Omega + v_\theta}\right) = \tan^{-1}\left(\frac{v_\infty(1 + a)}{\Omega r(1 + a')}\right) \quad (3.24)$$

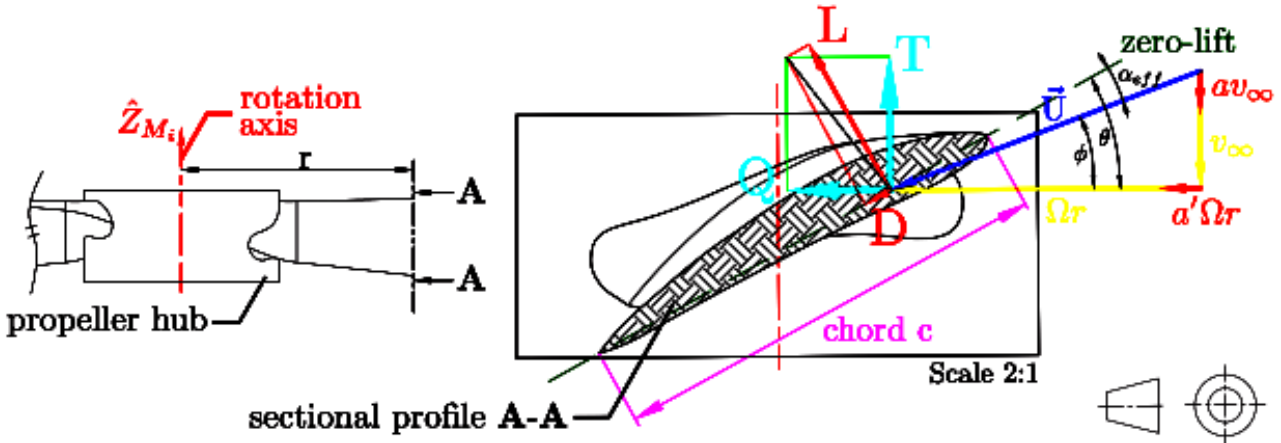


Figure 3.4: Blade element profile at radius r

In-plane fluid flow $\vec{U}(r, \phi)$, for an element at radius r with a local angle of attack ϕ , then contributes towards elemental lift and drag forces as a function of aerofoil's dimensionless lift, C_L , and drag, C_D , coefficients. Those coefficients are determined by the aerofoil's characteristics, but would be constant across the length of a variable pitch, hinged and untwisted hinged prop (Fig:3.2b).

$$\Delta L = \frac{1}{2} \rho \vec{U}(r, \phi)^2 c C_L \quad (3.25a)$$

$$\Delta D = \frac{1}{2} \rho \vec{U}(r, \phi)^2 c C_D \quad (3.25b)$$

With air density ρ typically taken at *stp*. Lift and drag forces, when taken parallel and perpendicular to the plane of rotation, are thrust T and torque F_q forces (Fig:3.4). The in-plane force applies an aerodynamic torque Q at the propellers hub because the force F_q acts at a radius r , [55].

$$dT = \frac{1}{2} \rho \vec{U}(r, \phi)^2 c (C_L \cos(\phi) + C_D \sin(\phi)) . dr \quad (3.26a)$$

$$dF_q = \frac{1}{2} \rho \vec{U}(r, \phi)^2 c (C_L \sin(\phi) + C_D \cos(\phi)) . dr \quad (3.26b)$$

$$\rightarrow dQ = \frac{1}{2} \rho \vec{U}(r, \phi)^2 c (C_L \sin(\phi) + C_D \cos(\phi)) r . dr \quad (3.26c)$$

$$\rightarrow dP = \Omega r dF_x . dr \quad (3.26d)$$

Rotational power expended is a product of angular velocity and the opposing in-plane torque; Eq:3.26d. Power is mostly used in lieu of torque or drag terms in Eq:3.26c or Eq:3.26b respectively. Calculating forces and power terms as per momentum theory for each element, in terms of axial and tangential induction factors:

$$dT = \rho 4\pi r^2 v_\infty (1 + a) a dr \quad (3.27a)$$

$$dP = \rho 4\pi r^2 v_\infty (1 + a) \Omega r (1 + a') dr \quad (3.27b)$$

Equating momentum and element terms produces the blade-element momentum equation(s) for aerodynamic thrust and power from a propeller. Following a few assumptions; most importantly that the lift coefficient C_L is a linear function of the effective angle of attack α_{eff} , typically characterised as:

$$C_L = a_L(\theta - \phi) \quad (3.28)$$

Firstly the lift coefficient curve gradient a_L is shown in [57] for an ideally twisted blade, like the fixed pitch propellers under consideration here, to be 2π . An ideal lift coefficient is then a function:

$$C_L = 2\pi(\theta - \phi) \quad (3.29)$$

Secondly assuming tangentially induced velocities, v_θ , are small when compared to the propeller's translational speed at radius r , $v(r) = \Omega r$. The tangential induction factor a' is then the ratio:

$$a' = \frac{v_\theta}{\Omega r} \ll 1 \quad (3.30)$$

Small angle approximations then apply to Eq:3.26a-3.26c; $\cos(\phi + \alpha_{eff}) \approx 1$ and $\sin(\phi + \alpha_{eff}) \approx \phi + \alpha_{eff}$. Similarly net inflow and axial velocities are $(v_\infty + v_i) \ll \Omega r$, the following integrals are then found:

$$T = \int_{r=0}^R \frac{1}{2} a_L b c \rho (\Omega r)^2 \left[\theta - \frac{v_\infty + v_i}{\Omega r} \right] dr \quad (3.31a)$$

$$P = \int_{r=0}^R \frac{1}{2} a_L b c \rho (\Omega r)^3 \left[\left(\theta - \frac{v_\infty + v_i}{\Omega r} \right) \left(\frac{v_\infty + v_i}{\Omega r} \right) + C_d \right] dr \quad (3.31b)$$

Where b is the number of blades the propeller has. In practice knowing exact pitch and chord values as a function of r/R is difficult and calculating integrals at each process step is cumbersome. Both Eq:3.31a and Eq:3.31b can be solved by equating element and momentum terms (a full solution is given in Appendix:A.2). Often dimensionless thrust, torque and power coefficients are defined across the entire blade's length:

$$C_T(J) \triangleq \frac{T}{\rho \Omega^2 D^4} \quad (3.32a)$$

$$C_P(J) \triangleq \frac{P}{\rho \Omega^3 D^5} \quad (3.32b)$$

Where Ω is the propeller's rotational speed in revolutions per second (*RPS*) and different from other inertial equations like Eq:3.64, with units $[\text{rad.s}^{-1}]$. The propeller diameter D is in [m]. For fixed pitch propellers the thrust and power coefficients are easily determined and remain consistent. Both Eq:3.32a and Eq:3.32b vary as a function of the dimensionless *advance ratio* J .

$$J \triangleq \frac{v_\infty}{\Omega R} \quad (3.33)$$

Typically the net upstream velocity v_∞ in Eq:3.33 is simply the perpendicular component (projected onto the plane's normal vector \hat{n} , shown later in Eq:3.35) of the vehicle's translational velocity in the body frame; $\vec{v}_b \perp \hat{n}$. For the case of a zero advance ratio, $J = 0$, the conditions are regarded as static. Static thrust and power coefficients are nominal in their values.

Propeller databases like [21] provide comprehensive coefficient values for a range of small and medium diameter propeller types at different advance ratios. Included in the database are blade profiles, pitch and chord lengths; all the results are outcomes of the investigation [22].

The introduction of those coefficients drastically reduces thrust estimation complexity. For a typical 6×4.5 inch propeller the following coefficients were linearly interpolated from similar pitched database results in [21] to match subsequent physical test values. Static thrust and power coefficients are respectively:

$$C_{T0} = 0.191 \quad (3.34a)$$

$$C_{P0} = 0.0877 \quad (3.34b)$$

Fig:3.5 plots coefficients for thrust, C_T , and power, C_P , as a function of the advance ratio J . As the incident upstream fluid velocity, v_∞ , increases, the thrust coefficient decreases. So too does the power coefficient and hence the aerodynamic torque. The thrust and power coefficients can be assumed constant for low advance ratios, or in the case considered here, translational velocities.

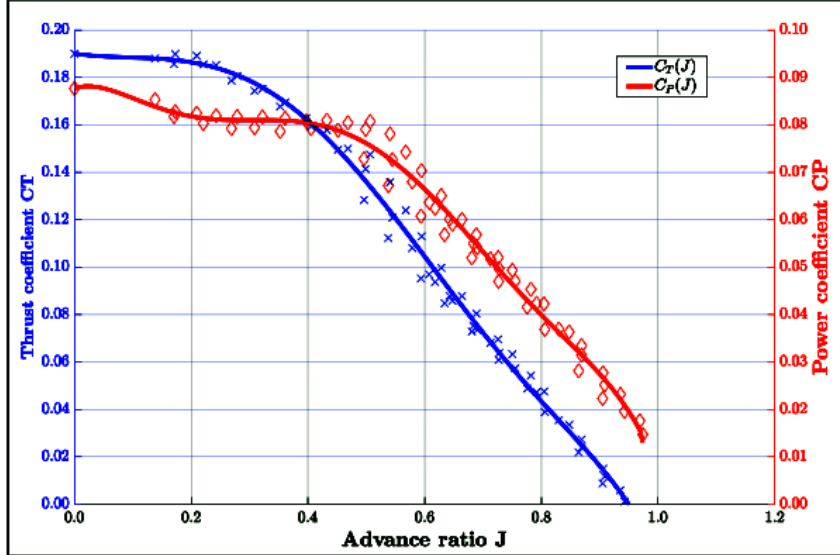
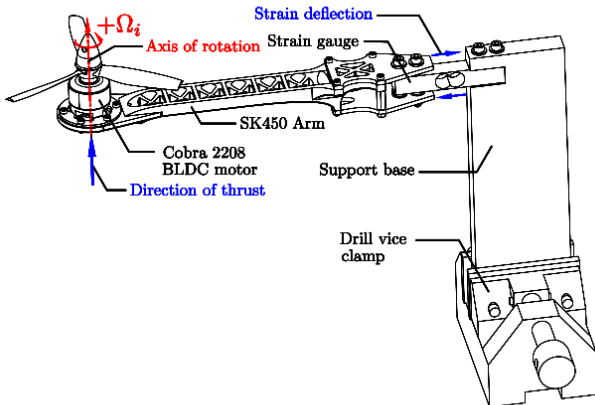
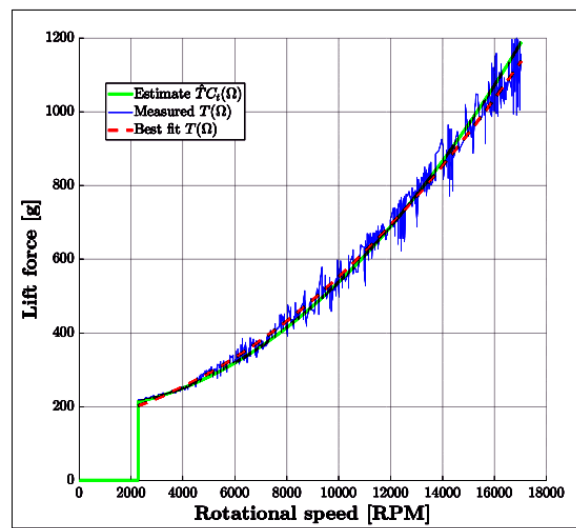


Figure 3.5: Power & thrust coefficients

Shown in Fig:3.6 and Fig:3.7, both thrust and torque test rigs and their static test results are illustrated. Measured values for each test are plotted; $T(\Omega)$ in Fig:3.6b for thrust and $Q(\Omega)$ in Fig:3.7b for torque. The physically tested values are fitted with quadratic trend-lines and plotted against static coefficient estimates using Eq:3.32a for thrust $\hat{T}C_t(\Omega)$ and Eq:3.32b for calculated torque $\hat{Q}C_p(\Omega)$. Results from Fig:3.5 are used as a lookup table and values from Eq:3.32 are calculated, induced propeller thrust and torques can be accurately modeled quadratically, the power term is cubic with respect to its rotational velocity.

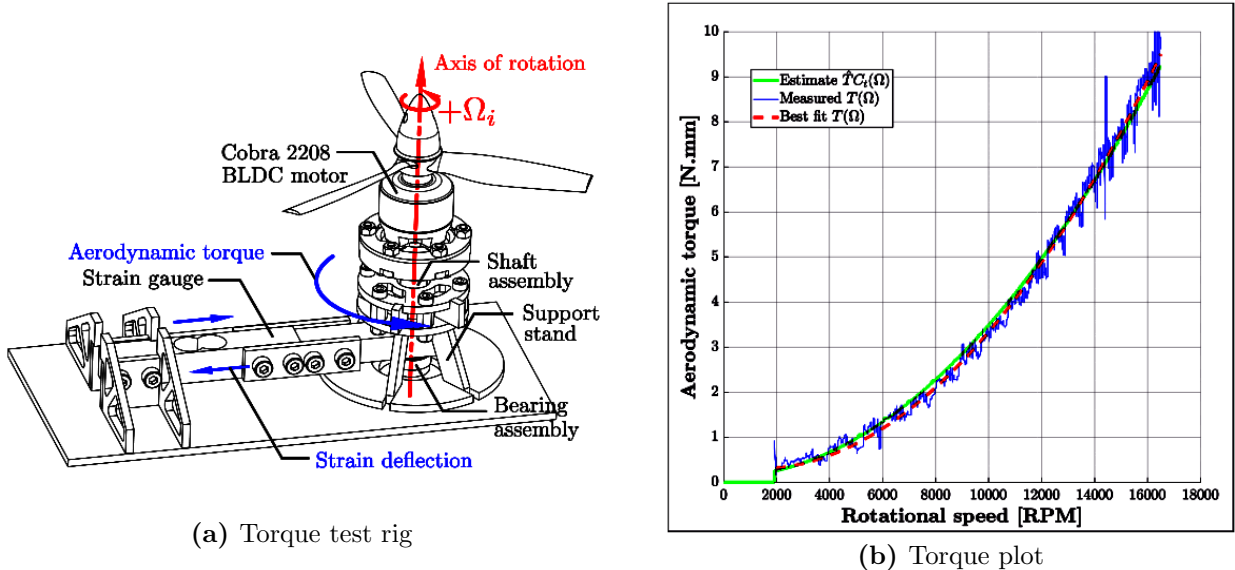


(a) Thrust deflection test rig



(b) Static thrust plot

Figure 3.6: Propeller thrust tests

**Figure 3.7:** Static torque tests

Advance ratios, Eq:3.33, or rather the propeller incident fluid flow(s) are dependent on the vehicle's net translational and angular velocity. Such that the fluid velocity's normal component to the propeller plane is given by:

$$v_\infty = (\vec{v}'_b + \vec{L}_{arm} \times \vec{\omega}'_b) \cdot \hat{n}(\lambda_i, \alpha_i) \in \mathcal{F}^{M_i} \quad (3.35)$$

Where \vec{v}'_b [m.s^{-1}] is the body's translational velocity and $\vec{\omega}'_b$ [rad.s^{-1}] is the body's angular velocity, both transformed to the propeller's frame, $\in \mathcal{F}^{M_i}$. Furthermore $\hat{n}(\lambda_i, \alpha_i)$ is the unit vector normal to the propeller's rotational plane, relative to the body velocity. Then J is calculated from Eq:3.33.

It's worth reiterating that the above static coefficients are indeed calculated from physical static tests. However advance ratio coefficient dependencies are linearly interpolated from the closest available matching data (APC Thin-Electric 8X6 propellers) cited from [21].

Clockwise and counterclockwise propellers and rotations were used for both thrust and torque tests. Despite the thrust and test rigs (Fig:3.6a and Fig:3.7a respectively) having been designed to isolate each response, results from opposing directional tests were averaged in the hopes that stray opposing effects were negated. Both clockwise and anti-clockwise rotational test results for thrust and torque measurements are included in Appendix:C.1

Discrepancies which emerge between the model or coefficient values derived can be accounted for with lumped uncertainty disturbance term(s). Model uncertainty compensation can easily be incorporated into adaptive backstepping or H_∞ control algorithms. The deviation of the modeled thrust or torques from their true values would be simple to incorporate into a plant dependent Lyapunov candidate function; Sec:4.6.3.

3.2.2 Hinged Propeller Conning & Flapping

Non-linear effects which adversely alter a propeller's performance have all been well documented in their own right; mostly in the context of helicopter aerodynamic and propeller fields [20,115]. Typically such effects are more pronounced when observing hinged variable pitch propellers (Fig:3.2b), fixed pitch propellers have a diminished effect. Moreover, low translational velocities suppress such responses but they're worth mentioning.

Conning and flapping are the two most significant aerodynamic effects encountered by a propeller. Other phenomenon like cyclic vortex ring states are deemed to not be applicable here and fall outside the scope of the investigation.

In translational flight, for a propeller without shrouding or a ducting, each blade encounters varying incident fluid flow throughout its cycle. The advancing blade relative to the body's translational direction encounters a greater fluid flow than the retreating blade, constructive and destructive interference from the body's translational velocity adds to local fluid flows. The effective local angle(s) of attack (Sectional Fig:3.4) for the advancing and retreating propeller blades are then asymmetrical. The unbalanced angles of attack produce a dissymmetry of lift across the propeller blade's surface.

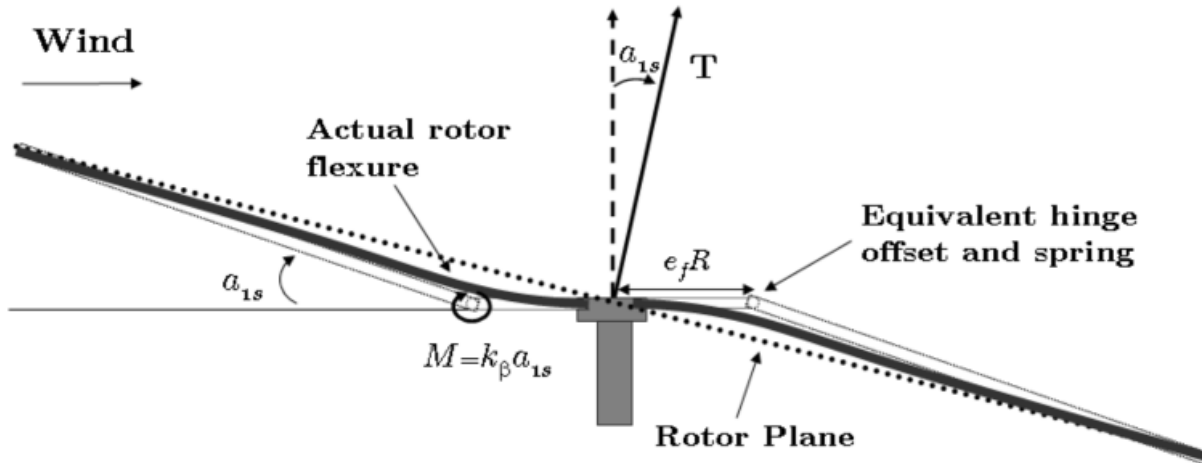


Figure 3.8: Propeller blade flapping; from [55]

Throughout each rotation the blade is forced up and down as it cycles through a varying fluid velocity field, applying a torque moment about the propeller's hub. That torque's magnitude is a function of the body's net translational velocity and the propeller material's stiffness (hence its susceptibility to deflection). The flapping pitches the effective propeller plane (*tip-path plane*), and hence the thrust vector line, away from its principle axis (Fig:3.8).

The propeller's resultant thrust vector is pitched away from its nominal perpendicular state by some deflection angle, α_{1s} in Fig:3.8, toward the direction of translational movement or wind disturbance. Propeller flapping is diminished at low translational velocities with small wind disturbances relative to propeller rotational speed. As such flapping is not applicable to the feasible flight envelope envisaged for the prototype here.

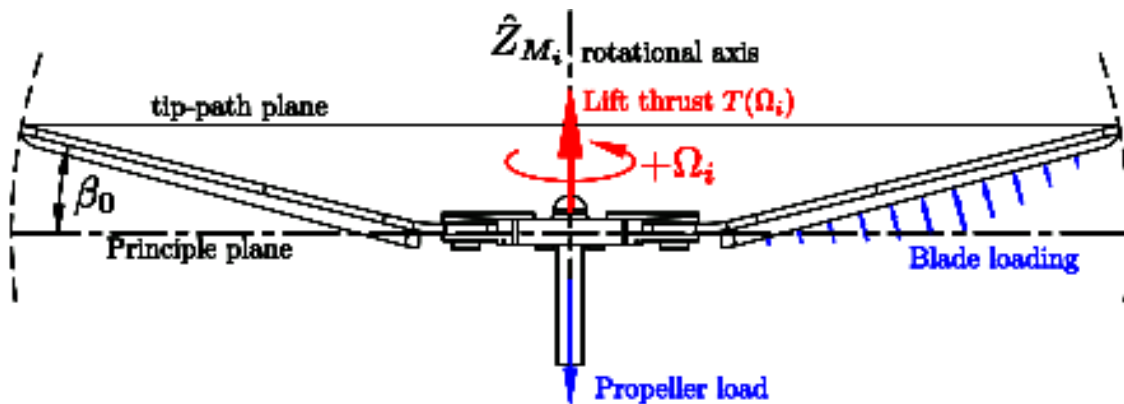


Figure 3.9: Propeller coning

Coning (illustrated in Fig:3.9) is another form of propeller deflection, which again is dependent on the blade material's stiffness. Coning causes both advancing and retreating propeller blades to both deflect upward. Distributed loading on the propeller surface from supporting a body's weight causes the upward deflection. The coning reduces the effective propeller disc's radius, adversely affecting thrust produced, Eq:3.31a. Increased loading accentuates the coning angle experienced by the propellers and as such reduces the tip-path-plane.

Both aerodynamic propeller deflections can be quantified numerically. Their derivation and resultant equations are cumbersome however. In practice both effects on the produced prototype are not significant enough to produce instability if neglected. The frame could potentially be affected in more adverse ways given certain flight conditions with higher translational velocities or incident wind and fluid flow disturbances...

3.2.3 Drag

For any solid body with some non-zero relative translational velocity motion within a fluid, there exists a second order damping response opposing translational velocity. The net drag force, \vec{D}_{net} , although locally dependent on individual component cross-sections can be abstracted to a drag coefficient matrix representing the whole body. For a vehicle's velocity \vec{v}_b :

$$\vec{v}_b = \begin{bmatrix} u \\ v \\ w \end{bmatrix} \quad [\text{m.s}^{-1}] \in \mathcal{F}^b \quad (3.36)$$

The drag force encountered by the vehicle is given by:

$$\vec{D}_{net}(\vec{v}_b) = \begin{bmatrix} D_{ii} & D_{ij} & D_{ik} \\ D_{ji} & D_{jj} & D_{jk} \\ D_{ki} & D_{kj} & C_{kk} \end{bmatrix} \begin{bmatrix} u \\ v \\ w \end{bmatrix}^2 \quad [\text{N}], \quad \in \mathcal{F}^b \quad (3.37)$$

Each drag coefficient's subscript; \hat{i}, \hat{j} and \hat{k} are dependent on the frame's directional cross-section area for each $\hat{X}_b, \hat{Y}_b, \hat{Z}_b$ axis respectively. Given a well designed and symmetrical frame, it can be assumed the off-diagonal elements are of little or no consequence and as such the drag equation can be simplified to a diagonal form:

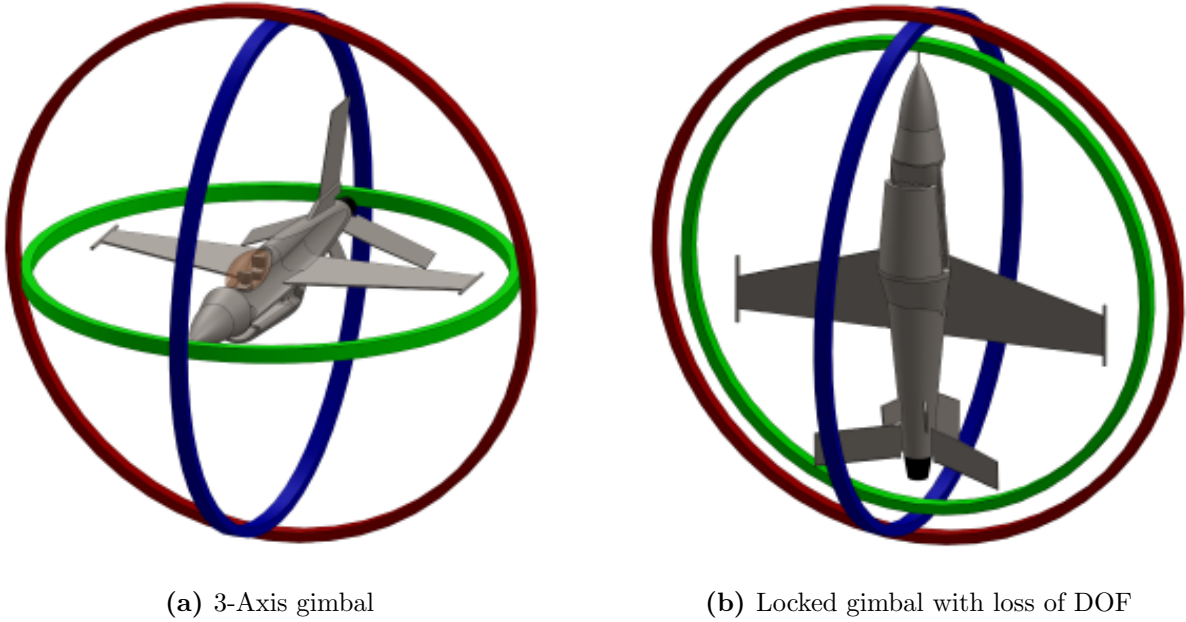
$$\vec{D}_{net}(\vec{v}_b) \approx \text{diag}(D_{ii}, D_{jj}, D_{kk}) \vec{v}_b^2 \quad \in \mathcal{F}^b \quad (3.38)$$

Due to the second order degree of translational velocity on the drag force; such terms can be relegated to a lumped disturbance terms to be adaptively compensated for in the control loop, Sec:4.6.3. The time scale separation between velocity and wind drag effects within the control loop accommodate such an assumption. Analogous rotational drag-like effects opposing angular rates exist but, for the intents and purposes of most practical flight envelopes, can be disregarded.

In simulation; if the plant has sufficient disturbance rejection then the drag term in Eq:3.37 would be easily accounted for in an adaptive backstepping algorithm. Furthermore it is possible to physically test for the drag coefficients to attain a higher certainty model but, given the flight conditions for this research, such effects will be small if not negligible. As such those tests are outside the scope of investigation here...

3.2.4 Rotation Matrix Singularity

The singularity inherent to Euler Angle parametrization is often mentioned but far less common is the mathematical demonstration of how that singularity manifests itself. A singularity occurs for some matrix A in $\vec{y} = A\vec{x}$ when the matrix has a zero determinate; losing rank and differentiability in terms of \vec{x} . The combined rotation matrix from the \mathcal{F}^I to \mathcal{F}^b is the singular component of an Euler parametrized sequence. Considering the case of a rotational 3-axis gimbal system (Fig:3.10a) which mimics the sequential nature of the Euler set. When the intermediary sequenced rotational angle is at $\pi/2$, the remaining two axes become co-linear (Fig:3.10b). In Z-Y-X rotation sequence adopted in this work, the singularity occurs from the rolling angle θ about \hat{Y} . Both the pitch ϕ or yaw ψ rotations will subsequently have the same rotational effect. Such a situation results in as a loss of a degree of freedom.

**Figure 3.10:** Mechanical gimbal lock

What is clear physically is not necessarily as obvious mathematically. A loss of rank occurs in the Euler Matrix $\Psi(\eta)$, defined previously in Eq:2.12g from Sec:2.2.1. That relation between angular velocity, in the inertial frame or inversely in the body frame, and the angular rates of the Euler Angles has a determinant:

$$\begin{bmatrix} \dot{\phi} \\ \dot{\theta} \\ \dot{\psi} \end{bmatrix} = \begin{bmatrix} 1 & \sin(\phi)\tan(\theta) & \cos(\phi)\tan(\theta) \\ 0 & \cos(\phi) & -\sin(\phi) \\ 0 & \sin(\phi)\sec(\theta) & \cos(\phi)\sec(\theta) \end{bmatrix} \begin{bmatrix} p \\ q \\ r \end{bmatrix} = \Phi(\eta)\omega_b \quad (3.39)$$

$$\rightarrow \det(\Phi(\eta)) = \cos(\phi)(\cos(\phi)\sec(\theta)) + \sin(\phi)(\sin(\phi)\sec(\theta)) = \sec(\theta) \quad (3.40)$$

$$\therefore \lim_{\theta \rightarrow \pi/2} |\Phi(\eta)| = \sec(\theta) \rightarrow \infty \quad (3.41)$$

The Euler matrix $\Phi(\eta)$ loses rank as $\theta \rightarrow \pi/2$, loosing differentiability as well. The physical consequence of this is the loss of a degree of freedom. More specifically, if one looks at how the Z-Y-X rotation (or transformation) matrices are formulated, from Eq:2.6.

$$R_I^b(\eta) = R_z(\psi)R_y(\theta)R_x(\phi) = \begin{bmatrix} c_\psi & -s_\psi & 0 \\ s_\psi & c_\psi & 0 \\ 0 & 0 & 1 \end{bmatrix} \begin{bmatrix} c_\theta & 0 & s_\theta \\ 0 & 1 & 0 \\ -s_\theta & 0 & c_\theta \end{bmatrix} \begin{bmatrix} 1 & 0 & 0 \\ 0 & c_\phi & -s_\phi \\ 0 & s_\phi & c_\phi \end{bmatrix} \quad (3.42a)$$

$$\therefore R_I^b(\eta) = \begin{bmatrix} c_\psi c_\theta & c_\psi s_\theta s_\phi - s_\psi c_\phi & c_\psi s_\theta c_\phi + s_\psi s_\phi \\ s_\psi c_\theta & s_\psi s_\theta s_\phi + c_\psi c_\phi & s_\psi s_\theta c_\phi - c_\psi s_\phi \\ -s_\theta & c_\theta s_\phi & c_\phi c_\theta \end{bmatrix} \quad (3.42b)$$

In the case where $\theta = \pi/2$, and using trigonometric double angles, the following can be reduced;

$$R_I^b(\eta) = \begin{bmatrix} 0 & c_\psi s_\phi - s_\psi c_\phi & c_\psi c_\phi + s_\psi s_\phi \\ 0 & s_\psi s_\phi + c_\psi c_\phi & s_\psi c_\phi - c_\psi s_\phi \\ -1 & 0 & 0 \end{bmatrix} \Big|_{\theta=\pi/2} \quad (3.42c)$$

$$= \begin{bmatrix} 0 & s(\phi - \psi) & c(\phi - \psi) \\ 0 & c(\phi - \psi) & s(\phi - \psi) \\ -1 & 0 & 0 \end{bmatrix} \quad (3.42d)$$

$$= R_{x'}(\phi - \psi) \quad (3.42e)$$

Where the resultant in Eq:3.42e represents an \hat{X}' -axis rotation in a new intermediate frame, post a $\pi/2$ rotation about the \hat{Y} -axis. Through trigonometric double angles a degree of freedom is lost at $\theta = \pi/2$, when both ϕ and ψ effect the same angle.

3.2.5 Quaternion Dynamics

An algorithm proposed in [117] suggested a solution to avoid Euler Angle singularities. The heuristic proposed involved switching between sequence conventions (ZYX,ZYZ etc...there are 12 in total) such that the singularity is always avoided. However the implementation of such an algorithm is cumbersome and computationally exhaustive. Far more elegant is the use of *quaternion* attitude representations in \mathbb{R}^4 (in [43, 46, 70] amongst others...most notably made popular by [116] for use in animation).

A quaternion is analogous to a rotation matrix in that it represents an attitude difference between two reference frames. An \mathbb{R}^3 attitude is parameterized as one rotation θ about a single unit *Euler* axis \hat{u} (demonstrated using the Rodriguez Formula in [84]). In brief a quaternion consists of a scalar component, q_0 , and complex vector component, $\vec{q} \in \mathbb{C}^3$, such that:

$$Q \triangleq \begin{bmatrix} q_0 \\ \vec{q} \end{bmatrix} \in \mathbb{R}^4 \quad (3.43)$$

The relationship between an Euler Angles rotation matrix $R_I^b(\eta)$ and a quaternion attitude Q_b is given by the Rodriguez formula:

$$R_I^b(\eta) = R(Q_b) = \mathbb{I}_{3 \times 3} + 2q_0[\vec{q}]_{\times} + 2[\vec{q}]_{\times}^2 \quad (3.44)$$

Where $[\cdot]_{\times}$ is the cross-product matrix defined previously in Eq:2.8c. All quaternions, unless otherwise specified, are unit quaternions $Q \in \mathbb{Q}_u$. Quaternions with a unity magnitude ensure that rotational operations maintain the vector operand's magnitude. A unit quaternion is defined:

$$\|Q\| = \sqrt{q_0^2 + \vec{q}^2} = 1 \quad (3.45)$$

Quaternion multiplication is distributive and associative, but not commutative. Specifically a quaternion multiplication operator is equivalent to the Hamilton product. For two quaternions, Q and P :

$$Q \otimes P = \begin{bmatrix} q_0 \\ \vec{q} \end{bmatrix} \otimes \begin{bmatrix} p_0 \\ \vec{p} \end{bmatrix} \quad (3.46a)$$

$$\triangleq \begin{bmatrix} q_0 p_0 - \vec{q} \cdot \vec{p} \\ q_0 \vec{p} + p_0 \vec{q} + \vec{q} \times \vec{p} \end{bmatrix} \quad (3.46b)$$

$$= q_0 p_0 - \vec{q} \cdot \vec{p} + p_0 \vec{q} + q_0 \vec{p} + \vec{q} \times \vec{p} \quad (3.46c)$$

Because the vector component of a quaternion is complex valued, it is natural that a quaternion complex conjugate exists, defined:

$$Q^* = \begin{bmatrix} q_0 \\ -\vec{q} \end{bmatrix} \quad (3.47)$$

It follows that the fundamental quaternion identity is:

$$Q \otimes Q^* = \mathbb{I}_{4 \times 4} \quad (3.48)$$

A right handed quaternion rotation applied to a vector $\vec{v} \in \mathbb{R}^3$ involves multiplication by two unit quaternions.

$$\begin{bmatrix} 0 \\ \vec{v}' \end{bmatrix} = Q \otimes \begin{bmatrix} 0 \\ \vec{v} \end{bmatrix} \otimes Q^* \quad (3.49)$$

Mostly, the zero scalar components are omitted in a rotation (*or transformation*) operation, it is implied that vector operands are substituted with zero scalar quaternions.

$$\vec{v}' = Q \otimes (\vec{v}) \otimes Q^* \quad (3.50)$$

In the case of rigid body attitude parametrization using quaternions, Q_b is the quaternion which represents the difference between body and inertial frames \mathcal{F}^b and \mathcal{F}^I respectively. A quaternion operator is equivalent to a rotation matrix operation, for some vector $\vec{\nu}_I \in \mathcal{F}^I$;

$$\vec{\nu}_b = R_I^b(\eta)\vec{\nu}_I \iff Q_b \otimes (\vec{\nu}_I) \otimes Q_b^* \quad (3.51)$$

Since quaternions are non-commutative, the construction of a body quaternion Q_b from an Euler angle set $\vec{\eta}$ is sequence dependent. Euler angles, despite being singular, are conceptually simpler terms for describing a body's orientation. A Z-Y-X sequenced body quaternion, Q_b , can be constructed from Euler angles as:

$$Q_b = Q_z \otimes Q_y \otimes Q_x = \begin{bmatrix} \cos(\psi/2) \\ 0 \\ 0 \\ \sin(\psi/2) \end{bmatrix} \otimes \begin{bmatrix} \cos(\theta/2) \\ 0 \\ \sin(\theta/2) \\ 0 \end{bmatrix} \otimes \begin{bmatrix} \cos(\phi/2) \\ \sin(\phi/2) \\ 0 \\ 0 \end{bmatrix} \quad (3.52)$$

A quaternion's time derivative, defined in [43], with Q_ω being a quaternion with a vector component equal to angular velocity $\vec{\omega}_{b/I}$ and a zero scalar component, is:

$$\frac{d}{dt} Q_b = \frac{1}{2} Q_b \otimes Q_\omega = \begin{bmatrix} -\frac{1}{2} \vec{q}^T \vec{\omega}_b \\ \frac{1}{2} ([\vec{q}]_\times + q_0 \mathbb{I}) \vec{\omega}_b \end{bmatrix} \quad (3.53)$$

Using quaternions to represent attitudes negates the need for an Euler Matrix, $\Phi(\eta)$ from Eq:2.12h, to represent attitudes and their rates. A body quaternion is fully defined in the inertial frame with respect to the body frame or inversely so. The first quaternion time derivative replaces angular velocity rate differentials in Eq:3.10a and Eq:3.10c respectively:

$$\dot{\mathcal{E}} = R_b^I(-\eta)\vec{v}_b \iff_Q Q_b(-\eta) \otimes \vec{v}_b \otimes Q_b^*(-\eta) = Q_b^* \otimes \vec{v}_b \otimes Q_b \in \mathcal{F}^I \quad (3.54a)$$

$$\dot{\eta} = \Phi(\eta)\vec{\omega}_b \in \mathcal{F}^{v2,v1,I} \iff_Q \dot{Q}_b = \frac{1}{2} Q_b \otimes Q_\omega \in \mathcal{F}^I \quad (3.54b)$$

Second order time derivatives for quaternion acceleration aren't as useful or concise as their higher order velocity counterparts. The second order derivative is provided here for the sake of completeness. If at all possible, quaternion accelerations are mostly avoided due to their complexity of their calculation. The quaternion analogue for angular acceleration (Eq:3.14b), dependent on net torque acting on a body $\vec{\tau}_{net}$ is given by:

$$\ddot{Q}(\dot{Q}, Q, t) = \dot{Q} \otimes Q^* \otimes \dot{Q} + \frac{1}{2} Q \otimes [J_b^{-1}(\vec{\tau}_{net} - 4(Q^* \otimes \dot{Q}) \times (J_b(Q^* \otimes \dot{Q})))] \quad (3.55)$$

An Euler angle attitude error state used for control plants is defined as the subtracted error between desired and existing attitude orientations $\vec{\eta}_d$ and $\vec{\eta}_b$ respectively. Where $\vec{\eta}_d$ is some attitude produced from a trajectory generator.

$$\vec{\eta}_e = \vec{\eta}_d - \vec{\eta}_b \quad (3.56)$$

In contrast with Eq:3.56, a quaternion attitude error is a multiplicative term defined as the difference between two quaternions Q_d and Q_b ;

$$Q_e = Q_b^* \otimes Q_d \quad (3.57)$$

Quaternion attitude control and its stability goals are expanded upon subsequently in Sec:4.6.1.

3.2.6 Quaternion Unwinding

Although quaternions are indeed better than their Euler angle parameterized attitude counterpart(s) and lacking the associated singularity, they do contain one caveat. Because a quaternion $Q = [q_0 \vec{q}]^T$ represents a body's attitude in \mathbb{R}^3 using \mathbb{R}^4 there is an infinite coverage of attitude states, [84].

Each unit quaternion, stemming from Euler-Rodriguez theorem, represents a single Euler-axis rotation of θ about a unit axis \hat{u} such that:

$$Q = \begin{bmatrix} q_0 \\ \vec{q} \end{bmatrix} = \begin{bmatrix} \cos(\theta/2) \\ \sin(\theta/2)\hat{u} \end{bmatrix} \quad (3.58)$$

That rotation is applied with a quaternion operator, Eq:3.50. For every attitude state in 3-D there exist two unique quaternions which correspond to the same orientation, differing by their rotational direction about the Euler-axis. The rotation angle θ about the Euler-axis \hat{u} is reciprocal in that $\theta = \theta + 2k\pi$, $k \in \mathbb{N}$. There are then two definitions for Q_b :

$$Q_b = \begin{bmatrix} q_0 \\ \vec{q} \end{bmatrix} = \begin{bmatrix} \cos(\theta/2) \\ \sin(\theta/2)\hat{u} \end{bmatrix} \quad (3.59a)$$

$$Q_b = \begin{bmatrix} \cos(\pi - \theta/2) \\ \sin(\pi - \theta/2)\hat{u} \end{bmatrix} = \begin{bmatrix} -\cos(\theta/2) \\ \sin(\theta/2)\hat{u} \end{bmatrix} \quad (3.59b)$$

$$\vec{\eta} \in \mathbb{R}^3 \iff \begin{bmatrix} \pm q_0 \\ \vec{q} \end{bmatrix} \in \mathbb{R}^4 \quad (3.59c)$$

Eq:3.59c asserts that for each attitude in \mathbb{R}^3 there are *two* corresponding quaternions in \mathbb{R}^4 ; $[\pm q_0 \ \vec{q}]^T$. A consequence of this is that two possible error state trajectories exist for every attitude difference. Both a clockwise, $+\theta$, and an anticlockwise, $2\pi - \theta$, rotation points to the same quaternion attitude error state. This could lead to an erroneous and unnecessary "unwinding" of a complete counter revolution. So for attitude controllers the requirement is that for positive and negative quaternion scalars the control input is consistent:

$$\vec{\nu}_d = h([q_0 \ \vec{q}]^T, t) = h([-q_0 \ \vec{q}]^T, t) \quad (3.60)$$

Or more simply that $Q_e \triangleq [|q_0| \ \vec{q}]^T$. The simplest solution adhering to that constraint, which is often used, is to neglect the quaternion scalar component altogether. Using a reduced error state, only the quaternion error vector as an argument for the control law; $h(\vec{q}_e, t)$. Such a solution is an oversimplification and would only ever be locally stable.

An alternative is to use only the absolute quaternion scalar, which ensures the error state represents a right-handed (clockwise) rotation and not necessarily the shortest path. If the resolution of trajectory co-ordinates generated is sufficiently fine the control plant won't encounter a problem.

One proposal presented in [23] suggested using a *signum* operator to design the controller coefficient sign for the desired virtual angular velocity, $\vec{\omega}_d$ control plant input.

$$\vec{\omega}_d = \frac{2}{\Gamma_1} sgn(q_0) \vec{q} \quad (3.61a)$$

Where the signum operator is defined as:

$$sgn(q_0) = \begin{cases} 1 & q_0 \geq 0 \\ -1 & q_0 < 0 \end{cases} \quad (3.61b)$$

Eq:3.61 was shown to be asymptotically stable but only locally in the case where the Euler-axis angle is constrained; $\theta \leq \pm\pi$. That control law would still need the control torques to be calculated from that angular velocity $\vec{\omega}_d$ setpoint.

In [10], the authors used a backstepping controller with a trajectory using the absolute quaternion scalar. The resultant was a global asymptotically stable control law which tracked quaternion setpoints for a satellite's attitude. Controllers presented in Sec:4.6 all incorporate the signed quaternion scalars into the control law; hence relying on the trajectory generation to provide the desired direction of the rotation path.

3.3 Multibody Nonlinearities

The unique component of the prototype's design which facilitates redirection of a propeller's thrust vector (Eq:2.16b and Sec:2.1.1) is also what makes finding the complete equations of motion drastically more complex. The relative (rotary) motion within the multibody system results in torque responses opposing those angular accelerations. Such induced responses, if left unmodelled, would almost definitely destabilize the attitude plant. Unmodelled inertia rate responses are shown to be destabilizing in [72]. Typically multibody dynamics are solved (and simulated) as a series of interacting torque and force constraints. There are different schools of thought on the subject, each proposing methodologies for stepping through the systems dynamics; *e.g* Implicit Euler integration [65, 134]...

The prototype investigated here is a multibody system connected with revolute joints, which permit a single degree of relative rotation between each connected rigid body. There are no translational degrees of freedom between each body. Opposed to the angular acceleration applied to a body are *gyroscopic* and *inertial* Newtonian torque responses. The responses from each body are solved independently and those excitation induced torque constraints are introduced as additive terms to the dynamic model derived in Sec:3.1.1.

A distinction must be made between torque responses here and those previously in Eq:3.10d. Recalling the classical differential equation of angular motion already derived:

$$\dot{\vec{\omega}}_b = J_b^{-1}(-\vec{\omega}_b \times J_b \vec{\omega}_b + \vec{\tau}_\mu) \quad [\text{m.s}^{-2}], \quad \in \mathcal{F}^b \quad (3.62)$$

Eq:3.62 treats the entire body as rigid; included terms are as a result of the entire multibody's collective motion. What follows is an extension of that attitude state to incorporate relative movements between each connected body. The objective here is to model the multibody dynamic system with clear responses induced from servo rotations of inner and middle ring bodies, $\Delta\lambda_i$ and $\Delta\alpha_i$ respectively. The subsequent derivations are Lagrangian analytical dynamics applied to the multibody system under consideration. For the purposes of this derivation it is assumed that no potential energy can be stored within the structure from material flexure. The only potential energy contribution is as a result of gravitational potential energy.

Alternatively the net dynamics could indeed be derived from a Lagrangian for the *entire* 13 body dynamic system. Where those connected bodies are; four rotor/propeller bodies (Fig:2.11), four inner ring bodies (Fig:2.12), four middle ring bodies (Fig:2.13) and finally the frame structure (Fig:2.17) each with 6 degrees of freedom. Constraints on the assembly's joints would eventually reduce the degrees of freedom and simplify solving for net responses. The purpose here is to model the body's response to changes in the actuation servos' positions, $\Delta\lambda_i$ and $\Delta\alpha_i$, so independent bodies are analyzed first. The final result is, in fact, a Lagrangian for those collective 13 bodies, whose partial derivative with respect to the net angular velocity relative to the inertial frame, $\partial\vec{\omega}_b$, produces the net torque acting on the system.

3.3.1 Relative Rotational Gyroscopic & Inertial Torques

Rotation matrices are used in the following derivations owing to the fact that induced torque responses are dependent on transformed rotational inertias. Quaternions, as mentioned in Sec:2.3, are ill-suited to inertia transformations.

Each of the four motor modules are symmetrical and so the induced torque response characteristics from one module can be extrapolated simply through a \hat{Z}_b reference frame rotation. Each motor module is positioned relative to the body frame's center of motion \vec{O}_b , as in Fig:2.9. Because each relative rotation from the actuator set, $u \in \mathbb{U}$, is actuated separately and upon a different body, their responses are calculated independently too.

Drawing again from Lagrangian theory and considering only the angular energy component for the inner ring assembly attached to frame \mathcal{F}^{M_i} . There is no relative translational motion between each connected body and thus can have no translational kinetic energy contribution. The translational kinetic energy for each module is an extension of body's net kinetic energy in Eq:3.7 and independent of any actuator's position. The motor module's translational motion is incorporated in Eq:3.14a. Considering the i^{th} motor module...

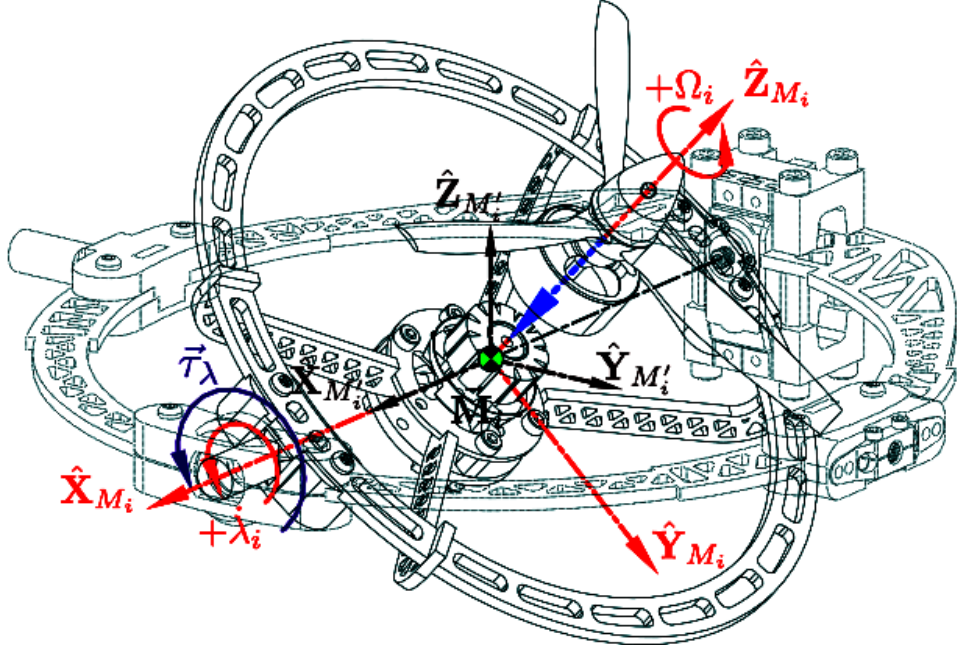


Figure 3.11: Exploded inner ring inertial bodies for $\vec{\tau}_\lambda$

Deriving dynamic responses for changes in the λ_i servo, acting on the inner ring frame \mathcal{F}^{M_i} relative to the middle ring frame $\mathcal{F}^{M'_i}$, requires a relative path co-ordinate to be defined. Seeing that the only path variable between the two frames is that servo's rotational position λ_i about the $\hat{\mathbf{x}}_{M_i}$ axis; the path co-ordinates $\vec{\mathbf{u}}(t) = [\lambda_i \ 0 \ 0]^T$ are used to produce the Lagrangian for the inner ring's energy relative the middle ring frame, $\mathcal{L}_{M'_i} \in \mathcal{F}^{M'_i}$.

The inner ring assembly consists of two separate bodies (exploded in Fig:3.11). Each with relative rotational motion and independent kinetic energies. Those bodies are; the rotor assembly with an inertia J_r (defined earlier in Eq:2.18) and the inner ring (*sans* rotor assembly) which has an inertia J_{ir} .

$$J_{ir} \triangleq J_n - J_r = J_{M_i} - J_r \quad \in \mathcal{F}^{M_i} \quad (3.63)$$

Where J_n (or J_{M_i}) is the net inertia for the inner ring assembly, explicitly defined in Eq:2.20. The rotor assembly has an angular velocity $\vec{\omega}_{r/M'_i}$ relative to the middle ring frame $\mathcal{F}^{M'_i}$ due to the BLDC motor's rotation Ω_i and the inner ring's servo rate $\dot{\lambda}_i$:

$$\vec{\omega}_{r/M'_i} \triangleq R_x(\lambda) \vec{\Omega}_i + \frac{d\lambda}{dt}(\vec{\lambda}_i) \quad \in \mathcal{F}^{M'_i} \quad (3.64a)$$

$$= R_x(\lambda) \vec{\Omega}_i + \dot{\vec{\lambda}}_i \quad (3.64b)$$

With the propeller's angular velocity vector; $\vec{\Omega}_i = [0 \ 0 \ \Omega_i]^T \in \mathcal{F}^{M_i}$ and measured in $[\text{rad.s}^{-1}]$, not in revolutions per second. The servo position is defined as a vector in the $\hat{\mathbf{x}}_{M'_i}$ axis; $\vec{\lambda}_i = [\lambda_i \ 0 \ 0]^T$ measured in $[\text{rad}]$. Next, the inner ring's angular velocity $\vec{\omega}_{M_i/M'_i}$ relative to the frame $\mathcal{F}^{M'_i}$ is only as a result of $\dot{\lambda}_i$:

$$\vec{\omega}_{M_i/M'_i} \triangleq \frac{d\lambda}{dt}(\vec{\lambda}_i) = \dot{\vec{\lambda}}_i \quad \in \mathcal{F}^{M'_i} \quad (3.65)$$

The Lagrangian for the inner ring's energy $\mathcal{L}_{M'_i}$, relative to the middle ring frame $\mathcal{F}^{M'_i}$, consists purely of rotational kinetic energy from angular velocities described in Eq:3.64 and Eq:3.65. The relative gravitation potential energy as a result of the rotated center of mass for the inner ring is neglected here as it is already included in Eq:2.34d and shown to simplify out later (subsequently in Eq:3.109) when considering the entire system as a whole. The inner ring Lagrangian is:

$$\mathcal{L}_{M'_i} = \frac{1}{2} \vec{\omega}_{r/M'_i}^T (J'_r) \vec{\omega}_{r/M'_i} + \frac{1}{2} \vec{\omega}_{M_i/M'_i}^T (J'_{ir}) \vec{\omega}_{M_i/M'_i} \quad (3.66a)$$

Both inertias for the rotor and inner ring bodies, J_r and J_{ir} respectively, are transformed to align with the middle ring frame $\mathcal{F}^{M'_i}$ using an $R_x(\lambda)$ rotation to align with frame $\mathcal{F}^{M'_i}$:

$$J'_r = R_x(\lambda)(J_r)R_x^{-1}(\lambda) \quad \text{and} \quad J'_{ir} = R_x(\lambda)(J_{ir})R_x^{-1}(\lambda) \quad (3.66b)$$

Then expanding the Lagrangian $\mathcal{L}_{M'_i}$ in Eq:3.66a with the above definitions for transformed inertias and relative angular velocities $\vec{\omega}_{r/M'_i}$ and $\vec{\omega}_{M_i/M'_i}$ yields:

$$\begin{aligned} \rightarrow \mathcal{L}_{M'_i} = \frac{1}{2} & \left(R_x(\lambda) \vec{\Omega}_i + \dot{\vec{\lambda}}_i \right)^T \left(R_x(\lambda)(J_r)R_x^{-1}(\lambda) \right) \left(R_x(\lambda) \vec{\Omega}_i + \dot{\vec{\lambda}}_i \right) \\ & + \frac{1}{2} \dot{\vec{\lambda}}_i^T \left(R_x(\lambda)(J_{ir})R_x^{-1}(\lambda) \right) \dot{\vec{\lambda}}_i \end{aligned} \quad (3.66c)$$

The inner ring's inertia J_{ir} is an independent body from the rotor assembly J_r . Recalling the Euler-Lagrange formulation from Eq:3.3 using path co-ordinates $\vec{u}(t)$ for the inner ring frame, $\mathcal{F}^{M'_i}$, relative to the middle ring frame, $\mathcal{F}^{M'_i}$. The generalized (torque) forces \vec{U} acting on the middle ring are then:

$$\vec{U}(\lambda) = \frac{d}{dt} \left(\frac{\partial \mathcal{L}_{M'_i}}{\partial \vec{u}} \right) - \frac{\partial \mathcal{L}_{M'_i}}{\partial \dot{\vec{u}}} \quad \in \mathcal{F}^{M'_i} \quad (3.67)$$

From [9] the partial derivative of a rotation matrix $R_x(\lambda)$ (and by extension the *transformation matrix* $R_x(-\lambda)$) is linearized using a Taylor series expansion. It follows that for some small perturbation $\partial\theta$ away from the nominal angle $\bar{\theta}$, a generalized rotation matrix about an axis \hat{u} by that angle θ becomes a first order approximation:

$$R_u(\bar{\theta} + \partial\theta) \approx \underbrace{\left(1 - [\Phi_u(\bar{\theta}) \partial\theta]_\times \right)}_{\text{infinitesimal rot}} R_u(\bar{\theta}) \quad (3.68)$$

Where $\Phi_u(\bar{\theta})$ is a generalized Euler matrix derivative analogous to Eq:2.12h. The consequence of Eq:3.68 is that transformed rotational inertias in Eq:3.66, both $R_x(\lambda)(J_r)R_x^{-1}(\lambda)$ and $R_x(\lambda)(J_{ir})R_x^{-1}(\lambda)$ can be approximated using their instantaneous transformation with no partial derivatives.

$$R_x(\lambda)(J_r)R_x^{-1}(\lambda) = J'_r \rightarrow \frac{\partial}{\partial \vec{u}} J'_r = \frac{\partial}{\partial \vec{\lambda}_i} J'_r \approx 0 \quad (3.69a)$$

$$R_x(\lambda)(J_{ir})R_x^{-1}(\lambda) = J'_{ir} \rightarrow \frac{\partial}{\partial \vec{u}} J'_{ir} = \frac{\partial}{\partial \vec{\lambda}_i} J'_{ir} \approx 0 \quad (3.69b)$$

Simplifications in Eq:3.69 are expanded upon and shown to be reasonable assumptions next in Sec:3.3.2. It follows that partial derivatives of the Lagrangian in Eq:3.66 with respect to \vec{u} are negligible; $\partial \mathcal{L}_{M'_i} / \partial \vec{u} \approx 0$. Only the partial derivative with respect to the path rate $\dot{\vec{u}}$ remain:

$$\therefore \vec{U}(\lambda) \approx \frac{d}{dt} \left(\frac{\partial \mathcal{L}_{M'_i}}{\partial \dot{\vec{u}}} \right) = \frac{d}{dt} \left((J'_r) \left(R_x(\lambda) \vec{\Omega}_i + \dot{\vec{\lambda}}_i \right) + (J'_{ir}) \dot{\vec{\lambda}}_i \right) \quad (3.70)$$

Transformed inertial rates \dot{J}'_r and \dot{J}'_{ir} must first be defined before evaluating the simplified Lagrangian derivative in Eq:3.70. Those inertial derivatives cannot be separated by time scale from the remainder of Eq:3.70 given that $\dot{\lambda}_i$ determines both inertial rates \dot{J}'_r and \dot{J}'_{ir} but is also a component of the kinetic energy in Eq:3.66c.

Starting with the general case; for some transformed inertia J to be aligned relative to a frame \mathcal{F}^b where the inertia is originally defined with respect to a frame \mathcal{F}^a . If the two frames differ by some rotation angle θ about an Euler axis \hat{u} , the generalized rotation matrix from frame \mathcal{F}^a to \mathcal{F}^b is given by $R_{\hat{u}}(\theta)$ calculated from Eq:2.7. The transformed inertia is then calculated as:

$$J' = R_{\hat{u}}(\theta)(J)R_{\hat{u}}^{-1}(\theta) \quad (3.71a)$$

Which, from the product rule and the rotation matrix time derivative definition in Eq:2.8, has its own derivative:

$$\dot{J}' = \frac{d}{dt} \left(R_{\hat{u}}(\theta)(J)R_{\hat{u}}^{-1}(\theta) \right) \quad (3.71b)$$

$$= \frac{d}{dt} \left(R_{\hat{u}}(\theta)(J)R_{\hat{u}}^{-1}(\theta) + R_{\hat{u}}(\theta) \left(\frac{d}{dt}(J) \right) R_{\hat{u}}^{-1}(\theta) + R_{\hat{u}}(\theta)(J) \frac{d}{dt} \left(R_{\hat{u}}^{-1}(\theta) \right) \right) \quad (3.71c)$$

$$= [\dot{\vec{\theta}}] \times R_{\hat{u}}(\theta)(J)R_{\hat{u}}^{-1}(\theta) + R_{\hat{u}}(\theta)(\dot{J})R_{\hat{u}}^{-1}(\theta) - R_{\hat{u}}(\theta)(J)[\dot{\vec{\theta}}] \times R_{\hat{u}}^{-1}(\theta) \quad (3.71d)$$

Where $\dot{\vec{\theta}} \triangleq \dot{\theta} \cdot \hat{u}$ is the projected angular velocity vector between the two frames. In most cases, the inertia won't be changing in its principle frame, or rather that $\dot{J} = 0$. Both the rotor assembly and inner ring inertias are constant in their principle frames, the transformed inertias then have the following derivatives. First for the rotor assembly:

$$\rightarrow \dot{J}'_r = \frac{d}{dt} \left(R_x(\lambda)(J_r)R_x^{-1}(\lambda) \right) \quad (3.72a)$$

$$= [\dot{\vec{\lambda}}_i] \times R_x(\lambda)(J_r)R_x^{-1}(\lambda) - R_x(\lambda)(J_r)[\dot{\vec{\lambda}}_i] \times R_x^{-1}(\lambda) \quad (3.72b)$$

Similarly for the inner ring's transformed inertial rate \dot{J}'_{ir} , without the rotor's contribution, is:

$$\rightarrow \dot{J}'_{ir} = \frac{d}{dt} \left(R_x(\lambda)(J_{ir})R_x^{-1}(\lambda) \right) \quad (3.73a)$$

$$= [\dot{\vec{\lambda}}_i] \times R_x(\lambda)(J_{ir})R_x^{-1}(\lambda) - R_x(\lambda)(J_{ir})[\dot{\vec{\lambda}}_i] \times R_x^{-1}(\lambda) \quad (3.73b)$$

Inserting those transformed inertial derivatives into Eq:3.70 and using Reynolds transportation theorem, Eq:3.5 for a vector's derivative in a rotating reference frame. The product rule then yields:

$$\begin{aligned} \rightarrow \frac{d}{dt} \left(\frac{\partial \mathcal{L}_{M'_i}}{\partial \dot{\vec{\mathbf{u}}}} \right) &= \left[(\dot{J}'_r)(R_x(\lambda)\vec{\Omega}_i + \dot{\vec{\lambda}}_i) + (J'_r)R_x(\lambda)\dot{\vec{\Omega}}_i + \vec{\omega}_{M_i/M'_i} \times (J'_r)R_x(\lambda)\vec{\Omega}_i + (J'_r)\ddot{\vec{\lambda}}_i \right. \\ &\quad \left. + \vec{\omega}_{M_i/M'_i} \times (J'_r)\dot{\vec{\lambda}}_i \right] + \left[(\dot{J}'_{ir})\dot{\vec{\lambda}}_i + (J'_{ir})\ddot{\vec{\lambda}}_i + \vec{\omega}_{M_i/M'_i} \times (J'_{ir})\dot{\vec{\lambda}}_i \right] = \vec{\mathbf{U}}(\lambda) \end{aligned} \quad (3.74)$$

Recombining inertial bodies with the same angular velocity ($J'_r + J'_{ir} = J'_n$) and recognizing that, from Eq:3.65, $\vec{\omega}_{M_i/M'_i} = \dot{\vec{\lambda}}$; the generalized net torque encountered by a $\Delta\lambda$ rotation is:

$$\therefore \vec{\mathbf{U}}(\lambda) = (J'_r)\vec{\Omega}'_i + (J'_r)\dot{\vec{\Omega}}'_i + \dot{\vec{\lambda}}_i \times (J'_r)\vec{\Omega}'_i + (J'_n)\dot{\vec{\lambda}}_i + (J'_n)\ddot{\vec{\lambda}}_i + \dot{\vec{\lambda}}_i \times (J'_n)\dot{\vec{\lambda}}_i \in \mathcal{F}^{M'_i} \quad (3.75a)$$

Where both $\vec{\Omega}'_i$ and $\dot{\vec{\Omega}}'_i$ are the respective transformed angular velocity and acceleration of the propeller in the middle ring frame:

$$\vec{\Omega}'_i = R_x(\lambda)\vec{\Omega}_i \in \mathcal{F}^{M'_i} \quad (3.75b)$$

$$\dot{\vec{\Omega}}'_i = \frac{d\vec{\Omega}}{dt}(R_x(\lambda)\vec{\Omega}_i) = R_x(\lambda)\dot{\vec{\Omega}}_i \in \mathcal{F}^{M'_i} \quad (3.75c)$$

The net torque response, $\hat{\tau}_\lambda$ from an $\Delta\lambda_i$ rotation, induced in the middle ring frame $\mathcal{F}^{M'_i}$, can be grouped into *inertial rates*, second order *inertial* and first order *gyroscopic* components;

$$\hat{\tau}_\lambda = \underbrace{(\dot{J}'_r)\vec{\Omega}'_i + (J'_n)\dot{\vec{\lambda}}_i}_{\text{Inertial rates}} + \underbrace{(J'_r)\dot{\vec{\Omega}}'_i + (J'_n)\ddot{\vec{\lambda}}_i}_{\text{Inertial}} + \underbrace{\dot{\vec{\lambda}}_i \times (J'_r)\vec{\Omega}'_i + \dot{\vec{\lambda}}_i \times (J'_n)\dot{\vec{\lambda}}_i}_{\text{Gyroscopic}} \in \mathcal{F}^{M'_i} \quad (3.76)$$

In Eq:3.76, a hat accent is used to denote the inner ring's servo torque vector; $\hat{\tau}_\lambda$. That equation represents an *estimation* of the true torque $\vec{\tau}_\lambda$, calculated using actuator states $\vec{\Omega}_i$ and $\dot{\vec{\lambda}}_i$ with their derivatives. The true physical torque $\vec{\tau}_\lambda$ would have to be physically measured with a torque transducer, not an estimate from system dynamics.

Similarly for the middle ring frame $\mathcal{F}^{M'_i}$ relative to the intermediary frame $\mathcal{F}^{M''_i}$, the only relative path variable is $\vec{v}(t) = [0 \ \alpha_i \ 0]^T$. The entire motor module's structure consists of three separate rotating bodies each with their own relative angular velocities; the *rotor* assembly, *inner* and *middle* ring structures (exploded in Fig:3.12).

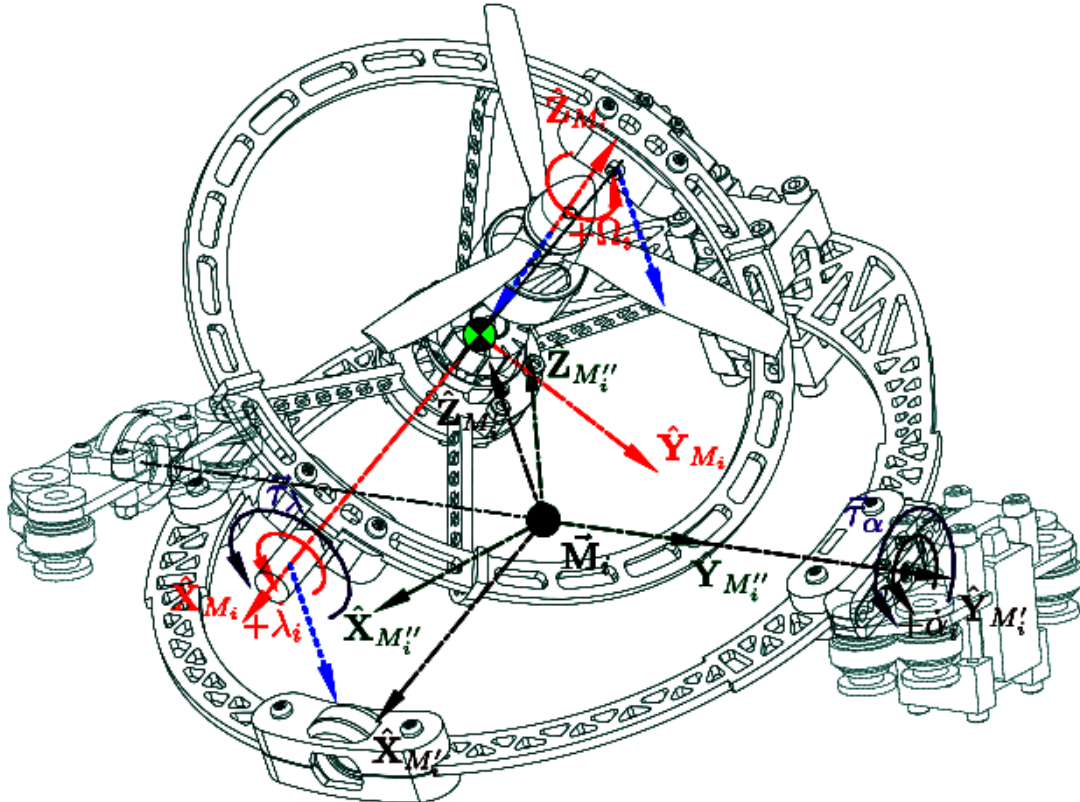


Figure 3.12: Exploded middle ring inertial bodies for $\vec{\tau}_\alpha$

Applying the same process to evaluate the α_i servo's response, the middle ring assembly Lagrangian $\mathcal{L}_{M''_i}$ is constructed but with respect to the intermediary frame $\mathcal{F}^{M''_i}$. First transforming the inertias; the rotor assembly, further rotated by α_i about its $\hat{Y}_{M'_i}$ axis, has an inertia aligned with axes in $\mathcal{F}^{M''_i}$:

$$J''_r = R_y(\alpha)(J'_r)R_y^{-1}(\alpha) = R_y(\alpha)R_x(\lambda)(J_r)R_x^{-1}(\lambda)R_y^{-1}(\alpha) \in \mathcal{F}^{M''_i} \quad (3.77a)$$

Which has a derivative \dot{J}''_r :

$$\dot{J}''_r = R_y(\alpha)(\dot{J}'_r)R_y^{-1}(\alpha) + [\dot{\vec{\alpha}}_i] \times R_y(\alpha)(J'_r)R_y^{-1}(\alpha) - R_y(\alpha)(J'_r)[\dot{\vec{\alpha}}_i] \times R_y^{-1}(\alpha) \quad (3.77b)$$

The inner ring structure has an inertia, still *without* including the rotor assembly:

$$J''_{ir} = R_y(\alpha)(J'_{ir})R_y^{-1}(\alpha) = R_y(\alpha)R_x(\lambda)(J_{ir})R_x^{-1}(\lambda)R_y^{-1}(\alpha) \in \mathcal{F}^{M''_i} \quad (3.78a)$$

Similarly with a derivative \dot{J}''_{ir} :

$$\dot{J}''_{ir} = R_y(\alpha)(\dot{J}'_{ir})R_y^{-1}(\alpha) + [\dot{\vec{\alpha}}] \times R_y(\alpha)(J'_{ir})R_y^{-1}(\alpha) - R_y(\alpha)(J'_{ir})[\dot{\vec{\alpha}}] \times R_y^{-1}(\alpha) \quad (3.78b)$$

Finally the middle ring structure's inertia from Eq:2.23a, with neither the rotor's nor the inner ring's contributions:

$$J'_m = R_y(\alpha)(J_m)R_y^{-1}(\alpha) \quad (3.79a)$$

Which, when using the collective motor module inertia J_p from Eq:2.23b, expands to:

$$= R_y(\alpha)(J_p)R_y^{-1}(\alpha) - R_y(\alpha)R_x(\lambda)(J_n)R_x^{-1}(\lambda)R_y^{-1}(\alpha) \quad (3.79b)$$

$$= J'_p - J''_n = J'_p - (J''_{ir} + J''_r) \in \mathcal{F}^{M''_i} \quad (3.79c)$$

Which has a derivative purely as a result of $\dot{\alpha}$:

$$\dot{J}'_m = [\dot{\vec{\alpha}}_i] \times R_y(\alpha)(J_m)R_y^{-1}(\alpha) - R_y(\alpha)(J_m)[\dot{\vec{\alpha}}_i] \times R_y^{-1}(\alpha) \quad (3.79d)$$

However; that derivative \dot{J}'_m , using \dot{J}''_r and \dot{J}''_{ir} from Eq:3.77b and Eq:3.78b respectively, expands to:

$$\dot{J}'_m = [\dot{\vec{\alpha}}_i] \times R_y(\alpha)(J_p)R_y^{-1}(\alpha) - R_y(\alpha)(J_p)[\dot{\vec{\alpha}}_i] \times R_y^{-1}(\alpha) - (\dot{J}''_{ir} + \dot{J}''_r) \quad (3.79e)$$

Note that introducing the relations of Eq:3.79c and Eq:3.79e to the collective body inertia J_p is to simplify the subsequent equations. Each body then has its own relative angular velocity with respect to the intermediate frame $\mathcal{F}^{M''_i}$. For the rotor; $\vec{\omega}_{r/M''_i}$ is the relative angular velocity of that assembly from the motor Ω_i and both inner and middle servo rates $\dot{\lambda}_i$ and $\dot{\alpha}_i$:

$$\vec{\omega}_{r/M''_i} \triangleq R_y(\alpha)R_x(\lambda)\vec{\Omega}_i + \frac{d\lambda}{dt}(R_y(\alpha)\vec{\lambda}_i) + \frac{d\alpha}{dt}(\vec{\alpha}_i) \in \mathcal{F}^{M''_i} \quad (3.80a)$$

$$= R_y(\alpha)R_x(\lambda)\vec{\Omega}_i + R_y(\alpha)\dot{\vec{\lambda}}_i + \dot{\vec{\alpha}}_i \quad (3.80b)$$

$$\rightarrow \vec{\omega}_{r/M''_i} = \vec{\Omega}''_i + \dot{\vec{\lambda}}'_i + \dot{\vec{\alpha}}_i \quad (3.80c)$$

Where $\vec{\Omega}''_i$ and $\dot{\vec{\lambda}}'_i$ are respectively propeller and inner servo velocities transformed to the frame $\mathcal{F}^{M''_i}$. Next, the inner ring has an angular velocity $\vec{\omega}_{M_i/M''_i}$ relative to the intermediate frame $\mathcal{F}^{M''_i}$ from the two servo rates $\dot{\lambda}_i$ and $\dot{\alpha}_i$:

$$\vec{\omega}_{M_i/M''_i} \triangleq \frac{d\lambda}{dt}(R_y(\alpha)\vec{\lambda}_i) + \frac{d\alpha}{dt}(\vec{\alpha}_i) \in \mathcal{F}^{M''_i} \quad (3.81a)$$

$$= R_y(\alpha)\dot{\vec{\lambda}}_i + \dot{\vec{\alpha}}_i = \dot{\vec{\lambda}}'_i + \dot{\vec{\alpha}}_i \quad (3.81b)$$

Finally the middle ring has an angular velocity $\vec{\omega}_{M'_i/M''_i}$ relative to the intermediary frame only as a result of $\dot{\alpha}_i$:

$$\vec{\omega}_{M'_i/M''_i} \triangleq \frac{d\alpha}{dt}(\vec{\alpha}_i) = \dot{\vec{\alpha}}_i \in \mathcal{F}^{M''_i} \quad (3.82)$$

Using the relative path co-ordinate $\vec{v}(t)$, the Lagrangian $\mathcal{L}_{M''_i}$ can be constructed for the combined motor module relative to the frame $\mathcal{F}^{M''_i}$ with kinetic energies of the rotor assembly, inner and middle ring structures respectively:

$$\mathcal{L}_{M''_i} = \frac{1}{2}\vec{\omega}_{r/M''_i}^T(J''_r)\vec{\omega}_{r/M''_i} + \frac{1}{2}\vec{\omega}_{M_i/M''_i}^T(J''_{ir})\vec{\omega}_{M_i/M''_i} + \frac{1}{2}\vec{\omega}_{M'_i/M''_i}^T(J'_m)\vec{\omega}_{M'_i/M''_i} \quad (3.83)$$

Where Eq:3.83 again does not include any potential gravitational energies as such quantities were already accounted for in Eq:2.34d. The Lagrangian from Eq:3.83 therefore expands to:

$$\begin{aligned} \therefore \mathcal{L}_{M''_i} = & \frac{1}{2} \left[R_y(\alpha)R_x(\lambda)\vec{\Omega}_i + R_y(\alpha)\dot{\vec{\lambda}}_i + \dot{\vec{\alpha}}_i \right]^T (J''_r) \left[R_y(\alpha)R_x(\lambda)\vec{\Omega}_i + R_y(\alpha)\dot{\vec{\lambda}}_i + \dot{\vec{\alpha}}_i \right] \\ & + \frac{1}{2} \left[R_y(\alpha)\dot{\vec{\lambda}}_i + \dot{\vec{\alpha}}_i \right]^T (J''_{ir}) \left[R_y(\alpha)\dot{\vec{\lambda}}_i + \dot{\vec{\alpha}}_i \right] + \frac{1}{2} \dot{\vec{\alpha}}_i^T (J'_m) \dot{\vec{\alpha}}_i \end{aligned} \quad (3.84)$$

Again, justifying the rotation matrix linearization using Eq:3.68; matrices J''_r , J''_{ir} and J'_m are all instantaneous transformed inertias. The Euler-Lagrange formulation then simplifies, with the partial derivative $\partial\mathcal{L}_{M''_i}/\partial\vec{v} \approx 0$. So the generalized forces $\vec{V}(\alpha, \lambda)$ are:

$$\vec{V}(\alpha, \lambda) = \frac{d}{dt} \left(\frac{\partial\mathcal{L}_{M''_i}}{\partial\dot{\vec{v}}} \right) - \frac{\partial\mathcal{L}_{M''_i}}{\partial\vec{v}} \approx \frac{d}{dt} \left(\frac{\partial\mathcal{L}_{M''_i}}{\partial\dot{\vec{v}}} \right) \in \mathcal{F}^{M''_i} \quad (3.85)$$

Finding the partial derivative of the Lagrangian $\mathcal{L}_{M''_i}$ in Eq:3.84 with respect to $\dot{\vec{v}}$ yields:

$$\frac{\partial \mathcal{L}_{M''_i}}{\partial \dot{\vec{v}}} = (J''_r) [\vec{\Omega}''_i + \dot{\vec{\lambda}}'_i + \dot{\vec{\alpha}}_i] + (J''_{ir}) [\dot{\vec{\lambda}}'_i + \dot{\vec{\alpha}}_i] + (J'_m) \dot{\vec{\alpha}}_i \quad (3.86a)$$

Which, with relative angular velocity definitions from Eq:3.80,3.81 and 3.82, expands to:

$$= (J''_r) [R_y(\alpha) R_x(\lambda) \vec{\Omega}_i + R_y(\alpha) \dot{\vec{\lambda}}_i + \dot{\vec{\alpha}}_i] + (J''_{ir}) [R_y(\alpha) \dot{\vec{\lambda}}_i + \dot{\vec{\alpha}}_i] + (J'_m) \dot{\vec{\alpha}}_i \quad (3.86b)$$

Then taking that parital derivative's time derivative and using inertial rates defined in Eq:3.77b,3.78b and 3.79e; split into product ruled derivative components:

$$\begin{aligned} \rightarrow \vec{V}(\alpha, \lambda) = \frac{d}{dt} \left(\frac{\partial \mathcal{L}_{M''_i}}{\partial \dot{\vec{v}}} \right) &= \left[(J''_r) (\vec{\Omega}''_i + \dot{\vec{\lambda}}'_i + \dot{\vec{\alpha}}_i) \right] \\ &+ \left[(J''_r) \dot{\vec{\Omega}}''_i + \vec{\omega}_{M_i/M''_i} \times (J'_r) \vec{\Omega}''_i + (J''_r) \ddot{\vec{\lambda}}'_i + \vec{\omega}_{M_i/M''_i} \times (J''_r) \dot{\vec{\lambda}}'_i + (J''_r) \ddot{\vec{\alpha}}_i + \vec{\omega}_{M'_i/M''_i} \times (J''_r) \dot{\vec{\alpha}}_i \right] \\ &+ \left[(J''_{ir}) (\dot{\vec{\lambda}}'_i + \dot{\vec{\alpha}}_i) \right] + \left[(J''_{ir}) \ddot{\vec{\lambda}}'_i + \vec{\omega}_{M_i/M''_i} \times (J''_{ir}) \dot{\vec{\lambda}}'_i + (J''_{ir}) \ddot{\vec{\alpha}}_i + \vec{\omega}_{M'_i/M''_i} \times (J''_{ir}) \dot{\vec{\alpha}}_i \right] \\ &+ \left[(J'_m) \dot{\vec{\alpha}}_i \right] + \left[(J'_m) \ddot{\vec{\alpha}}_i + \vec{\omega}_{M'_i/M''_i} \times (J'_m) \dot{\vec{\alpha}}_i \right] \end{aligned} \quad (3.86c)$$

With relative frame angular velocities; $\vec{\omega}_{M_i/M''_i}$ of the inner ring relative to the intermediate frame, and $\vec{\omega}_{M'_i/M''_i}$ of the middle ring relative to the intermediate frame. Both are defined respectively as:

$$\vec{\omega}_{M_i/M''_i} \triangleq R_y(\alpha) \dot{\vec{\lambda}}_i + \dot{\vec{\alpha}}_i = \dot{\vec{\lambda}}'_i + \dot{\vec{\alpha}}_i \in \mathcal{F}^{M''_i} \quad (3.86d)$$

$$\vec{\omega}_{M'_i/M''_i} \triangleq \dot{\vec{\alpha}}_i \in \mathcal{F}^{M''_i} \quad (3.86e)$$

Eq:3.86c is an ominous and decidedly complicated result to try expand and make sense of. However it can be simplified; recognizing that generalized torques in Eq:3.86c contain kinetic energies already introduced in Eq:3.76, but transformed to the frame $\mathcal{F}^{M''_i}$. After some mathematics, Eq:3.86c can be simplified with responses pertinent to $\Delta\alpha_i$ and then the transformed generalized force response $R_y(\alpha)\hat{\tau}_\lambda$:

$$\begin{aligned} \vec{V}(\alpha, \lambda) = R_y(\alpha) \frac{d}{dt} \left(\frac{\partial \mathcal{L}_{M'_i}}{\partial \dot{\vec{u}}} \right) &+ \left(R_y(\alpha) (J'_r) R_y^{-1}(\alpha) \right) \dot{\vec{\alpha}} + \left(J''_r - R_y(\alpha) (J'_r) R_y^{-1}(\alpha) \right) (\vec{\Omega}''_i + \dot{\vec{\lambda}}'_i + \dot{\vec{\alpha}}_i) \\ &+ (J''_r) \ddot{\vec{\alpha}}_i + \dot{\vec{\alpha}}_i \times (J''_r) (\vec{\Omega}''_i + \dot{\vec{\lambda}}'_i + \dot{\vec{\alpha}}_i) + \left(R_y(\alpha) (J'_{ir}) R_y^{-1}(\alpha) \right) \dot{\vec{\alpha}} + \left(J''_{ir} - R_y(\alpha) (J'_{ir}) R_y^{-1}(\alpha) \right) (\dot{\vec{\lambda}}'_i + \dot{\vec{\alpha}}_i) \\ &+ (J''_{ir}) \ddot{\vec{\alpha}}_i + \dot{\vec{\alpha}}_i \times (J''_{ir}) (\dot{\vec{\lambda}}'_i + \dot{\vec{\alpha}}_i) + (J'_m) \dot{\vec{\alpha}}_i + (J'_m) \ddot{\vec{\alpha}}_i + \dot{\vec{\alpha}}_i \times (J'_m) \dot{\vec{\alpha}}_i \end{aligned} \quad (3.86f)$$

Paying special attention to differentiate J''_r and J''_{ir} from Eq:3.77b and Eq:3.78b respectively with $R_y(\alpha)(J'_r)R_y^{-1}(\alpha)$ and $R_y(\alpha)(J'_{ir})R_y^{-1}(\alpha)$. Where the latter two terms are inertial rates from Eq:3.72 and Eq:3.73, but transformed to the frame $\mathcal{F}^{M''_i}$.

Generalized torques in Eq:3.86f can be further simplified by introducing combined inertial bodies $J_n = J_r + J_{ir}$ for the *entire* inner ring, from Eq:2.20, and $J_p = J_m + R_x(\lambda)(J_n)R_x^{-1}(\lambda)$ for the *entire* motor module's inertia, from Eq:2.23b. Using $J'_p = R_y(\alpha)(J_p)R_y^{-1}(\alpha)$ and $J'_n = R_y(\alpha)(J_n)R_y^{-1}(\alpha)$ for the net modules inertia and the entire inner ring inertia both respectively aligned with the frame $\mathcal{F}^{M''_i}$:

$$\begin{aligned} \rightarrow \vec{V}(\alpha, \lambda) = R_y(\alpha) \vec{U}(\lambda) &+ \left(R_y(\alpha) (J'_n) R_y(\alpha) \right) \dot{\vec{\alpha}}_i + \left(J'_p - R_y(\alpha) (J_p) R_y^{-1}(\alpha) \right) \dot{\vec{\alpha}}_i \\ &+ \left(J''_n - R_y(\alpha) (J'_n) R_y^{-1}(\alpha) \right) \dot{\vec{\lambda}}'_i + \left(J''_r - R_y(\alpha) (J'_r) R_y^{-1}(\alpha) \right) \vec{\Omega}''_i \\ &+ J'_p \ddot{\vec{\alpha}}_i + \dot{\vec{\alpha}}_i \times \left((J'_p) \dot{\vec{\alpha}}_i + (J''_n) \dot{\vec{\lambda}}'_i + (J''_r) \vec{\Omega}''_i \right) \end{aligned} \quad (3.86g)$$

Noting that $\dot{J}_p = \dot{J}'_r + \dot{J}'_{ir} + \dot{J}_m$ and that $\dot{J}_m = 0$, it follows that $\dot{J}_p = \dot{J}'_n$. Isolating the servo's torque response from $\Delta\alpha$, and again grouping inertial bodies with shared angular velocities together. The *inertial rates*, second order *inertial* and first order *gyroscopic* responses are then:

$$\begin{aligned}\hat{\tau}_\alpha(\lambda) = & \underbrace{\left(\dot{J}'_p \dot{\alpha}_i + \left(J''_n - R_y(\alpha)(\dot{J}'_n)R_y^{-1}(\alpha) \right) \dot{\lambda}'_i + \left(J''_r - R_y(\alpha)(\dot{J}'_r)R_y^{-1}(\alpha) \right) \dot{\Omega}''_i \right)}_{\text{Inertial rates}} \\ & + \underbrace{\left(J'_p \ddot{\alpha}_i + \dot{\alpha}_i \times \left((J'_p) \dot{\alpha}_i + (J''_n) \dot{\lambda}'_i + (J''_r) \dot{\Omega}''_i \right) \right)}_{\text{Inertial}} \quad \underbrace{\left((J'_p) \dot{\alpha}_i + (J''_n) \dot{\lambda}'_i + (J''_r) \dot{\Omega}''_i \right)}_{\text{Gyroscopic}} \quad \in \mathcal{F}^{M''_i} \quad (3.87)\end{aligned}$$

The servo response $\hat{\tau}_\alpha(\lambda)$ as a function of the inner ring's servo position is *not* the same as the generalized torque $\vec{V}(\alpha, \lambda)$ described in Eq:3.86g. The latter contains terms for the inner ring's servo response. Careful inspection could have yielded the inertial and gyroscopic components of both Eq:3.76 and Eq:3.87, however the effect of inertial rates on the torque system is a far less obvious result. The assumption in Eq:3.68 that rotated inertias can be linearized is shown to hold true next in Sec:3.3.2 where simulations and physical tests corroborate the above models.

Both servo's respective induced torques, $\vec{\tau}_\lambda$ and $\vec{\tau}_\alpha(\lambda_i)$, occur in sequential gimbal-like frames. The opposing negative responses to induced relative rotations effect the angular state dynamics in Eq:3.10d, and must be transformed to the common body frame:

$$\hat{\tau}_Q(u) = - \sum_{i=1}^4 \left(R_z(\sigma_i) R_y(\alpha_i) \hat{\tau}_\lambda + R_z(\sigma_i) \hat{\tau}_\alpha(\lambda_i) \right) \quad [\text{N.m}], \quad \in \mathcal{F}^b \quad (3.88a)$$

$$= - \sum_{i=1}^4 R_z(\sigma_i) \vec{V}(\alpha_i, \lambda_i) \quad (3.88b)$$

The final non-trivial torque term associated with the multibody motion which must be accounted for is the entire system's response to motion relative to the inertial frame \mathcal{F}^I . Specifically considering the responses relative rotations λ_i and α_i have to the net angular velocity of the entire multibody system $\vec{\omega}_b$. Such responses are an extension of the fundamental rigid 6-DOF differential equation for angular motion, reiterated from Eq:3.62:

$$\dot{\vec{\omega}}_b = (J_b^{-1}) \left(-\vec{\omega}_b \times (J_b) \vec{\omega}_b + \vec{\tau}_{net} \right) \quad [\text{rad.s}^{-s}], \quad \in \mathcal{F}^b \quad (3.89)$$

Before continuing with a Lagrangian formulation applied to the entire multibody system; it is worth first establishing a Lemma to add some clarity to the steps which follow. Consider the hypothetical, non-inertial, 2-D system illustrated in Fig:3.13.

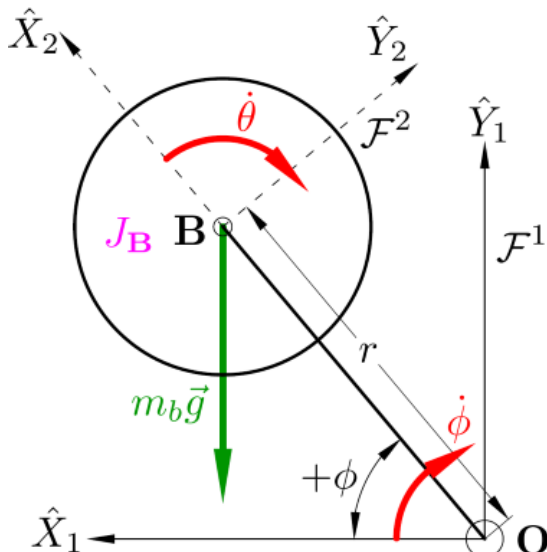


Figure 3.13: Rotating system

A massless rod of length r connects some rotational body, with a mass m_b , at point \mathbf{B} to a center pivot point \mathbf{O} . The principle frame \mathcal{F}^1 has axes \hat{X}_1 and \hat{Y}_1 as illustrated. The arm has a rotational velocity $\dot{\phi}$ relative to \hat{X}_1 in \mathcal{F}^1 , applied by some "motor". Attached to the end of the rod is a secondary frame \mathcal{F}^2 with an \hat{X}_2 axis co-linear to the rod and a perpendicular \hat{Y}_2 . The rotational body, centered at point \mathbf{B} , has a rotational inertia J_B about the point (or axis) at \mathbf{B} . That rotating body has a rotational velocity $\dot{\theta}$ from another "motor" relative to \mathcal{F}^2 . The question is then how to find the net torque applied to the system about point \mathbf{O} in terms of angular velocities $\dot{\phi}$ and $\dot{\theta}$ and their derivatives (or accelerations)?

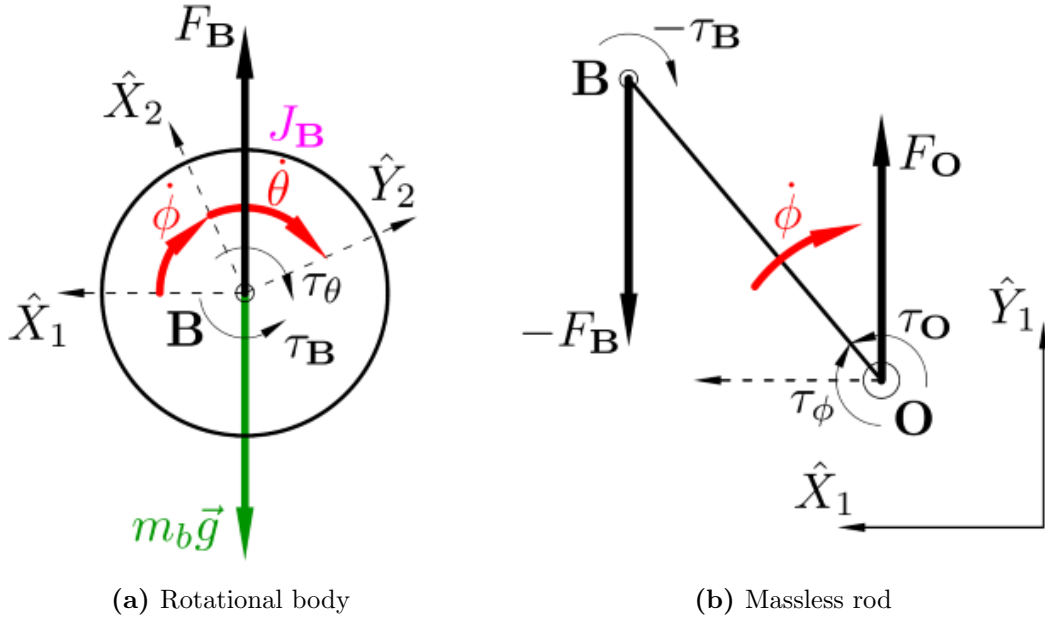


Figure 3.14: Free-body diagram for rotational system

Isolated free body diagrams for each body under consideration are illustrated in Fig:3.14. Considering the rotational body only, Fig:3.14a, the torque acting about point \mathbf{B} is simply an inertial response to combined angular accelerations of $\ddot{\theta}$ and $\ddot{\alpha}$:

$$\tau_B = -\tau_\theta = -J_B(\ddot{\theta} + \ddot{\phi}) \quad (3.90)$$

The net force acting on the rotational body is purely the gravitational force acting through point \mathbf{B} as a result of the mass m_b and some gravitational force vector $\vec{g} \in \mathcal{F}^2$:

$$F_B = -G = -m_b \vec{g} \quad (3.91)$$

That torque and force pair, F_B and τ_B , are transferred to the massless rod connecting point \mathbf{B} to \mathbf{O} , Fig:3.14b. The net torque acting around point \mathbf{O} is then comprised of three components; inferred torque from τ_B , a torque arm from force F_B and an inertial torque response to the effective "point-mass" at point \mathbf{B} relative to \mathbf{O} :

$$\tau_O = -\tau_\phi = -\tau_B - F_B r \cos \phi + m_b r^2 (\ddot{\phi}) \quad (3.92)$$

The net response force acting at point \mathbf{O} , F_O , is of no consequence to the calculation of net torques. The "motor" applies a torque τ_ϕ to the rod to induce some angular acceleration $\dot{\phi}$ on the whole system. Opposed to that angular acceleration is the torque τ_O which acts against that rotation. The torque τ_ϕ acting on the system can then be simplified:

$$\tau_\phi = J_B(\ddot{\theta} + \ddot{\phi}) + m_b r^2 (\ddot{\phi}) - m_b \vec{g} r \cos \phi \quad (3.93)$$

That result would not be as obvious when inferred from an energy equation. The equivalent Lagrangian for net kinetic and potential energy of the system, T and U respectively, would be:

$$\mathcal{L} = T(\theta, \phi) - U(\theta, \phi) \quad (3.94a)$$

$$\mathcal{L} = \frac{1}{2}\vec{\omega}_{\mathbf{B}}^T(J_{\mathbf{B}})\vec{\omega}_{\mathbf{B}} + \frac{1}{2}\vec{\omega}_{\mathbf{O}}^T(J_{\mathbf{O}})\vec{\omega}_{\mathbf{O}} - m_b\vec{g}r \sin \phi \quad (3.94b)$$

Where $\vec{\omega}_{\mathbf{B}}$ and $\vec{\omega}_{\mathbf{O}}$ are net angular velocities of the rotational body and massless connection rod respectively. The important thing to consider is that $J_{\mathbf{O}}$, the net rotational inertia about the point \mathbf{O} , is simply the point mass inertia $m_b r^2$ and NOT the expected parallel axis theorem $J_{\mathbf{O}} \neq J'_{\mathbf{B}} = J_{\mathbf{B}} + m_b r^2$. Expanding Eq:3.94b and applying the Euler-Lagrange formulation yields:

$$\rightarrow \mathcal{L} = \frac{1}{2}(\dot{\theta} + \dot{\phi})^T (J_{\mathbf{B}})(\dot{\theta} + \dot{\phi}) + (\dot{\phi})(m_b r^2)(\dot{\phi}) - m_b(-g)r \sin \phi \quad (3.94c)$$

$$\therefore \text{Generalized forces} = \frac{d}{dt}\left(\frac{\partial \mathcal{L}}{\partial \dot{\phi}}\right) - \frac{\partial \mathcal{L}}{\partial \phi} = \vec{\tau}_{\phi} \quad (3.94d)$$

$$= \frac{d}{dt}\left((J_{\mathbf{B}})(\dot{\theta} + \dot{\phi}) + (m_b r^2)(\dot{\phi})\right) - m_b g r \cos \phi \quad (3.94e)$$

$$\therefore \tau_{\phi} = J_{\mathbf{B}}(\ddot{\theta} + \ddot{\phi}) + m_b r^2(\ddot{\phi}) - m_b g r \cos \phi \quad (3.94f)$$

$$= J_{\mathbf{B}}\ddot{\theta} + J'_{\mathbf{B}}\ddot{\phi} + \tau_g \quad (3.94g)$$

Where J'_b is the parallel axis inertia and τ_g is the gravitational torque arm contribution. The above then leads to the corollary ascertained from the system in Fig:3.13:

Lemma 3.3.1. *A torque response opposed to angular acceleration of a doubly rotating body can be found as the contribution of the principle rotational inertia about the first axis of rotation with only the first rotational acceleration and a parallel axis inertia about the second rotational axis with the second, independent rotational acceleration.*

Or the same torque can be found as the inertial opposition to net angular acceleration (sum of both rotations) about the first axis and a point mass inertia opposed to the second rotation about its respective axis.

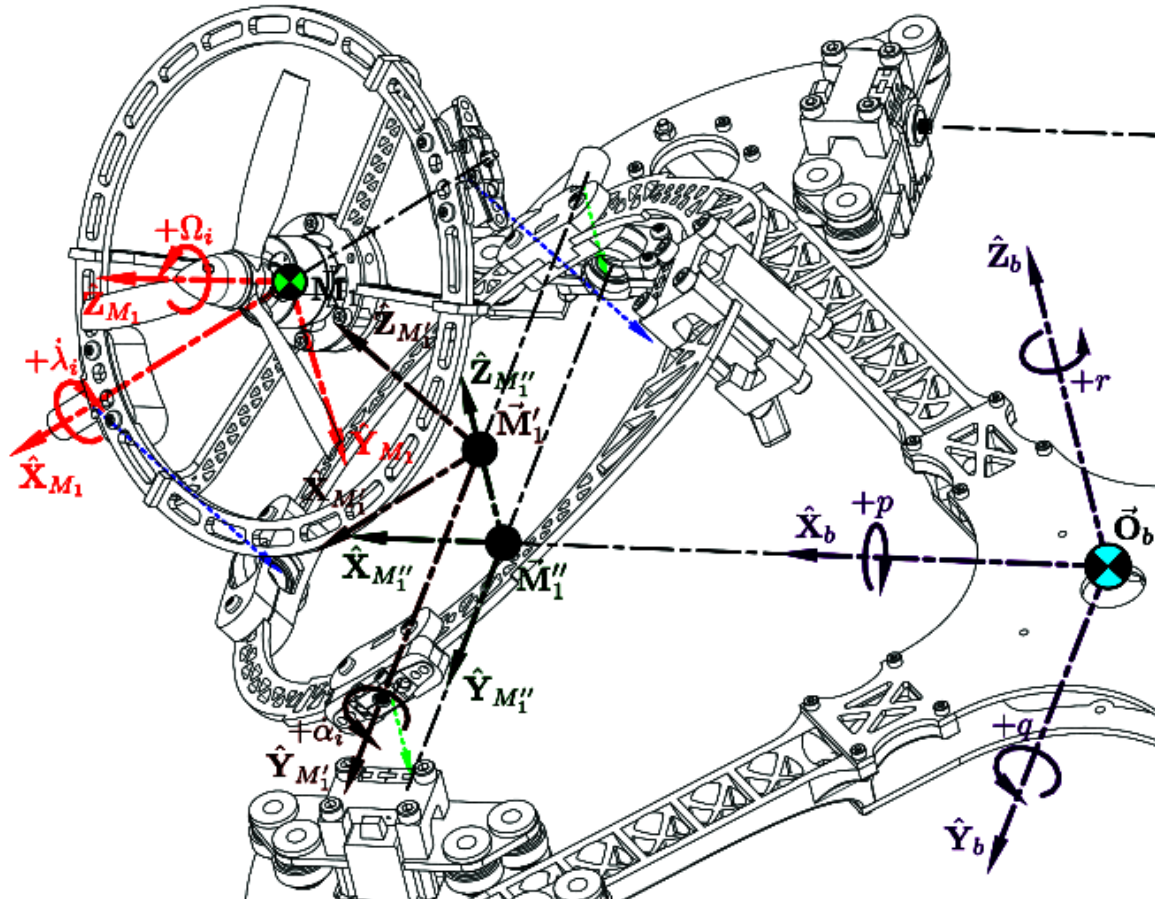


Figure 3.15: Exploded motor module inertial bodies for $\vec{\omega}_b$ response

Returning to the net multibody system and separating the motor module from the entire body structure first (exploded bodies for *motor module 1* in Fig:3.15). Considering only the additional contribution the angular velocity $\vec{\omega}_b$ has on a single motor module and later introducing the entire combined system; the Lagrangian derivation for motion relative to the inertial frame then follows...

The relative $\hat{Z}_{M_i''}$ rotation is what differentiates the intermediate frame $\mathcal{F}^{M_i''}$ (used for calculations pertinent to Fig:3.12) and the body frame \mathcal{F}^b . The now familiar rotor assembly, inner and middle ring structure's inertias from Eq:3.77a,3.78a and 3.79a have respective counterparts aligned with \mathcal{F}^b :

$$J_r''' = R_z(\sigma)(J_r'')R_z^{-1}(\sigma) = R_z(\sigma)R_y(\alpha)R_x(\lambda)(J_r)R_x^{-1}(\lambda)R_y^{-1}(\alpha)R_z^{-1}(\sigma) \quad (3.95a)$$

$$J_{ir}''' = R_z(\sigma)(J_{ir}'')R_z^{-1}(\sigma) = R_z(\sigma)R_y(\alpha)R_x(\lambda)(J_{ir})R_x^{-1}(\lambda)R_y^{-1}(\alpha)R_z^{-1}(\sigma) \quad (3.95b)$$

$$J_m'' = R_z(\sigma)(J_m')R_z^{-1}(\sigma) = R_z(\sigma)R_y(\alpha)(J_m)R_y^{-1}(\alpha)R_z^{-1}(\sigma) \quad (3.95c)$$

Where σ_i in Eq:3.95 is the relative orthogonal $\hat{Z}_{M_i''}$ difference between frames $\mathcal{F}^{M_i''}$ and \mathcal{F}^b defined before in Eq:2.16 and illustrated previously in Fig:2.9. Because σ_i is constant for each $i \in [1 : 4]$, the inertial rate for each component of the motor module is simply transformations of J_r'', J_{ir}'' and J_m' previously in Eq:3.77b,3.78b and 3.79e. Or more generally, for some constant inertia J :

$$\frac{d}{dt}(R_z(\sigma)(J)R_z^{-1}(\sigma)) = 0 \quad (3.96a)$$

So, dropping the σ argument, here $R_z(\sigma) \Rightarrow R_z$ is implied. The rotor, inner and middle inertial rates relative to the body frame \mathcal{F}^b then follow respectively:

$$\dot{J}_r''' = R_z(\dot{J}_r'')R_z^{-1} \quad (3.96b)$$

$$\dot{J}_{ir}''' = R_z(\dot{J}_{ir}'')R_z^{-1} \quad (3.96c)$$

$$\dot{J}_m'' = R_z(\dot{J}_m')R_z^{-1} \quad (3.96d)$$

Similarly, the angular velocities for each separate body (rotor, inner and middle rings) in \mathcal{F}^b but relative to the inertial frame \mathcal{F}^I are then, first for the rotor:

$$\vec{\omega}_{r/I} = \vec{\Omega}_i''' + \dot{\vec{\lambda}}_i'' + \dot{\vec{\alpha}}_i' + \vec{\omega}_{b/I} \quad (3.97a)$$

$$= R_z R_y(\alpha) R_x(\lambda) \vec{\Omega}_i + R_z R_y(\alpha) \dot{\vec{\lambda}}_i + R_z \dot{\vec{\alpha}}_i + \vec{\omega}_b \quad \in \mathcal{F}^b \quad (3.97b)$$

Extending that to the inner ring's rotational velocity:

$$\vec{\omega}_{M_i/I} = \dot{\vec{\lambda}}_i'' + \dot{\vec{\alpha}}_i' + \vec{\omega}_{b/I} \quad (3.98a)$$

$$= R_z R_y(\alpha) \dot{\vec{\lambda}}_i + R_z \dot{\vec{\alpha}}_i + \vec{\omega}_{b/I} \quad \in \mathcal{F}^b \quad (3.98b)$$

And lastly the middle ring structure has a relative angular rate:

$$\vec{\omega}_{M'_p/I} = \dot{\vec{\alpha}}_i' + \vec{\omega}_{b/I} \quad (3.99a)$$

$$= R_z \dot{\vec{\alpha}}_i + \vec{\omega}_b \quad \in \mathcal{F}^b \quad (3.99b)$$

Noting that Lemma:3.3.1 and the parallel axis term in Eq:3.94g refer to the parallel axis difference between the *center of mass* and the resultant rotational axis, the vector difference between the rotated center of mass for a motor module, $C.M'_p$, and the body frame origin \vec{O}_b is defined:

$$C.M'_p = \frac{m_n C.M''_n + m_m C.M'_m}{m_p} \quad (3.100a)$$

With $C.M'_n$ and $C.M'_m$ being rotated inner and middle ring centers of mass respectively from Eq:2.28d and Eq:2.29d:

$$\therefore C.M'_p = \frac{m_n R_z R_y(\alpha) R_x(\lambda) C.M_n + m_m R_z R_y(\alpha) C.M_m}{m_n + m_m} \quad (3.100b)$$

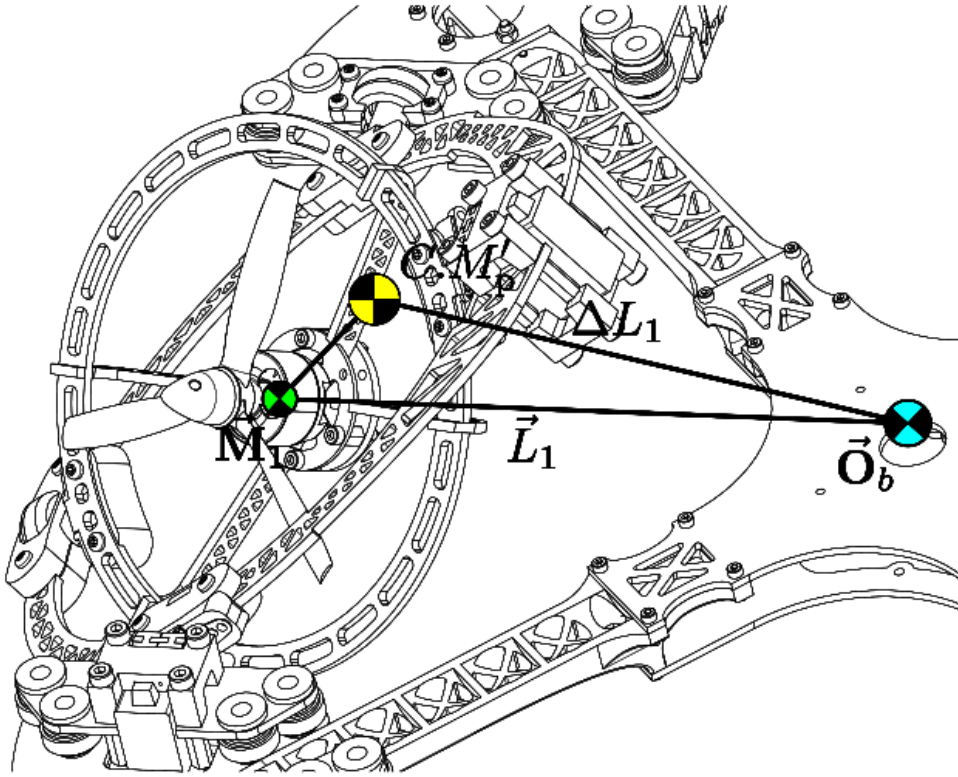


Figure 3.16: Illustration of rotated center of gravity $C.M'_p$

Which leads to the vector difference ΔL_i , with $L = 196.15$ [mm] illustrated for module 1 in Fig:3.16.

$$\Delta L_i = \vec{L}_i + C.M'_p \quad (3.100c)$$

The time derivative of that module's moving center of gravity, $d/dt(C.M'_p)$ relative to the origin \vec{O}_b , is:

$$\Delta \dot{L}_i = \frac{d}{dt}(C.M'_p) \quad (3.100d)$$

$$= \frac{1}{m_p} \left(m_n (R_z([\dot{\alpha}_i] \times R_y(\alpha) R_x(\lambda) C.M_n + R_y(\alpha) [\dot{\lambda}_i] \times R_x(\lambda) C.M_n) + m_m R_z[\dot{\alpha}_i] \times R_y(\alpha) C.M_m) \right) \quad (3.100e)$$

Then, extended from Lemma:3.3.1, the motor module's *point-mass* inertia J_H about the origin \vec{O}_b is defined, with net motor module mass $m_p = m_n + m_m$, using masses m_n and m_m from Eq:2.28a and Eq:2.29a:

$$J_H \triangleq m_p ((\Delta L_i \cdot \Delta L_i) \mathbb{I}_{3 \times 3} - \Delta L_i \otimes \Delta L_i) \quad (3.101a)$$

Or using the inner and outer products matrix definitions:

$$= m_p ([\Delta L_i]^T [\Delta L_i] - [\Delta L_i] [\Delta L_i]^T) \quad (3.101b)$$

Which leads to the that point mass's inertial rate $d/dt(J_H)$:

$$\dot{J}_H = m_p ([\Delta \dot{L}_i]^T [\Delta L_i] + [\Delta L_i]^T [\Delta \dot{L}_i] - [\Delta \dot{L}_i] [\Delta L_i]^T - [\Delta L_i] [\Delta \dot{L}_i]^T) \quad (3.101c)$$

Unfortunately that inertial rate, \dot{J}_H in Eq:3.101c, cannot be simplified further to a more concise form. The Lagrangian \mathcal{L}_{p_i} for the energy of a single motor module about the origin \vec{O}_b can then be constructed. This time, *including* the gravitational potential energy component:

$$\begin{aligned} \mathcal{L}_{p_i} = & \frac{1}{2} \vec{\omega}_{r/I}^T (J''') \vec{\omega}_{r/I} + \frac{1}{2} \vec{\omega}_{M_i/I}^T (J'''_{ir}) \vec{\omega}_{M_i/I} + \frac{1}{2} \vec{\omega}_{M'_i/I}^T (J''_m) \vec{\omega}_{M'_i/I} + \vec{\omega}_{b/I}^T (J_H) \vec{\omega}_{b/I} \\ & + m_p \vec{G}_b \cdot (R_I^b(\eta) \vec{\mathcal{E}} + \Delta L_i) \end{aligned} \quad (3.102)$$

Where the term $m_b \vec{G}_b \cdot (R_I^b(\eta) \vec{\mathcal{E}} + \Delta L_i)$ is the vector analogue of gravitational potential energy mgh with $R_I^b(\eta) \vec{\mathcal{E}}$ being the relative X-Y-Z inertial frame position in the body frame \mathcal{F}^b relative to the body origin $\vec{\mathbf{O}}_b$. Expanding \mathcal{L}_{p_i} with terms defined previously:

$$\begin{aligned} \rightarrow \mathcal{L}_{p_i} = & \left[\vec{\Omega}_i''' + \dot{\vec{\lambda}}_i'' + \dot{\vec{\alpha}}_i' + \vec{\omega}_b \right]^T (J_r''') \left[\vec{\Omega}_i''' + \dot{\vec{\lambda}}_i'' + \dot{\vec{\alpha}}_i + \vec{\omega}_b \right] + \left[\dot{\vec{\lambda}}_i'' + \dot{\vec{\alpha}}_i' + \vec{\omega}_b \right]^T (J_{ir}''') \left[\dot{\vec{\lambda}}_i'' + \dot{\vec{\alpha}}_i' + \vec{\omega}_b \right] \\ & \left[\dot{\vec{\alpha}}_i' + \vec{\omega}_b \right]^T (J_m'') \left[\dot{\vec{\alpha}}_i' + \vec{\omega}_b \right] + \vec{\omega}_b^T (m_p ([\Delta L_i]^T [\Delta L_i] - [\Delta L_i] [\Delta L_i]^T)) \vec{\omega}_b \\ & + m_p \vec{G}_b \cdot (R_I^b(\eta) \vec{\mathcal{E}} + \Delta L_i) \end{aligned} \quad (3.103)$$

Applying partial derivatives of the Lagrangian formulation to \mathcal{L}_{p_i} relative to the angular path coordinates $\vec{\eta}_b$ and $\vec{\omega}_b$ to find generalized forced $\vec{\mathbf{W}}(u \cdot i)$. Recalling $\vec{\eta}_b$ is the angular orientation from Eq:2.12d, defined entirely in the body frame \mathcal{F}^b , and similarly assuming that $\partial/\partial \vec{\eta}_b (\Delta L_i) \approx 0$:

$$\frac{d}{dt} \left(\frac{\partial \mathcal{L}_{p_i}}{\partial \dot{\vec{\eta}}_b} \right) - \frac{\partial \mathcal{L}_{p_i}}{\partial \vec{\eta}_b} = \frac{d}{dt} \left(\frac{\partial \mathcal{L}_{p_i}}{\partial \vec{\omega}_b} \right) - \frac{\partial \mathcal{L}_{p_i}}{\partial \vec{\eta}_b} = \vec{\mathbf{W}}(u \cdot i) = \hat{\tau}_M \quad (3.104a)$$

$$\begin{aligned} = & \frac{d}{dt} \left((J_r''') \left[\vec{\Omega}_i''' + \dot{\vec{\lambda}}_i'' + \dot{\vec{\alpha}}_i' + \vec{\omega}_b \right] + (J_{ir}''') \left[\dot{\vec{\lambda}}_i'' + \dot{\vec{\alpha}}_i' + \vec{\omega}_b \right] + (J_m'') \left[\dot{\vec{\alpha}}_i' + \vec{\omega}_b \right] + (J_H) \left[\vec{\omega}_b \right] \right) \\ & - m_p \vec{G}_b \times \Delta L_i \end{aligned} \quad (3.104b)$$

Then using inertial rate derivatives from Eq:3.96b-3.96d and \dot{J}_H from Eq:3.101c, and inserting relative angular velocities from Eq:3.97-3.99:

$$\begin{aligned} = & \left[(J_r''') (\vec{\Omega}_i''' + \dot{\vec{\lambda}}_i'' + \dot{\vec{\alpha}}_i' + \vec{\omega}_b) \right] + \left[(J_r''') \dot{\vec{\Omega}}_i''' + \vec{\omega}_{M_i/I} \times (J_r''') \vec{\Omega}_i''' + (J_r''') \ddot{\vec{\lambda}}_i'' + \vec{\omega}_{M_i/I} \times (J_r''') \dot{\vec{\lambda}}_i'' \right. \\ & \left. + (J_r''') \ddot{\vec{\alpha}}_i' + \vec{\omega}_{M'_i/I} \times (J_r''') \dot{\vec{\alpha}}_i' + (J_r''') \dot{\vec{\omega}}_b + \vec{\omega}_{b/I} \times (J_r''') \vec{\omega}_b \right] + \left[(J_{ir}''') (\dot{\vec{\lambda}}_i'' + \dot{\vec{\alpha}}_i' + \vec{\omega}_b) \right] + \left[(J_{ir}''') \ddot{\vec{\lambda}}_i'' \right. \\ & \left. + \vec{\omega}_{M_i/I} \times (J_{ir}''') \dot{\vec{\lambda}}_i'' + (J_{ir}''') \ddot{\vec{\alpha}}_i' + \vec{\omega}_{M'_i/I} \times (J_{ir}''') \dot{\vec{\alpha}}_i' + (J_{ir}''') \dot{\vec{\omega}}_b + \vec{\omega}_{b/I} \times (J_{ir}''') \vec{\omega}_b \right] + \left[(J_m'') (\dot{\vec{\alpha}}_i' + \vec{\omega}_b) \right] \\ & \left[(J_m'') \ddot{\vec{\alpha}}_i' + \vec{\omega}_{M'_i/I} \times (J_m'') \dot{\vec{\alpha}}_i' + (J_m'') \dot{\vec{\omega}}_b + \vec{\omega}_{b/I} \times (J_m'') \vec{\omega}_b \right] + \left[(\dot{J}_H) \vec{\omega}_b \right] + \left[(J_H) \dot{\vec{\omega}}_b + \vec{\omega}_{b/I} \times (J_H) \vec{\omega}_b \right] \\ & - \left[m_p \vec{G}_b \times \Delta L_i \right] \end{aligned} \quad (3.104c)$$

After expanding relative angular velocity terms; $\vec{\omega}_{M_i/I}$, $\vec{\omega}_{M'_i/I}$, $\vec{\omega}_{M''_i/I}$ and $\vec{\omega}_{b/I}$ and applying some mathematics, Eq:3.104c is shown to include a transformed component of Eq:3.86c.

$$\begin{aligned} \rightarrow \frac{d}{dt} \left(\frac{\partial \mathcal{L}_{p_i}}{\partial \vec{\omega}_b} \right) - \frac{\partial \mathcal{L}_{p_i}}{\partial \vec{\eta}_b} = & R_z \frac{d}{dt} \left(\frac{\partial \mathcal{L}_{M_i''}}{\partial \dot{\vec{\omega}}} \right) + (J_r''') \vec{\omega}_b + \vec{\omega}_b \times (J_r''') \vec{\Omega}_i''' + \vec{\omega}_b \times (J_r''') \dot{\vec{\lambda}}_i'' + \vec{\omega}_b \times (J_r''') \dot{\vec{\alpha}}_i' \\ & + \vec{\omega}_b \times (J_r''') \vec{\omega}_b + J_r''' \dot{\vec{\omega}}_b + (J_{ir}''') \vec{\omega}_b + \vec{\omega}_b \times (J_{ir}''') \dot{\vec{\lambda}}_i'' + \vec{\omega}_b \times (J_{ir}''') \dot{\vec{\alpha}}_i' + \vec{\omega}_b \times (J_{ir}''') \vec{\omega}_b + (J_{ir}''') \dot{\vec{\omega}}_b \\ & (J_m'') \vec{\omega}_b + \vec{\omega}_b \times (J_m'') \dot{\vec{\alpha}}_i' + \vec{\omega}_b \times (J_m'') \vec{\omega}_b + (J_m'') \dot{\vec{\omega}}_b + (\dot{J}_H) \vec{\omega}_b + (J_H) \dot{\vec{\omega}}_b + \vec{\omega}_b \times (J_H) \vec{\omega}_b \\ & - m_p \vec{G}_b \times \Delta L_i \end{aligned} \quad (3.104d)$$

Combining inertial bodies with the same angular velocities and introducing terms $\vec{\tau}_\lambda$ and $\vec{\tau}_\alpha$ from Eq:3.76 and Eq:3.87 respectively:

$$\begin{aligned} \therefore \vec{\mathbf{W}}(u_i) = \hat{\tau}_M = & R_z \hat{\tau}_\alpha(\lambda) + R_z R_y(\alpha) \hat{\tau}_\lambda + (J_r'''' + J_{ir}'''' + J_m'' + J_H) \vec{\omega}_b + (J_r'''' + J_{ir}'''' + J_m'' + J_H) \dot{\vec{\omega}}_b \\ & + \vec{\omega}_b \times (J_r'''' + J_{ir}'''' + J_m'' + J_H) \vec{\omega}_b + \vec{\omega}_b \times \left((J_r''') (\vec{\Omega}_i''' + \dot{\vec{\lambda}}_i'' + \dot{\vec{\alpha}}_i') + (J_{ir}''') (\dot{\vec{\lambda}}_i'' + \dot{\vec{\alpha}}_i') + (J_m'') (\dot{\vec{\alpha}}_i') \right) \\ & - m_p \vec{G}_b \times \Delta L_i \end{aligned} \quad (3.104e)$$

And recognizing that $(J_r'''' + J_{ir}'''' + J_m'' + J_H)$ can be simplified to a parallel axis translation of the transformed net motor module inertia J'_p from Eq:2.23b; analogous to the net motor module inertia defined in Eq:2.26b:

$$\begin{aligned} (J_r'''' + J_{ir}'''' + J_m'' + J_H) \triangleq & R_z R_y(\alpha) R_x(\lambda) (J_r) R_x^{-1}(\lambda) R_y^{-1}(\alpha) R_z^{-1} \\ & + R_z R_y(\alpha) R_x(\lambda) (J_{ir}) R_x^{-1}(\lambda) R_y^{-1}(\alpha) R_z^{-1} + R_z R_y(\alpha) (J_m) R_y^{-1}(\alpha) R_z^{-1} + J_H \end{aligned} \quad (3.105a)$$

$$= R_z(J_p)R_z^{-1} + m_p \left([\Delta L_i]^T [\Delta L_i] - [\Delta L_i][\Delta L_i]^T \right) = J'_{\vec{M}_i} \quad (3.105b)$$

Moreover, the above can be applied to the associated inertia rates; $\dot{J}_r''', \dot{J}_{ir}''', \dot{J}_m''$ and \dot{J}_H . Using Eq:3.96b,3.96c,3.96d and 3.101c it can be shown that:

$$(\dot{J}_r''' + \dot{J}_{ir}''' + \dot{J}_m'' + \dot{J}_H) = \dot{J}'_{\vec{M}_i} \quad (3.105c)$$

The generalized torque acting on a single motor module, $\hat{\tau}_M$ from Eq:3.104e, is then found as combinations of responses to servos λ_i and α_i , the changing inertial rates $\dot{J}'_{\vec{M}_i}$ as a result of those rotations and finally the net response to the entire frames angular velocity $\vec{\omega}_b$.

$$\begin{aligned} \hat{\tau}_M = & R_z \hat{\tau}_\alpha(\lambda) + R_z R_y(\alpha) \hat{\tau}_\lambda + (J'_{\vec{M}_i}) \vec{\omega}_b + (J'_{\vec{M}_i}) \dot{\vec{\omega}}_b + \vec{\omega}_b \times (J'_{\vec{M}_i}) \vec{\omega}_b \\ & + \vec{\omega}_b \times ((J''_p) \dot{\alpha}'_i + (J'''_n) \dot{\lambda}''_i + (J'''_r) \vec{\Omega}'''_i) - m_p \vec{G}_b \times \Delta L_i \triangleq \vec{W}(u \cdot i) \in \mathcal{F}^b \end{aligned} \quad (3.106)$$

Considering the rigid body torque response $\vec{\tau}_y$ for the body structure's motion, J_y . That structure's inertia J_y is a constant and independent of actuator positions in $u \in \mathbb{U}$; explicitly defined in Eq:2.24d.

$$\hat{\tau}_y = (J_y) \dot{\vec{\omega}}_b + \vec{\omega}_b \times (J_y) \vec{\omega}_b - C.M_y \times m_y \vec{G}_b \in \mathcal{F}^b \quad (3.107)$$

The net response for the *entire* multibody system is then a sum of Eq:3.106 for modules $i \in [1 : 4]$ and $\hat{\tau}_y$ in Eq:3.107. By inspection, without constructing a complete Lagrangian for the entire system, the effective torque, $\hat{\tau}_\mu$, acting on the body frame \mathcal{F}^b is shown to be:

$$\hat{\tau}_\mu = (J_y) \dot{\vec{\omega}}_b + \vec{\omega}_b \times (J_y) \vec{\omega}_b - C.M_y \times m_y \vec{G}_b + \sum_{i=1}^4 \hat{\tau}_M(u \cdot i) \in \mathcal{F}^b \quad (3.108)$$

Recalling the net vehicles rotational inertia $J_b(u)$, calculated as a function of the actuation matrix u , which was defined previously in 2.30a. It follows that Eq:3.108 reduces and expands to:

$$\begin{aligned} \hat{\tau}_\mu = & (J_b(u)) \dot{\vec{\omega}}_b + \vec{\omega}_b \times (J_b(u)) \vec{\omega}_b \\ & + \sum_{i=1}^4 \left[R_z \hat{\tau}_\alpha(\lambda) + R_z R_y(\alpha) \hat{\tau}_\lambda + (J'_{\vec{M}_i}) \vec{\omega}_b + \vec{\omega}_b \times ((J''_p) \dot{\alpha}'_i + (J'''_n) \dot{\lambda}''_i + (J'''_r) \vec{\Omega}'''_i) \right] \\ & - m_p \vec{G}_b \times \sum_{i=1}^4 \Delta L_i \end{aligned} \quad (3.109)$$

The external torque $\hat{\tau}_\mu$ acting on the vehicle is as a result of produced control action by the attitude controller, detailed next in Ch:4. The final sum of gravitational torque contributions can be simplified to $\vec{\tau}_g$ from Eq:2.34d which considers the *net* resultant center of gravity. Then, extending the angular differential equation Eq:3.10d to incorporate the multibody responses derived above:

$$\hat{\tau}_\mu = (J_b) \dot{\vec{\omega}}_b + \vec{\omega}_b \times (J_b) \vec{\omega}_b + \hat{\tau}_b(u) - \vec{\tau}_g \quad (3.110a)$$

Defining a new response torque $\hat{\tau}_b$ which represents collective responses from internal rotations relative each body. It can be considered a non-linear extension of the gyroscopic component of the torque $\vec{\omega}_b \times (J_b) \vec{\omega}_b$ acting on the system. That non-linear body torque is defined then as follows:

$$\hat{\tau}_b(u) \triangleq \dot{J}_b(u) \vec{\omega}_b + \sum_{i=1}^4 \left[R_z \hat{\tau}_\alpha(\lambda_i) + R_z R_y(\alpha_i) \hat{\tau}_\lambda + \vec{\omega}_b \times ((J''_p) \dot{\alpha}'_i + (J'''_n) \dot{\lambda}''_i + (J'''_r) \vec{\Omega}'''_i) \right] \quad (3.110b)$$

And using the net gravitational torque arm $\vec{\tau}_g$ defined earlier in Eq:2.34d:

$$\vec{\tau}_g \triangleq \Delta C.G \times m_b \vec{G}_b \quad (3.110c)$$

Noting that $\dot{J}_b(u)$ is another introduced term which is the sum of all module inertia rates from Eq:3.105c, given that body structures inertia J_y is constant:

$$\dot{J}_b(u) \triangleq \sum_{i=1}^4 (\dot{J}'_{\vec{M}_i}) + J_y = \sum_{i=1}^4 (\dot{J}'_{\vec{M}_i}) \quad (3.111)$$

The torque $\hat{\tau}_b$ from Eq:3.110b is the most important result here however; definitions of $\hat{\tau}_\alpha(\lambda)$ and $\hat{\tau}_\lambda$, in Eq:3.76 and Eq:3.87 respectively, were necessary to simplify and isolate different components of Eq:3.110b. The most complicated process in evaluating Eq:3.110b is calculating inertial rate derivatives at each sampling interval. Finding solutions to Eq:3.71d for each reconfigured inertial body is cumbersome; an alternative is to instead substitute continuous time inertia rates, calculated from angular velocities, with a discrete time approximations.

The difference of instantaneous calculations for $J_b(u)$, $J_p(u \cdot i)$, $J_m(u \cdot i)$ and $J_n(u \cdot i)$, for the net body structure, each net motor module and each body within a motor module respectively, between sample times n and $n - 1$ can be found simply as follows:

$$\Delta \tilde{J}_b(u) \triangleq (J_b(u_n) - J_b(u_{n-1})) / \Delta t \approx \dot{J}_b(u) \quad (3.112)$$

Each inertia has to be calculated at every control loop interval regardless, exploiting that fact will reduce computational overhead. Plots for magnitudes of both *true* torque response $\|\hat{\tau}\|_b$, and the discrete approximation $\|\tilde{\tau}\|_b$ which uses exclusively discrete inertia rates are shown in Fig:3.17. Both responses were calculated over a typical flight envelope which tracks an orbital trajectory, the focus here is on the quality of approximation proposed. The error between the approximated torque $\|\tilde{\tau}\|_b$ and the full complexity body torque $\|\hat{\tau}\|_b$ is similarly shown in Fig:3.18.

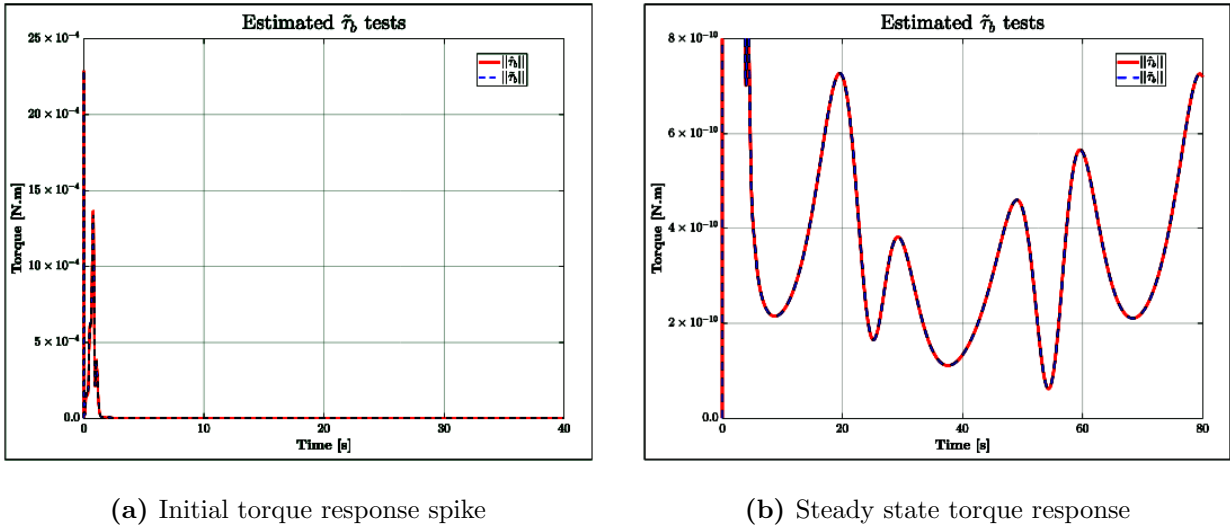
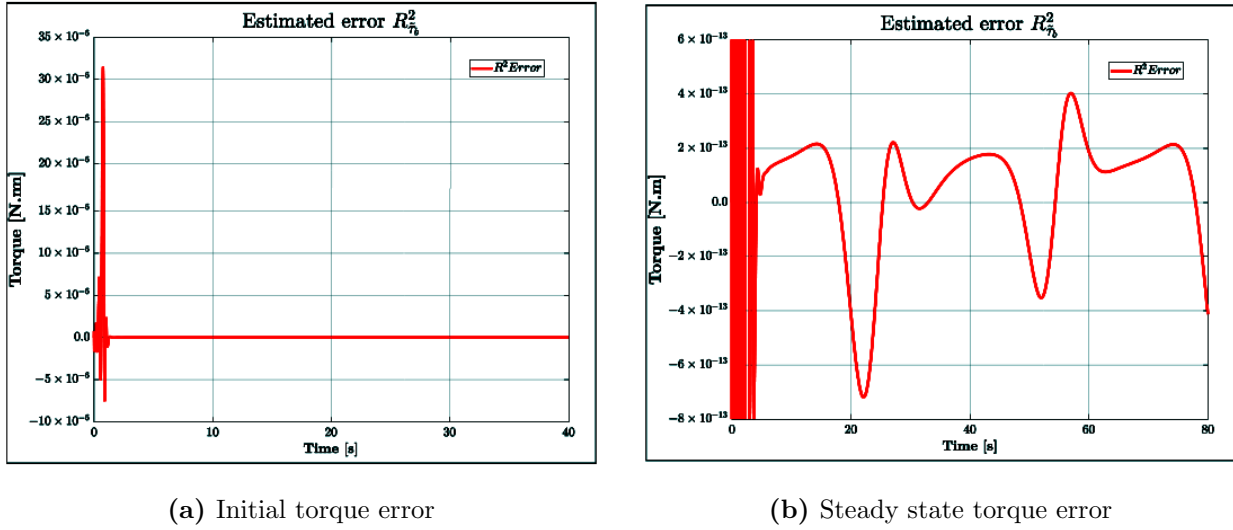


Figure 3.17: Approximated and true body torque responses

Sample rates of 100 [Hz] were used to evaluate the instantaneous inertia values throughout the trajectory. Initial torques spike from time $t_0 \rightarrow t_2$ [s] occurs as the vehicle first tracks the attitude trajectory from starting conditions, with an attitude centered at the origin (shown in Fig:3.17a). Once the vehicle settles to tracking the trajectory, the induced torque dramatically reduces (Fig:3.17b). The plot for $\|\tilde{\tau}_b\|$ uses discrete time derivatives as per Eq:3.112.

Fig:3.18 shows the error between $\|\hat{\tau}_b\|$ and approximated $\|\tilde{\tau}_b\|$. Again the initial spike is from starting configuration changes, thereafter the error reduces dramatically. On average the approximation asserted in Eq:3.112 is a reasonable one with an error typically three orders of magnitude smaller than the signal it represents, or $\times 10^{-3}$ [Nm] less than the estimated $\hat{\tau}_b$. The transfer block for the dynamics in simulation still make use of a continuous time derivative model whilst plant dependent controller compensation uses a reduced complexity approximation...

**Figure 3.18:** Approximated and true body torque responses

Any measurement or modeling errors associated with the above inertial response models and their explicit values presented in Sec:2.3 can easily be compensated for as plant disturbances. More specifically errors in the above system are modeled as plant dependent state uncertainties; and could be adaptively compensated for accordingly.

3.3.2 Simulation and verification of induced model

Linearization simulation and comparison

Previously, in Sec:3.3.1, the proposed Lagrangian energy functions for both $\Delta\lambda_i$ and $\Delta\alpha_i$ servo rotations and their response to body angular velocities $\vec{\omega}_b$ were derived. Reiterating those energy equations; the inner ring net (kinetic) energy Lagrangian from Eq:3.66 is:

$$\mathcal{L}_{M'_i} = \frac{1}{2} \vec{\omega}_{r/M'_i}^T (J'_r) \vec{\omega}_{r/M'_i} + \frac{1}{2} \vec{\omega}_{M_i/M'_i}^T (J'_{ir}) \vec{\omega}_{M_i/M'_i} \quad (3.113a)$$

$$= \frac{1}{2} \left(R_x(\lambda) \vec{\Omega}_i + \dot{\vec{\lambda}}_i \right)^T \left(R_x(\lambda) (J_r) R_x^{-1}(\lambda) \right) \left(R_x(\lambda) \vec{\Omega}_i + \dot{\vec{\lambda}}_i \right) + \frac{1}{2} (\dot{\vec{\lambda}}_i)^T \left(R_x(\lambda) (J_{ir}) R_x^{-1}(\lambda) \right) (\dot{\vec{\lambda}}_i) \quad (3.113b)$$

And similarly for the middle ring's net (kinetic) energy from Eq:3.83:

$$\mathcal{L}_{M''_i} = \frac{1}{2} \vec{\omega}_{r/M''_i}^T (J''_r) \vec{\omega}_{r/M''_i} + \frac{1}{2} \vec{\omega}_{M'_i/M''_i}^T (J''_{ir}) \vec{\omega}_{M'_i/M''_i} + \frac{1}{2} \vec{\omega}_{M'_i/M''_i}^T (J'_m) \vec{\omega}_{M'_i/M''_i} \quad (3.113c)$$

$$\begin{aligned} &= \frac{1}{2} \left(R_y(\alpha) R_x(\lambda) \vec{\Omega}_i + R_y(\alpha) \dot{\vec{\lambda}}_i + \dot{\vec{\lambda}}_i \right)^T \left(R_y(\alpha) (J'_r) R_y^{-1}(\alpha) \right) \left(R_y(\alpha) R_x(\lambda) \vec{\Omega}_i + R_y(\alpha) \dot{\vec{\lambda}}_i + \dot{\vec{\alpha}}_i \right) \\ &\quad \frac{1}{2} \left(R_y(\alpha) \dot{\vec{\lambda}}_i + \dot{\vec{\alpha}}_i \right)^T \left(R_y(\alpha) (J'_{ir}) R_y^{-1}(\alpha) \right) \left(R_y(\alpha) \dot{\vec{\lambda}}_i + \dot{\vec{\alpha}}_i \right) \\ &\quad + \frac{1}{2} (\dot{\vec{\alpha}}_i)^T \left(R_y(\alpha) (J_m) R_y^{-1}(\alpha) \right) (\dot{\vec{\alpha}}_i) \end{aligned} \quad (3.113d)$$

Solving for the generalized forces acting on each system requires application of Euler-Lagrange formulation, using partial derivatives relative to generalized path co-ordinates. Both the inner and middle ring systems were defined with relative co-ordinate paths for the angular servo position $\vec{u} = [\lambda_i \ 0 \ 0]^T$ and $\vec{v} = [0 \ \alpha_i \ 0]^T$ respectively. The generalized forces for both systems are then, using the Euler-Lagrange formulation:

$$\underbrace{\frac{d}{dt} \left(\frac{\partial \mathcal{L}_{M'_i}}{\partial \dot{\vec{u}}} \right) - \frac{\partial \mathcal{L}_{M'_i}}{\partial \vec{u}}}_{\text{Inner ring}} = \vec{U}(\lambda_i) \quad \text{and} \quad \underbrace{\frac{d}{dt} \left(\frac{\partial \mathcal{L}_{M''_i}}{\partial \dot{\vec{v}}} \right) - \frac{\partial \mathcal{L}_{M''_i}}{\partial \vec{v}}}_{\text{Middle ring}} = \vec{V}(\alpha_i, \lambda_i) \quad (3.114)$$

The assumption proposed in Eq:3.68, presented in [9], is used to linearize and reduce partial derivatives of the respective inner and middle ring Lagrangians in Eq:3.114. Those simplifications are such that both terms in Eq:3.114 respectively simplify to:

$$\frac{d}{dt} \left(\frac{\partial \mathcal{L}_{M'_i}}{\partial \dot{\vec{u}}} \right) = \vec{U}(\lambda_i) \Big|_{(\partial \mathcal{L}_{M'_i}/\partial \vec{u}) \approx 0} \quad \text{and} \quad \frac{d}{dt} \left(\frac{\partial \mathcal{L}_{M''_i}}{\partial \dot{\vec{v}}} \right) = \vec{V}(\alpha_i, \lambda_i) \Big|_{(\partial \mathcal{L}_{M''_i}/\partial \vec{v}) \approx 0} \quad (3.115)$$

Considering first the case of the inner ring Lagrangian $\mathcal{L}_{M'_i}$ from Eq:3.113b; the partial derivative taken with respect to path variable $\vec{u} = \vec{\lambda}_i$ was simplified:

$$\frac{\partial \mathcal{L}_{M'_i}}{\partial \vec{u}} = \frac{\partial}{\partial \vec{\lambda}_i} (\mathcal{L}_{M'_i}) \approx 0 \quad (3.116)$$

Expanding Eq:3.116 and finding the partial derivative of that Lagrangian, $\mathcal{L}_{M'_i}$ in Eq:3.113b, with respect to $\vec{u} = \vec{\lambda}_i$ yields:

$$\begin{aligned} \frac{\partial \mathcal{L}_{M'_i}}{\partial \vec{\lambda}_i} = & \frac{1}{2} \left(\frac{\partial}{\partial \vec{\lambda}_i} \left(R_x(\lambda) \vec{\Omega}_i \right) \right)^T \left(R_x(\lambda) (J_r) R_x^{-1}(\lambda) \right) \left(R_x(\lambda) \vec{\Omega}_i + \dot{\vec{\lambda}}_i \right) \\ & + \frac{1}{2} \left(R_x(\lambda) \vec{\Omega}_i + \dot{\vec{\lambda}}_i \right)^T \left(\frac{\partial}{\partial \vec{\lambda}_i} \left(R_x(\lambda) (J_r) R_x^{-1}(\lambda) \right) \right) \left(R_x(\lambda) \vec{\Omega}_i + \dot{\vec{\lambda}}_i \right) \\ & + \frac{1}{2} \left(R_x(\lambda) \vec{\Omega}_i + \dot{\vec{\lambda}}_i \right)^T \left(R_x(\lambda) (J_r) R_x^{-1}(\lambda) \right) \left(\frac{\partial}{\partial \vec{\lambda}_i} \left(R_x(\lambda) \vec{\Omega}_i \right) \right) \\ & + \frac{1}{2} \left(\dot{\vec{\lambda}}_i \right)^T \left(\frac{\partial}{\partial \vec{\lambda}_i} \left(R_x(\lambda) (J_r) R_x^{-1}(\lambda) \right) \right) \left(\dot{\vec{\lambda}}_i \right) \end{aligned} \quad (3.117)$$

Testing that assumption, presented in Eq:3.68; the partial derivative components of Eq:3.117 are explicitly calculated. First, considering the rotor's transformed inertia $J'_r = R_x(\lambda) (J_r) R_x^{-1}(\lambda)$ with a partial derivative as per the differential product rule:

$$\frac{\partial}{\partial \vec{u}} J'_r = \frac{\partial}{\partial \vec{\lambda}_i} \left(R_x(\lambda) (J_r) R_x^{-1}(\lambda) \right) \quad (3.118a)$$

$$= \frac{\partial}{\partial \vec{\lambda}_i} \left(R_x(\lambda) \right) (J_r) R_x^{-1}(\lambda) + R_x(\lambda) (J_r) \frac{\partial}{\partial \vec{\lambda}_i} \left(R_x^{-1}(\lambda) \right) \quad (3.118b)$$

Similarly for the inner ring transformed inertia's contribution, $J'_{ir} = R_x(\lambda) (J_{ir}) R_x^{-1}(\lambda)$ from Eq:3.113b, however, *without* including the rotor body's inertia:

$$\frac{\partial}{\partial \vec{u}} J'_{ir} = \frac{\partial}{\partial \vec{\lambda}_i} \left(R_x(\lambda) \right) (J_{ir}) R_x^{-1}(\lambda) + R_x(\lambda) (J_{ir}) \frac{\partial}{\partial \vec{\lambda}_i} \left(R_x^{-1}(\lambda) \right) \quad (3.118c)$$

The final partial derivative to take note of is that for the rotor's angular velocity $\vec{\Omega}_i$, in [rad.s⁻¹], but transformed to the inner ring frame $\mathcal{F}^{M'_i}$ which the Lagrangian in Eq:3.113a is taken with respect to:

$$\frac{\partial}{\partial \vec{\lambda}_i} \left(R_x(\lambda) \vec{\Omega}_i \right) \quad (3.118d)$$

The application of the rotation matrix linearization, from Eq:3.68, to the partial derivative rotations in Eq:3.118b-3.118d is:

$$R_x(\bar{\lambda}_i + \partial \lambda_i) \approx \left(1 - [\Phi_x(\bar{\lambda}_i) \partial \lambda_i]_{\times} \right) R_x(\bar{\lambda}_i) \quad (3.119a)$$

Where $\Phi_x(\bar{\lambda}_i)$ is simply the partial derivative of the Euler matrix, $\Phi(\eta)$ from Eq:2.12h, with respect to an \hat{X} axis rotation. That being:

$$\Phi_x(\bar{\lambda}_i) = \begin{bmatrix} 0 & 0 & 0 \\ 0 & \sin \bar{\lambda}_i & \cos \bar{\lambda}_i \\ 0 & -\cos \bar{\lambda}_i & \sin \bar{\lambda}_i \end{bmatrix} \quad (3.119b)$$

So then, for some nominal angle $\bar{\lambda}_i$ perturbed by some small deviation $\partial\lambda_i$, Eq:3.119a expands to:

$$\therefore R_x(\bar{\lambda}_i + \partial\lambda_i) \approx R_x(\bar{\lambda}_i) - \begin{bmatrix} 0 & 0 \\ 0 & (c^2\bar{\lambda}_i - s^2\bar{\lambda}_i) \\ 0 & (s\bar{\lambda}_i c\bar{\lambda}_i + c\bar{\lambda}_i s\bar{\lambda}_i) \end{bmatrix} \begin{bmatrix} 0 \\ (-c\bar{\lambda}_i s\bar{\lambda}_i - s\bar{\lambda}_i c\bar{\lambda}_i) \\ (c^2\bar{\lambda}_i - s^2\bar{\lambda}_i) \end{bmatrix} \partial\lambda_i \quad (3.119c)$$

Which, obviously, when the perturbations $\partial\lambda_i$ away from a nominal $\bar{\lambda}_i$ are small, it follows that:

$$\rightarrow R_x(\bar{\lambda}_i + \partial\lambda_i) \approx R_x(\bar{\lambda}_i) \Big|_{\partial\lambda_i \ll 1} \quad (3.119d)$$

That simplification then applies to Eq:3.118b,3.118c and 3.118d, for a small $\partial\lambda_i$:

$$\frac{\partial}{\partial \vec{\lambda}_i} J'_r \approx 0 \quad (3.120a)$$

$$\frac{\partial}{\partial \vec{\lambda}_i} J'_{ir} \approx 0 \quad (3.120b)$$

$$\frac{\partial}{\partial \vec{\lambda}_i} R_x(\lambda) \vec{\Omega}_i \approx 0 \quad (3.120c)$$

It can therefore be said that the assumption in Eq:3.116 is not without merit, or that:

$$\frac{\partial \mathcal{L}_{M'_i}}{\partial \vec{u}} \approx 0 \rightarrow \frac{d}{dt} \left(\frac{\partial \mathcal{L}_{M'_i}}{\partial \dot{\vec{u}}} \right) - \frac{\partial \mathcal{L}_{M'_i}}{\partial \vec{u}} \approx \frac{d}{dt} \left(\frac{\partial \mathcal{L}_{M'_i}}{\partial \dot{\lambda}_i} \right) = \vec{U}(\lambda) = \hat{\tau}_\lambda \quad (3.121)$$

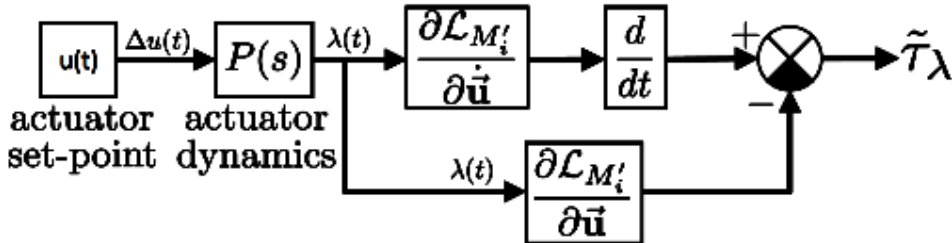


Figure 3.19: Simulink Lagrangian block

A final verification of the suggested simplifications is done with a **Simulink** model, shown in Fig:3.19. The model applies a direct comparison of $\tilde{\tau}_\lambda$, originally from Eq:3.76, both *with* and *without* the rotation matrix linearization. Convention has it that estimated or simulated values are denoted with a hat accent. Therefore a calculated inner ring torque response, *with linearized* partial derivatives as per Eq:3.120, is termed as $\hat{\tau}_\lambda$. The true representation of the induced torque response, $\tilde{\tau}_\lambda$, is calculated from the block model detailed in Fig:3.19. The simulated $\tilde{\tau}_\lambda$ applies no partial derivative simplifications or linearizations, calculating the full inner ring Euler-Lagrange formulation from Eq:3.114.

The block $u(t)$ in Fig:3.19 represents some commanded change in actuator position, within the actuator space $u \in \mathbb{U}$. That space consists of propeller speeds Ω_i and servo positions λ_i and α_i for $i \in [1 : 4]$; as detailed in Eq:2.17. Each actuator has its own transfer function, driven by the collective dynamic block $P(s)$, such transfer characteristics were empirically determined in Sec:2.4.1. That actuator argument $u(t)$ then leads to some time varying inner ring servo position $\lambda_i(t)$, with a rate $\dot{\lambda}_i(t)$. Both of which are used to calculate the complete Euler-Lagrange equation:

$$\frac{d}{dt} \left(\frac{\partial \mathcal{L}_{M'_i}}{\partial \dot{\vec{u}}} \right) - \frac{\partial \mathcal{L}_{M'_i}}{\partial \vec{u}} = \tilde{\tau}_\lambda \quad (3.122)$$

Seeing that Eq:3.122 produces a 3-D vector result and not a scalar; vector magnitudes $\|\hat{\tau}_\lambda\|$ and $\|\tilde{\tau}_\lambda\|$ are considered. The objective here is to quantify the effect a rotation matrix linearization has on the estimated generalized torque calculations detailed above.

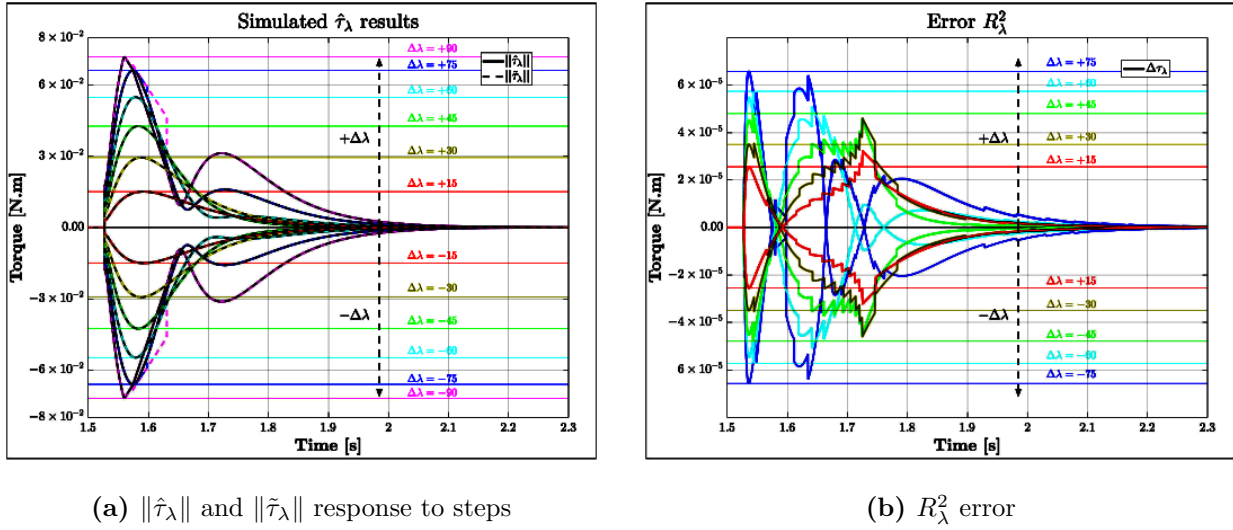


Figure 3.20: Inner ring induced torque responses for $\Delta\lambda_i$

Plotted in Fig:3.20a are both estimated $\|\hat{\tau}_\lambda\|$ and simulated $\|\tilde{\tau}_\lambda\|$ torques, calculated with a nominal constant angular propeller speed $\vec{\Omega}_i = 6000$ [RPM]. Increasing positive and negative step sizes for changes in $\Delta\lambda_i$ are shown, resulting in greater torque responses. The R_λ^2 error between $\|\hat{\tau}_\lambda\|$ and $\|\tilde{\tau}_\lambda\|$ is plotted in Fig:3.20b. That difference between $\|\hat{\tau}_\lambda\|$ and $\|\tilde{\tau}_\lambda\|$ is precisely the partial derivative contribution $\partial\mathcal{L}_{M'_i}/\partial\vec{\mathbf{u}}$. Or rather that, mathematically:

$$R_\lambda^2 = \|\hat{\tau}_\lambda\| - \|\tilde{\tau}_\lambda\| \quad (3.123a)$$

$$= \left\| \left(\frac{d}{dt} \left(\frac{\partial \mathcal{L}_{M'_i}}{\partial \dot{\mathbf{u}}} \right) \right) \right\| - \left\| \left(\frac{d}{dt} \left(\frac{\partial \mathcal{L}_{M'_i}}{\partial \dot{\mathbf{u}}} \right) - \frac{\partial \mathcal{L}_{M'_i}}{\partial \vec{\mathbf{u}}} \right) \right\| \quad (3.123b)$$

$$\therefore R_\lambda^2 = \left\| \frac{\partial \mathcal{L}_{M'_i}}{\partial \vec{\mathbf{u}}} \right\| \quad (3.123c)$$

The simulation for R_λ^2 suffered from tolerance errors within the MatLab integral approximator, this was as a result of the small deviations which were being calculated. Despite that; the differences, using the inertial matrices and dimensions defined for the prototype in Sec:2.3, were typically in the order of $\times 10^{-5}$ [Nm] for steps in $\Delta\lambda_i$.

Only for large angular changes in $\Delta\lambda_i$ does the approximation begin to deteriorate. Mostly both $\hat{\tau}_\lambda$ and $\tilde{\tau}_\lambda$ were three orders of magnitude greater than their errors; torques were in the range of $\times 10^{-2}$ [Nm]. The error for when $\lambda = \pi/2$ was not included in Fig:3.21b because it was the only error which did not fit on the $\times 10^{-5}$ [Nm] scale, being an order of magnitude greater.

The same process was then applied to the middle ring Lagrangian, $\mathcal{L}_{M''_i}$ from Eq:3.113d, to evaluate $\hat{\tau}_\alpha(\lambda_i)$. Those results are plotted collectively in Fig:3.21. Note that both $\|\hat{\tau}_\alpha\|$ and $\|\tilde{\tau}_\alpha\|$ are plotted, not the generalized torques $\vec{\mathbf{V}}(\alpha_i, \lambda_i)$ acting on the system. The generalized torque response $\vec{\mathbf{V}}(\alpha_i, \lambda_i)$ from Eq:3.114 and expanded in Eq:3.86g includes the inner ring energy component $\vec{\mathbf{U}}(\lambda_i)$ or $\vec{\tau}_\lambda$; whilst $\hat{\tau}_\alpha(\lambda_i)$ and $\tilde{\tau}_\alpha(\lambda_i)$ do not. From Eq:3.87, $\hat{\tau}_\alpha(\lambda)$ is defined as a function of $\vec{\mathbf{V}}(\alpha_i, \lambda_i)$ and $\vec{\mathbf{U}}(\lambda_i)$:

$$\hat{\tau}_\alpha(\lambda_i) \triangleq \vec{\mathbf{V}}(\alpha_i, \lambda_i) - R_y(\lambda) \vec{\mathbf{U}}(\lambda_i) \quad (3.124)$$

Plots for the net generalized torque response $\vec{\mathbf{V}}(\alpha_i, \lambda_i)$ acting on the system with combined changes for $\Delta\alpha_i$ and $\Delta\lambda_i$ are included in App:C.3. Moreover only a constant value for the λ_i servo position was used for the tests in Fig:3.21. The same constant propeller speed $\vec{\Omega}_i = 6000$ [RPM] was used together with a constant $\lambda_i = 0$ [rad] origin position for the inner ring's servo, maintaining a constant inertia.

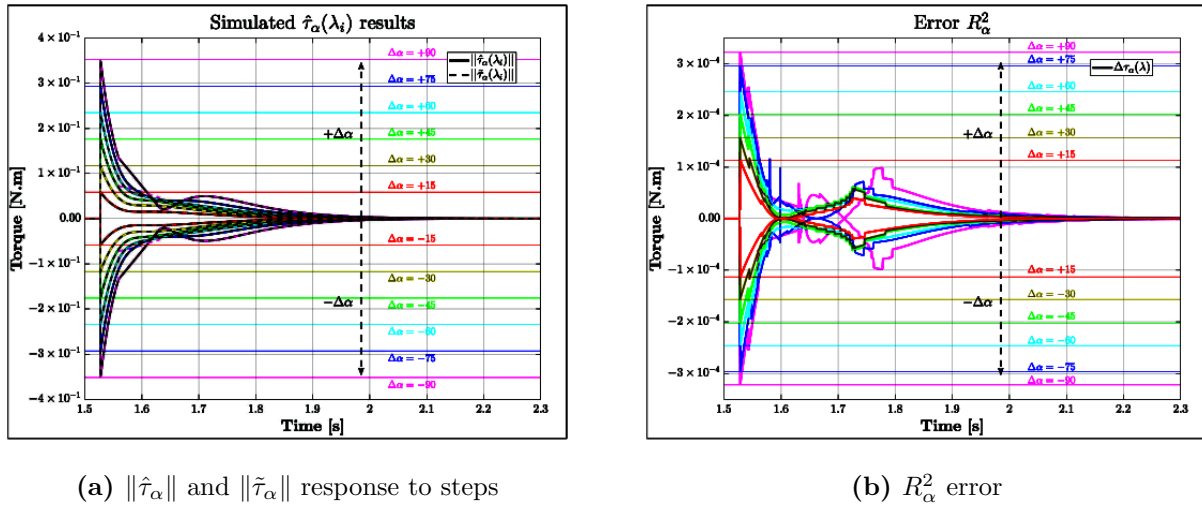


Figure 3.21: Middle ring induced torque responses for $\Delta\alpha$

The initial torque spike for $\tau_\alpha(\lambda_i)$ shown in Fig:3.21a is as a result of the significantly larger rotational inertia, J_p for the entire motor module, encountered by a second order angular acceleration $\ddot{\alpha}_i$. That response is depreciated in the case of the inner ring for τ_λ because of how much smaller that rotational inertia, J_n for the inner ring only, physically is. As per power calculations for the servo using parameters from Sec:2.4.1; the servo's angular acceleration is rate limited to 472 [rad.s⁻²], but neither tests come close to reaching saturation.

The second torque peak which begins to manifest in the inner ring response for τ_λ shown in Fig:3.20a is as a result of the angular velocity rate limit $\dot{\lambda}_{max} = 7.4799$ [rad.s⁻¹] being encountered. The same limit is encountered for the middle ring response $\tau_\alpha(\lambda_i)$ in Fig:3.21a but is far less significant in relation to the initial second order acceleration torque peak.

The deviation between $\|\hat{\tau}_\alpha(\lambda_i)\|$ and $\|\tilde{\tau}_\alpha(\lambda_i)\|$ is only of the order of 10^{-4} [N.m] whilst typical induced torque values are again three orders of magnitude greater, or of the order 10^{-1} [N.m]. Only at large angular changes for both $\Delta\lambda_i$ and $\Delta\alpha_i$ do the simplifications proposed begin to deteriorate.

From plots in both Fig:3.20a and Fig:3.21a; it is clear that a linearized rotation matrix to reduce complexity of generalized torque calculations in Eq:3.114 is a fair simplification. The linearization(s) proposed in Eq:3.115 holds true so long as the step sizes for $\Delta\lambda_i$ or $\Delta\alpha_i$ are small enough, typically having an error three orders of magnitude smaller than the induced response considered. The control loop will only ever be dealing with minor step size changes for servo positions and so, the linearization is an appropriate one that will reduce interval computational complexity.

Dynamic model verification

In spite of the rigorous mathematical approached applied to the multibody system above, physical corroboration of the proposed model(s) is still required. The systems described in Eq:3.76 for $\hat{\tau}_\lambda(\lambda_i)$, Eq:3.87 for $\hat{\tau}_\alpha(\lambda_i, \alpha_i)$ and Eq:3.110b for $\hat{\tau}_b(\vec{\omega}_b, u)$ require further verification before an accurate and reliable simulation can be constructed based upon them. Two test rigs were designed and constructed (Fig:3.22 and Fig:3.24) to physically measure the induced torques in question. The first test rig recreates the relative motion of the inner ring actuated by the λ_i servo. Similarly the second test platform mimics the middle ring's response when driven by the outer α_i servo.

The net body response, $\hat{\tau}_b(\vec{\omega}_b, u)$ relating to net angular body velocity $\vec{\omega}_b$ in Eq:3.110b, is harder to recreate on an isolated test rig. Such results are only discussed in the context of simulation. Considering first the inner most ring assembly; Fig:3.22 shows the test rig used to isolate and measure $\hat{\tau}_\lambda(\lambda_i)$ responses to $\Delta\lambda$ rotations. The inner ring is supported by two bearing assemblies; an extended shaft in the $-\hat{X}_{M_i}$ direction connects the inner ring to the driving servo block.

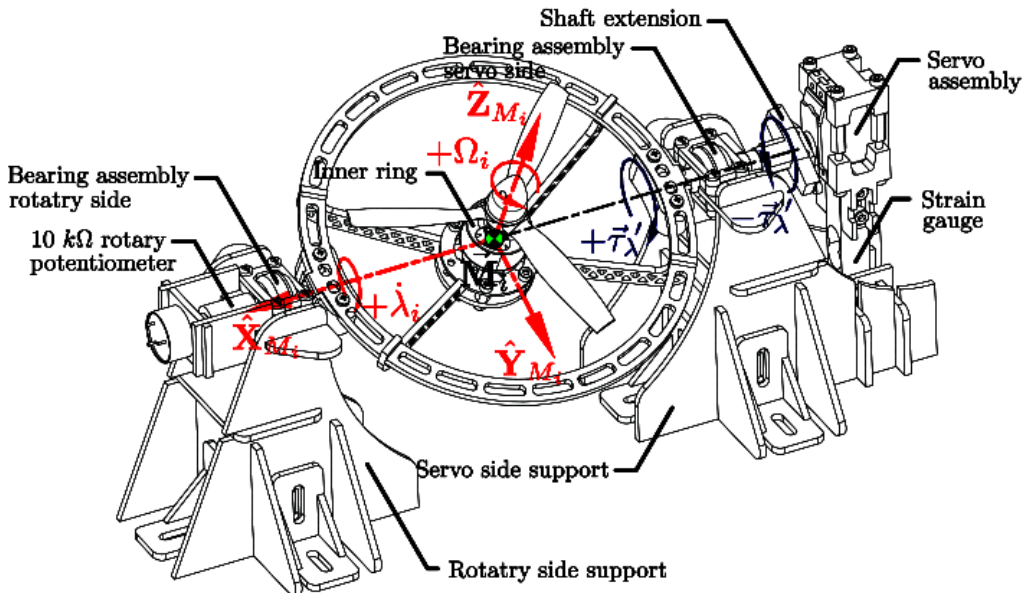


Figure 3.22: Inner ring torque test rig

Rotational torque $\hat{\tau}_\lambda(\lambda_i)$ is transferred through the shaft extension from the servo to the inner ring. The servo block is secured only by a vertically aligned (and calibrated, see App:B.3) strain gauge. Deflection of the strain gauge is then proportional to the torque applied by the servo to rotate the inner ring structure. It is important to mention that, whilst the bearing assembly facilitates the transfer of the servo's rotational torque, the assembly isolates only the $\hat{X}_{M'_i}$ component of the induced torque. If $\vec{\tau}'_\lambda$ is the deflection torque measured; its relationship with the induced torque vector $\hat{\tau}_\lambda(\lambda_i)$ is given by:

$$\hat{\tau}'_\lambda = \hat{\tau}_\lambda(\lambda_i) \cdot \hat{X}_{M'_i} \in \mathcal{F}^{M'_i} \quad (3.125)$$

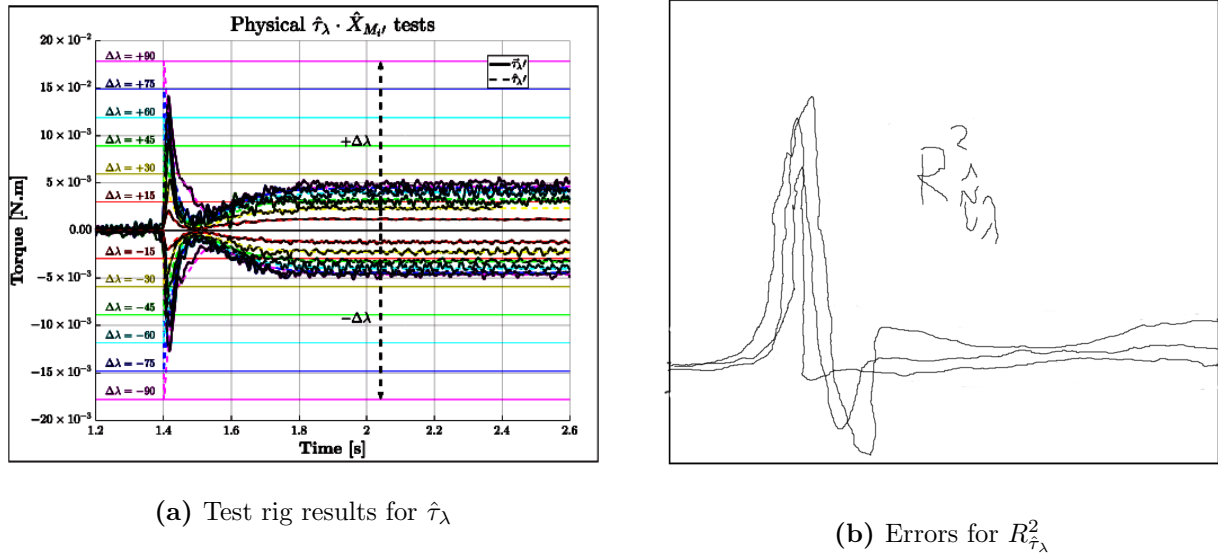
One final thing to consider is that the equation for $\hat{\tau}_\lambda(\lambda_i)$, previously in Eq:3.76, does not account for the gravitational torque from an eccentric center of gravity (Fig:2.12) or induced aerodynamic torque about the propellers hub (Fig:3.7 and Eq:3.31b). The derivations earlier in Sec:3.3.1 introduce net gravitational torque for an effective center of gravity \vec{r}_g into Eq:3.110a. Moreover aerodynamic torque $\vec{Q}(\Omega_i)$ about the propeller's rotational axis is to be included as an additive term.

The torque response opposed to angular steps of $\Delta\lambda_i$, and hence its acceleration $\ddot{\lambda}_i$, induced by the servo is then; from Eq:3.76 with introduced gravitational and aerodynamic torque components relative to $\mathcal{F}^{M'_i}$:

$$\begin{aligned} \hat{\tau}_\lambda(\lambda_i) = & (J'_r)\vec{\Omega}'_i + (J'_n)\dot{\vec{\lambda}}_i + (J'_r)\dot{\vec{\Omega}}'_i + (J'_n)\ddot{\vec{\lambda}}_i + \dot{\vec{\lambda}}_i \times (J'_r)\vec{\Omega}'_i + \dot{\vec{\lambda}}_i \times (J'_n)\dot{\vec{\lambda}}_i \\ & R_x(\lambda)(Q(\Omega_i) \cdot \hat{Z}_{M_i}) + m_n(R_x(\lambda)C.M_n) \times \vec{G}_{M'_i} \in \mathcal{F}^{M'_i} \end{aligned} \quad (3.126)$$

The term $m_n(R_x(\lambda)C.M_n) \times \vec{G}_{M'_i}$ is the gravitational torque from the rotated center of mass, $C.M_n$; first defined in Eq:2.28d. The torque $Q(\Omega_i) \cdot \hat{Z}_{M_i}$ is the scalar projection of aerodynamic torque from Fig:3.7b onto the propeller's \hat{Z}_{M_i} axis, rotated onto the middle ring $\mathcal{F}^{M'_i}$ frame. Note the strain gauge's measured response encountered will be the negative torque response $-\hat{\tau}_\lambda(\lambda_i)$.

The plot illustrated in Fig:3.23a shows tests for the inner ring torque response at increments of relative servo step sizes: $\Delta\lambda = \pm[1/12\pi, 2/12\pi \dots 5/12\pi, 6/12\pi]$. A constant propeller rotational speed $\Omega_i = +6000$ [RPM] was used. Step changes in the propeller's speed manifest as a gyroscopic cross products and won't affect the projected $\hat{X}_{M'_i}$ term $\hat{\tau}'_\lambda$ from Eq:3.125. As per convention, in the plot Fig:3.23a, $\vec{\tau}'_\lambda$ represents the physically measured torque on the test rig illustrated in Fig:3.22 and $\hat{\tau}'_\lambda$ is the simulated torque calculated from Eq:3.126. Both torques are the projected $\hat{X}_{M'_i}$ components of the induced torque vector.

**Figure 3.23:** Inner ring response

Error deviation between the physically measured and simulated values is also shown in Fig:3.23b. The torque peak increased with greater step sizes in $\Delta\lambda_i$. The co-axial support bearings, despite being de-greased and cleaned, still damped faster elements of the transient torque response, moreover the magnitude of the signal measured left it susceptible to noise from vibrations induced by the propellers rotation. There is, however, a clear correlation between the simulated and physically measured signal. Within a margin of error and considering the simplicity of the test setup used, the step changes verify the proposed inner ring model in Eq:3.126.

Corroborating the dynamics for the middle ring response requires more in-depth discussion. Unlike the inner rings response, described in Eq:3.126; the middle ring's torque $\hat{\tau}_\alpha(\lambda_i, \alpha_i)$ from Eq:3.87 is not equivalent to the generalized torque response acting on the middle ring system $\vec{V}(\alpha_i, \lambda_i)$, Eq:3.86g. As mentioned previously, $\vec{V}(\alpha_i, \lambda_i)$ includes a transformed component of the inner ring's generalized response, $R_y(\alpha)\vec{U}(\lambda_i)$ from Eq:3.75a, whilst the servo response torque $\hat{\tau}_\alpha(\lambda_i, \alpha_i)$ does not...

To differentiate the servo's response torque $\hat{\tau}_\alpha(\lambda_i, \alpha_i)$ and the physical (generalized) torque being considered here, $\hat{\Gamma}_\alpha(\lambda_i \alpha_i)$ is used to indicate the induced torque response from the middle ring assembly's rotation. That torque is the measured component of the middle ring response and equivalent to the generalized torque response. Reiterating the equation for the expected generalized torque $\vec{V}(\alpha_i, \lambda_i)$ from Eq:3.86g, now with an included gravitational and aerodynamic torque components and induced torques as a result of the inner ring's rotation:

$$\begin{aligned} \hat{\Gamma}_\alpha(\lambda_i, \alpha_i) &= R_y(\alpha)\vec{U}(\lambda_i) + (J'_p)\dot{\alpha}_i + \left(J''_n - R_y(\alpha)(J'_n)R_y^{-1}(\alpha) \right) \dot{\lambda}'_i + \left(J''_r - R_y(\alpha)(J'_r)R_y^{-1}(\alpha) \right) \dot{\Omega}'_i \\ &+ (J'_p)\ddot{\alpha}_i + \dot{\alpha}_i \times \left((J'_p)\dot{\alpha}_i + (J''_n)\dot{\lambda}'_i + (J''_r)\dot{\Omega}'_i \right) + R_y(\alpha)R_x(\lambda)(Q(\Omega_i) \cdot \hat{Z}_{M_i}) + m_p C.M'_p(\alpha_i, \lambda_i) \times \vec{G}_{M''_i} \\ &= \vec{V}(\lambda_i, \alpha_i) \in \mathcal{F}^{M''_i} \quad (3.127) \end{aligned}$$

Where the term $C.M'_p(\alpha_i, \lambda_i)$ is the net rotated center of gravity for the entire motor module as a function of both servo positions:

$$C.M'_p(\alpha_i, \lambda_i) = \frac{m_n R_y(\alpha) R_x(\lambda) C.M_n + m_m R_y(\alpha) C.M_m}{m_m + m_n} \quad (3.128)$$

With m_m and m_n being inner and middle ring structure's respective masses, $m_m = 98$ [g] and $m_n = 92$ [g] from Sec:2.3.

Fig:3.24 shows the test rig used to measure torque responses for the motor module assembly, containing both inner and middle ring assemblies.

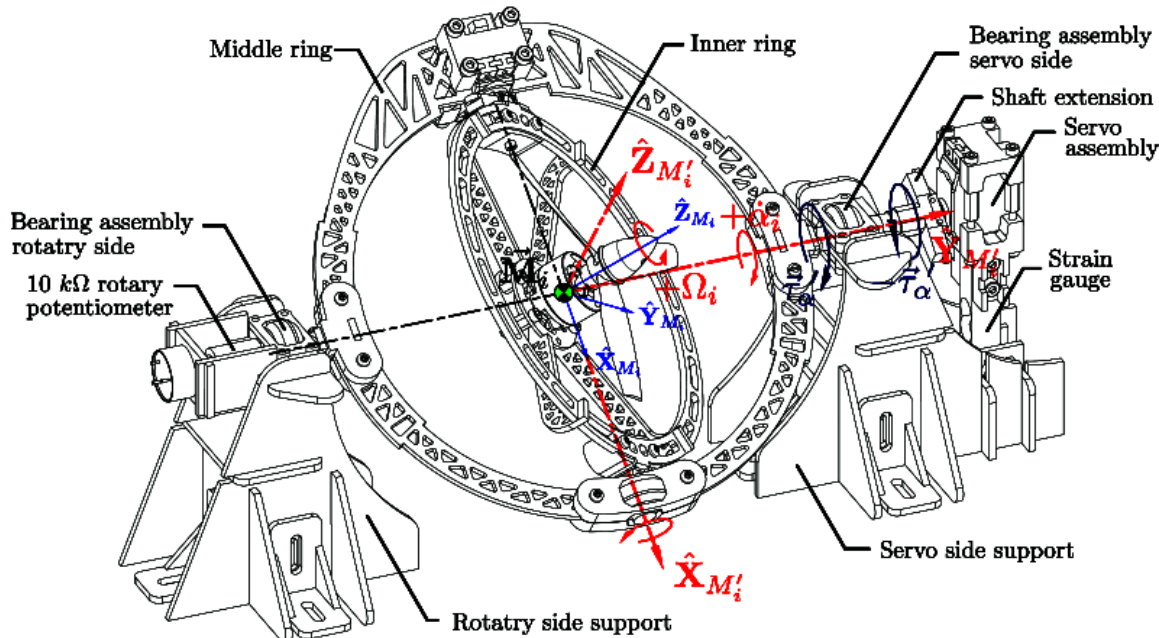


Figure 3.24: Middle ring torque test rig

The inner ring servo λ_i is held at constant intervals to represent varying inertias for the net module $J_p(u \cdot i)$ described in Eq:2.23b. The middle ring servo α_i applies an accelerating torque $\hat{\Gamma}_\alpha(\lambda)$ to the body, the rig isolates only the $\hat{Y}_{M_i''}$ component of that torque, as such the strain gauge deflection represents only:

$$\hat{\Gamma}_\alpha'(\lambda) = \hat{\Gamma}_\alpha(\lambda) \cdot \hat{Y}_{M_i''} \quad (3.129)$$

Furthermore, the included inner torque term $R_y(\alpha)\hat{\tau}_\lambda = R_y(\alpha)\vec{U}(\lambda_i)$ is going to be small for any case where the propeller's rotational speed and the inner ring's servo speed are both constant; $\dot{\vec{\Omega}}_i = 0$ and $\vec{\lambda}_i = 0$. With no inner ring step contribution, only the inner ring's gravitational torque affects Eq:3.127.

Plotted in Fig:3.25a shows results for measured torques $\tilde{\tau}_\alpha'(\lambda)$, expected simulated torque values $\hat{\tau}_\alpha(\lambda)$ and resultant SimScape simulation values for $\tilde{\tau}_\alpha(\lambda)$. Tests are conducted with a constant propeller rotational velocity $\vec{\Omega}_i = 6500$ [RPM] but differing rotational positions for the inner ring servo λ_i . That angular position affects the net encountered rotational inertial $J_p(\lambda)$.

(a) Test rig results for $\tilde{\tau}_\alpha(\lambda)$ (b) Errors for $R_{\tilde{\tau}_\alpha(\lambda)}^2$

Figure 3.25:

The final simulated module is that of $\hat{\tau}_b$

The above responses are pertinent to simulation and plant dependent feedback compensation. The simulation environment is structured such that the torques are produced as responses from Newtonian movement at every step interval. In due course it would be more efficient (and less stiff) for the simulation to exploit an implicit Euler [65, 134] coordinate system in lieu of the cartesian response equations developed above. However this was not implemented in Chapter:6 and remains open to further testing and simulation...

3.4 Consolidated Model

Reiterating the different aspects detailed above and consolidating the state equations from Eq:3.10a-3.10d. Then lifting the attitude states to $\mathbb{Q} \in \mathbb{R}^4$ space using quaternions. Also introducing the non-linear inertial and gyroscopic responses to induced perturbations, $\hat{\tau}_\lambda$ and $\hat{\tau}_\alpha(\lambda_i)$ from Eq:3.76 and Eq:3.87 respectively, with non-linear inertial matrix terms $J_b(u)$ from Section:2.3. Net forces and torques \vec{F}_μ and $\vec{\tau}_\mu$ are control inputs to be designed by a higher level set-point tracking controller discussed next in Ch:4. The exact actuator effectiveness and allocation rules are explored thereafter in Ch:5.

The vehicle's inertial position and *body frame* velocity differential equations are:

$$\dot{\mathcal{E}} = Q_b^* \otimes \vec{v}_b \otimes Q_b \quad [\text{m.s}^{-1}], \quad \in \mathcal{F}^I \quad (3.130\text{a})$$

$$\dot{\vec{v}}_b = m^{-1}(-\vec{\omega}_b \times m\vec{v}_b + Q_b \otimes m\vec{G}_I \otimes Q_b^* - \vec{D}_{\text{net}}(\vec{v}_b) + \vec{F}_\mu(u)) \quad [\text{m.s}^{-2}], \quad \in \mathcal{F}^b \quad (3.130\text{b})$$

Similarly the vehicle's attitude quaternion rate and angular acceleration are respectively:

$$\dot{Q}_b = \frac{1}{2}Q_b \otimes \vec{\omega}_b \quad \in \mathcal{F}^I \quad (3.130\text{c})$$

$$\dot{\vec{\omega}}_b = J_b(u)^{-1}(-\vec{\omega}_b \times J_b(u)\vec{\omega}_b - \hat{\tau}_b(u) + \vec{\tau}_g + \sum_{i=1}^4 \vec{Q}(\Omega_i, \lambda_i, \alpha_i) + \vec{\tau}_\mu(u)) \quad [\text{rad.s}^{-2}], \quad \in \mathcal{F}^b \quad (3.130\text{d})$$

And an actuator space as per Eq:2.17, each with their own transfer function described in Sec:2.4.1:

$$u = [\Omega_1^+, \lambda_1, \alpha_1, \dots, \Omega_4^-, \lambda_4, \alpha_4] \quad \in \mathbb{U} \in \mathbb{R}^{12} \quad (3.130\text{e})$$

Control force and torque plant inputs, $\vec{F}_\mu(u)$ and $\vec{\tau}_\mu(u)$ respectively, are a combination of Eq:3.15 with three dimensional thrust vectors $\vec{T}(\Omega_i)$ as per the quaternion analogue of Eq:2.16b. Both are later abstracted to virtual control inputs later in the control allocation design Ch:5.

$$\vec{F}_\mu(u) = \sum_{i=1}^4 \vec{T}(\Omega_i, \lambda_i, \alpha_i) = \sum_{i=1}^4 Q_{M_i}^* \otimes T(\Omega_i) \otimes Q_{M_i} \quad [\text{N}], \quad \in \mathcal{F}^b \quad (3.131\text{a})$$

$$\vec{\tau}_\mu(u) = \sum_{i=1}^4 \vec{L}_i \times \vec{T}(\Omega_i, \lambda_i, \alpha_i) = \sum_{i=1}^4 \vec{L}_i \times (Q_{M_i}^* \otimes T(\Omega_i) \otimes Q_{M_i}) \quad [\text{Nm}], \quad \in \mathcal{F}^b \quad (3.131\text{b})$$

Scalar thrust $T(\Omega_i)$ is a function of the propeller's rotational velocity whereas $\vec{T}(\Omega_i, \lambda_i, \alpha_i)$ is that thrust's three dimensional counterpart in \mathcal{F}^b . Equivalently $Q(\Omega_i)$ is the scalar aerodynamic torque in \mathcal{F}^{M_i} about each motor's rotor \vec{Z}_{M_i} -axis, whereas $\vec{Q}(\Omega_i, \lambda_i, \alpha_i)$ is the torque vector counterpart in \mathcal{F}^b . Both thrust and aerodynamic torque terms are calculated from their respective coefficients (plotted in Fig:3.5):

$$T(\Omega_i) = C_T(J)\rho\Omega_i^2 D^4 \quad [\text{N}] \quad (3.132\text{a})$$

$$Q(\Omega_i) = C_P(J)\rho\Omega_i^3 D^5 (1/R\Omega) \quad [\text{Nm}] \quad (3.132\text{b})$$

Reiterating that Ω_i for aerodynamic calculations in Eq:3.132a and Eq:3.132b has units [RPS]. The non-linear torque responses from multibody configuration changes in Eq:3.110b are introduced as feedback compensation terms;

$$\hat{\tau}_b(u) \triangleq \dot{J}_b(u)\vec{\omega}_b + \sum_{i=1}^4 \left[\hat{\tau}'_\alpha(\lambda_i) + \hat{\tau}''_\lambda + \vec{\omega}_b \times \left((J_p'')\dot{\vec{\alpha}}'_i + (J_r'')\dot{\vec{\lambda}}''_i + (J_r''')\vec{\Omega}'''_i \right) \right] \quad [\text{Nm}], \quad \in \mathcal{F}^b \quad (3.133)$$

With $\hat{\tau}'_\alpha(\lambda_i)$ and $\hat{\tau}''_\lambda$ both transformed to the body frame \mathcal{F}^b . Then including variable gravitational torque as a result of an eccentric center of gravity from Eq:2.33b; also dependent on the vehicles configuration:

$$\vec{\tau}_g = \Delta C.G \times \vec{G}_b = (\vec{O}_b - C.M_b(u)) \times \vec{G}_b \quad [\text{Nm}], \quad \in \mathcal{F}^b \quad (3.134)$$

And finally the vehicles net rotational inertia, aligned and centred with the body frame. That inertia is calculated as a function of all actuator positions; taken from Eq:2.30a and given as:

$$J_b(u) = J'_y + \sum_{i=1}^4 J_n(u \cdot i) + \sum_{i=1}^4 J_m(u \cdot i) \quad [\text{kg.m}^{-2}], \quad u \in \mathbb{U} \quad (3.135)$$

Both attitude (euler angles $\vec{\eta}$ or quaternions Q_b) and translational position states $\vec{\mathcal{E}}$ could indeed be combined into a single state \vec{x}_b . That could then be used for a complete state feedback control law which could potentially exploit or linearize the cross-coupling between the angular and translational plants. Such an approach would, however, dramatically increase the complexity in tuning actual control parameters (see Sec:6.1). Controllers for attitude and position loops are designed and optimized independently...

Chapter 4

Controller Development

4.1 Control Loop

The control problem here is, as outlined in Ch:1, to achieve non-zero set-point tracking (*attitude and position* states) on a quadrotor by solving the problem of its inherent under-actuation. For the purposes of the subsequent controller development, the plant is described in the following typical non-linear state space form:

$$\frac{d}{dt}\vec{\mathbf{x}} = f(\vec{\mathbf{x}}, t) + g(\vec{\mathbf{x}}, \vec{\nu}, t) \quad (4.1a)$$

$$\vec{y} = c(\vec{\mathbf{x}}, t) + d(\vec{\mathbf{x}}, \vec{\nu}, t) \quad (4.1b)$$

Where the plant's dynamics are governed by state progression $f(\vec{\mathbf{x}}, t)$ and the plant's input response $g(\vec{\mathbf{x}}, \vec{\nu}, t)$ for a given control input $\vec{\nu}$. The latter could take the affine form; $g(\vec{\mathbf{x}}, t)\vec{\nu}$. Set-point tracking aims for the output to track the plant's state; namely $\vec{y} = c(\vec{\mathbf{x}}, t) = \vec{\mathbf{x}}$. As such, the control problem is to design a stabilizing control law h for some error state \mathbf{x}_e :

$$\vec{\nu}_d = h(\mathbf{x}_e, t) = h(\mathbf{x}_b, \dot{\mathbf{x}}_b, \mathbf{x}_d, \dot{\mathbf{x}}_d, t) \quad (4.2)$$

Such that the controlled plant is asymptotically stabilizing or that $\lim_{t \rightarrow \infty} \mathbf{x}_e = 0$. Trajectory stability conditions are further defined next in Sec:4.3. Note that it is possible to combine attitude and position states into a single common trajectory state such that:

$$\vec{\mathbf{x}} = \begin{bmatrix} \vec{\mathcal{E}} & Q_b \end{bmatrix}^T \quad (4.3)$$

The body's trajectory is then fully described by $\vec{\mathbf{x}}(t)$. Separate control laws are developed for attitude and position tracking and hence those states are not combined in the context of this control project. However for the purposes of describing the control plant, a single major loop is considered.

Because of the plant's overactuatedness the control loop is split into two blocks; first a higher level *set-point tracking* controller designs a virtual control input $\vec{\nu}_d$. That being net forces \vec{F}_d and torques $\vec{\tau}_d$ to act on the body. A lower level *allocator* then solves for explicit actuator positions from $\vec{\nu}_d$ to physically actuate that *virtual* control input. The actuator set then implements a commanded control input $\vec{\nu}_c$ through its effectiveness function (Eq:3.132)

$$\vec{\nu}_c = B(\vec{\mathbf{x}}, u, t) \quad (4.4)$$

The allocator solves for actuator values $u \in \mathbb{U}$ such that $\vec{\nu}_c \rightarrow \vec{\nu}_d$. That allocation function, B^\dagger , can be *roughly* referred to as the effectiveness inverse:

$$u_{\in \mathbb{U}} = B^\dagger(\vec{\mathbf{x}}, \vec{\nu}_d, t) \quad (4.5)$$

This chapter derives higher level controllers for $\vec{v}_d = h(\vec{x}_e, t)$; allocation rules are discussed next in Ch:5. A collection of attitude and position controllers are presented here whose stability is proven with Lyapunov theorem [15, 56, 105]. Each controller is compared in the context of an over actuated quadrotor plant. Similarly a series of proposed allocation schemes are presented. Controller comparisons, their details and efficacy are evaluated in Ch:6.

A generalized over-actuated control loop consists of a series of cascaded control blocks (Fig:4.1). From the trajectory's error state \vec{x}_e , a control law designs a virtual control input \vec{v}_d which is applied to the allocation block. The allocation law $B^\dagger(\mathbf{x}, \vec{v}_d, t)$ solves for physical actuator positions $u \in \mathbb{U}$. Actuator positions command a physical input $\vec{v}_c = B(\mathbf{x}, u, t)$ which is an input to the state's dynamics, Eq:4.1. Finally the output tracking state is estimated with some filter $\hat{\mathbf{x}} = A(\mathbf{x}, t)$ which is used to calculate the error state (Sec:6.8).

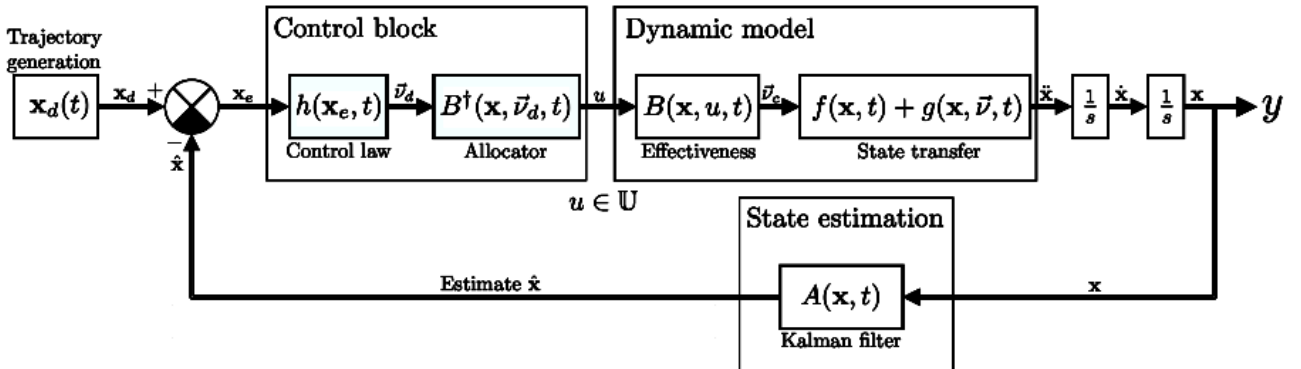


Figure 4.1: Generalized control loop with allocation

Fig:4.1 is a generalized illustration of the control loop's structure; the plant's dynamics from Eq:3.130 include state derivative feedback. Moreover aspects of the state transfer function includes multi-body non-linearities dependent on actuator positions and rates as detailed in Sec:3.3. That generalized case is now refined in the context of an over-actuated quadcopter.

4.2 Control Plant Inputs

Control inputs for the differential state equations, from Eq:3.130, have mostly been described with net forces and torques; $\vec{F}_\mu(u)$ and $\vec{\tau}_\mu(u)$. The relationship (*effectiveness function*) between each propeller's rotational speed and servo positions with the produced thrust vector is calculated from Eq:3.131.

$$\vec{v}_c \triangleq \begin{bmatrix} \vec{F}_\mu(u) & \vec{\tau}_\mu(u) \end{bmatrix}^T = B(\vec{x}, u, t) \quad \in \mathbb{R}^6, \quad u \in \mathbb{U} \quad (4.6a)$$

$$\vec{F}_\mu(u) = \sum_{i=1}^4 Q_{M_i}^*(\lambda_i, \alpha_i) \otimes T(\Omega_i) \otimes Q_{M_i}(\lambda_i, \alpha_i) \quad \in \mathcal{F}^b \quad (4.6b)$$

$$\vec{\tau}_\mu(u) = \sum_{i=1}^4 \vec{L}_i \times (Q_{M_i}^*(\lambda_i, \alpha_i) \otimes T(\Omega_i) \otimes Q_{M_i}(\lambda_i, \alpha_i)) \quad \in \mathcal{F}^b \quad (4.6c)$$

As mentioned previously, a higher level controller designs desired net plant inputs $\vec{v}_d = [\vec{F}_d \quad \vec{\tau}_d]^T$ whilst a lower level allocator commands physical inputs $u = B^\dagger(\vec{x}, \vec{v}_d, t)$. This allows for independent comparison of proposed control and allocation laws. However, typical allocation rules like pseudo-inversion require an affine relationship between plant and control inputs (Sec:1.2.2). The relationship in Eq:4.6 is not reducible to a single multiplicative relationship with the actuator matrix $u \in \mathbb{U}$. So the effectiveness function needs an extra layer of abstraction to incorporate a multiplicative relationship.

Rather than calculating explicit actuator positions directly from $\vec{\nu}_d$; a set of four 3-D thrust vectors $\vec{T}_{1 \rightarrow 4}$ for each motor module are first calculated.

$$\vec{\nu}_c = \begin{bmatrix} \vec{F}_\mu(u) \\ \vec{\tau}_\mu(u) \end{bmatrix} = \begin{bmatrix} 1 & 1 & 1 & 1 \\ [\vec{L}_1]_\times & [\vec{L}_2]_\times & [\vec{L}_3]_\times & [\vec{L}_4]_\times \end{bmatrix} \begin{bmatrix} \vec{T}_1 & \vec{T}_2 & \vec{T}_3 & \vec{T}_4 \end{bmatrix}^T \quad (4.7a)$$

$$\rightarrow \vec{\nu}_f = B'(\vec{x}, t) \begin{bmatrix} \vec{T}_1 & \vec{T}_2 & \vec{T}_3 & \vec{T}_4 \end{bmatrix}^T \quad (4.7b)$$

Where $[\vec{L}_i]_\times$ is the cross product vector of the i^{th} torque arm. Explicit actuator positions for each module, $[\Omega_i, \lambda_i, \alpha_i]^T$, can then be solved from those thrust vectors \vec{T}_i for $i \in [1 : 4]$ with some trigonometry, "unwinding" transformations applied in Eq:4.6. That trigonometric inversion is detailed later in Sec:5.1 but is described as the function R^\dagger :

$$[\Omega_i, \lambda_i, \alpha_i]^T = R^\dagger(\vec{x}, \vec{T}_i, t) \quad \text{for } i \in [1 : 4] \quad (4.8)$$

The generalized control loop illustrated in Fig:4.1 is extended to include the abstracted allocation blocks of Eq:4.7 and Eq:4.8, shown in Fig:4.2. The net control block still solves for the same actuator matrix $u \in \mathbb{U}$. The entire loop accommodates for comparison of various $B^\dagger(\vec{x}, \vec{\nu}_d, t)$ allocation rules without having to redesign the remainder of the loop's structure.

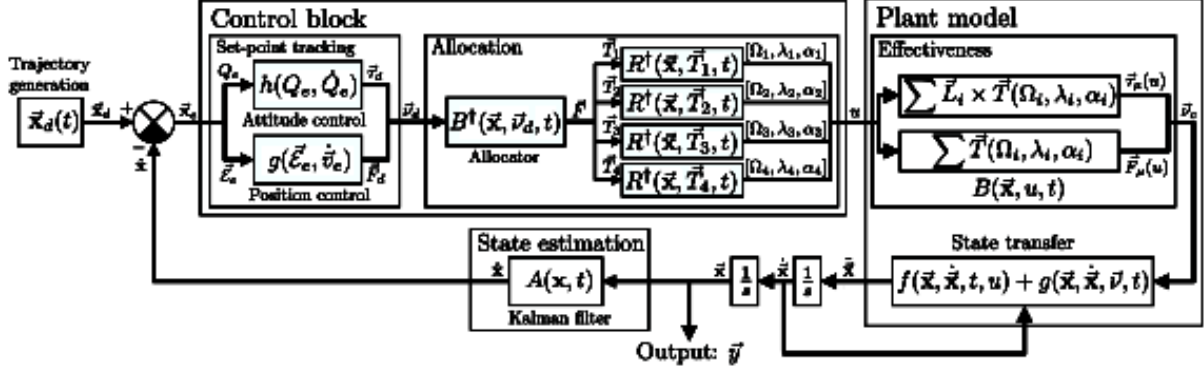


Figure 4.2: Extended control loop with over-actuation

In summary; each controller designs a net force and torque to act on the body. Allocation rules decompose that virtual input into four separate 3-D thrust vectors, or 12 directional components. The force components are an abstracted allocation layer in place of explicit actuator positions, which are subsequently solved for...

$$B^\dagger(\vec{x}, \vec{\nu}_d, t) = [T_{1x}, T_{1y}, T_{1z}, \dots, T_{4x}, T_{4y}, T_{4z}]^T \quad (4.9)$$

Each control law is co-dependent on an accompanying allocation algorithm. Traditional control loops (under-actuated or well matched) typically have a unity allocation rule and as such require no consideration so they're mostly disregarded. Separate control laws for attitude ad position control are presented in Section:4.6 and 4.7 respectively. Thereafter a series of allocation rules are proposed in Ch:5. Although presented independently, the controller and allocation laws are mutually inclusive. The stability of each controller is proven objectively but explicit controller coefficients are optimized in the subsequent Ch:6, in Sec:6.1.

4.3 Stability

Before undertaking the control plant derivations, it is worth outlining definitions of what the control objectives are. The research question aims to achieve non-zero set-point tracking of state's trajectory. A control loop then aims to *stabilize* the dynamics described previously in Sec:3.4 whilst tracking particular trajectories for attitude and position, $\mathbf{x}_d(t) = [\vec{\mathcal{E}}_d(t) \ Q_d(t)]^T$.

The entire system's control loop was previously detailed in Sec:4.1. Stability in the context of trajectory tracking must be defined. Generalized trajectory stability definitions are not uncommon in the context of energy based control design, or Lyapunov theorem (Sec:4.4). Stability definitions pertinent to Lyapunov's stability theorem are briefly presented here; the following is adapted from [15, 56]. In general for some autonomous trajectory $\vec{\mathbf{x}}(t)$, an equilibrium point $\vec{\mathbf{x}}(t_0)$ is said to be stable (**S**) if and only if (*iff*) the following is true:

$$\forall \varepsilon > 0, \exists \delta_0(t_0, \varepsilon) : \|\vec{\mathbf{x}}(t_0)\| < \delta_0(t_0, \varepsilon) \quad (4.10a)$$

$$\Rightarrow \|\vec{\mathbf{x}}(t)\| < \varepsilon, \forall t \geq t_0 \quad (4.10b)$$

The implication of which is that if, for some initial condition $\vec{\mathbf{x}}(t_0)$ whose magnitude is bound by the manifold $\delta_0(t_0, \varepsilon)$, the entire subsequent trajectory of $\vec{\mathbf{x}}(t)$ is bound from above by some other manifold ε . Basic stability is illustrated in Fig:4.3a for a 2-D trajectory.

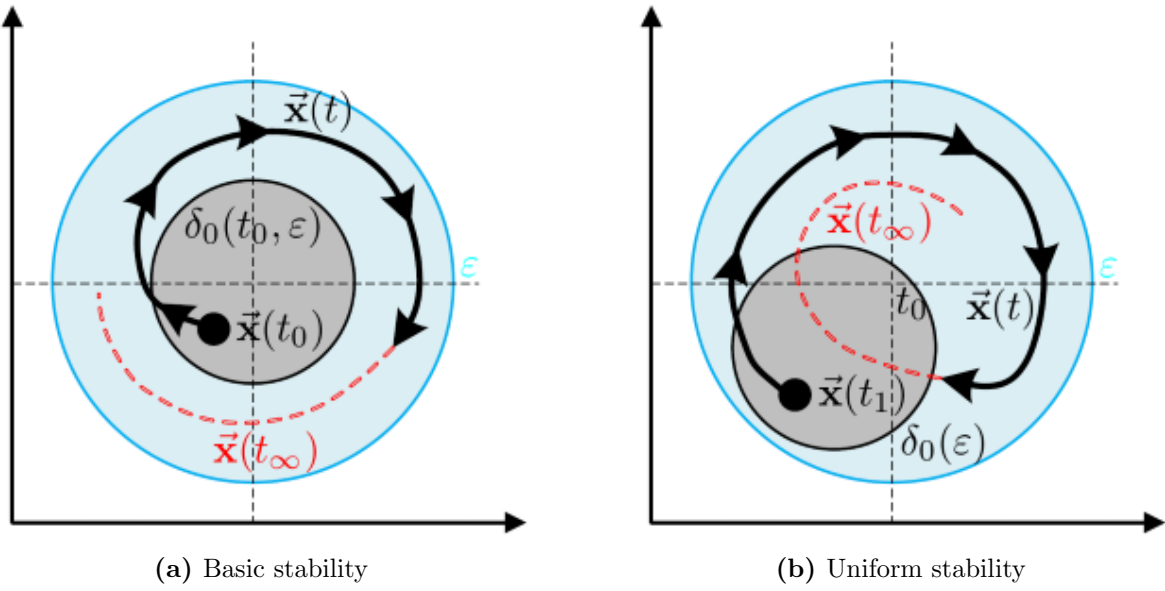


Figure 4.3: Trajectory illustrations for **S** and **US**

An equilibrium point is further said to be uniformly stable (**US**) *iff* for the time $t \in [t_0, \infty)$ the following criteria, being an extension of basic stability, is met:

$$\forall \varepsilon > 0, \exists \delta_0(\varepsilon) > 0 : \|\vec{\mathbf{x}}(t_1)\| < \delta_0(\varepsilon), \quad t_1 > t_0 \quad (4.11a)$$

$$\Rightarrow \|\vec{\mathbf{x}}(t)\| < \varepsilon, \quad \forall t \geq t_1 \quad (4.11b)$$

US similarly bounds a trajectory from above by ε if the trajectory originates from within $\delta_0(\varepsilon)$. The difference is that the principle trajectory region $\delta_0(\varepsilon)$ is independent of t_0 in the case of **US**. The two surfaces are effectively non-concentric; a **US** trajectory is illustrated in Fig:4.3b. Uniform stability is a subset of general stability, **US** \subset **S**, however the converse is not true. Furthermore **US** is a stronger assertion of stability.

Extending stability definitions to include settling; an equilibrium point is said to be asymptotically stable (**AS**) *iff* conditions for **S** are met (Eq:4.10) and that the following holds true:

$$\exists \delta_1(t_0, \varepsilon) > 0 : \|\vec{\mathbf{x}}(t_0)\| < \delta_1(t_0, \varepsilon) \quad (4.12a)$$

$$\Rightarrow \lim_{t \rightarrow \infty} \|\vec{\mathbf{x}}(t)\| \rightarrow 0 \quad (4.12b)$$

This asserts that trajectories originating within some finer region $\delta_1(t_0, \varepsilon)$, being a subset of $\delta_0(t_0, \varepsilon)$, the trajectory tends to and *asymptotically* settles at the origin. In the case of **AS** the origin is both stable and attractive (shown in Fig:4.4a). Asymptotic stability is typically the first requirement for any control law, being a stronger stability than both **US** and **S**...

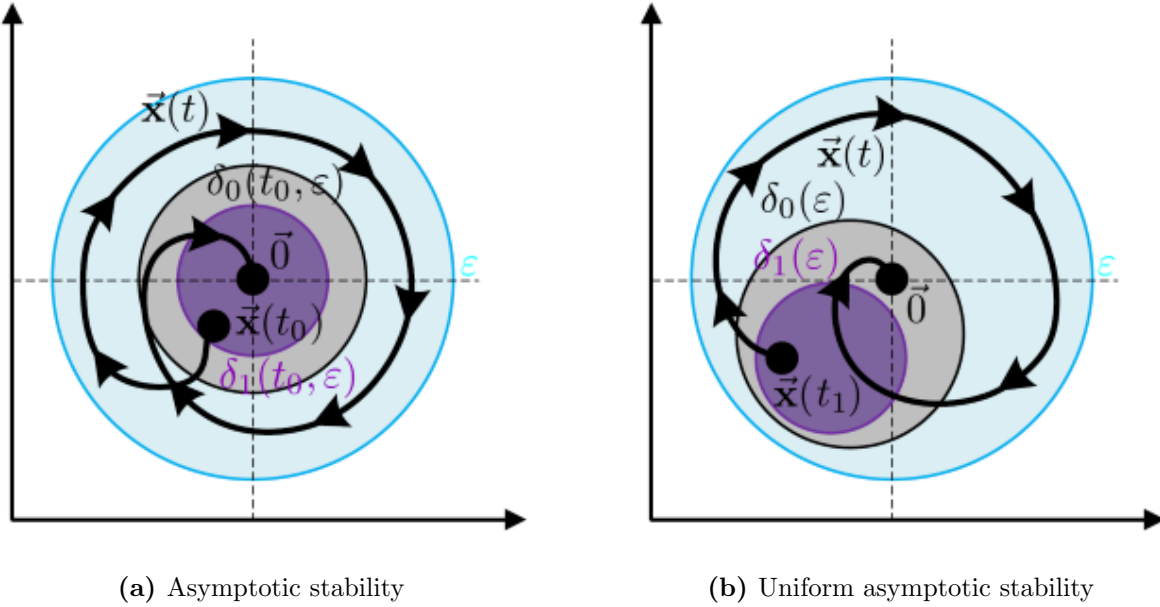


Figure 4.4: Trajectory illustrations for **AS** and **UAS**

Uniform asymptotic stability (**UAS**), an extension of uniform stability, occurs when the asymptotically stable bound region $\delta_1(\varepsilon)$ is independent of the principle starting t_0 . An equilibrium point is **UAS** iff conditions for **S** are met and that:

$$\exists \delta_1(\varepsilon) > 0 : \|\vec{x}(t_1)\| < \delta_1(\varepsilon), \quad t_1 \geq t_0 \quad (4.13a)$$

$$\Rightarrow \lim_{t \rightarrow \infty} \|\vec{x}(t)\| \rightarrow 0 \quad (4.13b)$$

A uniformly asymptotic equilibrium point implies stability from a non-concentric ball of attraction; settling to the origin (illustrated in Fig:4.4b).

An equilibrium point is regarded as exponentially stable (**UES**) if conditions for **UAS** are met and that there exist $\exists a, b, r$ that bound the settling of the trajectory such that:

$$\|\vec{x}(t, t_0, \vec{x}_0)\| \leq a \|\vec{x}_0\| e^{-bt}, \quad \forall \|\vec{x}_0\| \leq r \quad (4.14)$$

The term $a \|\vec{x}_0\| e^{-bt}$ bounds the rate at which the trajectory settles to the origin, illustrated in Fig:4.5. The initial point of the trajectory, \vec{x}_0 is bound from above by some $r \triangleq \delta_1(\varepsilon)$. Moreover uniform stability is implied with exponential stability.

The above definitions of stability are only locally defined, and so the stabilities hold true only for local trajectories, only in the case of $\vec{x}(t_0) \leq \varepsilon$. Extending **UAS** to global uniform asymptotic stability (**GUAS**); the origin's equilibrium point is **GUAS** iff conditions for **UAS** are first met, the origin is only the equilibrium point and the asymptotic approach can be extended such that:

$$\exists \delta_1(\varepsilon) > 0 : \|\vec{x}(t_1)\| < \delta_1(\varepsilon), \quad t_1 \geq t_0 \quad (4.15a)$$

$$\Rightarrow \lim_{t \rightarrow \infty} \|\vec{x}(t)\| \rightarrow \vec{0}, \quad \forall \vec{x}(t_0) \quad (4.15b)$$

Similarly exponential stability can extend to the global case iff **UES** conditions are first met. In the global case, the origin can be the only equilibrium point. Stability from Eq:4.14 is then globally:

$$\|\vec{x}(t, t_0)\| \leq a \|\vec{x}_0\| e^{-bt}, \quad \forall \|\vec{x}_0\| \quad (4.16)$$

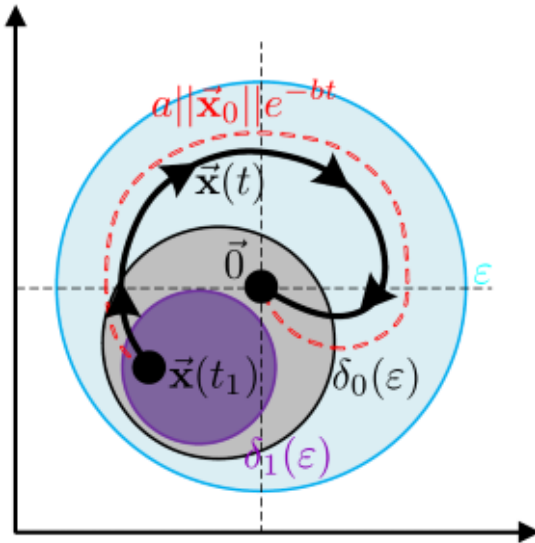


Figure 4.5: Exponential stability, UES

Initial equilibrium point conditions are dropped in Eq:4.16. It follows that, irrespective of the starting point for the trajectory, the system always settles to the origin. **GUES** is the strongest sense of stability and further provides insight into the rate at which the trajectory stabilizes. The most desirable control design outcome is a controller which applies globally uniform exponential stability to a plant.

4.4 Lyapunov Stability Theorem

Lyapunov's stability theory is an important aspect of non-linear control design. An abundance of literature exists on the subject, included in almost every meritable textbook or control paper. If the reader is unfamiliar with Lyapunov's theorem, [15, 85, 105] all explain in detail the concept. The following is adapted from [15] and [56] and briefly outlines how Lyapunov's stability theorem is used to prove (*global*) asymptotic stability for continuous time invariant systems, linear or otherwise.

The theory analyses a generalized energy function of a system's autonomous trajectory. If the trajectory has a negative energy derivative that implies the system's energy will always dissipate towards a stable equilibrium point.

Lyapunov analysis is a powerful method for stability verification, the system's trajectory itself need not be explicitly defined for stability to be ascertained. Proof of Lyapunov's theorem is done with a contradiction disproof and, as such, the theoretical underpinning is somewhat cumbersome.

It's worth reiterating its fundamentals given that backstepping controllers are proposed later in Sec:4.6.3 for attitude control. A backstepping controller iteratively enforces Lyapunov stability criterion onto the system through the control structure, [10, 68, 130]. In general, given a non-linear time invariant system that follows some continually differentiable trajectory $\mathbf{x}(t)$, typically the trajectory is going to progress subject to some rule:

$$\dot{\mathbf{x}}(t) = f(\mathbf{x}(t), u) \quad (4.17)$$

Then, constructing a generalized positive-definite function (generalized energy or *Lyapunov function candidate*) $V(\mathbf{x})$ for a trajectory $\mathbf{x}(t)$. A positive definite matrix, M , is defined such that:

$$\mathbf{z}^T M \mathbf{z} \geq 0 \quad \forall \mathbf{z} \quad (4.18)$$

As such an LFC typically, but not exclusively, has the quadratic and positive-definite form:

$$V(\mathbf{x}) = \mathbf{x}^T P \mathbf{x} \quad (4.19)$$

An LFC could simply be positive semi-definite over the trajectory's bound, the quadratic form is convenient for the use of backstepping. From its definition the trajectory is continually differentiable; there is then a gradient matrix for each component of $V(\vec{x})$ in the form:

$$\nabla V(\vec{x}) \triangleq \left[\frac{\partial V(\vec{x})}{\partial x_1} \frac{\partial V(\vec{x})}{\partial x_2} \dots \frac{\partial V(\vec{x})}{\partial x_n} \right] \quad \vec{x} \in \mathbb{R}^n \quad (4.20)$$

The energy function's derivative, otherwise referred to as the *Lie derivative* [85, 105] is calculated as follows:

$$\dot{V}(\vec{x}) \triangleq \nabla V(\vec{x})^T \frac{d}{dt} f(\vec{x}) = \frac{\delta V(x)}{\delta x_1} \frac{df_1(x)}{dt} + \frac{\delta V(x)}{\delta x_2} \frac{df_2(x_2)}{dt} + \dots + \frac{\delta V(x)}{\delta x_n} \frac{df_n(x)}{dt} \quad (4.21)$$

Lyapunov's theorem states that *iff* the candidate function $V(\vec{x})$ is positive definite with $V(\vec{0}) = 0$ and its derivative is strictly negative; $\dot{V}(\vec{x}) < 0 \quad \forall \vec{x}(t) \neq 0$, the system is then asymptotically stable (**AS** from Eq:4.12). Mathematically that means, for any $\vec{x}(t)$ with $t \geq t_0$:

$$V(\vec{x}(t)) = V(\vec{x}(t_0)) + \int_{t_0}^t \dot{V}(\vec{x}(t)).dt \leq V(\vec{x}(t_0)) \quad (4.22)$$

Which can be physically interpreted as the system's generalized energy function dissipating, irrespective of the trajectory path taken. With a strictly decreasing energy function, the system will stabilize to an equilibrium point.

$$\lim_{t \rightarrow \infty} \|V(\vec{x}(t))\| \rightarrow 0 \quad (4.23)$$

The trajectory's asymptotic stability can be extended to exponential stability boundedness, such that *iff* the same conditions are met and there exists some positive coefficient $\alpha > 0$ such that $\dot{V}(\vec{x}) \leq -\alpha V(\vec{x})$. That implies the system is globally exponentially stable as is bound in such a way that:

$$\|V(\vec{x}(t))\| \leq M e^{-\alpha t/2} \|V(\vec{x}(t_0))\| \quad (4.24)$$

4.5 Model Dependent & Independent Controllers

Two classes of controllers are included for a full state trajectory tracking control loop; both attitude and position control laws. Attitude set-point tracking is the primary focus of this research project (Sec:4.6.1) and incorporates a more detailed schedule of controller design and evaluation.

The allocation law combines both virtual control inputs from attitude and position controllers, $\vec{\nu}_d = [\vec{F}_\mu(u) \ \vec{\tau}_\mu(u)]^T$, to solve for explicit actuator positions. Controller dependency on the plant's state is as a consequence of the actuator responses and complex inertial dynamics, as derived previously in Sec:3.3.1. Whilst not a prerequisite for stability, plant dependent compensation obviously improves controller performances. Independent and dependent cases are only considered for one type of controller; the most basic case PD controller in Section:4.6.2 and tested in Sec:6.2.1. All other control laws compensate for unwanted plant dynamics in a feedback configuration.

The plant dependency makes backstepping controllers an effective controller choice for this dissertation's context. The proposed plant dependent control laws compensate for undesirable dynamics their design, basic PD and PID control structures (*and the like*) will not. The first and most basic control solution, used as a reference case, is a PD controller for attitude and position with direct-inversion (Pseudo or Moore-Penrose inversion) allocation.

4.6 Attitude Control

4.6.1 The Attitude Control Problem

The set-point tracking control problem ([126]) for the attitude plant is to design a stabilizing control torque $\vec{\tau}_d = h(\mathbf{x}_e, t)$ such that for any desired attitude quaternion, $\forall Q_d \in \mathbb{Q}$, and an instantaneous attitude body quaternion, $Q_b(t) \in \mathbb{Q}$, the error state asymptotically stabilizes to the origin; $Q_e \rightarrow [1 \ \vec{0}]^T$. Or that:

$$\vec{\tau}_d = h(Q_d, \dot{Q}_d, Q_b(t), \dot{Q}_b(t)) \text{ such that } \lim_{t \rightarrow \infty} Q_b(t) \rightarrow Q_d \quad (4.25)$$

Quaternion attitude error states are defined as the Hamilton product (*difference*) between the desired and instantaneous quaternion attitude states. Quaternion error states are multiplicative, in contrast with the subtractive relationship for Euler angle error states. The attitude error state is calculated as:

$$Q_e \triangleq Q_b^*(t) \otimes Q_d \quad (4.26)$$

The relative angular velocity error between the body frame, \mathcal{F}^b , and the trajectory's desired frame, \mathcal{F}^d , is given as $\vec{\omega}_e$. The body angular velocity, $\vec{\omega}_b$ is subject to the differential Eq:3.130d. As such there is an angular rate error:

$$\vec{\omega}_e \triangleq \vec{\omega}_d - \vec{\omega}_b(t) \quad (4.27a)$$

The desired angular velocity is taken with respect to the desired angular attitude frame, and so it must be transformed back onto the existing body frame.

$$\vec{\omega}_e = Q_e^* \otimes \vec{\omega}_d \otimes Q_e - \vec{\omega}_b(t) \quad (4.27b)$$

Typically for the trajectories generated here the desired angular velocity is zero; $\vec{\omega}_d = \vec{0}$. It follows that the angular rate error is then simply the negative body angular velocity. It would be easy to incorporate a non-zero angular velocity setpoint to accommodate for higher order state derivative tracking trajectories.

$$\vec{\omega}_e = -\vec{\omega}_b(t) \Big|_{\vec{\omega}_d=\vec{0}} \quad (4.27c)$$

The time derivative of the quaternion error state is calculated from the quaternion derivative definition Eq:3.53. The derivative \dot{Q}_e is then dependent on the angular velocity error and calculated as follows:

$$\dot{Q}_e = \frac{1}{2} Q_e \otimes \vec{\omega}_e = -\frac{1}{2} Q_e \otimes \vec{\omega}_b(t) \Big|_{\vec{\omega}_d=\vec{0}} \quad (4.28)$$

4.6.2 Linear Controllers

PD Controller

The following control law is used as a reference case for comparison of the remaining controllers derived. It is a simple Proportional-Derivative attitude controller, adapted from [37] and following a stability proof similar to the one derived in [126]. An attitude PD controller is proportional only to the vector quaternion error. Such that the error is the same dimension as the angular velocity error; $\in \mathbb{R}^3$. A PD controller designs the control torque as:

$$\vec{\tau}_{PD} = K_d \vec{\omega}_e + K_p \vec{q}_e \quad [Nm], \quad \in \mathcal{F} \quad (4.29)$$

Where both K_d and K_p are positive definite symmetrical 3×3 coefficient matrices to be determined later. Eq:4.29 neglects the quaternion scalar error and is therefore susceptible to unwinding. Using a positive-definite Lyapunov function candidate V_{PD} for the attitude trajectory:

$$V_{PD}(\vec{q}_e, \vec{\omega}_e) = K_p \vec{q}_e^T \vec{q}_e + K_p (|q_0| - 1)^2 + \frac{1}{2} \vec{\omega}_e^T J_b(u) \vec{\omega}_e \quad (4.30)$$

Recalling the angular velocity differential equation from Eq:3.130d, $\dot{\vec{\omega}}_b$ is:

$$\dot{\vec{\omega}}_b = J_b^{-1}(u) \left(-\vec{\omega}_b \times J_b(u)\vec{\omega}_b - \hat{\tau}_b(u) + \vec{\tau}_g + \vec{\tau}_Q + \vec{\tau}_\mu(u) \right) \in \mathcal{F}^b \quad (4.31)$$

Where $\vec{\tau}_Q$ is a simplified representation of the net aerodynamic torque experienced by the body from the rotating propellers, drawn from Eq:3.132b. Then, exploiting a unit quaternion's inherent property, it follows that:

$$\|Q\| = \vec{q}^T \vec{q} + q_0^2 = \vec{q}^2 + q_0^2 = 1 \quad (4.32)$$

Substituting the angular velocity error state, $\vec{\omega}_e = -\vec{\omega}_b$, the proportional derivative LFC in Eq:4.30 is simplified:

$$V_{PD} = K_p \vec{q}_e^2 + K_p(|q_0|^2 - 2|q_0|) + 1 + \frac{1}{2} \vec{\omega}_e^T J_b(u) \vec{\omega}_e \quad (4.33a)$$

$$= 2K_p(1 - |q_0|) + \frac{1}{2} \vec{\omega}_b^T J_b(u) \vec{\omega}_b \quad (4.33b)$$

Similarly, using the fact that a quaternion's derivative is defined as:

$$\dot{Q} = \begin{bmatrix} -\frac{1}{2} \vec{q}^T \vec{\omega} \\ \frac{1}{2} ([\vec{q}]_\times + q_0 \mathbb{I}_{3 \times 3}) \vec{\omega} \end{bmatrix} \quad (4.34)$$

Substituting the above into the LFC derivative, \dot{V}_{PD} , yields:

$$\dot{V}_{PD} = 2K_p \frac{1}{2} \vec{q}_e^T \vec{\omega}_e + \frac{1}{2} \vec{\omega}_b^T J_b(u) \vec{\omega}_b + \frac{1}{2} \vec{\omega}_b J_b(u) \dot{\vec{\omega}}_b^T \quad (4.35a)$$

$$= -K_p \vec{q}_e^T \vec{\omega}_b + \vec{\omega}_b^T J_b(u) \dot{\vec{\omega}}_b \quad (4.35b)$$

Expanding the angular acceleration $\dot{\vec{\omega}}_b$ and introducing the PD control law from Eq:4.29, $\vec{\tau}_{PD}$ substituted back into the LFC derivative:

$$\rightarrow \dot{V}_{PD} = -K_p \vec{q}_e^T \vec{\omega}_b + \vec{\omega}_b^T \left(-\vec{\omega}_b \times J_b(u) \vec{\omega}_b - \hat{\tau}_b + \vec{\tau}_g + \vec{\tau}_Q - K_d \vec{\omega}_b + K_p \vec{q}_e \right) \quad (4.36a)$$

$$= -K_p \vec{q}_e^T \vec{\omega}_b + K_p \vec{\omega}_b^T \vec{q}_e - \vec{\omega}_b^T K_d \vec{\omega}_b + \vec{\omega}_b^T \left(-\vec{\omega}_b \times J_b(u) \vec{\omega}_b - \hat{\tau}_b + \vec{\tau}_g + \vec{\tau}_Q \right) \quad (4.36b)$$

It follows that the transpose term $\vec{q}_e^T \vec{\omega}_b \iff \vec{\omega}_b^T \vec{q}_e$ is interchangeable as its resultant product is the same. The LCF derivative then simplifies:

$$\therefore \dot{V}_{PD} = -\vec{\omega}_b^T K_d \vec{\omega}_b + \vec{\omega}_b^T \left(-\vec{\omega}_b \times J_b(u) \vec{\omega}_b - \hat{\tau}_b + \vec{\tau}_g + \vec{\tau}_Q \right) \quad (4.36c)$$

Then, as long as $(-\vec{\omega}_b \times J_b(u) \vec{\omega}_b - \hat{\tau}_b + \vec{\tau}_g + \vec{\tau}_Q) \leq \vec{0}$, some basic stability is guaranteed. Under specific circumstances the following assumptions can be made to ensure the asymptotic stability proof can be applied. The stability obviously breaks down if any of the assumptions fail, as such the stability is not global...

1. The inertial matrix, $J_b(u)$, is approximately diagonal which, given the inertia ranges from Eq:2.31 and Eq:2.32, is reasonable. Similarly that the angular rate can be made small with appropriately slow trajectory updates such that the torque gyroscopic cross-product is negligible:

$$\vec{\omega}_b^T (\vec{\omega}_b \times J_b(u) \vec{\omega}_b) \approx \vec{0}$$

2. The actuator rate torque response, $\hat{\tau}_b(u)$, is a second order effect dependent on \dot{u} . Typically the actuator rates are going to be kept small, Fig:3.17 shows torques $\hat{\tau}_b(u)$ for a typical trajectory. For slow attitude steps those position changes are small enough to be considered negligible. The approximation is made:

$$\hat{\tau}_b(u) \approx \vec{0}$$

3. Finally, for the sake of the stability proof, the eccentric gravitational torque arm is neglected, $\vec{\tau}_g \approx \vec{0}$. Such a situation only holds true if $u \approx \vec{0}$ or that servo actuator positions are close to their zero positions.

All of the above assumptions are made under extraneous circumstances and can not be assumed for almost all of the prototype's flight envelope. The plant independent case is considered and simulated in Sec:6.2.1 purely for contrition; mainly to demonstrate the need for plant dependent compensation.

If each of the assumptions made hold true, then the Lyapunov function's derivative is approximately negative definite. The stability proof for a very local trajectory is then:

$$\dot{V}_{PD} \approx -K_p \vec{q}_e^T \vec{\omega}_b + \vec{\omega}_b^T (-K_d \vec{\omega}_b + K_p \vec{q}_e) \quad (4.37a)$$

$$\rightarrow \dot{V}_{PD} = -\vec{\omega}_b^T K_d \vec{\omega}_b = -K_d \|\vec{\omega}_b\|^2 < 0 \quad (4.37b)$$

From Lyapunov stability theorem there then exists the limits for *local* asymptotic stability:

$$\lim_{t \rightarrow \infty} \vec{\omega}_e \rightarrow \vec{0} \quad \therefore \quad \lim_{t \rightarrow \infty} \vec{\omega}_b \rightarrow \vec{0}^- \quad (4.38a)$$

$$\lim_{t \rightarrow \infty} \vec{q}_e \rightarrow \vec{0} \quad \text{and} \quad \lim_{t \rightarrow \infty} (1 - q_0) \rightarrow 0 \quad (4.38b)$$

Hence the quaternion error stabilizes $Q_e \rightarrow [1 \ \vec{0}]^T$ as $t \rightarrow \infty$. The stability shown in Eq:4.37b is only local; introducing plant dependent compensation to the PD control law in Eq:4.29 alleviates the stringent requirements on assumptions 1 through 3. Obviously compensation terms are *state estimates* and so a small degree of uncertainty exists (stability is discussed in Sec:6.6.1):

$$\vec{\tau}_{PD} = \vec{\omega}_b \times J_b(u) \vec{\omega}_b + \hat{\tau}_b(u) - \vec{\tau}_g - \vec{\tau}_Q + K_d \vec{\omega}_e + K_p \vec{q}_e \quad (4.39)$$

The resultant stability proof for the plant dependent case Eq:4.39 is much the same as that for the independent controller, Eq:4.29. The same LCF from Eq:4.30 shows that Eq:4.37b holds for all global trajectories:

$$\rightarrow \dot{V}_{PD} = -\vec{\omega}_b^T K_d \vec{\omega}_b = -K_d \|\vec{\omega}_b\|^2 < \vec{0} \quad \forall(Q_e, \vec{\omega}_b) \quad (4.40)$$

A plant dependent controller is not reliant on the very limiting assumptions needed for independent asymptotic stability to be achieved. The dynamic compensation in Eq:4.39 is simple to implement; especially considering the form of unwanted dynamics which have already quantified and corroborated previously in Sec:3.3.2.

Auxiliary Plant Controller

Expanding on what has, in practice (Table:1.1, Sec:1.2.1), proven to be a popular and effective controller for attitude stabilization, [123] proposed an auxiliary plant term to a P-D attitude controller. Most significantly, the altered PD controller adds auxiliary terms proportional to the quaternion rate error (Eq:3.53). Moreover part of the auxiliary plant is proportional to the *quaternion scalar* q_0 , a term that is otherwise neglected in the previous PD control law (Sec:4.6.2) and prevents unwinding if incorporated. The *auxilliarily* PD control torque is a function of errors states:

$$\vec{\tau}_{XPD} = \underbrace{-\Gamma_2 \tilde{\Omega} - \Gamma_3 \vec{q}_e + J_b(u) \dot{\tilde{\Omega}}}_{\text{Independent}} + \underbrace{\vec{\omega}_b \times J_b(u) \vec{\omega}_b + \hat{\tau}_b - \vec{\tau}_g - \vec{\tau}_Q}_{\text{Compensation}} \quad (4.41)$$

Wherein the coefficients Γ_2 and Γ_3 are both diagonal positive definite coefficient matrices whilst Γ_1 , used next in Eq:4.42, is a symmetrical matrix. Each coefficient matrix is explicitly determined later. Auxiliary plants $\tilde{\Omega}$ and $\dot{\tilde{\Omega}}$ are defined as follows. The first auxiliary plant $\tilde{\Omega}$ is proportional to the quaternion error and hence its derivative $\dot{\tilde{\Omega}}$ is a quaternion rate:

$$\tilde{\Omega} \triangleq -\Gamma_1 \vec{q}_e \quad \therefore \quad \dot{\tilde{\Omega}} = -\Gamma_1 \dot{\vec{q}}_e \quad (4.42a)$$

$$\rightarrow \dot{\tilde{\Omega}} = -\frac{1}{2} \Gamma_1 (q_0 \mathbb{I}_{3 \times 3} + [\vec{q}_e]_{\times}) \vec{\omega}_e \quad (4.42b)$$

$$= \frac{1}{2} \Gamma_1 (q_0 \mathbb{I}_{3 \times 3} + [\vec{q}_e]_{\times}) \vec{\omega}_b \Big|_{\vec{\omega}_e = -\vec{\omega}_b} \quad (4.42c)$$

The second auxiliary plant, $\tilde{\Omega}$, is proportional to both quaternion vector and angular velocity errors.

$$\tilde{\Omega} \triangleq \vec{\omega}_e - \bar{\Omega} = \vec{\omega}_e + \Gamma_1 \vec{q}_e \quad (4.43a)$$

$$= -\vec{\omega}_b + \Gamma_1 \vec{q}_e \Big|_{\vec{\omega}_e = -\vec{\omega}_b} \quad (4.43b)$$

Using an LFC similar to the basic V_{PD} function candidate from Eq:4.30, but substituting an auxiliary term $\tilde{\Omega}$ for the body's angular velocity $\vec{\omega}_b$ into the LFC V_{XPD} :

$$V_{XPD}(\vec{q}_e, \tilde{\Omega}) = \vec{q}_e^T \vec{q}_e + (|q_0| - 1)^2 + \frac{1}{2} \tilde{\Omega}^T (\Gamma_3^{-1} J_b(u)) \tilde{\Omega} \quad (4.44)$$

Again using the simplification from a quaternion's inherent properties in Eq:4.32, the LFC from Eq:4.44 then simplifies with the following derivative:

$$V_{XPD} = 2(1 - |q_0|) + \frac{1}{2} \tilde{\Omega}^T (\Gamma_3^{-1} J_b(u)) \tilde{\Omega} \quad (4.45a)$$

$$\dot{V}_{XPD} = 2 \frac{1}{2} \vec{q}_e^T \vec{\omega}_e + \frac{1}{2} \dot{\tilde{\Omega}}^T (\Gamma_3^{-1} J_b(u)) \tilde{\Omega} + \frac{1}{2} \tilde{\Omega}^T (\Gamma_3^{-1} J_b(u)) \dot{\tilde{\Omega}} \quad (4.45b)$$

$$\dot{V}_{XPD} = -\vec{q}_e^T \vec{\omega}_b + \frac{1}{2} \dot{\tilde{\Omega}}^T (\Gamma_3^{-1} J_b(u)) \tilde{\Omega} + \frac{1}{2} \tilde{\Omega}^T (\Gamma_3^{-1} J_b(u)) \dot{\tilde{\Omega}} \Big|_{\vec{\omega}_e = -\vec{\omega}_b} \quad (4.45c)$$

It then follows, substituting $\dot{\vec{\omega}}_b$ from Eq:4.43, the auxiliary plant's derivative $\dot{\tilde{\Omega}}$ is:

$$\dot{\tilde{\Omega}} = -\dot{\vec{\omega}}_b + \Gamma_1 \dot{\tilde{\Omega}} \quad (4.46a)$$

$$\rightarrow \dot{\vec{\omega}}_b = J_b^{-1}(u)(-\vec{\omega}_b \times J_b(u)\vec{\omega}_b - \hat{\tau}_b + \vec{\tau}_g + \vec{\tau}_Q + \vec{\tau}_{XPD}) \quad (4.46b)$$

$$\therefore \dot{\tilde{\Omega}} = -J_b^{-1}(u)(-\vec{\omega}_b \times J_b(u)\vec{\omega}_b - \hat{\tau}_b + \vec{\tau}_g + \vec{\tau}_Q + \vec{\tau}_{XPD}) - \Gamma_1 \dot{\tilde{\Omega}} \quad (4.46c)$$

Substituting the auxiliary PD control law, $\vec{\tau}_{XPD}$ from Eq:4.41, into the auxiliary derivative $\dot{\tilde{\Omega}}$:

$$\rightarrow \dot{\tilde{\Omega}} = J_b^{-1}(u)(J_b(u)\dot{\tilde{\Omega}} - \Gamma_2 \tilde{\Omega} - \Gamma_3 \vec{q}_e) - \dot{\tilde{\Omega}} \quad (4.46d)$$

$$= J_b^{-1}(u)(-\Gamma_2 \tilde{\Omega} - \Gamma_3 \vec{q}_e) \quad (4.46e)$$

From the *approximately* diagonal inertial matrix $J_b(u)$ and the positive symmetric (or *diagonal*) properties of the coefficient matrices Γ_1, Γ_2 and Γ_3 ; the auxiliary plant $\dot{\tilde{\Omega}}$ has a transpose:

$$\dot{\tilde{\Omega}}^T = J_b^{-1}(-\Gamma_2 \tilde{\Omega}^T - \Gamma_3 \vec{q}_e^T) \quad (4.47)$$

The PD auxiliary plant component(s) in the LFC derivative \dot{V}_{XPD} in Eq:4.44 simplifies:

$$\frac{1}{2} \dot{\tilde{\Omega}}^T (\Gamma_3^{-1} J_b(u)) \tilde{\Omega} = \frac{1}{2} (-\Gamma_2 \tilde{\Omega}^T - \Gamma_3 \vec{q}_e^T) \Gamma_3^{-1} \tilde{\Omega} \quad (4.48a)$$

$$= \frac{1}{2} (-\tilde{\Omega}^T \Gamma_2 \Gamma_3^{-1} \tilde{\Omega} - \vec{q}_e^T \tilde{\Omega}) \quad (4.48b)$$

Substituting Eq:4.43 for $\vec{q}_e^T \tilde{\Omega}$ into Eq:4.48b:

$$\rightarrow \frac{1}{2} \dot{\tilde{\Omega}}^T (\Gamma_3^{-1} J_b(u)) \tilde{\Omega} = \frac{1}{2} (-\tilde{\Omega}^T \Gamma_2 \Gamma_3^{-1} \tilde{\Omega} + \vec{q}_e^T \vec{\omega}_b - \vec{q}_e^T \Gamma_1 \vec{q}_e) \Big|_{\vec{q}_e^T \tilde{\Omega} = -\vec{q}_e^T \vec{\omega}_b + \Gamma_1 \vec{q}_e^T} \quad (4.48c)$$

Similarly, for the transposed counterpart of Eq:4.48c in Eq:4.45c:

$$\frac{1}{2} \tilde{\Omega}^T (\Gamma_3^{-1} J_b(u)) \dot{\tilde{\Omega}} = \frac{1}{2} (-\tilde{\Omega}^T \Gamma_2 \Gamma_3^{-1} \tilde{\Omega}^T + \vec{q}_e^T \vec{\omega}_b^T - \vec{q}_e^T \Gamma_1 \vec{q}_e^T) \quad (4.48d)$$

Which, when substituted back into Eq:4.45c, then simplifies the LFC derivative to negative definite:

$$\Rightarrow \dot{V}_{XPD} = -\vec{q}_e^T \Gamma_1 \vec{q}_e - \tilde{\Omega} \Gamma_2 \Gamma_3^{-1} \tilde{\Omega}^T < 0 \quad \forall (\vec{q}_e, \tilde{\Omega}) \quad (4.49)$$

As such, the control law $\vec{\tau}_{XPD}$ asymptotically stabilizes the attitude plant globally. Both $\tilde{\Omega}$ and \vec{q}_e tend to $\vec{0}$, or more specifically the following global stability limits exist:

$$\lim_{t \rightarrow \infty} \vec{q}_e = \vec{0} \quad \text{and} \quad \lim_{t \rightarrow \infty} \tilde{\Omega} = \vec{0} \quad (4.50a)$$

Then, from the auxiliary plant definition(s) in Eq:4.43, the extended limits present themselves;

$$\lim_{t \rightarrow \infty} \vec{\omega}_b = \vec{0} \Big|_{\vec{\omega}_d = \vec{0}} \quad \text{and} \quad \lim_{t \rightarrow \infty} \bar{\Omega} = \vec{0} \quad (4.50b)$$

Whilst global asymptotic stability is indeed satisfactory, faster exponential stability is obviously more desirable. The stability proof for V_{XPD} can be extended to a stable exponentially bounded trajectory. From a quaternion's inherent definition it follows that $0 \leq |q_0| \leq 1$. It can then be stated that:

$$1 - |q_0| \leq 1 - q_0^2 = \|\vec{q}_e\|^2 \quad (4.51)$$

Exponential stability is a maximum boundedness proof; the relationship Eq:4.51 can then replace the quaternion scalar term $2(1 - |q_0|)$ in V_{XPD} as an upper bound. The LFC is then rewritten in terms of its component's norm(s) to produce a bounding inequality:

$$V_{XPD} = \vec{q}_e^T \vec{q}_e + (|q_0| - 1)^2 + \frac{1}{2} \tilde{\Omega}^T (\Gamma_3^{-1} J_b(u)) \tilde{\Omega} \quad (4.52a)$$

$$\rightarrow V_{XPD} \leq 2 \|\vec{q}_e\|^2 + \frac{1}{2} \Gamma_3^{-1} J_b(u) \|\tilde{\Omega}\|^2 \quad (4.52b)$$

Similarly the LFC's derivative can be written in terms of its norms as:

$$\dot{V}_{XPD} \leq -\Gamma_2 \Gamma_3^{-1} \|\tilde{\Omega}\|^2 - \Gamma_1 \|\vec{q}_e\|^2 \quad (4.52c)$$

The LFC, V_{XPD} , has a maximum such that:

$$V_{XPD} \leq \max \left\{ 2, \frac{\lambda_{\max}(\Gamma_3^{-1} J_b(u))}{2} \right\} (\|\vec{q}_e\|^2 + \|\tilde{\Omega}\|^2) \quad (4.53)$$

Where the function λ_{\max} represents the maximum eigenvalue of its argument; in this case $\Gamma_3^{-1} J_b(u)$. Similarly the *negative definite* LCF derivative is bound by the minimum:

$$\dot{V}_{XPD} \leq -\min \{ \lambda_{\min}(\Gamma_1), \lambda_{\min}(\Gamma_2 \Gamma_3^{-1}) \} (\|\vec{q}_e\|^2 + \|\tilde{\Omega}\|^2) \quad (4.54)$$

Therefore there exists some ratio $\alpha > 0$ that satisfies the relationship requirement between the LCF and its derivative; $\dot{V}_{XPD} \leq -\alpha V_{XPD}$, where α is defined as the ratio:

$$\alpha = \frac{\min \{ \lambda_{\min}(\Gamma_1), \lambda_{\min}(\Gamma_2 \Gamma_3^{-1}) \}}{\max \{ 2, \frac{\lambda_{\max}(\Gamma_3^{-1} J_b(u))}{2} \}} \quad (4.55)$$

The attitude trajectory $(\vec{q}_e(t), \tilde{\Omega}(t))$ is then exponentially bounded by:

$$(\|\vec{q}_e(t)\|, \|\tilde{\Omega}(t)\|) \leq M e^{-\alpha t/2} (\|\vec{q}_e(0)\|, \|\tilde{\Omega}(0)\|) \quad (4.56)$$

The bounding exponential coefficient α can be found using maximum Eigen values for the maximum inertia $J_b(u_\Lambda)$ from Eq:2.31. Using the relationship in Eq:4.56 and testing proposed controller coefficients for Γ_1 , Γ_2 , Γ_3 the settling rate can be optimized.

The above stability proof for the auxiliary attitude controller was expanded upon and derived from [123], adapted to fit attitude setpoint tracking. Introduction of the quaternion error, which is dependent on the quaternion scalar, dramatically improves controller performance. The exponential stability notably improves settling times and overshoot errors, demonstrated in Sec:6.2.2.

Interestingly a previously [64] was the precursor for PD based attitude plants with asymptotic exponential stability. That proposed control law first did not make use of any defined *auxiliary plants*, unlike Eq:4.41; however equivalent terms were effectively incorporated. The control law was developed for spacecraft attitude tracking and proposed a very similar exponentially stabilizing control scheme to that of $\vec{\tau}_{XPD}$. That controller, when changed to the notational convention used above, designs body torque as:

$$\vec{\tau}'_{XPD} = -\frac{1}{2} \left[([\vec{q}_e]_\times + q_0 \mathbb{I}_{3 \times 3}) \Gamma_1 + \alpha (1 - q_0 \mathbb{I}_{3 \times 3}) \right] \vec{q}_e - \Gamma_2 \vec{\omega}_b \in \mathcal{F}^b \quad (4.57)$$

Eq:4.57 could easily incorporate plant dependent compensation to accomodate for unwanted non-linear dynamics. Both exponentially stabilizing PD controllers, from Eq:4.41 and above Eq:4.57, bear a striking similarity to the ideal backstepping controllers derived next in Eq:4.66.

4.6.3 Non-linear Controllers

Backstepping controllers([10,67,69],etc...) are a popular choice for non-linear attitude control plants. The process, through iterative design, enforces Lyapunov stability criteria to ensure asymptotic stability. A report, [130], surveys the fundamentals of backstepping procedure. Ideal backstepping control (*IBC*) is a precise control solution which requires exact plant matching, something that is difficult to achieve in practice. Considering that some state estimate, $\hat{\mathbf{x}}(t)$ is used for feedback control. The caveat of IBC control is poor robust stability performance; being especially susceptible to state dependent uncertainty. Unmodelled disturbances could easily drive the energy function away from stability conditions. The ideal backstepping algorithm can then be extended to incorporate such uncertainties. Adatively including disturbance and *estimate* uncertainty into the LFC energy function improves the stability's robustness (Adaptive backstepping control, *ABC*). By Lyapunov's theorem the respective estimation error terms are stabilized.

Ideal Backstepping Controller

Starting with the ideal case for the first proposed backstepping controller, similar to [69]; it is assumed the attitude plant described in Eq:3.130d from the consolidated model in Sec:3.4 exactly matches the dynamics of the physical prototype. The ideal backstepping controller aims to compensate for the plant's dynamic response to trajectory inputs perfectly. Neglecting uncertainties associated with the dynamic model, the aim here is to apply a stabilizing torque design. Recalling the quaternion tracking error from Eq:4.26; $Q_e = Q_b^* \otimes Q_e$, considering the first LFC proposal:

$$V_1(\vec{q}_e) = \vec{q}_e^T \vec{q}_e + (|q_0| - 1)^2 \quad (4.58)$$

The absolute $|q_0|$ quaternion scalar is applied to ensure global stability. After substituting in the quaternion derivatives and *without* using the quaternion simplification in Eq:4.33, has a Lie derivative:

$$\dot{V}_1 = 2\vec{q}_e^T \frac{1}{2} ([\vec{q}_e]_\times + q_0 \mathbb{I}_{3 \times 3}) \vec{\omega}_e - 2(q_0 - 1) \frac{1}{2} \vec{q}_e^T \vec{\omega}_e \quad (4.59a)$$

$$= \vec{q}_e^T ([\vec{q}_e]_\times + q_0 \mathbb{I}_{3 \times 3}) \vec{\omega}_e - q_0 \vec{q}_e^T \vec{\omega}_e + \vec{q}_e^T \vec{\omega}_e \quad (4.59b)$$

Simplifying and then substituting $\vec{\omega}_e = \vec{\omega}_d - \vec{\omega}_b = \vec{0} - \vec{\omega} - b$:

$$= \vec{q}_e^T [\vec{q}_e]_\times \vec{\omega}_e + \vec{q}_e^T \vec{\omega}_e \quad (4.59c)$$

$$= -\vec{q}_e^T [\vec{q}_e]_\times \vec{\omega}_b - \vec{q}_e^T \vec{\omega}_b \Big|_{\vec{\omega}_e = -\vec{\omega}_b} \quad (4.59d)$$

Then choosing the first virtual backstepping control input γ_d . Note that γ_d is used here to *differentiate the backstepping design value* from the trajectory commanded $\vec{\omega}_d$, Eq:4.27a. Choosing γ_d such that the first LFC Eq:4.58 is negative definite, $\dot{V}_1 < 0$:

$$\vec{\omega}_b \Rightarrow \gamma_d = \Gamma_1 \vec{q}_e \quad (4.60)$$

Where Γ_1 is the first symmetric positive definite gain matrix, a fact that is important to stress due to positive definite matrix's invertability. That backstepping input simplifies the LFC derivative \dot{V}_1 to the negative definite term:

$$\dot{V}_1 = -\vec{q}_e^T [\vec{q}_e]_{\times} \gamma_d - \vec{q}_e^T \gamma_d \quad (4.61a)$$

$$= -\vec{q}_e^T [\vec{q}_e]_{\times} \Gamma_1 \vec{q}_e - \vec{q}_e^T \Gamma_1 \vec{q}_e \quad (4.61b)$$

And considering a vector cross product with itself has a zero resultant, $\vec{q}_e^T [\vec{q}_e]_{\times} = \vec{0}$, \dot{V}_1 then reduces:

$$= -\vec{q}_e^T \Gamma_1 \vec{q}_e < 0 \quad (4.61c)$$

However, that backstepping input γ_d has its own associated error. A stabilizing law z_1 needs to control that error:

$$z_1 \triangleq \gamma_d - \vec{\omega}_b = \Gamma_1 \vec{q}_e - \vec{\omega}_b \Big|_{\gamma_d=\Gamma_1 \vec{q}_e} \quad (4.62a)$$

$$\rightarrow \vec{\omega}_b = \Gamma_1 \vec{q}_e - z_1 \quad (4.62b)$$

$$\therefore \dot{V}_1 = -\vec{q}_e^T \vec{\omega}_b = -\vec{q}_e^T (\Gamma_1 \vec{q}_e - z_1) \Big|_{\vec{\omega}_b \Rightarrow \gamma_d} \quad (4.62c)$$

$$= -\vec{q}_e^T \Gamma_1 \vec{q}_e + \vec{q}_e^T z_1 \quad (4.62d)$$

Introducing that error z_1 into a second LCF, which expands the first proposed V_1 . And exploiting the fact that Γ_1 is symmetrical:

$$V_2(\vec{q}_e, z_1) = V_1(\vec{q}_e) + \frac{1}{2} z_1^T z_1 \quad (4.63a)$$

$$= \vec{q}_e^T \vec{q}_e + (|q_0| - 1)^2 + \frac{1}{2} z_1^T z_1 \quad (4.63b)$$

That first error z_1 has its own time derivative, and recalling the body's angular acceleration $\dot{\vec{\omega}}_b$ from earlier with an undefined input $\vec{\tau}_{IBC}$, which still has plant dependency compensation.

$$\dot{z}_1 = \Gamma_1 \dot{\vec{q}}_e - \dot{\vec{\omega}}_b \quad (4.64a)$$

$$= \frac{\Gamma_1}{2} ([\vec{q}_e]_{\times} + q_0 \mathbb{I}_{3 \times 3}) \vec{\omega}_e - \dot{\vec{\omega}}_b \quad (4.64b)$$

$$= -\dot{\vec{\omega}}_b - \frac{\Gamma_1}{2} ([\vec{q}_e]_{\times} + q_0 \mathbb{I}_{3 \times 3}) \vec{\omega}_b \Big|_{\vec{\omega}_e=-\vec{\omega}_b} \quad (4.64c)$$

$$= -J_b(u)^{-1} (-\vec{\omega}_b \times J_b(u) \vec{\omega}_b - \hat{\tau}_b(u) + \vec{\tau}_g + \vec{\tau}_Q + \vec{\tau}_{IBC}) - \frac{\Gamma_1}{2} ([\vec{q}_e]_{\times} + q_0 \mathbb{I}_{3 \times 3}) \vec{\omega}_b \quad (4.64d)$$

So then, following from Eq:4.64d, finding the derivative of \dot{V}_2 with $\dot{V}_1 = -\vec{q}_e^T (\Gamma_1 \vec{q}_e - z_1)$:

$$\begin{aligned} \dot{V}_2 &= -\vec{q}_e^T (\Gamma_1 \vec{q}_e - z_1) - z_1^T \left(J_b^{-1}(u) (-\vec{\omega}_b \times J_b(u) \vec{\omega}_b - \hat{\tau}_b(u) + \vec{\tau}_g + \vec{\tau}_Q + \vec{\tau}_{IBC}) \right. \\ &\quad \left. + \frac{\Gamma_1}{2} ([\vec{q}_e]_{\times} + q_0 \mathbb{I}_{3 \times 3}) \vec{\omega}_b \right) \end{aligned} \quad (4.65a)$$

$$\begin{aligned} &= -\vec{q}_e^T \Gamma_1 \vec{q}_e - z_1^T \left(J_b^{-1}(u) (-\vec{\omega}_b \times J_b(u) \vec{\omega}_b - \hat{\tau}_b(u) + \vec{\tau}_g + \vec{\tau}_Q + \vec{\tau}_{IBC}) \right. \\ &\quad \left. - \vec{q}_e + \frac{\Gamma_1}{2} ([\vec{q}_e]_{\times} + q_0 \mathbb{I}_{3 \times 3}) \vec{\omega}_b \right) \end{aligned} \quad (4.65b)$$

So then proposing the exactly matched stabilizing backstepping control law:

$$\vec{\tau}_{IBC} = J_b(u) \vec{q}_e - \frac{J_b(u) \Gamma_1}{2} ([\vec{q}_e]_{\times} + q_0 \mathbb{I}_{3 \times 3}) \vec{\omega}_b + J_b(u) \Gamma_2 z_1 + \vec{\omega}_b \times J_b(u) \vec{\omega}_b + \hat{\tau}_b(u) - \vec{\tau}_g - \vec{\tau}_Q \quad (4.66a)$$

Noting that $z_1 = \vec{\omega}_b - \Gamma_1 \vec{q}_e$, the torque law simplifies:

$$\begin{aligned}
 &= J_b(u) \underbrace{\left(\Gamma_1(1 + \Gamma_2)\vec{q}_e - \frac{\Gamma_1}{2}([\vec{q}_e]_{\times} + q_0 \mathbb{I}_{3 \times 3})\vec{\omega}_b - \Gamma_2 \vec{\omega}_b \right)}_{\text{Ideal backstepping}} \\
 &\quad + \underbrace{\vec{\omega}_b \times J_b(u)\vec{\omega}_b + \hat{\tau}_b(u) - \vec{\tau}_g - \vec{\tau}_Q}_{\text{Compensation}} \in \mathcal{F}^b \quad (4.66b)
 \end{aligned}$$

With Γ_2 being another positive semi-definite symmetric coefficient matrix. Then with the control law $\vec{\tau}_{IBC}$ introduced into the LCF derivative \dot{V}_2 simplifies to negative definite:

$$\dot{V}_2 = -\vec{q}_e^T \Gamma_1 \vec{q}_e - z_1^T \Gamma_2 z_1 < 0 \quad \forall (\vec{q}_e, z_1) \quad (4.67)$$

As such $\vec{q}_e \rightarrow 0$ & $q_0 \rightarrow 1$ as $t \rightarrow \infty$. Similarly $z_1 \rightarrow 0$, which leads to the limit:

$$\lim_{t \rightarrow \infty} (\vec{\omega}_b - \Gamma_1 \vec{q}_e) = 0 \quad (4.68)$$

Because the quaternion error vector already tends to 0; $\vec{q}_e \rightarrow 0$, it follows that $\vec{\omega}_b \rightarrow 0$. It can also be said that, from the definition of $\vec{\omega}_e$, that the angular velocity error stabilizes too. There is a distinct similarity in the structure of $\mu \vec{\tau}_{IBC}$ from Eq:4.66 and that of the auxiliary PD controller presented in Eq:4.41. Furthermore, using the same reasoning from Eq:4.52, the exponential stability proof then follows:

$$V_{IBC} \leq V_2 = 2 \|\vec{q}_e\|^2 + \frac{\Gamma_1^{-1}}{2} \|z_1\|^2 \quad (4.69a)$$

$$\dot{V}_{IBC} \leq \dot{V}_2 = -\Gamma_1 \|\vec{q}_e\|^2 - \Gamma_2 \|z_1\|^2 \quad (4.69b)$$

Then both the energy function and its derivative are bound respectively by:

$$V_{IBC} \leq \max \left\{ 2, \frac{\lambda_{\max}(\Gamma_1^{-1})}{2} \right\} (\|\vec{q}_e\|^2 + \|z_1\|^2) \quad (4.70a)$$

$$\dot{V}_{IBC} \leq \min \{ \lambda_{\min}(\Gamma_1), \lambda_{\min}(\Gamma_2) \} (\|\vec{q}_e\|^2 + \|z_1\|^2) \quad (4.70b)$$

Which then leads to a similar exponential stability trajectory boundedness such that:

$$\dot{V}_{IBC} \leq \alpha V_{IBC} \quad (4.71a)$$

$$\therefore (\|\vec{q}_e(t)\|, \|z_1(t)\|) \leq M e^{-\alpha t/2} (\|\vec{q}_e(0)\|, \|z_1(0)\|) \quad (4.71b)$$

Adaptive Backstepping Controller

As effective as the control law defined above in Section:4.6.3 may be, it lacks suitable disturbance rejection properties. Any plant uncertainties or disturbances encountered would adversely affect the controller in a dramatic manner (Sec:6.6). Introducing a term for lumped uncertainty/disturbance torques, \vec{L} , into the dynamic equations leads to:

$$\dot{\vec{\omega}}_b = \mathbb{I}_b^{-1} (-\vec{\omega}_b \times \mathbb{I}_b \vec{\omega}_b + \vec{\tau}_Q + \vec{\tau}_g + \vec{Q} + \vec{L} + \mu \vec{\tau}) \quad (4.72)$$

It would obviously be easy to simply introduce a compensation term for $-\vec{L}$ into the control law. In practice, however, it is very difficult to approximate a disturbance term without *apriori* knowledge about any of its properties. Noise compensation in sensors can be done easily due to the known frequency bandwidth which that noise occurs in, the same cannot be said for wind disturbances and the like.

An approximate estimation term \hat{L} has to be used for that disturbance compensation in the designed control torque $\mu \vec{\tau}$. That estimate term is then going to have its own error from the physical disturbance affecting the system:

$$\tilde{L} = \vec{L} - \hat{L} \quad (4.73)$$

The purpose of adaptive backstepping is to introduce that estimate error term into an LCF and develop a derivative term for $\dot{\hat{L}}$, or a disturbance update law, such that even the estimate error asymptotically stabilizes. Typically, that disturbance update rule is the contribution of satellite and general attitude control papers. Similar terms can be introduced for plant uncertainty which can similarly be adapted for but are not included here...

The estimate error is then introduced into the LCF from an ideal backstepping control, in order for it to be dissipated as per Lyapunov theorem.

$$V_{ABC}(\vec{q}_e, z_1, \tilde{L}) = V_{IBC}(\vec{q}_e, z_1) + \frac{1}{2}\tilde{L}^T\Gamma_L^{-1}\tilde{L} \quad (4.74a)$$

$$= \vec{q}_e^T\vec{q}_e + (q_0 - 1)^2 + \frac{1}{2}z_1^T\Gamma_1^{-1}z_1 + \frac{1}{2}\tilde{L}^T\Gamma_L^{-1}\tilde{L} \quad (4.74b)$$

Where the positive symmetric matrix $\Gamma_L \geq 0 \in \mathbb{R}^{3 \times 3}$ is termed as the adaptation gain coefficient matrix. Those particular coefficients determine how responsive the system is to disturbances and the rate at which it adapts to compensate for them. Then, to prove stability one starts with the Lie derivative \dot{V}_{ABC} :

$$\dot{V}_{ABC}(\vec{q}_e, z_1, \tilde{L}) = \dot{V}_{IBC}(\vec{q}_e, z_1) + \frac{1}{2}\dot{\tilde{L}}^T\Gamma_L^{-1}\tilde{L} + \frac{1}{2}\tilde{L}^T\Gamma_L^{-1}\dot{\tilde{L}} \quad (4.75)$$

Recalling the definition of \tilde{L} from Eq:4.73. For its derivative $\dot{\tilde{L}}$ it's reasonable to assume the dynamics of the physical disturbance \tilde{L} are far slower than the time constant of the control system, or that $\dot{\tilde{L}} \ll \dot{\hat{L}}$. Then it follows:

$$\dot{\tilde{L}} = \dot{\hat{L}} - \dot{\hat{L}} \approx \vec{0} - \dot{\hat{L}} = -\dot{\hat{L}} \quad (4.76)$$

Substituting that estimation error rate back into the derivative \dot{V}_{ABC} , which expands upon Eq:4.65, yields:

$$\begin{aligned} \dot{V}_{ABC}(\vec{q}_e, z_1, \tilde{L}) &= \vec{q}_e^T(z_1 - \Gamma_1\vec{q}_e) + z_1^T\Gamma_1^{-1}\left(\mathbb{I}_b^{-1}(-\vec{\omega}_b \times \mathbb{I}_b\vec{\omega}_b + \vec{\tau}_Q + \vec{\tau}_g + \vec{Q} + \vec{L} + \mu\vec{\tau})\right. \\ &\quad \left.+ \frac{\Gamma_1}{2}([\vec{q}_e]_\times + q_0\mathbb{I}_{3 \times 3})\vec{\omega}_b\right) - \tilde{L}^T\Gamma_L^{-1}\dot{\hat{L}} \end{aligned} \quad (4.77a)$$

And using a similar control law to $\mu\vec{\tau}_{IBC}$, which has a disturbance estimate compensation term:

$$\mu\vec{\tau}_{ABC} = \vec{\omega}_b \times \mathbb{I}_b\vec{\omega}_b - \vec{\tau}_Q - \vec{\tau}_g - \vec{Q} - \hat{L} - \mathbb{I}_b\Gamma_1\vec{q}_e - \frac{\Gamma_1\mathbb{I}_b}{2}([\vec{q}_e]_\times + q_0\mathbb{I}_{3 \times 3})\vec{\omega}_b - \mathbb{I}_b\Gamma_2z_1 \quad (4.78a)$$

Which reduces the energy function's derivative to:

$$\dot{V}_{ABC} = -\vec{q}_e^T\Gamma_1\vec{q}_e - z_1^T\Gamma_2z_1 + z_1^T\Gamma_1^{-1}\left(\mathbb{I}_b^{-1}(\vec{L} - \hat{L})\right) - \tilde{L}^T\Gamma_L^{-1}\dot{\hat{L}} \quad (4.78b)$$

$$= -\vec{q}_e^T\Gamma_1\vec{q}_e - z_1^T\Gamma_2z_1 + z_1^T(\Gamma_1^{-1}\mathbb{I}_b^{-1})\tilde{L} - \tilde{L}^T\Gamma_L^{-1}\dot{\hat{L}} \quad (4.78c)$$

$$= -\vec{q}_e^T\Gamma_1\vec{q}_e - z_1^T\Gamma_2z_1 + \tilde{L}^T\Gamma_L^{-1}(\Gamma_1^{-1}\Gamma_L\mathbb{I}_b^{-1}z_1 - \dot{\hat{L}}) \quad (4.78d)$$

The decision then needs to be made as to how the disturbance estimate is going to be updated, or what $\dot{\hat{L}}$ is defined as. The clear choice would be to compensate for the final term in the LCF, making it purely negative definite:

$$\dot{\hat{L}} = \Gamma_1^{-1}\Gamma_L\mathbb{I}_b^{-1}z_1 = \Gamma_1^{-1}\Gamma_L\mathbb{I}_b^{-1}\vec{\omega}_b - \Gamma_L\mathbb{I}_b^{-1}\vec{q}_e \quad (4.79)$$

The disturbance is therefore compensated for and the estimate error is ensured to have asymptotic stability seeing that V_{ABC} is positive definite.

$$\dot{V}_{ABC} = -\vec{q}_e^T\Gamma_1\vec{q}_e - z_1^T\Gamma_2z_1 < \vec{0} \quad \forall (\vec{q}_e, z_1, \tilde{L}) \quad (4.80)$$

Exponential stability for the plant however cannot be proven with the above control and disturbance laws, there is no non-zero estimate error coefficient in the LCF derivative. A lot of work has been done on the statistical nature of disturbance approximation and how best to adapt a non-linear control system to the influence of unwanted disturbances. An interesting approach would be to use the previous disturbance estimate, $\tilde{L} = \hat{L}_{n-1}$, such that:

$$\tilde{L}' = \tilde{L} - \hat{L} = (\hat{L}_{n-1} - \hat{L}_n) \quad (4.81a)$$

$$\dot{\hat{L}} = \Gamma_1^{-1} \Gamma_L \mathbb{I}_b^{-1} z_1 + \tilde{L}' \quad (4.81b)$$

$$\dot{\hat{L}} = \Gamma_1^{-1} \Gamma_L \mathbb{I}_b^{-1} \vec{\omega}_b - \Gamma_L \mathbb{I}_b^{-1} \vec{q}_e + (\hat{L}_{n-1} - \hat{L}_n) \quad (4.81c)$$

$$\therefore \dot{V}'_{ABC} = -\vec{q}_e^T \Gamma_1 \vec{q}_e - z_1^T \Gamma_2 z_1 - \tilde{L}^T \Gamma_L^{-1} \tilde{L}' \quad (4.81d)$$

Given that the starting estimate $\hat{L}_0 = \vec{0}$ and that the change of disturbance over a single control cycle is going to be small once the approximator has settled, its fair to assume the following:

$$\lim_{t \rightarrow \infty} \tilde{L}' = (\hat{L}_{n-1} - \hat{L}_n) \rightarrow \tilde{L} \quad (4.82)$$

Then, it leads to the following LCF derivative which can then prove exponential stability. It clear that a coefficient $\dot{V}'_{ABC} \leq \alpha V_{ABC}$ exists and can be found:

$$\dot{V}'_{ABC}(\vec{q}_e, z_1, \tilde{L}) = -\vec{q}_e^T \Gamma_1 \vec{q}_e - z_1^T \Gamma_2 z_1 - \tilde{L}^T \Gamma_L^{-1} \tilde{L} \quad (4.83)$$

The assumption in Eq:4.82 is going to need to be tested in simulation later in Chapter:6; the adaptive gain matrix Γ_L is something that will similarly need to be designed. For control coefficients a separate optimization loop will be run, later disturbance will be introduced and the adaptive gain will independently be attained and optimized.

4.7 Position Control

Only two control laws for position control are proposed. Due to the nature of Coriolis cross-coupling, an attitude plant can be stabilized independently from the position plant, the converse is however not true. A basic Proportional-Derivative control structure is presented as the reference case, thereafter a more complicated adaptive backstepping control algorithm is derived...

The dynamics for position control, Eq:3.130b, include a coupled angular velocity element.

$$\dot{\vec{v}}_b = m^{-1}(-\vec{\omega}_b \times m\vec{v}_b + Q_b^* \otimes m\vec{G}_I \otimes Q_b + \mu\vec{F}) \quad \in \mathcal{F}^b \quad (4.84)$$

Typically, given the standard operating conditions of a quadrotor, it's assumed that $\vec{\omega}_b \approx \vec{0}$. As such the inherent angular velocity coupled dynamics are negligible; $\vec{\omega}_b \times m\vec{v}_b \approx 0$. If the entire state vector, both attitude and position $\mathbf{x}(t) = [\mathcal{E}, Q_b]^T$, of the plant is known then it's easy to compensate for those dynamics rather than making assumptions about their influence on the system given particular operating conditions. That plant dependency can be introduced in the control force $\mu\vec{F}$.

The translational velocity, \vec{v}_b , defined in the body frame is related to the inertial frame through a quaternion transformation:

$$\dot{\mathcal{E}} = Q_b \otimes \vec{v}_b \otimes Q_b^* \quad \in \mathcal{F}^I \quad (4.85)$$

The difference in reference frames is an important distinction between the position and attitude control loops. Position error is calculated purely as a subtractive term:

$$\mathcal{E}_e = \mathcal{E}_d - \mathcal{E}_b \quad \in \mathcal{F}^I \quad (4.86)$$

With $\mathcal{E}_d(t)$ being some desired position designed by the trajectory generation block. The translational velocity error can be similarly calculated but, in the same way angular velocity $\vec{\omega}_d = \vec{0}$, the desired translational velocity is zero.

$$\dot{\mathcal{E}}_e = \dot{\mathcal{E}}_d - \dot{\mathcal{E}}_b = -\dot{\mathcal{E}}_b \Big|_{\dot{\mathcal{E}}_d=\vec{0}} \quad (4.87)$$

The objective for position setpoint tracking is analogous to that of the attitude setpoint tracking. In particular the aim is to produce a stabilizing control law that ensures the position tracking error asymptotically tends to $\vec{0}$:

$$\mu \vec{F} = g(\mathcal{E}_e, \dot{\mathcal{E}}_e) \text{ such that } \lim_{t \rightarrow \infty} \mathcal{E}_e = \vec{0} \quad (4.88)$$

Where $\mu \vec{F}$ is the control force to effect Eq:4.84 $\in \mathcal{F}^b$.

4.7.1 PD Controller

Starting with a simple PD structure to use as a reference case. A plant dependent controller designs the net force proportional to both the position error and the first derivative velocity error¹.

$$\mu \vec{F}_{PD} = K \dot{\mathcal{E}}_e + \alpha \mathcal{E}_e + \vec{\omega}_b \times m \vec{v}_b - m \vec{G}_b \in \mathcal{F}^b \quad (4.89)$$

For the stability proof the error states must be transformed to the body frame \mathcal{F}^b such that the control input and error states all act in a common frame. So defining an error state in the body frame X_e :

$$X_e = Q_b^* \otimes (\mathcal{E}_d - \mathcal{E}_b) \otimes Q_b = X_d - X_b \quad (4.90a)$$

$$\dot{X}_e = Q_b^* \otimes (\dot{\mathcal{E}}_d - \dot{\mathcal{E}}_b) \otimes Q_b = -Q_b^* \otimes \dot{\mathcal{E}}_b \otimes Q_b = -\vec{v}_b \Big|_{\dot{\mathcal{E}}_d=\vec{0}} \quad (4.90b)$$

As such the control law from Eq:4.89, despite being $\in \mathcal{F}^b$ has arguments $\mathcal{E}, \dot{\mathcal{E}} \in \mathcal{F}^I$, which must similarly transform to:

$$\mu \vec{F}_{PD} = K \dot{X}_e + \alpha X_e + \vec{\omega}_b \times m \vec{v}_b - m \vec{G}_b \quad (4.91a)$$

$$= -K \vec{v}_b + \alpha X_e + \vec{\omega} \times m \vec{v}_b - m \vec{G}_b \quad (4.91b)$$

Then using a p.d Lyapunov candidate function:

$$V_{PD}(X_e, \dot{X}_e) = \frac{\alpha}{2} X_e^T X_e + \frac{m}{2} \dot{X}_e^T \dot{X}_e = \frac{\alpha}{2} X_e^T X_e + \frac{m}{2} \vec{v}_b^T \vec{v}_b \quad (4.92)$$

Then calculating the LCF derivative with the PD control law substituted:

$$\dot{V}_{PD} = \alpha X_e^T \dot{X}_e + \vec{v}_b^T m \vec{v}_b = -\alpha X_e^T \vec{v}_b + \vec{v}_b^T m \vec{v}_b \quad (4.93a)$$

$$= -\alpha X_e^T \vec{v}_b + \vec{v}_b^T (-\vec{\omega}_b \times m \vec{v}_b + m \vec{G}_b + \mu \vec{F}_{PD}) \quad (4.93b)$$

$$= -\alpha X_e^T \vec{v}_b + \vec{v}_b^T (-K \vec{v}_b + \alpha X_e) \quad (4.93c)$$

$$\Rightarrow \dot{V}_{PD} = -K \vec{v}_b^T \vec{v}_b < \vec{0} \quad \forall (X_e, \dot{X}_e) \quad (4.93d)$$

It then follows that the following global asymptotically² stabilizing limits exist:

$$\lim_{t \rightarrow \infty} X_e = Q_b^* \otimes (\mathcal{E}_d - \mathcal{E}_b) \otimes Q_b = \vec{0} \quad (4.94a)$$

$$\therefore \lim_{t \rightarrow \infty} \mathcal{E}_b = \mathcal{E}_d \quad (4.94b)$$

$$\lim_{t \rightarrow \infty} \dot{X}_e = Q_b^* \otimes (\dot{\mathcal{E}}_d - \dot{\mathcal{E}}_b) \otimes Q_b = -\vec{v}_b \Big|_{\dot{\mathcal{E}}_d=\vec{0}} = 0 \quad (4.94c)$$

¹The same P and D coefficient symbols are used for continuity.

²Not exponentially stabilizing however.

4.7.2 Adaptive Backstepping Controller

An adaptive backstepping algorithm, similar to the attitude controller derived previously in Sec:4.6.3, is now applied to position control. The disturbance term, $\vec{D} \in \mathcal{F}^b$, introduced to the differential Eq:4.84 represents any lumped drag and wind forces encountered by the body which weren't quantified numerically in Sec:3.2.3. The backstepping iterations of the position control loop first need to stabilize the position error and then compensate for those disturbances...

$$\dot{\vec{v}}_b = m^{-1}(-\vec{\omega}_b \times m\vec{v}_b + m\vec{G}_b + \vec{D}_b + \mu\vec{F}) \in \mathcal{F}^b \quad (4.95)$$

Obviously the compensation for \vec{D} is going to be an approximation of that physical disturbance term; \hat{D} . Beginning the backstepping process for position with the position state tracking error:

$$z_1 = \mathcal{E}_d - \mathcal{E}_b \quad (4.96)$$

Which then has its own derivative:

$$\dot{z}_1 = \dot{\mathcal{E}}_d - \dot{\mathcal{E}}_b = Q_b \otimes (\vec{0} - \vec{v}_b) \otimes Q_b^* = -Q_b \otimes \vec{v}_b \otimes Q_b^* \quad (4.97)$$

Transforming that error, z_1 , to the body frame \mathcal{F}^b , in the same way as Eq:4.90a, makes the stability proof more concise. That reference frame transformation doesn't affect the Lie derivative as the energy function's gradient depends on its partial derivative w.r.t it's positional trajectory only, namely $\mathcal{E}_e(t)$.

$$\hat{z}_1 = X_e = Q_b^* \otimes z_1 \otimes Q_b = Q_b^* \otimes (\mathcal{E}_d - \mathcal{E}_b) \otimes Q_b \quad (4.98a)$$

$$\therefore \dot{\hat{z}}_1 = Q_b^* \otimes \dot{z}_1 \otimes Q_b = Q_b^* \otimes (\dot{\mathcal{E}}_d - \dot{\mathcal{E}}_b) \otimes Q_b = -\vec{v}_b \quad (4.98b)$$

Then proposing the first positive definite LCF, $V_1(\hat{z}_1)$, in terms of that tracking error:

$$V_1(\hat{z}_1) = \frac{1}{2}\hat{z}_1^T \hat{z}_1 \quad (4.99a)$$

$$\Rightarrow \dot{V}_1 = \hat{z}_1^T \dot{\hat{z}}_1 = -\hat{z}_1^T \vec{v}_b \Big|_{\dot{\mathcal{E}}_d = \vec{0}} \quad (4.99b)$$

The first stabilizing velocity function³, Ω_d , and its associated error, \hat{z}_2 , can be defined as:

$$\vec{v}_b \Rightarrow \Omega_d = \Gamma_1 \hat{z}_1 \quad (4.100a)$$

$$\hat{z}_2 = \Omega_d - \vec{v}_b = \Gamma_1 \hat{z}_1 - \vec{v}_b \quad (4.100b)$$

$$\therefore \vec{v}_b = \Gamma_1 \hat{z}_1 - \hat{z}_2 \quad (4.100c)$$

So that second error state \hat{z}_2 has a derivative:

$$\dot{\hat{z}}_2 = \dot{\Omega}_d - \dot{\vec{v}}_b = \Gamma_1 \dot{\hat{z}}_1 - m^{-1}(-\vec{\omega}_b \times m\vec{v}_b + m\vec{G}_b + \vec{D}_b + \mu\vec{F}) \quad (4.101a)$$

$$= -\Gamma_1 \vec{v}_b - m^{-1}(-\vec{\omega}_b \times m\vec{v}_b + m\vec{G}_b + \vec{D}_b + \mu\vec{F}) \quad (4.101b)$$

Introducing that second error \hat{z}_2 into a new LCF V_2 :

$$V_2(\hat{z}_1, \hat{z}_2) = V_1(\hat{z}_1) + \frac{1}{2}\hat{z}_2^T \hat{z}_2 = \frac{1}{2}\hat{z}_1^T \hat{z}_1 + \frac{1}{2}\hat{z}_2^T \hat{z}_2 \quad (4.102)$$

Which has a derivative:

$$\dot{V}_2 = \hat{z}_1^T \dot{\hat{z}}_1 + \hat{z}_2^T \dot{\hat{z}}_2 = -\hat{z}_1^T \vec{v}_b + \hat{z}_2^T \dot{\hat{z}}_2 \quad (4.103a)$$

$$= -\hat{z}_1^T \vec{v}_b + \hat{z}_2^T \left(-\Gamma_1 \vec{v}_b - m^{-1}(-\vec{\omega}_b \times m\vec{v}_b + m\vec{G}_b + \vec{D}_b + \mu\vec{F}) \right) \quad (4.103b)$$

³Using Ω_d to differentiate from \vec{v}_d which would otherwise be the translational velocity produced from the desired trajectory...

And substituting Eq:4.100c for \vec{v}_b into only the first energy term of the LCF derivative. Specifically; $-\hat{z}_1^T \vec{v}_b = -\hat{z}_1^T (\Gamma_1 \hat{z}_1 - \hat{z}_2)$. The remaining terms for \vec{v}_b are left unchanged:

$$= -\hat{z}_1^T (\Gamma_1 \hat{z}_1 - \hat{z}_2) + \hat{z}_2^T \left(-\Gamma_1 \vec{v}_b - m^{-1} (-\vec{\omega}_b \times m\vec{v}_b + m\vec{G}_b + \vec{D}_b + \mu\vec{F}) \right) \quad (4.103c)$$

$$= -\hat{z}_1^T \Gamma_1 \hat{z}_1 + \hat{z}_2^T \left(-\hat{z}_1 - \Gamma_1 \vec{v}_b - m^{-1} (-\vec{\omega}_b \times m\vec{v}_b + m\vec{G}_b + \vec{D}_b + \mu\vec{F}) \right) \quad (4.103d)$$

An ideal backstepping control law, with the assumption that \vec{D}_b is precisely known, is then:

$$\mu\vec{F}_{IBC} = \vec{\omega}_b \times m\vec{v}_b - m\vec{G}_b - \vec{D}_b - m\hat{z}_1 - m\Gamma_1 \vec{v}_b + m\Gamma_2 \hat{z}_2 \quad (4.104a)$$

$$= \vec{\omega}_b \times m\vec{v}_b - m\vec{G}_b - \vec{D}_b + (\Gamma_1 \Gamma_2 - m) \hat{z}_1 - m(\Gamma_1 + \Gamma_2) \vec{v}_b \quad (4.104b)$$

$$\Rightarrow \dot{V}_{IBC} = \dot{V}_2 = -\hat{z}_1^T \Gamma_1 \hat{z}_1 - \hat{z}_2^T \Gamma_2 \hat{z}_2 < \vec{0} \quad \forall (\hat{z}_1, \hat{z}_2) \& \forall (z_1, z_2) \quad (4.104c)$$

Which clearly leads to asymptotic (*extended to exponential next*) stability under the assumption that the disturbance term \vec{D}_b is known and can be compensated for well. In the controller both Γ_1 & Γ_2 are symmetric positive definite control coefficient matrices to be determined later...

Adjusting the backstepping rule and proposed LCF to incorporate an adaptive disturbance approximation term \hat{D} , similar to the adaptive backstepping attitude controller previously in Sec:4.6.3. That approximation leads to an estimation error \tilde{D} , once again assuming the physical disturbance dynamics \vec{D}_b are far slower than the control dynamics; $\dot{\vec{D}}_b \ll \dot{\hat{D}}$.

$$\tilde{D} = \vec{D}_b - \hat{D} \quad \in \mathcal{F}^b \quad (4.105a)$$

$$\dot{\tilde{D}} = \dot{\vec{D}}_b - \dot{\hat{D}} \approx \vec{0} - \dot{\hat{D}} = -\dot{\hat{D}} \quad (4.105b)$$

$$\rightarrow \mu\vec{F}_{ABC} = \vec{\omega}_b \times m\vec{v}_b - m\vec{G}_b - \hat{D} - m\hat{z}_1 - m\Gamma_1 \vec{v}_d + m\Gamma_2 \hat{z}_2 \quad (4.105c)$$

$$= \vec{\omega}_b \times m\vec{v}_b - m\vec{G}_b - \hat{D} + (\Gamma_1 \Gamma_2 - m) \hat{z}_1 - m(\Gamma_1 + \Gamma_2) \vec{v}_b \quad (4.105d)$$

Then proposing an LCF which includes that disturbance estimate error \tilde{D} and finding its derivative:

$$V_{ABC} = \frac{1}{2} \hat{z}_1^T \hat{z}_1 + \frac{1}{2} \hat{z}_2^T \hat{z}_2 + \frac{1}{2} \tilde{D}^T \Gamma_D^{-1} \tilde{D} \quad (4.106a)$$

$$\Rightarrow \dot{V}_{ABC} = \hat{z}_1^T \dot{\hat{z}}_1 + \hat{z}_2^T \dot{\hat{z}}_2 + \tilde{D}^T \Gamma_D^{-1} \dot{\tilde{D}} \quad (4.106b)$$

$$= -\hat{z}_1^T \Gamma_1 \hat{z}_1 + \hat{z}_2^T \left(-\hat{z}_1 - \Gamma_1 \vec{v}_b - m^{-1} (-\vec{\omega}_b \times m\vec{v}_b + m\vec{G}_b + \vec{D}_b + \mu\vec{F}_{ABC}) \right) - \tilde{D}^T \Gamma_D^{-1} \dot{\hat{D}} \quad (4.106c)$$

$$= -\hat{z}_1^T \Gamma_1 \hat{z}_1 + \hat{z}_2^T \left(-\Gamma_2 \hat{z}_2 - m^{-1} (\vec{D}_b - \hat{D}) \right) - \tilde{D}^T \Gamma_D^{-1} \dot{\hat{D}} \quad (4.106d)$$

$$= -\hat{z}_1^T \Gamma_1 \hat{z}_1 - \hat{z}_2^T \Gamma_2 \hat{z}_2 - \hat{z}_2^T m^{-1} \tilde{D} - \tilde{D}^T \Gamma_D^{-1} \dot{\hat{D}} \quad (4.106e)$$

$$= -\hat{z}_1^T \Gamma_1 \hat{z}_1 - \hat{z}_2^T \Gamma_2 \hat{z}_2 - \tilde{D}^T \Gamma_D^{-1} (m^{-1} \Gamma_D \hat{z}_2 + \dot{\hat{D}}) \quad (4.106f)$$

Then, a self-evident choice for the disturbance update law would be; $\dot{\hat{D}} = -m^{-1} \Gamma_D \hat{z}_2$, which would ensure asymptotic stability. Expanding on that, an interesting solution which could potentially enforce exponential stability would be to use \hat{D}_{n-1} as a disturbance estimate:

$$\dot{\hat{D}} = -m^{-1} \Gamma_D \hat{z}_2 + (\hat{D}_{n-1} - \hat{D}) \quad (4.107a)$$

$$\therefore \dot{V}_{ABC} = -\hat{z}_1^T \Gamma_1 \hat{z}_1 - \hat{z}_2^T \Gamma_2 \hat{z}_2 - \tilde{D}^T \Gamma_D^{-1} (\hat{D}_{n-1} - \hat{D}) \quad (4.107b)$$

$$\approx -\hat{z}_1^T \Gamma_1 \hat{z}_1 - \hat{z}_2^T \Gamma_2 \hat{z}_2 - \tilde{D}^T \Gamma_D^{-1} \tilde{D} < \vec{0} \quad \forall (\hat{z}_1, \hat{z}_2, \tilde{D}) \quad (4.107c)$$

Similarly for the suggested exponentially stable adaptive backstepping controller for the attitude plant, using \hat{D}_{n-1} for an existing disturbance estimate will need to be simulated in order to ascertain if it's a suitable conjecture. Note here that adaptive control laws refer to adaptability to unknown disturbances and not plant model uncertainty which would take a different approach to the backstepping algorithm.

Chapter 5

Controller Allocation

5.1 Allocator slack

Following the higher level control laws, a distribution algorithm is needed to *allocate* out the desired virtual control inputs, $\vec{\nu}_d = [\mu\vec{F} \ \mu\vec{\tau}]^T$, to commanded actuator positions, $u_c \in \mathbb{U}$. The allocation block, $B^\dagger(\mathbf{x}, \vec{\nu}_d, t)$, from the control loop, Fig:4.1, constructs physical actuator positions from the virtual control input. For regular, unconstrained control allocation the solution is posed as an optimization¹ problem; aiming to minimize deviation between the virtual and commanded control inputs, $\vec{\nu}_d$ & $\vec{\nu}_c$ respectively.

$$\min_{u \in \mathbb{U}^{12}, s \in \mathbb{R}^6} (\|Q_s\|) \text{ such that } \vec{\nu}_d - \vec{\nu}_c = h(\mathbf{x}_e, t) - B(\mathbf{x}, t, u) = s \quad (5.1)$$

Where Q_s is some cost function to prioritize the slack variable, s , requirements. Typically that cost function will just be the L_2 norm of the slack. In Eq:5.1 a generalized controller, $h(\mathbf{x}_e, t)$, is used; in the context of a 6-DOF control loop. That controller would combined virtual control inputs $\mu\vec{F}$ and $\mu\vec{\tau}$ for position and attitude control respectively. In the over-actuated case, there exists an entire family of suitable actuator positions u which are all solutions to Eq:5.1. The over-allocation solution is to introduce a secondary cost function², $J(\mathbf{x}, t, u)$, into the optimization problem of Eq:5.1.

$$\min_{u \in \mathbb{U}^{12}, s \in \mathbb{R}^6} (\|Q_s\| + J(\mathbf{x}, u, t)) \text{ such that } h(\mathbf{x}_e, t) - B(\mathbf{x}, u, t) = s \quad (5.2)$$

That secondary control objective $J(\mathbf{x}, t, u)$ and its associated *explicit* solution to Eq:5.2 is the subject of control allocation research. Not much work has been done on over-allocation for aerospace vehicles outside the field of satellite attitude control (Section:1.2.2 for examples). Often satellites are over actuated for the sake of fault tolerance and redundancy [6, 77]. Actuator rate constraints can be further introduced such that u is limited by Δu , constraining sequential actuator position changes.

$$\therefore \min_{u \in \mathbb{U}^{12}, s \in \mathbb{R}^6} (\|Q_s\| + J(\mathbf{x}, u, t)) \text{ s.t. } h(\mathbf{x}_e, t) - B(\mathbf{x}, u, t) = s \\ \text{subject to } u = u_{n-1} + \Delta u, \Delta u \in \mathbb{C} \quad (5.3)$$

Most control allocation paradigms assume a linear, multiplicative relationship with the effectiveness function, hence the abstraction layer which was introduced previously in Eq:4.7. The allocator effectiveness function, when abstracted to a linear matrix multiplication, reduces to:

$$\vec{\nu}_d = h(\mathbf{x}_e, t) \iff B(\mathbf{x}, u, t) = B(\mathbf{x}, t)u = \vec{\nu}_c \quad (5.4)$$

¹Control Allocation by Johansen, et al. [2012] [61] and Control allocation for over actuated systems by Oppenheimer, et al. [2006] [92] both detail the nature of generalized nonlinear allocation loops.

²Or control objective.

With $\vec{\nu}_d$ & $\vec{\nu}_c \in \mathbb{R}^n$, $u \in \mathbb{U} \in \mathbb{R}^m$, $B \in \mathbb{R}^{m \times n}$. That assumption makes addressing the allocation conceptually simpler, accommodating the use of inversion based allocation laws (Sec:??,5.1.2,5.1.3). That abstraction to a multiplicative relationship with decomposed thrust components was suggested in Eq:4.7. The subsequent rotation "inversion" function, $R^\dagger(\mathbf{x}, \vec{F}_i, t)$, to solve for physical actuator positions $(\Omega_i, \lambda_i, \alpha_i)$, is however as yet undefined.

Assuming for the moment there is some allocation rule that, from $\vec{\nu}_d$, designs well four decomposed stabilizing 3-dimensional thrust vectors $\vec{T}_{1 \rightarrow 4}$ to be produced by each motor module. It then follows that each of those four thrust vectors then relate³ to their individual associated actuator positions through a quaternion *rotation*:

$$\vec{T}_i = Q_{M_i} \otimes \vec{T}(\Omega_i) \otimes Q_{M_i}^* \in \mathcal{F}^b \quad (5.5a)$$

$$= Q_z(\sigma_i)Q_y(\alpha_i)Q_x(\lambda_i) \otimes \vec{T}(\Omega_i) \otimes Q_x^*(\lambda_i)Q_y^*(\alpha_i)Q_z^*(\sigma_i) \quad (5.5b)$$

Where each motor thrust vector, $\vec{T}(\Omega_i)$, is:

$$\vec{T}(\Omega_i) = \begin{bmatrix} 0 \\ 0 \\ T(\Omega_i) \end{bmatrix} = \begin{bmatrix} 0 \\ 0 \\ C_T(J)\rho\Omega_i^2 D^4 \end{bmatrix} \in \mathcal{F}^{M_i} \quad (5.5c)$$

In the transformation Eq:5.5a the angle σ_i is an orthogonal \hat{Z} transformation from $\mathcal{F}^b \rightarrow \mathcal{F}^{M_i''}$ from Eq:2.16a. The thrust function $T(\Omega_i)$ is the BEM theory equation using thrust coefficients, Eq:3.132a, in the direction of the rotor shaft's axis of rotation, bound to \hat{Z}_{M_i} . Seeing that quaternion rotation (*transformation*) operators change the reference frame whilst retaining the vector operand's magnitude, it follows that $T(\Omega_i)$, and by extension the propeller speed Ω_i , can be solved for:

$$|\vec{T}_i| = \sqrt{\|[T_x \ T_y \ T_z]\|} = \sqrt{T_x^2 + T_y^2 + T_z^2} = |T(\Omega_i)| = |C_T(J)\rho\Omega_i^2 D^4| \quad (5.6a)$$

$$\rightarrow \Omega_i = \sqrt{\frac{|\vec{T}_i|}{C_T(J)\rho D^4}} = \sqrt{\frac{\sqrt{T_x^2 + T_y^2 + T_z^2}}{C_T(J)\rho D^4}} \quad (5.6b)$$

Then reversing (or *undoing*) the transformation from motor module to body frame in Eq:5.5a:

$$\vec{T}(\Omega_i) = Q_z^*(\sigma_i)Q_y^*(\alpha_i)Q_x^*(\lambda_i) \otimes \vec{T}_i \otimes Q_x(\lambda_i)Q_y(\alpha_i)Q_z(\sigma_i) \in \mathcal{F}^{M_i} \quad (5.7a)$$

$$\rightarrow \vec{T}(\Omega_i) = Q_{M_i}^* \otimes \vec{T}_i \otimes Q_{M_i} \in \mathcal{F}^{M_i} \quad (5.7b)$$

Knowing only $\vec{T}(\Omega_i)$ and \vec{T}_i in the motor frame and body frame respectively requires solving for a quaternion which relates the two. If both vectors are of unit length, \hat{T}_i & $\hat{T}(\Omega_i)$; then the following relationship can be exploited to find a relative quaternion:

$$\hat{T}_i = \frac{\vec{T}_i}{|\vec{T}_i|} = \frac{\vec{T}_i}{\sqrt{T_x^2 + T_y^2 + T_z^2}} \in \mathcal{F}^b \quad (5.8a)$$

$$\hat{T}(\Omega_i) = \frac{\vec{T}(\Omega_i)}{|\vec{T}(\Omega_i)|} = \frac{\vec{T}(\Omega_i)}{|C_T(J)\rho\Omega^2 D^4|} = [0 \ 0 \ 1]^T \in \mathcal{F}^{M_i} \quad (5.8b)$$

$$Q_{M_i} = \begin{bmatrix} q_0 \\ \vec{q} \end{bmatrix} = \begin{bmatrix} 1 + \hat{T}_i \cdot \hat{T}(\Omega_i) \\ -\hat{T}_i \times \hat{T}(\Omega_i) \end{bmatrix} \quad (5.8c)$$

Where Eq:5.8c is an extension of the inherent quaternion definition which rotates a vector around a single Euler axis, Eq:3.46c, when applied to two unit vectors. That quaternion can indeed be used to solve for relative pitch, roll and yaw Euler angles (Appendix:A.3). The problem is that Eq:5.8c solves for the **most direct, shortest path** rotation from one vector to another. In most cases, a sequenced

³Using the quaternion analogue of rotation $\mathcal{F}^{M_i} \rightarrow \mathcal{F}^b$ from Eq:2.16a.

Z-Y-X rotation is by no means the shortest possible path. As a result solutions for $[\phi, \theta, \psi]^T$ from Eq:5.8c won't be meaningful for trying to resolve suitable servo positions λ_i and α_i .

The associated $[\phi, \theta, \psi]^T$ solutions to Eq:A.16 are then of no consequence in trying to solve for sequence of rotation angles⁴ $[\lambda_i, \alpha_i, \sigma_i]^T$. Furthermore, when considering a sequenced Z-Y-X quaternion, no further insight can be extracted without applying cumbersome trigonometric inversions;

$$Q_b = \begin{bmatrix} \cos \frac{\psi}{2} \\ 0 \\ 0 \\ \sin \frac{\psi}{2} \end{bmatrix} \otimes \begin{bmatrix} \cos \frac{\theta}{2} \\ 0 \\ \sin \frac{\theta}{2} \\ 0 \end{bmatrix} \otimes \begin{bmatrix} \cos \frac{\phi}{2} \\ \sin \frac{\phi}{2} \\ 0 \\ 0 \end{bmatrix} \quad (5.9a)$$

$$= \begin{bmatrix} c \frac{\psi}{2} c \frac{\theta}{2} c \frac{\phi}{2} + s \frac{\psi}{2} s \frac{\theta}{2} s \frac{\phi}{2} \\ c \frac{\psi}{2} c \frac{\theta}{2} s \frac{\phi}{2} - s \frac{\psi}{2} s \frac{\theta}{2} c \frac{\phi}{2} \\ c \frac{\psi}{2} s \frac{\theta}{2} c \frac{\phi}{2} + s \frac{\psi}{2} c \frac{\theta}{2} s \frac{\phi}{2} \\ s \frac{\psi}{2} c \frac{\theta}{2} c \frac{\phi}{2} - c \frac{\psi}{2} s \frac{\theta}{2} s \frac{\phi}{2} \end{bmatrix} = \begin{bmatrix} q_0 \\ q_x \\ q_y \\ q_z \end{bmatrix} = \begin{bmatrix} q_0 \\ \vec{q} \end{bmatrix} \quad (5.9b)$$

$$\rightarrow \vec{T}_i = \begin{bmatrix} c \frac{\psi}{2} c \frac{\theta}{2} c \frac{\phi}{2} + s \frac{\psi}{2} s \frac{\theta}{2} s \frac{\phi}{2} \\ c \frac{\psi}{2} c \frac{\theta}{2} s \frac{\phi}{2} - s \frac{\psi}{2} s \frac{\theta}{2} c \frac{\phi}{2} \\ c \frac{\psi}{2} s \frac{\theta}{2} c \frac{\phi}{2} + s \frac{\psi}{2} c \frac{\theta}{2} s \frac{\phi}{2} \\ s \frac{\psi}{2} c \frac{\theta}{2} c \frac{\phi}{2} - c \frac{\psi}{2} s \frac{\theta}{2} s \frac{\phi}{2} \end{bmatrix} \otimes \vec{T}(\Omega_i) \otimes \begin{bmatrix} s \frac{\psi}{2} s \frac{\theta}{2} s \frac{\phi}{2} + c \frac{\psi}{2} c \frac{\theta}{2} c \frac{\phi}{2} \\ s \frac{\psi}{2} s \frac{\theta}{2} c \frac{\phi}{2} - c \frac{\psi}{2} c \frac{\theta}{2} s \frac{\phi}{2} \\ -c \frac{\psi}{2} s \frac{\theta}{2} c \frac{\phi}{2} - s \frac{\psi}{2} c \frac{\theta}{2} s \frac{\phi}{2} \\ c \frac{\psi}{2} s \frac{\theta}{2} s \frac{\phi}{2} - s \frac{\psi}{2} c \frac{\theta}{2} c \frac{\phi}{2} \end{bmatrix} \quad (5.9c)$$

Instead; returning to rotation matrices for the inverse transformation and reiterating that Euler angle equivalents for the servos are; $[\phi, \theta, \psi]^T \iff [\lambda_i, \alpha_i, \sigma_i]^T$. It then follows (where i^{th} motor subscripts $1 \rightarrow 4$ are implied):

$$\vec{T}_i = \begin{bmatrix} c\sigma & -s\sigma & 0 \\ s\sigma & c\sigma & 0 \\ 0 & 0 & 1 \end{bmatrix} \begin{bmatrix} c\alpha & 0 & s\alpha \\ 0 & 1 & 0 \\ -s\alpha & 0 & c\alpha \end{bmatrix} \begin{bmatrix} 1 & 0 & 0 \\ 0 & c\lambda & -s\lambda \\ 0 & s\lambda & c\lambda \end{bmatrix} \vec{T}(\Omega_i) \quad (5.10a)$$

$$\Rightarrow \vec{T}_i = \begin{bmatrix} c\sigma c\alpha & c\sigma s\alpha s\lambda - s\sigma c\lambda & c\sigma s\alpha c\lambda + s\sigma s\lambda \\ s\sigma c\alpha & s\sigma s\alpha s\lambda + c\sigma c\lambda & s\sigma s\alpha c\lambda - c\sigma s\lambda \\ -s\alpha & c\alpha s\lambda & c\alpha c\lambda \end{bmatrix} \begin{bmatrix} 0 \\ 0 \\ T(\Omega_i) \end{bmatrix} \quad (5.10b)$$

$$\Rightarrow \begin{bmatrix} T_x \\ T_y \\ T_z \end{bmatrix} = \begin{bmatrix} s\sigma s\lambda + c\sigma s\alpha c\lambda \\ s\sigma s\alpha c\lambda - c\sigma s\alpha \\ c\alpha c\lambda \end{bmatrix} T(\Omega_i) \quad (5.10c)$$

Where σ is an orthogonal multiple which rotates the vector about the \hat{Z}_b axis. The fact that the principle thrust vector $\vec{T}(\Omega_i)$ has only a \hat{Z}_{M_i} component in the motor frame makes the solution for servo angles dramatically less complex to solve. Then Eq:5.10c simplifies even further to the following four trigonometric relations respectively for each motor module:

$$\begin{bmatrix} T_x \\ T_y \\ T_z \end{bmatrix} = \left[\begin{bmatrix} s\alpha c\lambda \\ -s\lambda \\ c\alpha c\lambda \end{bmatrix}, \begin{bmatrix} s\lambda \\ s\alpha c\lambda \\ c\alpha c\lambda \end{bmatrix}, \begin{bmatrix} -s\alpha c\lambda \\ s\lambda \\ -s\alpha c\lambda \end{bmatrix}, \begin{bmatrix} -s\lambda \\ -s\alpha c\lambda \\ c\alpha c\lambda \end{bmatrix} \right] T(\Omega_i) \quad \text{for } i \in [1, 2, 3, 4] \quad (5.11)$$

It then becomes a simple case of inverse trigonometry to solve for both λ_i and α_i respectively, for the example case of $i = 1$, the following holds true and can be similarly applied to the remaining motor modules.

Using $T(\Omega_i) = \|\vec{T}_i\|$ and the four quadrant secondary arctangent2 function⁵, $\text{arctan2}(x, y)$, for both inversion solutions to get full quadrature⁶ results:

$$\lambda = \text{arctan2}\left(-T_y, \sqrt{\|\vec{T}_i\|^2 - T_y^2}\right) \quad (5.12a)$$

⁴ σ_i is already known to be an orthogonal multiplicate...

⁵More on the arctan2 function in Appendix:A.3.

⁶Exploiting the fact that $\text{arctan}(x) = \text{arcsin}(x/\sqrt{1-x^2})$.

$$\alpha_i = \arctan2(T_x, T_z) \quad (5.12b)$$

Therefore, the secondary component of the control allocation block, $R^\dagger(\mathbf{x}, \vec{T}_i, t)$ from Fig:4.2 is then summarized as a single rotation inversion function (for motor module $i = 1$):

$$\begin{bmatrix} \Omega_i \\ \lambda_i \\ \alpha_i \end{bmatrix} = R^\dagger(\mathbf{x}, \vec{T}_i, t) = \begin{bmatrix} \left(\sqrt{T_x^2 + T_y^2 + T_z^2} / C_T(J) \rho D^4 \right)^{\frac{1}{2}} \\ \arctan2(T_x^2, ||\vec{T}_i|| \sqrt{||\vec{T}_i||^2 - T_x^2}) \\ -\arctan2(T_x, T_z ||\vec{T}_i||) \end{bmatrix} \quad (5.13)$$

Further simplifications could be drawn from the definitions of each element included in Eq:5.13, but it would just be superfluous as each servo angle can be solved for. At this stage the only remaining undefined component of the entire control block is the abstracted allocation algorithms, $B^\dagger(\mathbf{x}, \vec{\nu}_d, t)$, which are now addressed...

5.1.1 Pseudo Inverse Allocator

Conceptually the simplest control allocation solutions to Eq:5.2 stems from what are categorized as "inversion" based cost optimizations (the first three proposed allocators in Sec:??, 5.1.2 & 5.1.3). As alluded to previously, the requirements for inversion based allocation is that the effectiveness function $B(\mathbf{x}, u, t)$ is a linear relationship which can be abstracted to $B(\mathbf{x}, t)u$. The objective of inversion is that for the control problem $\vec{\nu}_c = B(\mathbf{x}, t)u$ to find some matrix $B^\dagger(\mathbf{x}, t)$ such that for some $\vec{\nu}_d$:

$$\vec{\nu}_c = \vec{\nu}_d = B(\mathbf{x}, t)u \Rightarrow B^\dagger(\mathbf{x}, t)\vec{\nu}_d = B^\dagger(\mathbf{x}, t)B(\mathbf{x}, t)u \quad (5.14a)$$

With the inversion identity:

$$B(\mathbf{x}, t)B^\dagger(\mathbf{x}, t) = \mathbb{I}_{m \times m} \quad (5.14b)$$

$$\rightarrow u = B^\dagger(\mathbf{x}, t)\vec{\nu}_d \quad (5.14c)$$

Or more generally, without the dependency of linearity:

$$u = B^\dagger(\mathbf{x}, \vec{\nu}_d, t) \quad (5.14d)$$

Where $B(\mathbf{x}, t) \in \mathbb{R}^{m \times n}$. When the B matrix has full rank; that being $m > n$, the inversion of B^\dagger , short of online iterative techniques to solve for the inversion, is not so trivial. A linear least squares technique is the basis of the direct inversion allocation schemes. The secondary control objective, $J(\mathbf{x}, u, t)$, is chosen to be a quadratic cost function that can be solved as an explicit least squares problem. The net effect of which aims to minimize controller effort (*magnitude*), such that:

$$J(\mathbf{x}, u, t) = \min_{u \in \mathbb{U}} \frac{1}{2} (u - u_p)^T W (u - u_p) \text{ such that } \vec{\nu}_c = B(\mathbf{x}, u, t) \quad (5.15)$$

Its worth mentioning that Eq:5.15 has no slack variable to be optimized, unlike Eq:5.2. The matrix W is a positive definite matrix of weighting⁷ coefficients that prioritises different actuators in the actuator matrix u higher than others. Similarly u_p is the preferred actuator position matrix⁸ which the system tends towards.

The least squares solution [42] to Eq:5.15 for that inversion matrix $B^\dagger(\mathbf{x}, t)$ is then:

$$u = (\mathbb{I} - CB(\mathbf{x}, t))u_p + C\vec{\nu}_d \quad (5.16a)$$

$$C = W^{-1}B^T(\mathbf{x}, t)(B(\mathbf{x}, t)W^{-1}B^T(\mathbf{x}, t))^{-1} \quad (5.16b)$$

⁷Discussed in full next in Sec:5.1.2.

⁸Priority acutator positions are detailed in Sec:5.1.3.

The solution in Eq:5.16 is referred to as the generalized inverse with weighted and preferred actuators positions. In the special case where there are no weightings, $W = \mathbb{I}_{n \times n}$, and no preferred actuator values are given, $u_p = \vec{0}$, the solution reduces to:

$$u = B^T(\mathbf{x}, t) (B(\mathbf{x}, t) \cdot B^T(\mathbf{x}, t))^{-1} \vec{\nu}_d \quad (5.17a)$$

$$= B^\dagger(\mathbf{x}, t) \vec{\nu}_d \quad (5.17b)$$

The simplified unique case of Eq:5.17 is termed a Moore-Penrose or pseudo-inversion of the actuator effectiveness matrix $B(\mathbf{x}, t)$. The pseudo-inversion is the most basic of allocation techniques, with a least squares minimization of controller effort. For an effectiveness $B(\mathbf{x}, t)$ matrix from Eq:4.8 relating to the layout described in Fig:2.9, the pseudo-inversion allocator is:

$$B(\mathbf{x}, t) = \begin{bmatrix} 1 & 0 & 0 & 1 & 0 & 0 & 1 & 0 & 0 & 1 & 0 & 0 \\ 0 & 1 & 0 & 0 & 1 & 0 & 0 & 1 & 0 & 0 & 1 & 0 \\ 0 & 0 & 1 & 0 & 0 & 1 & 0 & 0 & 1 & 0 & 0 & 1 \\ 0 & 0 & 0 & 0 & 0 & L & 0 & 0 & 0 & 0 & 0 & -L \\ 0 & 0 & -L & 0 & 0 & 0 & 0 & 0 & L & 0 & 0 & 0 \\ 0 & L & 0 & -L & 0 & 0 & 0 & -L & 0 & L & 0 & 0 \end{bmatrix} \in \mathbb{R}^{12 \times 6} \quad (5.18a)$$

$$\Rightarrow B^\dagger(\mathbf{x}, t) = B^T(B \cdot B^T)^{-1} \quad (5.18b)$$

$$= \begin{bmatrix} \frac{1}{4} & 0 & 0 & 0 & 0 & 0 \\ 0 & \frac{1}{4} & 0 & 0 & 0 & \frac{1}{4L} \\ 0 & 0 & \frac{1}{4} & 0 & \frac{-1}{2L} & 0 \\ \frac{1}{4} & 0 & 0 & 0 & 0 & \frac{-1}{4L} \\ 0 & \frac{1}{4} & 0 & 0 & 0 & 0 \\ 0 & 0 & \frac{1}{4} & \frac{1}{2L} & 0 & 0 \\ \frac{1}{4} & 0 & 0 & 0 & 0 & 0 \\ 0 & \frac{1}{4} & 0 & 0 & 0 & \frac{-1}{4L} \\ 0 & 0 & \frac{1}{4} & \frac{1}{2L} & 0 & 0 \\ \frac{1}{4} & 0 & 0 & 0 & 0 & \frac{1}{4L} \\ 0 & \frac{1}{4} & 0 & 0 & 0 & 0 \\ 0 & 0 & \frac{1}{4} & \frac{-1}{2L} & 0 & 0 \end{bmatrix} \in \mathbb{R}^{6 \times 12} \quad (5.18c)$$

Such that the pseudo-inversion allocation rule $u = B^\dagger(\mathbf{x}, t) \vec{\nu}_d$ produces a feasible set of control thrust vectors, $\vec{T}_{1 \rightarrow 4}$, for some virtual control input $\vec{\nu}_d = h(\mathbf{x}_e, t)$. Those thrust vectors, numbered $1 \rightarrow 4$, are then solved for as explicit actuator positions $[\Omega_i, \lambda_i, \alpha_i]^T = R^\dagger(\mathbf{x}, \vec{T}_i, t)$ to construct the actuator matrix $u \in \mathbb{U} \in \mathbb{R}^{12}$. Noting that $B(\mathbf{x}, t)$ does not necessarily have to be static with respect to either the state vector \mathbf{x} or time t . The allocation rule in Eq:5.18 is the most simplified case of the least squares quadratically optimized equation for Eq:5.2 and is used as the base reference allocation law to which all other proposed rules are compared against.

The direct (*pseudo*) inversion solution guarantees the commanded virtual control input is met and that actuators aren't necessarily saturated. In certain cases it may be desired to completely saturate certain actuators before exploiting other actuator plant inputs. That would entail an iterative "daisy chaining" [61] allocation to be performed numerically online, enforcing saturation for atleast some actuators and achievement of control objectives. That particular approach is avoided here as completely saturating an actuator isn't desirable; in the context of thrust generation (or vectoring) with propeller's saturation is something to be avoided...

5.1.2 Weighted Pseudo Inverse Allocator

A weighted inversion still treats the preferred actuator positions as negligible, or that $u_p = \vec{0}$ in Eq:5.16, but adds priority to different actuators in the form of a W matrix. The positive definite (*symmetrical*)

weighting matrix is square with respect to the actuator dimension, $W \in \mathbb{R}^{12 \times 12}$ (or more generally $W \in \mathbb{R}^{m \times m}$). The Moore-Penrose inversion assumes that all actuators are equally weighted and purely diagonal, $W = \mathbb{I}$. A time dependent adaptive weighting matrix could prioritize actuators following control faults or actuator deterioration. The control objective of a weighted inversion is to design the explicit weighting coefficients as per some preferred heuristic or optimization⁹.

Each weighting coefficient determines how the least squares solution to Eq:5.2 preferentially biases a particular actuator, in this case the weighting matrix's divisions correlate to mixed actuator thrust vector values. The 3×3 diagonal groupings $W_{1 \rightarrow 4}$ relate to individual thrust component biasing (T_{ix}, T_{iy}, T_{iz}) whilst off-centre 3×3 groupings mix separate thrust terms $\vec{T}_{1 \rightarrow 4}$.

Pseudo-inversion, previously, will exactly match the virtual control input $\vec{\nu}_d = B(\mathbf{x}, u, t) = \vec{\nu}_c$ so long as the actuators aren't saturated. Biasing actuators with an explicit weighting matrix could otherwise introduce a slack between the desired control requirements and their commanded counterparts. Such a case could result in instability given that trajectory tracking is stabilized through Lyapunov's theorem in the design of $\vec{\nu}_d$, not solving for allocated actuator positions. Short of iteratively¹⁰ processing variable weights until a viable solution is found, a constraint on the nature of the weighting matrix needs to be introduced.

$$\begin{aligned} \vec{T}_1 &\Rightarrow \begin{matrix} \vec{T}_1 \downarrow \\ \vec{T}_2 \downarrow \\ \vec{T}_3 \downarrow \\ \vec{T}_4 \downarrow \end{matrix} \quad \begin{bmatrix} W_{1:1}W_{1:2}W_{1:3} \\ W_{1:4}W_{1:5}W_{1:6} \\ W_{1:7}W_{1:8}W_{1:9} \end{bmatrix} \begin{bmatrix} 0 & 0 & 0 \\ 0 & 0 & 0 \\ 0 & 0 & 0 \end{bmatrix} \begin{bmatrix} W_{5:1}W_{5:2}W_{5:3} \\ W_{5:4}W_{5:5}W_{5:6} \\ W_{5:7}W_{5:8}W_{5:9} \end{bmatrix} \begin{bmatrix} 0 & 0 & 0 \\ 0 & 0 & 0 \\ 0 & 0 & 0 \end{bmatrix} \\ \vec{T}_2 &\Rightarrow \begin{bmatrix} 0 & 0 & 0 \\ 0 & 0 & 0 \\ 0 & 0 & 0 \end{bmatrix} \begin{bmatrix} W_{2:1}W_{2:2}W_{2:3} \\ W_{2:4}W_{2:5}W_{2:6} \\ W_{2:7}W_{2:8}W_{2:9} \end{bmatrix} \begin{bmatrix} 0 & 0 & 0 \\ 0 & 0 & 0 \\ 0 & 0 & 0 \end{bmatrix} \begin{bmatrix} W_{6:1}W_{6:2}W_{6:3} \\ W_{6:4}W_{6:5}W_{6:6} \\ W_{6:7}W_{6:8}W_{6:9} \end{bmatrix} \\ \vec{T}_3 &\Rightarrow \begin{bmatrix} W_{5:1}W_{5:2}W_{5:3} \\ W_{5:4}W_{5:5}W_{5:6} \\ W_{5:7}W_{5:8}W_{5:9} \end{bmatrix} \begin{bmatrix} 0 & 0 & 0 \\ 0 & 0 & 0 \\ 0 & 0 & 0 \end{bmatrix} \begin{bmatrix} W_{3:1}W_{3:2}W_{3:3} \\ W_{3:4}W_{3:5}W_{3:6} \\ W_{3:7}W_{3:8}W_{3:9} \end{bmatrix} \begin{bmatrix} 0 & 0 & 0 \\ 0 & 0 & 0 \\ 0 & 0 & 0 \end{bmatrix} \\ \vec{T}_4 &\Rightarrow \begin{bmatrix} 0 & 0 & 0 \\ 0 & 0 & 0 \\ 0 & 0 & 0 \end{bmatrix} \begin{bmatrix} W_{6:1}W_{6:2}W_{6:3} \\ W_{6:4}W_{6:5}W_{6:6} \\ W_{6:7}W_{6:8}W_{6:9} \end{bmatrix} \begin{bmatrix} 0 & 0 & 0 \\ 0 & 0 & 0 \\ 0 & 0 & 0 \end{bmatrix} \begin{bmatrix} W_{4:1}W_{4:2}W_{4:3} \\ W_{4:4}W_{4:5}W_{4:6} \\ W_{4:7}W_{4:8}W_{4:9} \end{bmatrix} \end{aligned}$$

Figure 5.1: Weighting matrix biasing

So long each horizontal and vertical weighting groups contributing to each thrust vector, $W_{T_i} \in \mathbb{R}^{3 \times 12}$, each have a unit norm, the designed control torque and force inputs will be met. Physically the resultant thrusts and torque (thrust differentials) would be balanced amongst similarly directed components. Furthermore, an additional restraint is that only permissible thrust vector mixings are between opposing pairs; $\vec{T}_1 \& \vec{T}_3$ and $\vec{T}_2 \& \vec{T}_4$. Such a constraint simplifies the time spent optimizing weighting coefficients in Sec:6.4.

The physical consequences of giving priority biasing to thrust vector components in the \hat{X}_b & \hat{Y}_b ¹¹ directions is that the allocation block prioritizes using pitch or roll servos, λ_i & α_i respectively, before changing the propeller's rotational speed Ω_i . Similarly balancing the off-diagonal thrust vector

⁹Not considered or discussed are adaptive weightings as those are out of the scope of this work and pertain more to FTC [6].

¹⁰Online iterative solutions are avoided given their increased computational complexity and the possibility that, given an infinite processing time, a solution may not necessarily be found.

¹¹Recalling that the allocator block designs $\vec{T}_{1 \rightarrow 4}$ in the body frame, $\in \mathcal{F}^b$. Then the rotation inversion block $R^\dagger(\mathbf{x}, \vec{T}_i, t)$ from Eq:5.13 finds $(\Omega_i, \lambda_i, \alpha_i)$ to transform $\vec{T}(\Omega_i)$ to the body frame; effectively mapping $\mathcal{F}^{M_i} \rightarrow \mathcal{F}^b$.

mixing blends controller effort amongst opposing actuators.

The explicit weighting coefficients are to be optimized iteratively in simulation, Sec:6.4; aiming to minimize some performance metric. That metric, which evaluates relative performance of a proposed set of weighting coefficients, is penalized¹² from actuator slew rate times and a slack variable norm;

$$\int (a \|t^{\nu_d - \nu_c} - 1\| + b \|s\|) dt \quad (5.19)$$

Where the integral is run until $t \rightarrow \infty$ over the length of a single simulation cycle. As such, the weighting matrix coefficients try to reduce the transient time taken for the actuator block to settle whilst ensuring stability isn't compromised. Optimization iterations for the weight coefficients are completely independent from the controller coefficient loops to be run in Sec:6.1...

5.1.3 Priority Norm Inverse Allocator

The last allocator based on typical inversion applies a non-zero preferred actuator position from Eq:5.2; or that $u_p \neq \vec{0} \in \mathbb{U}$. The preferred actuator position is the matrix value of u which the allocator naturally tends toward. An obvious choice for that value are the conditions required for stable hovering, those which simply keep the quadcopter airborne. There are however some intricacies which must be discussed with respect to what hovering conditions are.

For a generalized body of weight m , a net gravitational force opposes upward movement in the inertial frame; $\vec{M} = [0, 0, -G \cdot m]^T \in \mathcal{F}^I$. At the hover state there are no net forces or torques¹³ acting on the system, all dynamics are balanced. As such the hovering conditions are then simply:

$$\begin{bmatrix} \mu \vec{F}_p \\ \mu \vec{\tau}_p \end{bmatrix} = \begin{bmatrix} \vec{M} \\ \vec{0} \end{bmatrix} \in \mathcal{F}^I \quad (5.20)$$

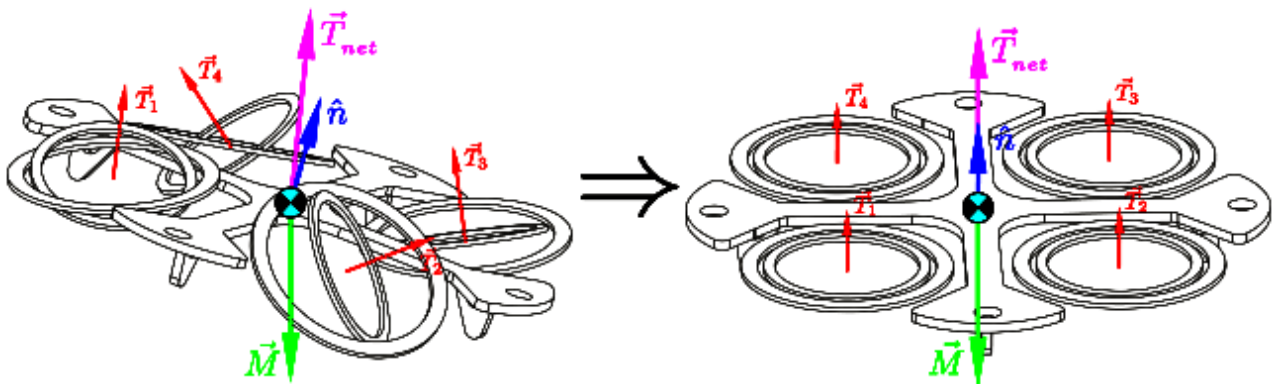


Figure 5.2: Hover conditions W.R.T the inertial frame \mathcal{F}^I

However, calculating hover conditions purely in the inertial frame give no indication on what attitude the body has. Two options present themselves on how to solve for hover values. First; take hover conditions with respect to the inertial frame, such that the body's attitude tends to the origin always. The free body diagram in Fig:5.2 illustrates this.

$$\vec{\nu}_I = \begin{bmatrix} \mu \vec{F}_p \\ \mu \vec{\tau}_p \end{bmatrix} = \begin{bmatrix} \vec{M} \\ \vec{0} \end{bmatrix} \in \mathcal{F}^b \quad (5.21)$$

¹²More on simulations and optimizations next in Chapter:6-Simulations & Results.

¹³Unwanted system dynamics like torques from an eccentric gravitational center or disturbances are compensated for in a plant dependent control law $\mu \vec{\tau} = h(\mathbf{x}_e, t)$.

Conversely, the second option is to take hover conditions with respect to the body frame (Fig:5.3). The difference is that the body's preferred actuator positions are dependent on each instantaneous orientation. That attitude stays constant whilst the actuators are redirected to produce inertial hovering conditions; irrespective of the attitude. The preferred hovering conditions are then always dependent on the commanded attitude trajectory.

$$\vec{\nu}_b = \begin{bmatrix} \mu \vec{F}_p \\ \mu \vec{\tau}_p \end{bmatrix} = \begin{bmatrix} Q_b^* \otimes \vec{M} \otimes Q_b \\ \vec{0} \end{bmatrix} \in \mathcal{F}^b \quad (5.22)$$

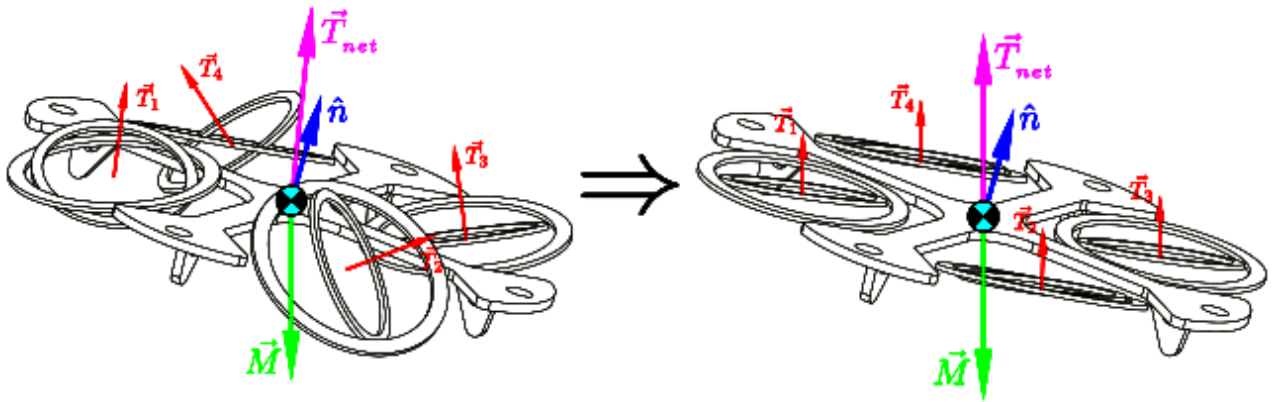


Figure 5.3: Hover conditions W.R.T the body frame \mathcal{F}^b

Explicit actuator positions are then solved for Eq:5.21 & Eq:5.22 using pseudo inversion from Eq:5.17. The two solutions are then as follows:

$$u_p^I = R^\dagger(\mathbf{x}, (B^\dagger(\mathbf{x}, \vec{\nu}_I, t)), t) \quad (5.23a)$$

$$u_p^b = R^\dagger(\mathbf{x}, (B^\dagger(\mathbf{x}, \vec{\nu}_b, t)), t) \quad (5.23b)$$

Where the inverse rotation operator, R^\dagger from Eq:5.23, is applied to all four thrust vectors produced by the allocation operator B^\dagger . Both actuator matrices are then applied to Eq:5.16 and could be combined with a non-diagonal weighting matrix.

$$u_{\in \mathbb{U}} = (\mathbb{I} - CB(\mathbf{x}, t))u_p + C\vec{\nu}_d \quad (5.24a)$$

$$C = W^{-1}B^T(\mathbf{x}, t)(B(\mathbf{x}, t)W^{-1}B^T(\mathbf{x}, t))^{-1} \quad (5.24b)$$

The physical consequences of either preferred actuator positions are demonstrated in simulation in Sec:6.6.3. Priority actuator positions aren't simulated together with weighting matrices, the two are compared independently...

5.1.4 Non-linear Plant Control Allocation

Despite the added actuation, each complex dynamic response from an actuator excitation is not fully exploited. The dynamics of an actuator's motor module, Sec:3.3.1, until now has been treated as an element to be compensated for in feedback structure. An alternative approach, seen in Gasco, et al. [2012] [2, 38], is to use the actuator reactions as additional non-linear actuator plants. In [2, 38] the actuator plants and their resultant dynamics were introduced as additional dimensions to the actuator matrix $u \in \mathbb{U}$.

Such an approach was achievable because the authors, despite adding two extra degrees of freedom for each propeller, hadn't vectored the propeller thrust. The non-linear proposal here is to first calculate a Pseudo-inversion actuator solution *without* plant compensation¹⁴, then introducing those induced actuator responses from such an excitation to alleviate the control plant requirement. A subsequent revised virtual control plant input is used iteratively to find a subsequent pseudo-inversion solution; the process is cycled until the control requirements are met.

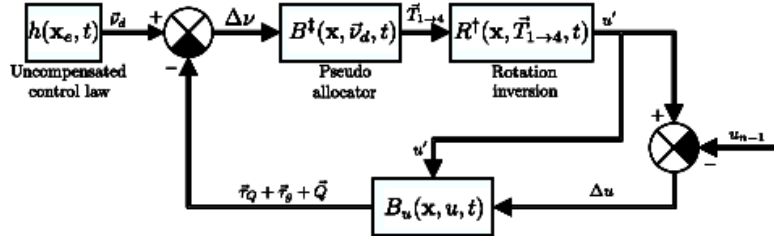


Figure 5.4: Allocation loop iteration

In Fig:5.4 the iteration loop is shown, each iteration is run online and settles at a balance point. In the loop, the block $B_u(\mathbf{x}, u, t)$ is a combination of non-linear actuator response terms from Eq:3.133,2.34d & 3.132b; those being $\vec{\tau}_Q$, $\vec{\tau}_g$ & \vec{Q} respectively. The settling point, where possible, a portion of the commanded control input \vec{v}_d is achieved from the otherwise compensated for actuator response dynamics.

5.1.5 Online Optimized Secondary Goal Allocator

¹⁴Disregarding $\vec{\tau}_Q$, $\vec{\tau}_g$ & \vec{Q} .

Chapter 6

Simulations & Results

6.1 Controller Tuning

6.1.1 Partical Swarm Based Optimization

6.1.2 Performance Metric

6.1.3 Global & Local Minima

6.1.4 Fmincon Differences

6.2 Attitude Controllers

6.2.1 PD

Dependent Performance

Independent Performance

6.2.2 XPD

6.2.3 IBC

6.2.4 ABC

6.3 Position Controllers

6.3.1 PD

6.3.2 ABC

6.4 Allocator Optimization

6.5 Simulation Block

Chapter 7

Conclusion

- Lagrange dynamics for multibody system could have produced a more concise model etc . . .
- Particule multibody dynamics with interactions could provide a more verbose simulation environment rather than the very newtonian simulation loop constructed
- Implicit equation dynamics in simulation may improve optimization loops in PSO algorithm
- Firmware changes to ESC drastically improved transfer function time constant, made assumption that servos would improve actuator response times redundant.
- Difficulty with non-linear multibody in Sec:3.3 causes stiffness in control optimization. Same troubles with time varying inertias caused Osprey inspiration issues too...
- non-linear multibody dynamics required multiple revisions, took longer than expected
- suffered time constraints as a result
- same multibody dynamics which caused issues with the original osprey testing []
- track angular momentum state, not angular position state. Could potentially remove the complexities of calculating explicit inertial values at discrete simulation intervals however 'unwinding' analogue could be detrimental. Given the high degree of freedom the system has, each angular momentum state probably has an entire set of solutions.
- complexities from non-zero $\dot{J}(t)$ for inertial equations and lagrange mechanics in appropriate chapter. At design stage it was elected to design around a smaller frame. If the rigid component of the frame, J_y in Ch:??, was sufficiently greater than the inertias of actuated components, the complexities from τ_b could be simplified greater. Moreover the inherent inertial damping would compensate for a lot of the torque spikes shown in Eq:?? from Ch:??.
- Model for τ_b , Eq:?? from Ch:??, is made such that an alternative model could easily be incorporated.
- Probably should've used principle axes for inertias, would have made calculating derivatives easier but there are just too many bodies to keep track of, making the inertia transformations an easier choice...
- Model assumes no downwash effects

Appendix A

Expanded Equations

A.1 Standard Quadrotor Dynamics

Following the fundamental 6-DOF equations of motion for a rigid body derived in Sec:3.1.1, the common linearizations typically applied for generic "+" configured quadrotors are now presented. Reiterating those four differential equations, Eq:3.10, which describe a rigid body's motion (using rotation matrices and not quaternions):

$$\dot{\vec{\varepsilon}} = \mathbb{R}_b^I(-\eta) \vec{v}_b \quad \in \mathcal{F}^I \quad (\text{A.1a})$$

$$\dot{\vec{v}}_b = m_b^{-1} [-\vec{\omega}_b \times m_b \vec{v}_b + m_b \mathbb{R}_I^b(-\eta) \vec{G}_I + \vec{F}_{net}] \quad \in \mathcal{F}^b \quad (\text{A.1b})$$

$$\dot{\vec{\eta}} = \Phi(\eta) \vec{\omega}_b \quad \in \mathcal{F}^{v2}, \mathcal{F}^{v1}, \mathcal{F}^I \quad (\text{A.1c})$$

$$\dot{\vec{\omega}}_b = J_b^{-1} [-\vec{\omega}_b \times J_b \vec{\omega}_b + \vec{\tau}_{net}] \quad \in \mathcal{F}^b \quad (\text{A.1d})$$

With the Euler matrix, $\Phi(\eta)$, defined in Eq:2.12h. The net heave thrust produced by motors $i \in [1 : 4]$, bound perpendicularly to the \hat{Z}_b axis, is given by:

$$\vec{T} = \sum_{i=1}^4 F(\Omega_i) \cdot \hat{Z}_b \quad \in \mathcal{F}^b \quad (\text{A.2a})$$

The simplified relationship between the thrust scalar $T(\Omega_i)$ and the propeller's rotational speed Ω_i in [RPS] is approximately quadratic:

$$F(\Omega_i) \approx k_1 \Omega_i^2 \quad (\text{A.2b})$$

Similarly the aerodynamic torque opposing each rotating propeller, about the propellers \hat{Z}_b axis, is:

$$Q(\Omega_i) \approx k_2 \Omega_i^2 \quad (\text{A.3})$$

Coefficients k_1 & k_2 are typically determined from physical thrust tests. The controllable pitch and roll torques, τ_ϕ & τ_θ about the \hat{X}_b and \hat{Y}_b axes respectively, are generated by opposing differential lift forces. Lastly the yaw torque, τ_ψ about the \hat{Z}_b axis, is generated only a net response to the rotational aerodynamic propeller torques. The control torque inputs are then defined as:

$$\tau_\phi = L_{arm}(F(\Omega_1) - F(\Omega_3)) \cdot \hat{X}_b \quad (\text{A.4a})$$

$$\tau_\theta = L_{arm}(F(\Omega_2) - F(\Omega_4)) \cdot \hat{Y}_b \quad (\text{A.4b})$$

$$\tau_\psi = \sum_{i=1}^4 (-1)^i Q(\Omega_i) \cdot \hat{Z}_b \quad (\text{A.4c})$$

Then expanding the translational position and attitude state differentials, Eq:A.1b & Eq:A.1d, to their component forms (assuming the vehicle's inertial matrix J_b is diagonal):

$$\begin{pmatrix} \dot{u} \\ \dot{v} \\ \dot{w} \end{pmatrix} = \begin{pmatrix} rv - qw \\ pw - ru \\ qu - pv \end{pmatrix} + \begin{pmatrix} -g\sin(\theta) \\ g\cos(\theta)\sin(\phi) \\ g\cos(\theta)\cos(\phi) \end{pmatrix} + \frac{1}{m} \begin{pmatrix} 0 \\ 0 \\ T \end{pmatrix} \in \mathcal{F}^b \quad (\text{A.5a})$$

$$\begin{pmatrix} \dot{p} \\ \dot{q} \\ \dot{r} \end{pmatrix} = \begin{pmatrix} \frac{J_{yy}-J_{zz}}{J_{xx}} qr \\ \frac{J_{zz}-J_{xx}}{J_{yy}} pr \\ \frac{J_{xx}-J_{yy}}{J_{zz}} pq \end{pmatrix} + J_b^{-1} \begin{pmatrix} \tau_\phi \\ \tau_\theta \\ \tau_\psi \end{pmatrix} \in \mathcal{F}^b \quad (\text{A.5b})$$

Considering the size of a typical angular rate, $\vec{\omega}_b \approx \vec{0}$; the gyroscopic and Coriolis effects on the body (namely both cross product terms) are sufficiently small enough to be regarded as negligible. Assuming too that the body has a (*roughly*) diagonal inertial matrix. Then the following holds true around the origin when $\vec{\omega}_b \approx \vec{0}$:

$$\begin{pmatrix} rv - qw \\ pw - ru \\ qu - pv \end{pmatrix} \approx \vec{0} \quad \text{and} \quad \begin{pmatrix} \frac{J_{yy}-J_{zz}}{J_{xx}} qr \\ \frac{J_{zz}-J_{xx}}{J_{yy}} pr \\ \frac{J_{xx}-J_{yy}}{J_{zz}} pq \end{pmatrix} \approx \vec{0} \quad (\text{A.6})$$

As a result, state differentials in Eq:A.5 can then reduce to the following:

$$\begin{pmatrix} \dot{u} \\ \dot{v} \\ \dot{w} \end{pmatrix} = \begin{pmatrix} -g\sin(\theta) \\ g\cos(\theta)\sin(\phi) \\ g\cos(\theta)\cos(\phi) \end{pmatrix} + \frac{1}{m} \begin{pmatrix} 0 \\ 0 \\ T \end{pmatrix} \quad \text{and} \quad \begin{pmatrix} \dot{p} \\ \dot{q} \\ \dot{r} \end{pmatrix} = \begin{pmatrix} \frac{1}{I_x} \tau_\phi \\ \frac{1}{I_y} \tau_\theta \\ \frac{1}{I_z} \tau_\psi \end{pmatrix} \quad (\text{A.7})$$

Similarly, at an attitude near to the origin and at hovering conditions the following simplification applies to the Euler matrix $\Phi(\eta)$:

$$\Phi(\eta) \approx \vec{1} \quad \text{for } \eta \approx \vec{0} \quad (\text{A.8})$$

And so from Eq:A.1c the body's *Euler rates* are approximately equivalent to its angular velocity:

$$(\dot{p} \quad \dot{q} \quad \dot{r})^T \approx (\ddot{\phi} \quad \ddot{\theta} \quad \ddot{\psi})^T \Rightarrow \dot{\eta} \approx \omega_b \quad (\text{A.9})$$

The above Eq:A.9 is not an insignificant result. The difficulty with Euler angle parameterization for body attitude is that each Euler angle is defined with respect to a sequential reference frame, Eq:2.12. As such, the state equations for Eq:A.5 then reduce to the following six SISO controllable plants when the vehicle's angular velocity is small:

$$\ddot{x} = (-\cos(\phi)\sin(\theta)\cos(\psi) - \sin(\phi)\sin(\psi)) \frac{1}{m} T \quad (\text{A.10a})$$

$$\ddot{y} = (-\cos(\phi)\sin(\theta)\sin(\psi) + \sin(\phi)\cos(\psi)) \frac{1}{m} T \quad (\text{A.10b})$$

$$\ddot{z} = g - (\cos(\phi)\cos(\theta)) \frac{1}{m} T \quad (\text{A.10c})$$

$$\ddot{\phi} = \frac{1}{J_{xx}} \tau_\phi \quad (\text{A.10d})$$

$$\ddot{\theta} = \frac{1}{J_{yy}} \tau_\theta \quad (\text{A.10e})$$

$$\ddot{\psi} = \frac{1}{J_{zz}} \tau_\psi \quad (\text{A.10f})$$

Typically, the simplified Eq:A.10 is abstracted to an "augmented pilot control system". In such a case the controllable inputs are abstracted to T , $\ddot{\phi}$, $\ddot{\theta}$, $\ddot{\psi}$. Wherein the pilot dictates the attitude torques and net heave thrust for the quadrotor, mostly with various flavours of PD control for each channel.

A.2 Blade-Element Momentum Expansion

Expanding on the Blade-Element Momentum equations from Eq:3.27 and Eq:3.31a. Reiterating the integral equations, they are:

$$dT = \rho 4\pi r v_\infty (1+a) a dr \quad (\text{A.11a})$$

$$dT = \frac{1}{2} a_L b c \rho (\Omega r)^2 \left(\theta - \frac{v_\infty + v_i}{\Omega r} \right) dr \quad (\text{A.11b})$$

Both Eq:A.11a-A.11b are integrals taken across the length of the propeller blade. Equating the two and defining an inflow ratio term $\lambda = \frac{v_\infty + v_i}{\Omega r} = \frac{v_\infty(1+a)}{\Omega r}$ yields the following quadratic equation:

$$\lambda^2 + \left(\frac{\sigma a_L}{8} + \lambda_c \right) \lambda - \frac{\sigma a_L}{8} \theta \frac{r}{R} = 0 \quad (\text{A.12})$$

Where λ_c is the nominal free-stream inflow ratio when $v_i = 0$. Another term, σ , is defined as the propeller solidity and is given by:

$$\sigma = \frac{bc}{\pi R} \quad (\text{A.13})$$

Then, solving Eq:A.12 for λ :

$$\lambda = \sqrt{\left(\frac{\sigma a_L}{16} - \frac{\lambda_c}{2} \right)^2 + \frac{\sigma a_L}{8} \theta \frac{r}{R}} - \left(\frac{\sigma a_L}{16} - \frac{\lambda_c}{2} \right) \quad (\text{A.14})$$

So then the inflow ratio can be solved as a function of the propeller element's aerofoil profile and its static inflow factor. In static conditions, the inflow factor is:

$$\lambda = \frac{v_i}{\Omega r} = \sqrt{\frac{C_{T0}}{2}} \quad (\text{A.15})$$

Then substituting λ back into Eq:3.31a and solving the integral produces an instantaneous thrust value. The difficulty of solving the blade-element momentum integrals is knowing the exact chord profile and local angle of attack.

A.3 Euler-Angles from Quaternions

The solution for Euler angles from an attitude quaternion is an easy trigonometric inversion. Noting that the transformation from the body frame to each motor frame follows the Z-Y-X sequence, and using an inversion solution adapted from [118], where the transformation to quaternions is based on Shoemake's [116] definition. Each quaternion can be constructed from sequenced Euler angles, as in Eq:3.52. Then, solving for each euler angle using simultaneous solutions and inverse trigonometry:

$$\begin{bmatrix} \phi \\ \theta \\ \psi \end{bmatrix} = \begin{bmatrix} \arctan2(2(q_0 q_x + q_y q_z), 1 - 2(q_x^2 + q_y^2)) \\ \arcsin(2(q_0 q_y - q_x q_z)) \\ \arctan2(2(q_0 q_z + q_x q_y), 1 - 2(q_y^2 + q_z^2)) \end{bmatrix} \quad (\text{A.16})$$

Where $\arctan2(x, y)$ is the four-quadrant tangent inverse [36], producing the principle argument of the complex operands;

$$\arctan2(x, y) = PR \arg(x + yi) = Arg(x + yi) \quad (\text{A.17})$$

The use of an full quadrature arctangent function is to find solutions for Euler angles that are not only acute.

Appendix B

Design Bill of Materials

B.1 Parts List

Part Name	No. Used	Unit Weight[g]
Electronics		
SPRacing F3 Deluxe Flight Controller	1	8
OrangeRx 615X 2.4 GHz 6CH Receiver	1	9.8
Signal Converter SBUS-PPM-PWM	1	5.0
STLink-V2 Debugger	1	3
RotorStar Super Mini S-BEC 10A	1	30
128x96" OLED Display	1	7
XBee-Pro S1	2	4
HobbyWing XRotor 20A Opto ESC	4	15
OrangeRX RPM Sensor	4	2
HobbyKing Multi-Rotor Power Distribution Board	1	49
Motors		
Corona DS-339MG	8	32
Cobra 2208 2000KV Brushless DC	4	44.2
Frame Components		
APM Flight Controller Damping Platform	1	7
HobbyKing SK450 Replacement Arm (2 pcs)	2	51
SK450 Extended Landing Skid	1	23.25
Alloy Servo Arm (FUTABA)	8	4
10X18X6 Radial Ball Bearing	8	5
80g Damping Ball	32	≈ 0
Plastic Retainers for Damping Balls	32	≈ 0
3/5mm Aluminum Prop Adapter	4	≈ 1
6x4.5 Gemfam 3-Blade Propeller	4	6
M3 6mm Hex Nylon Spacer	8	≈ 0
M3 16mm Hex Nylon Spacer	32	≈ 0
M3 25mm Nylon Screw	128	≈ 0.08
M2.5x10mm Socket Head Cap Screw	36	≈ 0.2
M2.5x25mm Socket Head Cap Screw	20	≈ 0.6
M2.5 A-Lok Nut	16	≈ 0

Table B.1: Parts List

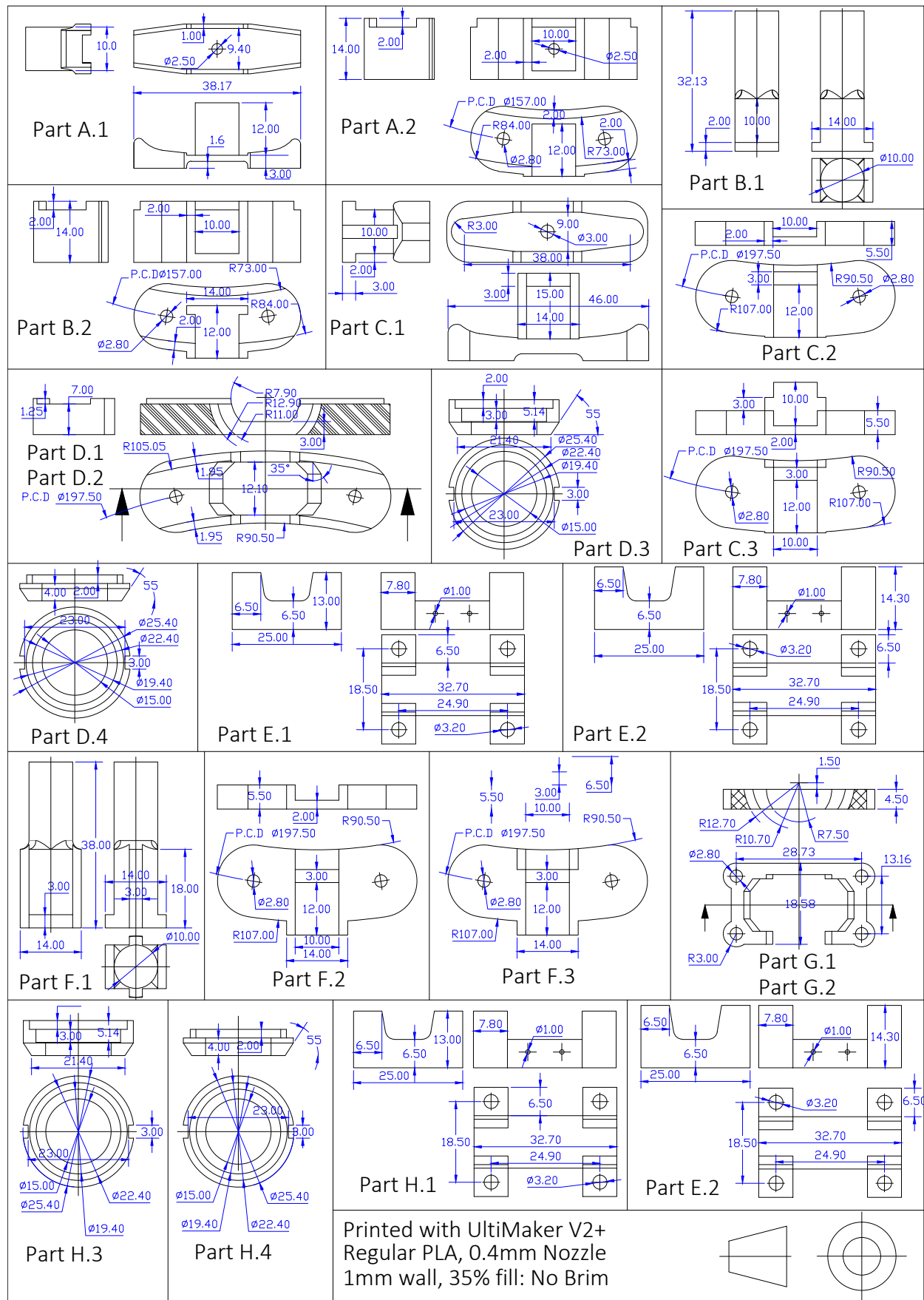


Table B.2: 3D Printed Parts

Bracket Assemblies 2

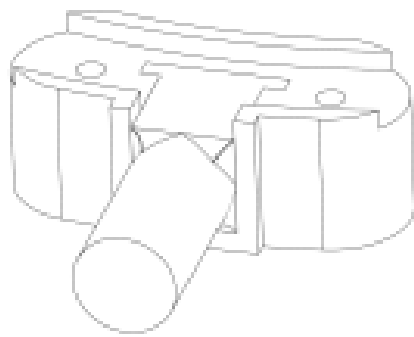


Figure B.1: Bearing Bracket Inner Ring Assembly
Parts: A.1, A.2

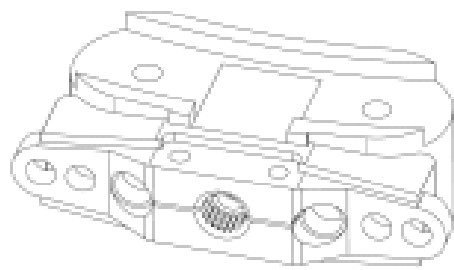


Figure B.2: Servo Bracket Inner Ring Assembly
Parts: B.1, B.2, M3 Servo Horn

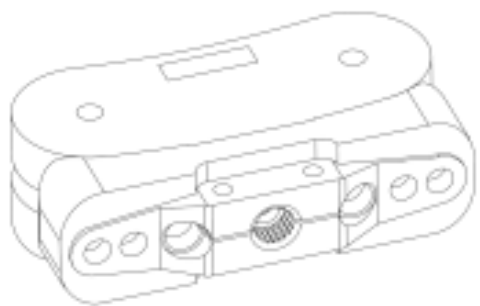


Figure B.3: Servo Bracket Middle Ring Assembly
Parts: C.1, C.2, C.3, M3 Servo Horn

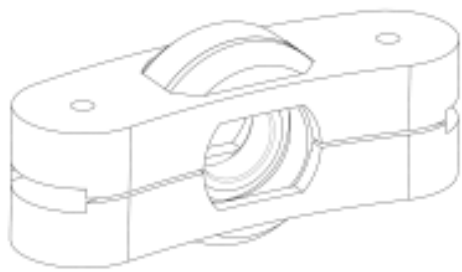


Figure B.4: Bearing Holder Middle Ring Assembly
Parts: D.1, D.2, D.3, D.4, 18-10 Bearing

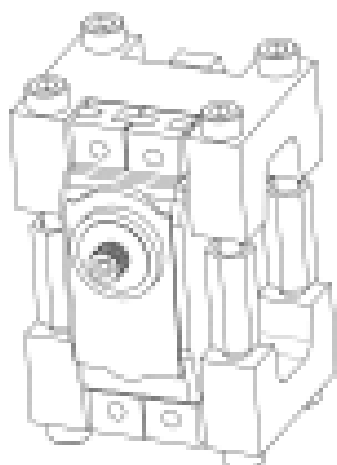


Figure B.5: Servo Mount Middle Ring Assembly
Parts: E.1, E.2, Corona Servo & Fasteners



Figure B.6: Bearing Shaft Middle Ring Assembly
Parts: F.1, F.2, F.3

Table B.3: Inner & Middle Ring Assemblies

Bracket Assemblies 2

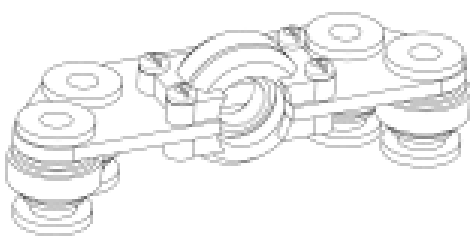


Figure B.7: Bearing Holder Damping Assembly
Parts: G.1, G.2, G.3, G.4, 18-10 Bearing, 80g Damping Balls, Bearing Holder Damping Bracket

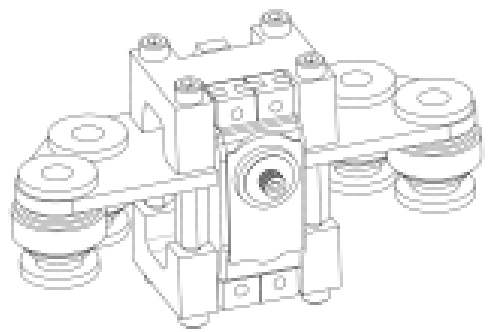


Figure B.8: Servo Mount Damping Assembly
Parts: H.1, H.2, Corona Servo & Fasteners, 80g Damping Balls, Servo Mount Damping Bracket

Table B.4: Damping Assemblies

Laser Cut Brackets

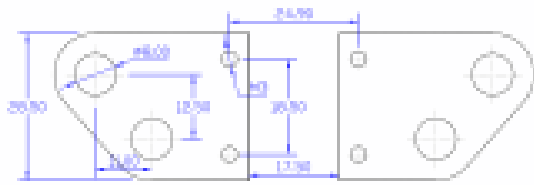


Figure B.9: Servo Mount Damping Bracket

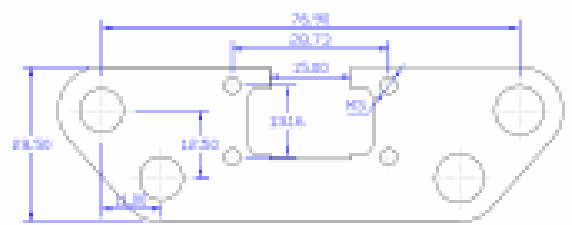


Figure B.10: Bearing Holder Damping Bracket

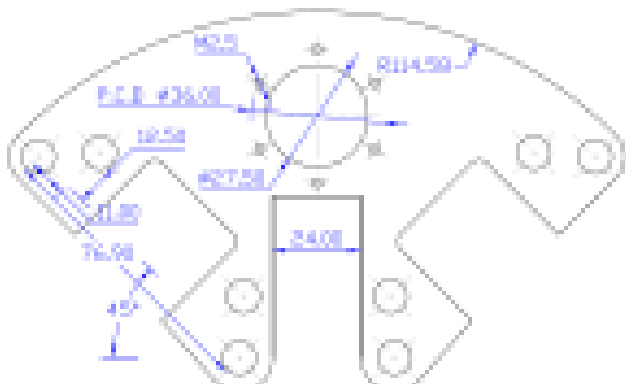


Figure B.11: Arm Mount Damping Bracket

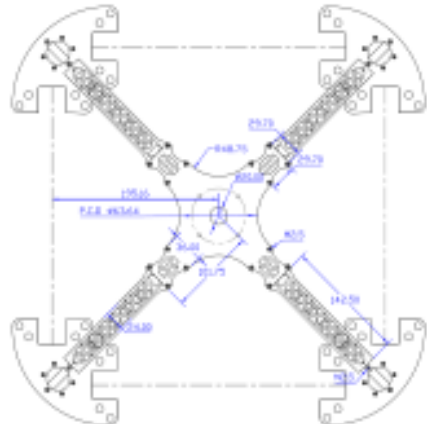


Figure B.12: Frame Brackets

Table B.5: Laser Cut Damping Brackets

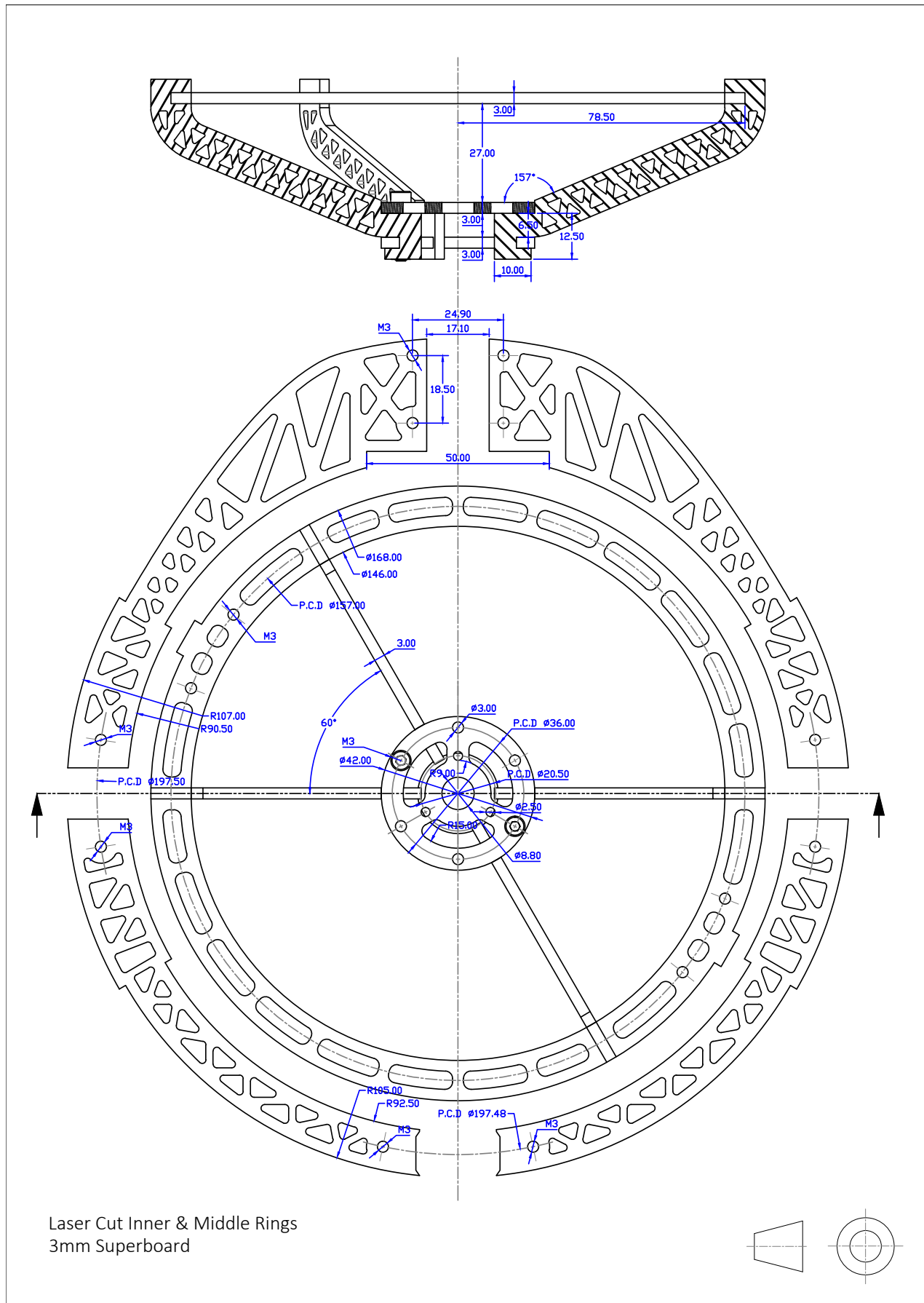


Table B.6: Laser Cut Parts

B.2 F3 Deluxe Schematic Diagram

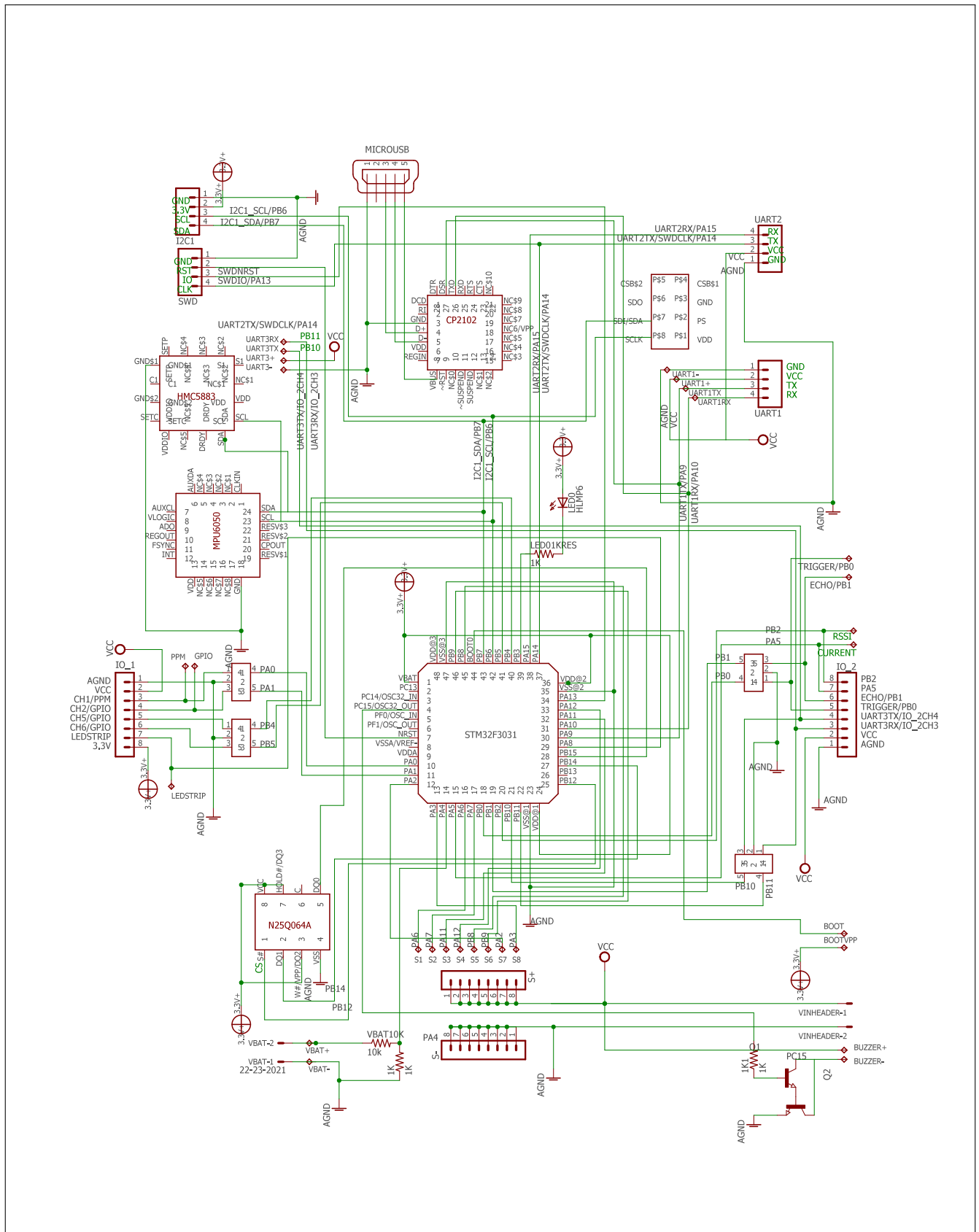


Figure B.13: F3 Deluxe Flight Controller Hardware Schematic

B.3 Strain Gauge Amplification

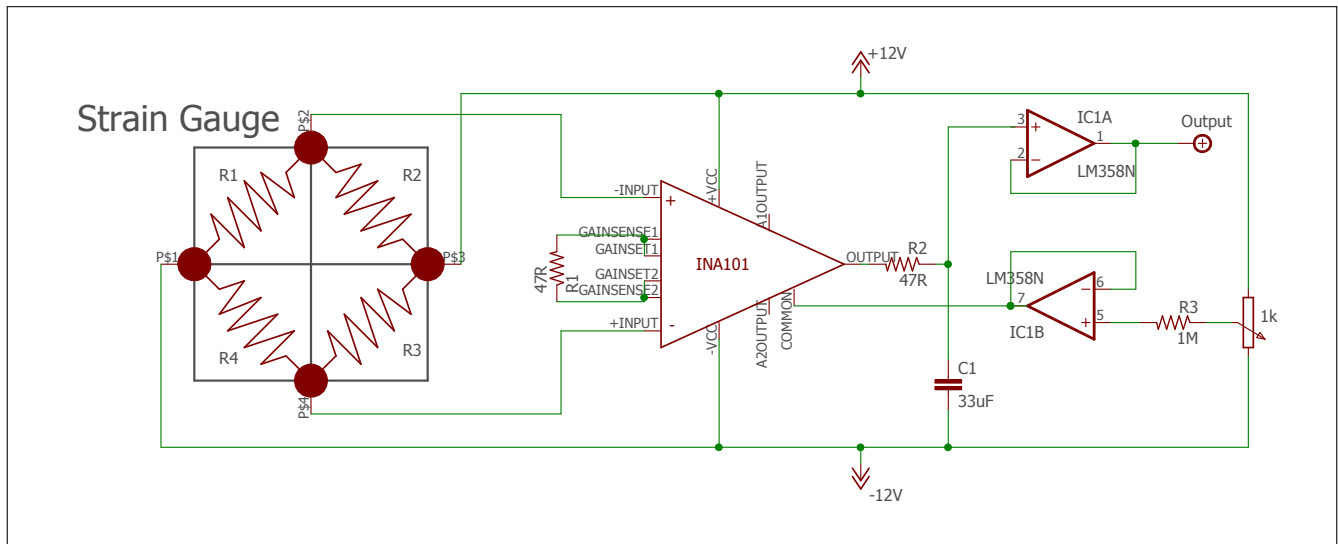


Figure B.14: Strain gauge full bridge amplifier

Appendix C

System ID Test Data

C.1 Thrust and Torque Test Data

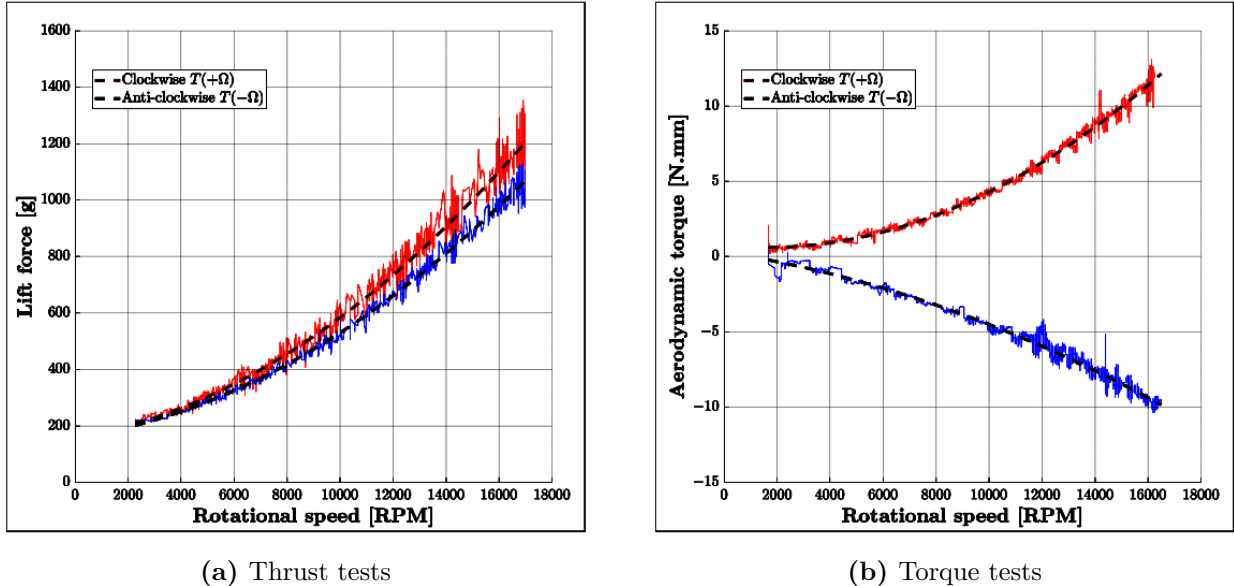


Figure C.1: Clockwise and counterclockwise rotation tests

Thrust tests in Fig:C.1a causes lateral deflection of the strain gauge thrust test rig illustrated in Fig:3.6a. The deflection is in the direction of the propeller's rotational sense, as a result of the torque applied to the propeller. Clockwise and counter-clockwise tests where summed together and averaged to produce the thrust tests plotted in Fig:3.6.

Torque tests in Fig:C.1b shows thrust deflection in the rotational torque test rig in Fig:3.7a. Upward thrust still resulted in some small deflection in the resultant measurements so opposing clockwise and counter-clockwise results were subtracted and averaged out to produce the torque tests plotted in Fig:3.7.

C.2 Cobra CM2208-200KV Thrust Data

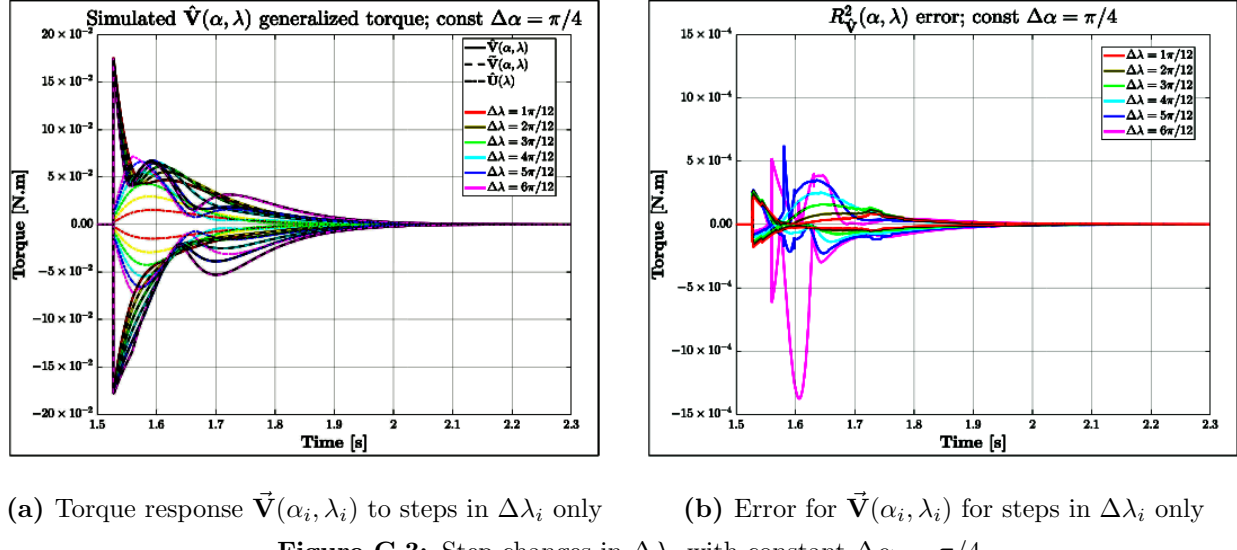
Cobra CM-2208/20 Motor Propeller Data										
Magnets 14-Pole	Motor Wind 20-Turn Delta	Motor Kv 2000 RPM/Volt		No-Load Current $I_o = 0.77$ Amps @ 10v	Motor Resistance $R_m = 0.076$ Ohms		I Max 20 Amps	P Max (3S) 220 W		
Stator 12-Slot	Outside Diameter 27.7 mm, 1.091 in.	Body Length 24.0 mm, 0.945 in.		Total Shaft Length 45.2 mm, 1.780 in.	Shaft Diameter 3.17 mm, 0.125 in.		Motor Weight 44.2 gm, 1.56 oz			
Test Data From Sample Motor		Input	6.0 V	8.0 V	10.0V	12.0V	Measured Kv value 1988 RPM/Volt @ 10v	Measured Rm Value 0.076 Ohms		
Io Value	0.59 A	0.67 A	0.77 A	0.87 A						
Prop Manf.	Prop Size	Li-Po Cells	Input Voltage	Motor Amps	Input Watts	Prop RPM	Pitch Speed in MPH	Thrust Grams	Thrust Ounces	Thrust Eff. Grams/W
APC	5.25x4.75-E	3	11.1	13.34	148.1	17,507	78.7	451	15.91	3.05
APC	5.5x4.5-E	3	11.1	13.67	151.7	17,388	74.1	456	16.08	3.01
APC	6x4-E	3	11.1	14.87	165.1	17,003	64.4	630	22.22	3.82
APC	7x4-SF	3	11.1	21.82	242.2	13,985	53.0	840	29.63	3.47
APC	7x5-E	3	11.1	24.02	266.6	13,272	62.8	797	28.11	2.99
FC	5x4.5	3	11.1	8.66	96.1	19,061	81.2	428	15.10	4.45
FC	5x4.5x3	3	11.1	12.38	137.4	17,825	76.0	534	18.84	3.89
FC	6x4.5	3	11.1	15.47	171.7	16,792	71.6	721	25.43	4.20
GemFan	5x3	3	11.1	6.67	74.0	19,801	56.3	374	13.19	5.05
HQ	5x4	3	11.1	7.13	79.1	18,182	68.9	373	13.16	4.71
HQ	5x4x3	3	11.1	9.25	102.7	17,401	65.9	449	15.84	4.37
HQ	5x4.5-BN	3	11.1	11.17	124.0	16,902	72.0	487	17.18	3.93
HQ	6x3	3	11.1	7.34	81.5	18,128	51.5	419	14.78	5.14
HQ	6x4.5	3	11.1	13.53	150.2	16,206	69.1	645	22.75	4.29
HQ	6x4.5x3	3	11.1	17.60	195.4	15,137	64.5	762	26.88	3.90
HQ	7x4	3	11.1	20.71	229.9	14,250	54.0	850	29.98	3.70
HQ	7x4.5	3	11.1	20.31	225.4	14,351	61.2	865	30.51	3.84
Prop Manf.	Prop Size	Li-Po Cells	Input Voltage	Motor Amps	Input Watts	Prop RPM	Pitch Speed in MPH	Thrust Grams	Thrust Ounces	Thrust Eff. Grams/W
APC	5.25x4.75-E	4	14.8	17.29	255.9	20,560	92.5	603	21.27	2.36
APC	5.5x4.5-E	4	14.8	17.87	264.5	20,436	87.1	635	22.40	2.40
APC	6x4-E	4	14.8	20.15	298.2	19,829	75.1	837	29.52	2.81
FC	5x4.5	4	14.8	10.89	161.2	22,511	95.9	588	20.74	3.65
FC	5x4.5x3	4	14.8	16.43	243.2	20,828	88.8	718	25.33	2.95
FC	6x4.5	4	14.8	20.09	297.3	19,809	84.4	998	35.20	3.36
HQ	4x4.5-BN	4	14.8	10.45	154.7	22,661	96.6	477	16.83	3.08
HQ	5x3	4	14.8	6.88	101.8	23,580	67.0	442	15.59	4.34
HQ	5x4	4	14.8	10.22	151.3	22,739	86.1	589	20.78	3.89
HQ	5x4x3	4	14.8	13.26	196.2	21,763	82.4	710	25.04	3.62
HQ	5x4.5-BN	4	14.8	16.10	238.3	20,899	89.1	744	26.24	3.12
HQ	6x3	4	14.8	11.06	163.7	22,512	64.0	679	23.95	4.15
HQ	6x4.5	4	14.8	19.62	290.4	19,948	85.0	982	34.64	3.38

Figure C.2: Official Test Results for Cobra Motors

C.3 Combined Simulated Torque Responses

The process in Sec:3.3.2 applied simulation tests to the generalized torque responses derived in Sec:3.3.1. Previous simulations only considered separate singular perturbations in either λ_i or α_i rotational positions alone. The generalized torque response $\hat{V}(\alpha_i, \lambda_i)$, from Eq:3.86g, acts as a response to *net motor module* rotations of both inner and middle ring servos λ_i and α_i respectively.

The plot in Fig:C.3 shows varying steps for $\Delta\lambda_i$ with a constant $\Delta\alpha_i = \pi/4$ step. The error between an estimated value $\hat{V}(\alpha_i, \lambda)$, with a linearized rotation partial derivative, and the true $\tilde{V}(\alpha_i, \lambda)$ is shown in Fig:C.3b. That error is mostly of the order $\times 10^{-4}$ [N.m]; whilst both $\hat{V}(\alpha_i, \lambda_i)$ and $\tilde{V}(\alpha_i, \lambda_i)$ are in the order of $\times 10^{-1}$ [N.m].

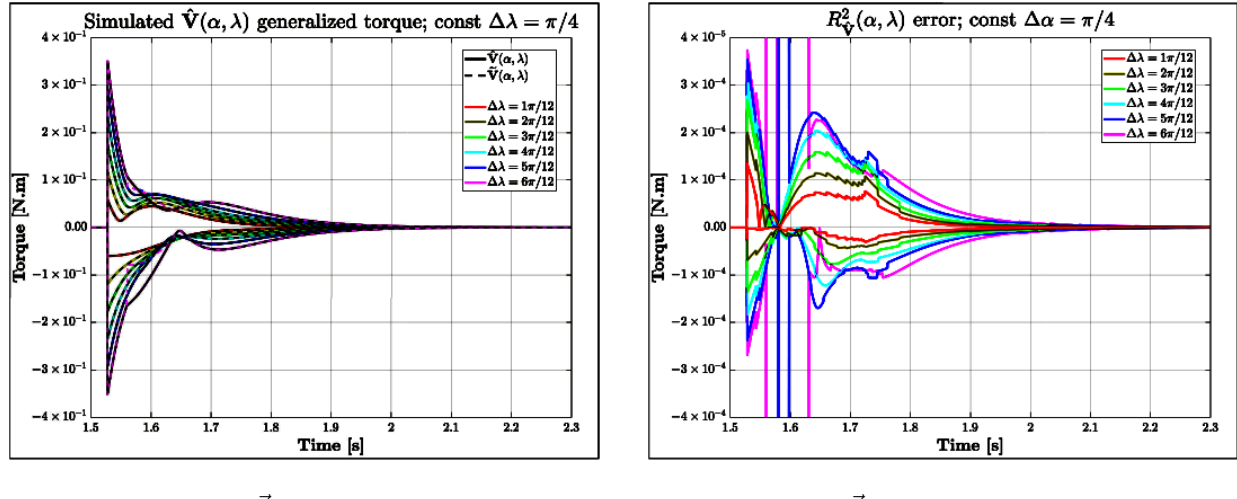


(a) Torque response $\hat{V}(\alpha_i, \lambda_i)$ to steps in $\Delta\lambda_i$ only

(b) Error for $\hat{V}(\alpha_i, \lambda_i)$ for steps in $\Delta\lambda_i$ only

Figure C.3: Step changes in $\Delta\lambda_i$ with constant $\Delta\alpha_i = \pi/4$

Similarly, Fig:C.4a shows the same tests run for varying step sizes of $\Delta\alpha_i$ with a constant step size for $\Delta\lambda_i = \pi/4$. Again, the plot Fig:C.4b shows the error which, on average, is in the order of $\times 10^{-4}$ [N.m]. The error between a simplified $\hat{V}(\alpha_i, \lambda_i)$ and the true $\tilde{V}(\alpha_i, \lambda_i)$ only becomes significant as the step size $\Delta\alpha_i$ tends to $\pi/2$.



(a) Torque response $\hat{V}(\alpha_i, \lambda_i)$ to steps in $\Delta\alpha_i$ only

(b) Error for $\hat{V}(\alpha_i, \lambda_i)$ for steps in $\Delta\alpha_i$ only

Figure C.4: Step changes in $\Delta\alpha_i$ with constant $\Delta\lambda_i = \pi/4$

It is interesting to note that positive and negative step directions are not symmetrical in their responses for Fig:C.3a and Fig:C.4a. This is as a result of the gyroscopic cross product in the calculations for $\hat{V}(\alpha_i, \lambda_i)$. Both tests shown in Fig:C.3 and Fig:C.4 further corroborate the model proposed previously in Sec:3.3.1.

C.4 Combined Torque Response Tests

Bibliography

- [1] Parrot AG. Parrot ar drone 2.0. <https://www.parrot.com/fr/drones/parrot-ardrone-20-elite-edition#technical>, 2016. [Accessed:2017-01-16].
- [2] Yazan Al-Rihani. *Development of a dual axis tilt rotorcraft uav: Design, prototyping and control.*, volume 1. Cranfield University: School of Engineering, 2012.
- [3] N. Amiri, A. Ramirez-Serrano, and Davies R. Modelling of opposed lateral and longitudinal tilting dual-fan unmanned aerial vehicle. *International Federation of Automatic Control*, pages 2054–2059, September 2011.
- [4] APMCopter. Arducopter main page. Website: <http://www.arducopter.co.uk/>, 6 2016. Arducopter (APM) Official Website.
- [5] E. Balasubramanian and R. Vasantharaj. Dynamic modelling and control of quadrotor. *International Journal of Engineering and Technology*, pages 63–39, February 2013.
- [6] P. Baldi, B. Mogens, P. Castaldi, N Mimmo, and S. Simani. Adatpive ftc based on control allocation and fault accomodation for satellite reaction wheels. In *Conference on Control and Fault-Tolerant Systems*, volume 3, pages 1–6, 9 2016.
- [7] M. Bangura and R. Mahony. Non-linear dynamic modelling for high performance control of a quadrotor. In *Australasian Conference on Robotics and Automation, Victoria University of Wellington*. Victoria University of Wellington, 12 2012. Published in Conference Proceedings.
- [8] M. Bangura, M Melega, R. Naldi, and R. Mahony. Aerodynamics of rotorblades for quadrotors. Report, Colaboration: Australian National University & University of Bologna, 1 2016. ArXiv Published:<https://arxiv.org/abs/1601.00733>.
- [9] T. Barfoot, J. Forbes, and P. Furgale. Pose estimation using linearized rotations and quaternion algebra. Report, University of Toronto, Institute for Aerospace Studies, 6 2011.
- [10] Mohd Ariffanan Basri, Abdul R. Husain, and Kumeresan A. Danapalasingam. Intelligent adaptive backstepping control for mimo uncertain non-linear quadrotor helicopter systems. *Institute of Measurement Control Transactions*, pages 1–17, 2014.
- [11] BetaFlight. Betaflight fc4 repo. Forked from the CleanFlight repo,<https://github.com/betaflight/betaflight>, 2016. [Accessed:2016-9-17].
- [12] BLHeli. Blheli master branch (silabs). <https://github.com/bitdump/BLHeli/tree/master/SiLabs>, 2016. [Accessed:2016-11-05].
- [13] Charles Blouin and Eric Lanteigne. Pitch control on an oblique active tilting bi-rotor. *International Conference on Unmanned Aircraft Systems*, pages 791–799, May 2014.
- [14] R. Bodrany, W. Steyn, and M. Crawford. In-orbit estimation of the inertia matrix and thruster parameters of uosat-12. In *Conference on Small Satellites*, volume 14, pages 1–11. American Institute of Aeronautics and Astronautics, 2000.

- [15] Edward Boje. Lyapunov stability analysis. Report, University of Kwazulu-Natal: School of Electrical, Electronic and Computer Engineering, 1 2005. Course notes for: Control Systems ENEL4CN.
- [16] Hossein Bolandi, Mohammed Rezaei, Rezo Mohsenipour, Hossein Nemati, and Seed Majid Smailzadeh. Attitude control of a quadrotor with optimized pid. *Intelligent Control and Automation*, pages 335–342, August 2013.
- [17] S. Bouabdallah and R. Siegward. Backstepping and sliding mode techniques applied to an indoor micro quadrotor. *IEEE International Conference on Intelligent Robots and Systems*, pages 2247–2252, 4 2005.
- [18] S. Bouabdallah and R. Siegwart. Full control of a quadrotor. *IEEE International Conference on Intelligent Robots and Systems*, pages 153–158, 11 2007. Written for Autonomous Systems Lab at Swiss Federal Institute of Technology.
- [19] Samir Bouabdallah, Andre Noth, and Roland Siegward. Pid vs lq control techniques applied to an indoor micro quadrotor. *IEEE International Conference on Intelligent Robots and Systems*, pages 2451–2456, 9 2004.
- [20] A.R.S Bramwell, D. Balmford, and G. Done. *Bramwell's Helicopter Dynamics*, chapter 1-3, pages 1–144. Elsevier Ltd, 2 edition, 1999.
- [21] J. Brandt, R. Deters, G. Ananda, and M. Selig. Uiuc propeller data site. Univesity of Illinois Urbana-Champaign; Department of Aerospace Engineering: <http://www.steadidrone.com/>, 2008. [Accessed:2016-13-12].
- [22] J. Brandt and M. Selig. Propeller performance data at low reynolds numbers. *American Institute of Aeronautics and Astronautics Sciences Meeting, 49th*, pages 1–18, January 2011.
- [23] D. Brescianini, M. Hehn, and R D'Andrea. Nonlinear quadrocopter attitude control. Technical report, Institute for Dynamic Systems and Control, ETH Zurich, 10 2013.
- [24] Z. Cai and M. S. de Queiroz. Asymptotic adaptive regulation of parametric strict-feedback systems with additive disturbance. In *ME Graduate Student Conference*, pages 3–5, Baton Rouge, Louisiana, 4 2005. LSU Graduate School.
- [25] Jian Chen, Aman Behal, and Darren M. Dawson. Adaptive output feedback control for a class of mimo nonlinear systems. In *Proceedings of the American Control Conference*, pages 5300–5306, Minneapolis, Minnesota, US, 6 2006. American Control Conference.
- [26] Arindam B. Chowdhury, Anil Kulhare, and Guarav Raina. A generalized control method for tilt-rotor uav stabilization. *IEEE International Conference on Cyber Technology in Automation, Control and Intelligent Systems*, pages 309–314, May 2012.
- [27] CleanFlight. Cleanflight repo. <https://github.com/cleanflight/cleanflight>, 2016. [Accessed:2016-11-13].
- [28] Dominic Clifton. Spracing f3 deluxe flight controller. <http://seriouslypro.com/spracingf3>, 2015. [Accessed:2016-10-04].
- [29] R.F. de Olivera, F.T. de Salvi, and E.M. Belo. Dynamic modelling, simulation and control of an autonomous quadcopter aircraft. *International Congress of Mechanical Engineering*, pages 1–9, November 2009.
- [30] Innov8tive Designs. Cobra cm2208/2000 motors. <http://innov8tivedesigns.com/cobra-cm-2208-20-motor-kv-2000>, 2016. [Accessed:2016-06-10].

- [31] D. DGaranin. Rotational motion of rigid bodys. Technical report, City University of New York, Department of Engineering, 11 2008. Course Notes cited from: http://www.lehman.edu/faculty/dgaranin/teaching-analytical_mechanics-Fall-2008.php.
- [32] Chen Diao, Bin Xian, Qiang Yin, Wei Zeng, Haotao Li, and Yungao Yang. A nonlinear adaptive control approach for quadrotor uavs. In *Asian Control Conference Proceedings*, volume 8, pages 223–228, Kaohsiung, Taiwan, 5 2011. Asian Control Conference.
- [33] DJI Drones. Dji inspire one. <http://www.dji.com/product/inspire-1>, 2016. [Accessed:2016-07-10].
- [34] DJI Drones. Dji phantom. <http://www.dji.com/products/phantom>, 2016. [Accessed:2016-06-12].
- [35] Honeywell Solid State Electronics. Hmc5833 magnetometer datasheet. Advanced Information Data Sheet, 10 2010. Available From:<https://strawberry-linux.com/pub/HMC5833L.pdf>.
- [36] Internation Organization for Standardization/International Electrotechnical Commission. Programming language c. Open PDF for Library:<http://www.open-std.org/jtc1/sc22/wg14/www/docs/n1124.pdf>, 2005. Section 7.12.4.4:The atan2 functions, Page 219.
- [37] Emil Fresk and George Nikolakopoulos. Full quaternion based attitude control for a quadrotor. *European Control Conference*, pages 3864–3869, 6 2013.
- [38] Pau. S Gasco. *Development of a Dual Axis Tilt Rotorcraft UAV: Modelling, Simulation and Control*, volume 1. Cranfield University: School of Engineering, 2012.
- [39] J. Gertler. V-22 osprey tilt-rotor aircraft: Background and issues for congress. Report, Congressional Research Service, 3 2011.
- [40] GetFPV.com. Cobra 2208 2000kv bldc motor product page. <http://www.getfpv.com>, 2016. [Accessed:2017-02-19].
- [41] HiSystems GmbH. Mikrokopter quadroxl. <http://www.mikrokopter.de/en/products/kits>, 2016. [Accessed:2016-06-13].
- [42] G. Golub and C. Van Loan. *Matrix Computations*, volume 3. Johns Hopkins University Press., 1996.
- [43] Basile Graf. Quaternions and dynamics. Publication for Mathematics - Dynamical Systems, 2 2007.
- [44] Gary R. Gress. Lift fans as gyroscopes for controlling compact vtol air vehicles: Overview and development status of oblique active tilting. In *American Helicopter Society Annual Forum*, volume 63, Virginia Beach, 5 2007. American Helicopter Society, American Helicopter Society Inc. Forum Proceedings.
- [45] Gary R. Gress. *Passive Stabilization of VTOL Aircraft Having Obliquely Tilting Propellers*. University of Calgary, Department of Mechanical Engineering, Calgary, Alberta, 2014.
- [46] Karsten Groekatthfer and Zizung Yoon. Introudction into quaternions for spacecraft attitude representation. *Technical University of Berlin: Department of Astronautics and Aeronautics*, pages 1–16, May 2012.
- [47] N. Guenard, T. Hamel, and V. Moreau. Dynamic modelling and control strategy for an x4-flyer. *International Conference on Control and Automation*, pages 141–146, June 2005.

- [48] M. Hehn and R. D'Andrea. Quadrocopter trajectory generation and control. In *International Federation of Automatic Control Conference*. Institute for Dynamic Systems and Control, Swiss Federal Institute of Technology; Zurich, 2011. Published in Conference Proceedings.
- [49] Drone HiTech. Xrotor 20a esc. http://dronehitech.com/wp-content/uploads/2016/04/IMG_0524.jpg, 2016. [Accessed:2016-11-05].
- [50] HobbyKing. Orangerx rpm sensor. http://www.hobbyking.com/hobbyking/store/_61511_Orange_RPM_Sensor.html, 2016. [Accessed:2016-10-09].
- [51] HobbyKing. Rotorstar super mini s-bec. http://www.hobbyking.com/hobbyking/store/_33987_RotorStar_Super_Mini_S_BEC_6S_10A.html, 2016. [Accessed:2016-10-08].
- [52] HobbyKing. Signal converter module sbus-ppm-pwm. http://www.hobbyking.com/hobbyking/store/_88384_Signal_Converter_Module_SBUS_PPM_PWM_S2PW_.html, 2016. [Accessed:2016-10-09].
- [53] HobbyKing.com. A281 920kv brushless outrunn with variable pitch prop assembly. https://hobbyking.com/en_us/a281-920kv-brushless-outrunner-w-variable-pitch-prop-assembly.html?store=en_us, 2016. [Accessed:2017-19-0].
- [54] HobbyKing.com. Hobby king: The ultimate hobby experience. <http://www.hobbyking.com/hobbyking/store/index.asp>, 2016. [Accessed:2016-06-12].
- [55] G. Hoffmann, H. Huang, S. Waslander, and C. Tomlin. Quadrotor helicopter flight dynamics and control: Theory and experiment. In *Guidance, Navigation and Control Conference and Exhibit*, pages 1–19, Hilton Head, South Carolina, 8 2010. American Institute of Aeronautics and Astronautics, American Institute of Aeronautics and Astronautics. Derivation of advanced aerodynamic affects on STARMAC Quadrotor Prototype.
- [56] P.A Hokayem and E. Gallestey. Lyapunov stability theorem. Course notes: Nonlinear systems and control, Swiss Federal Institute of Technology: Department of Information Technology and Electrical Engineering, 4 2015.
- [57] E.L Houghton and E.W Carpenter. *Aerodynamics for Engineering Students*, volume 5. Butterworth-Heinemann, 2003.
- [58] InvenSense Inc. Mpu6050 6-axis gyroscope/accelerometer datasheet. Product Specification Data Sheet, 8 2013. Available From:https://www.cdiweb.com/datasheets/invensense/MPU-6050_DataSheet_V3%204.pdf.
- [59] Digi International. Xbee/xbee pro rf modules. Technical Data Sheet, 9 2009. Available From:<https://www.sparkfun.com/datasheets/Wireless/Zigbee/XBee-Datasheet.pdf>.
- [60] W. Jia, Z. Ming, Y. Zhiwei, and L. Bin. Adaptive back-stepping lpv control of satellite attitude maneuvers with sum of squares. In *World Congress on Intelligent Control and Automation*, volume 8, pages 1747–1752. IEEE, 7 2010.
- [61] Tor A. Johansen and Thor I. Fossen. Control allocation - a survey. *Automatica*, 45:10871103, 11 2012. Prepared for: Department of Engineering Cybernetics - Norwegian University of Science and Technology.
- [62] Tor A. Johansen, Thor I. Fossen, and Petter Tondel. Efficient optimal constraint control allocation via multi-parametric programming. White paper, Department of Engineering Cybernetics, Nowegian University of Science and Technology, N/A 2005.

- [63] Tor A. Johansen and Johannes Tjnnns. Adaptive control allocation. White paper, Department of Engineering Cybernetics, Norwegian University of Science and Technology, N/A 2008.
- [64] S.M Joshi, A.G Keklar, and J.T Wen. Robust attitude stabilization of spacecraft using nonlinear feedback. *IEEE Transactions on Automatic Control*, pages 1800–1803, October 1995.
- [65] C. Karen Liu and S. Jain. Tutorial on multibody dynamics. Georgia Institute of Technology: Online Course Content, N/A, 10 2012. Available at: http://www.cc.gatech.edu/~karenliu/Home_files/dynamics_1.pdf.
- [66] Farid Kendoul, Isabelle Fantoni, and Rogelio Lozano. Modeling and control of a small autonomous aircraft having two tilting rotors. *IEEE Conference on Decision and Control*, pages 8144–8149, December 2005.
- [67] A. Koshkouei, A. Zinober, and K. Burnham. Adaptive sliding mode backstepping control of nonlinear systems with unmatched uncertainty. *Asian Journal of Control*, pages 447–453, 12 2004.
- [68] P. Krishnamurthy and F. Khorrami. Adaptive backstepping and theta-d based controllers for a tilt-rotor aircraft. *Mediterranean Conference on Control and Automation*, pages 540–545, June 2011.
- [69] Raymond Kristiansen and Per J. Nicklasson. Satellite attitude control by quaternion-based backstepping. *American Control Conference*, N/A:907–912, 6 2005. Published by Department of Computer Science, Electrical Engineering and Space Technology; Narvik University College.
- [70] Jack B. Kuipers. *Quaternions and Rotation Sequences: A Prior with Application to Orbital Aerospace and Virtual Reality*, pages 127–143. Princeton University Press, September 2002. Used for Quaternion and Rotation Matrix reference.
- [71] Peter Lambert. Nakazawa, banton and jin, bai x. Technical Report N/A, Computer and Electrical Engineering: University of Victoria, Victoria, Canada, 12 2013.
- [72] W.E. Lang and J.P Young. Effect of inertia properties on attitude stability of nonrigid spin-stabilized spacecraft. *National Aeronautics and Space Administration*, pages 1–20, 1974.
- [73] Prof Allan J. Laub. The moore-penrose pseudo inverse. UCLA Math33A Course Content, UCLA, Los Angeles, 3 2008. Course Notes cited from <http://www.math.ucla.edu/~laub/33a.2.12s/mppseudoinverse.pdf>.
- [74] Jang-Ho Lee, Byoung-Mun Min, and Eung-Tai Kim. Autopilot design of tilt-rotor uav using particle swarm optimization method. *International Conference on Control, Automation and Systems*, pages 1629–1633, October 2007.
- [75] LibrePilot. Openpilot/librepilot wiki. Website: <http://opwiki.readthedocs.io/en/latest/index.html>, 5 2016. Information wiki page for LibrePilot/OpenPilot firmware.
- [76] Hyon Lim, Jaemann Park, Daewon Lee, and H.J. Kim. Build your own quadrotor. *IEEE ROBOTICS & AUTOMATION MAGAZINE*, pages 33–45, 9 2012. Publication on Opensource Autopilot systems.
- [77] C. Liu, B. Jiang, X. Song, and S. Zhang. Fault-tolerant control allocation for over-actuated discrete-time systems. *Journal of The Franklin Institute*, 352:2297–2313, 3 2015. Research output by Nanjing College of Automation Engineering, University of Aeronautics and Astronautics.
- [78] Kilowatt Classroom LLC. Vfd fundamentals. Report, Kilowatt Classroom LLC, 2 2003.
- [79] SteadiDrone PTY LTD. Steadidrone home. <http://www.steadidrone.com/>, 2016. [Accessed:2016-06-08].

- [80] Teppo Luukkonen. Modelling and control of a quadcopter. Master's thesis, Aalto University: School of Science, Eepso, Finland, 8 2011. Independent research project in applied mathematics.
- [81] Tarek Madani and Abdelaziz Benallegue. Backstepping control for a quadrotor helicopter. *International Conference on Intelligent Robots and Systems*, pages 3255–3260, October 2006.
- [82] I. Mandre. Rigid body dynamics using euler's equations, rungekutta and quaternions. Unpublished, 2 2006.
- [83] Carlos J. Mantas and Jose M. Puche. Artificial neural networks are zero-order tsk fuzzy systems. In *IEE Transactions on Fuzzy Systems*, volume 16, pages 630–644, 6 2008.
- [84] Christopher G. Mayhew, Ricardo G. Sanfelice, and Andrew R. Teel. On quaternion based attitude control and the unwinding phenomenon. *American Control Conference*, pages 299–304, June 2011.
- [85] A. Megretski. Dynamics on nonlinear systems: Finding lyapunov functions. Technical report, Department of Electrical Engineering and Computer Sciences: Massachusetts Institute of Technology, 7 2003.
- [86] Ashfaq A. Mian and Wang Daoboo. Modelling and backstepping-based nonlinear control of a 6dof quadrotor helicopter. *Chinese Journal of Aeronautics*, 21:261–268, 3 2008. Simulated Backstepping Control.
- [87] Svein Rivli Napsholm. Prototype of a tiltrotor helicopter. Master's thesis, Norwegian University of Science and Technology: Department of Engineering Cybernetics, Norway, 1 2013.
- [88] A. Nemati and M. Kumar. Modeling and control of a single axis tilting quadcopter. *American Control Conference*, pages 3077–3082, June 2014.
- [89] Kenzo Nonami, Farid Kendoul, Satoshi Suzuki, Wei Wang, and Daisuke Nakazawa. *Autonomous Flying Robots: Unmanned Aerial Vehicles and Micro Aerial Vehicles*, chapter 2, pages 44–48. Springer Japan, 1 edition, 2010. References to Cyclic-Pitch Control relevant subsections.
- [90] Kenzo Nonami, Farid Kendoul, Satoshi Suzuki, Wei Wang, and Daisuke Nakazawa. *Autonomous Flying Robots: Unmanned Aerial Vehicles and Micro Aerial Vehicles*, chapter 8, page 166. Springer Japan, 1 edition, 2010.
- [91] Gustavo P. Oliveira. Quadcopter civil applications. Master's thesis, Informatics and Computer Engineering: University of Portugal, Portugal, 2 2014.
- [92] M. Oppenheimer, D. Doman, and M. Bolender. Control allocation for over-actuated systems. In *Mediterranean conference on Control and Automation*, volume 14, page 1, 6 2006.
- [93] OrangeRx. Orangerx r615x receiver. User Manual, 10 2014. Available From:<http://www.hobbyking.com/hobbyking/store/uploads/672761531X1606554X18.pdf>.
- [94] M. Orsag and S. Bogdan. Influence of forward and descent flight on quadrotor dynamics. Report, Department of Control and Computer Engineering, University of Zagreb, Croatia, 2 2012.
- [95] Christos Papachristos, Kostas Alexis, and Anthony Tzes. Design and experimental attitude control of an unmanned tilt-rotor aerial vehicle. *International Conference on Advanced Robotics*, pages 465–470, June 2011.
- [96] Parth N. Patel, Malav A. Patel, Rahul M. Faldu, and Yash R. Dave. Quadcopter for agricultural surveillance. In *Advance in Electronic and Electrical Engineering*, volume 3, India, 2013.
- [97] Google Patents. V22 osprey paten. <https://www.google.com/patents/US20110177748>, 2010. [Accessed:2017-03-03].

- [98] J. Peraire and S. Widnall. 3d rigid body dynamics: Euler angles. Lecture notes for Dynamics Course, 2009. Dynamics course notes, fall 2007.
- [99] J. Peraire and S. Widnall. 3d rigid body dynamics: The inertia tensor. Lecture notes for Dynamics Course, 2009. Dynamics course notes, fall 2007.
- [100] D. Peters. Eighth amendment of the civil aviation regulations. Goverment Gazette Notice, 5 2015. In Amendment to the Civil Aviation Act, 2009 (Act No.13 of 2009).
- [101] Jean-Baptiste Pomet and Laurent Praly. Adaptive nonlinear regulation: Estimation from the lyupanov equation. In *IEEE Transactions on Automatic Control*, volume 37, pages 729–740. IEEE, 6 1992.
- [102] P. Pounds, R. Mahony, P. Hynes, and J. Roberts. Design of a four-rotor aerial robot. *Australasian Conference on Robotics and Automation*, pages 145–150, November 2002.
- [103] Dmitry Prof. Garanin. Rotational motion of rigid bodies. Analytical Dynamics Course Notes, 11 2008. Content for City University of New York.
- [104] G Rajagopalan. Froudes momentum theory: (actuator disk theory). Technical report, Iowa State University, Department of Engineering, 7 2002. Course Notes cited from: <http://www.public.iastate.edu/~aero442/unit2.pdf>.
- [105] F. Ramponi and J. Lygeros. Lecture notes on linear system theory. Technical report, Department of Information Engineering, University of Brescia, 1 2015. Course Notes cited from: http://home.mit.bme.hu/~virosztek/docs/mt_literature/LectureNotes.pdf.
- [106] Beard Randal. Quadrotor dynamics and control. Report, Brigham Young University, 2 2008. Part of the Electrical and Computer Engineering Commons.
- [107] O. Rawashdeh, H.C. Yang, R. AbouSleiman, and B. Sababha. Microraptor: A low cost autonomous quadrotor system. *International Design Engineering Technical Conferences & Computers and Information in Engineering Conference*, pages 1–8, August 2009.
- [108] Anastasia Razinkove, Igor Gaponov, and Hyun-Chan Cho. Adaptive control over quadcopter uav under disturbances. *International Conference on Control, Automation and Systems*, pages 386–390, October 2014.
- [109] M.K. Rwigema. Propeller blade element momentum theory with vortex wake deflection. *International Congress of the Aeronautical Sciences, 27th*, pages 1–9, January 2010.
- [110] M. Ryll, H. Bulthoff, and P. Robuffo Giordano. Modelling and control of a quadrotor uav with tilting propellers. *IEEE International Conference on Robotics and Automation*, pages 4606–4613, May 2012.
- [111] M. Ryll, H. Bulthoff, and P. Robuffo Giordano. First flight tests of a quadrotor uav with tilting propellers. *IEEE International Conference on Robotics and Automation*, pages 295–302, May 2013.
- [112] S. Salazar-Cruz, A. Palomino, and R. Lozano. Trajectory tracking for a four rotor mini-aircraft. In *IEEE Conference on Decision and control, the European Control Conference*, pages 2505–2510, Seville, Sapin, 12 2005. IEEE, IEEE 2005.
- [113] Inc. Saleae. Logic8. <https://www.saleae.com/>, 2017. [Accessed:2017-03-12].
- [114] A. Sanchez, J. Escareo, O. Garcia, and R. Lozano. Autonomous hovering of a noncyclic tiltrotor uav: Modeling, control and implementation. *The International Federation of Automatic Control*, pages 803–808, July 2008.

- [115] J. Seddon. *Basic Helicopter Aerodynamics*, chapter 2-5, pages 4–66. BSP Professional Books, 1 edition, 1990.
- [116] K. Shoemake. Quaternions. Siggraph course lecture notes, Department of Computer and Information Science; University of Pennsylvania, N/A 1987.
- [117] Puneet Singla, Daniele Mortari, and John L. Junkins. How to avoid singularity when using euler angles? *Advances in the Astronautical Sciences*, pages 1409–1426, January 2005.
- [118] G. Slabaugh. Computing euler angles from a rotation matrix. Lecture notes, City University, London, 5 1999.
- [119] Measurement Speacialties. Ms5611 barometric pressure sensor. Technical Data Sheet, 10 2012. Available From:http://www.amsys.info/sheets/amsys.en.ms5611_01ba03.pdf.
- [120] STMicroElectronics. St-link/v2 in circuit debugger/programmer for stm32.
- [121] STMicroElectronics. Rm0316 reference manual. Online Micro-Controller Reference Manual, 3 2016. Available From:http://www.st.com/content/st_com/en/products/microcontrollers/stm32-32-bit-arm-cortex-mcus/stm32f3-series/stm32f303.html?querycriteria=productId=LN1531.
- [122] Prof S. Tavoularis. Reynolds transportation theorem. Course Notes on MCG3350 - Fluid Mechanics 1, 2008. Fluid Mechanics notes, fall 2008, http://web.mit.edu/1.63/www/Lec-notes/chap1_basics/1-3trans-thm.pdf.
- [123] Abdelhamid Tayebi and Stephen McGilvray. Attitude stabilization of a vtol quadrotor aircraft. *IEEE Transactions on Control Systems Technology*, pages 562–571, May 2006.
- [124] B. Theys, G. Dimitriadis, P. Hendrick, and J. De Schutter. Influence of propeller configuration on propulsion system efficiency of multi-rotor unmanned aerial vehicles. In *International Conference on Unmanned Aircraft Systems*, pages 195–201, Arlington, Virginia, 6 2016. IEEE, IEEE 2016.
- [125] Stephen T. Thornton and Jerry B. Marion. *Classical Dynamics of Particles and Systems*, chapter 7, pages 228–289. Thompson Brooks/Cole, 5 edition, 2003.
- [126] John Ting-Yung Wen and Kenneth Kreutz-Delgado. The attitude control problem. *IEEE Transactions on Automatic Control*, pages 1148–1162, October 1991.
- [127] David Tong. Lagrange formalism. Lectures of Classic Dynamics, Course Notes, 2005. Classical Mechanics Notes.
- [128] P. Tsotras, M. Corless, and J.m Longuski. A novel approach to the attitude control of axisymmetric spacecraft. *Automatica*, 31:1099–1112, 3 1995. Control Automatica, Printed in Great Britan.
- [129] Ultimaker. Ultimaker v2+ product page. <https://ultimaker.com/en/products/ultimaker-2-plus#volume>, 2016. [Accessed:2016-9-11].
- [130] E. van Kampen and M. M. van Paassen. Ae4301: Automatic flight control system design. Delft Centre for Systems and Control; MSc Notes, 1 2008. Course Notes cited from: <http://aerostudents.com/master/advancedFlightControl.php>.
- [131] Ronny Votel and Doug Sinclair. Comparison of control moment gyros and reaction wheels for small earth-observing satellites. In *Conference on Small Satellites*, volume 26, pages 1–7. Utah State University, 8 2012. Open access on AIAA conference website.
- [132] Tao Wang, Tao Zhao, Du Hao, and Mingxi Wang. Transformable aerial vehicle, 09 2014.

- [133] A Weiss, I. Kolmanovsky, D.S Bernstein, and A. Sanyal. Inertia-free spacecraft attitude control using reaction wheels. In *Journal of Guidance, Control and Dynamics*, volume 36, pages 1425–1439. AIAA, 8 2013.
- [134] A. Witkin and D. Baraff. Physically based modeling: Principles and practice. CMU: Online Siggraph Course notes, N/A, 9 1997. Course Notes cited from <http://www.cs.cmu.edu/~baraff/sigcourse/>.
- [135] X. Xiaozhu, L. Zaozhen, and C. Weining. Intelligent adaptive backstepping controller design based on the adaptive particle swarm optimization. *Chinese Control and Decision Conference*, pages 13–17, September 2009.
- [136] Song Xin and Zou Zaojian. A fuzzy sliding mode controller with adaptive disturbance approximation for an underwater robot. In *International Asia Conference on Informatics in Control, Automation and Robotics*, volume 2, pages 50–53, 10 2010.